Single-walled Carbon Nanotube Networks and Related Composite Materials for Gas Sensing Applications.

Gwyn P. Evans

Principal supervisor: Professor I. P. Parkin

Subsidiary supervisor: Professor N. T. Skipper

Internal examiner: Dr C. A. Howard

External examiner: Professor J. W. Gardner

A thesis submitted in partial fulfillment

of the requirements for the degree of

Doctor of Philosophy

of

University College London.

Department of Security and Crime Science, Department of Chemistry

University College London

March 18, 2018

I, Gwyn P. Evans, confirm that the work presented in this thesis is my own. Where information has been derived from other sources, I confirm that this has been indicated in the work.

Abstract

In this thesis, the gas sensing properties of single-walled carbon nanotube (SWCNT) networks and SWCNT-Zeolite composite materials were investigated in a variety of environmental conditions. The aim of the project was to establish the effect that adsorbed water vapour had on the electrical properties of SWCNT networks, along with any subsequent impact on the NO_2 sensing responses of SWCNT-based chemiresistors. Motivated by these investigations, the sensitivity of the SWCNT networks to water vapour was exploited to develop the water-assisted regeneration (WAR) method, enabling the improved recovery of the baseline sensing signal. Zeolites, known as molecular sieves due to their selective adsorption properties, were utilised in SWCNT-Zeolite composite sensing layers to reduce the cross-sensitivity of functionalised SWCNTs to water vapour.

Functionalisation of the SWCNTs with a range of anionic, cationic and non-ionic surfactants to aid solution processing was found to enhance the conductance-humidity effect, in some cases by a factor of 10. An interesting bi-directional switch in conductance change was observed when anionic (conductance decrease) *vs* cationic (conductance increase) were used.

Under experimental conditions, fluctuations in atmospheric humidity levels were shown to alter the gas sensing characteristics of the SWCNT networks. Formed from interconnected metallic and semiconducting SWCNTs, the chemiresistive sensors demonstrated increased response magnitudes, adsorption rates and recovery rates at higher levels (> 50% RH) of relative humidity.

Raman spectroscopy, UV-Vis-NIR spectroscopy, electron microscopy and electrical characterisation techniques were used in conjunction with gas sensing

experiments to study changes in the properties of the sensing elements, helping to elucidate potential mechanisms. Extraction of key sensing parameters was facilitated by the application of a model for completely irreversible adsorption of NO_2, whilst a model based on partially reversible desorption was found to best describe the sensing data.

Acknowledgements

Firstly, huge thanks go to my principle supervisor Prof. Ivan Parkin, for the guidance and opportunities he has provided throughout my PhD. His seemingly endless reservoir of encouragement has been a huge help to me over the past four years. Similarly, I would like to thank Prof. Neal Skipper, who has provided enthusiasm, much needed advice and an important alternative perspective to my work, sometimes with only a moments notice.

I must thank the Department of Security and Crime Science for providing me with the opportunity to pursue my PhD here at UCL, for which I am extremely grateful. I'd also like to thank Dr. Steve Firth and Dr. Steven Hudziak for lending their experimental expertise throughout my time in the Department of Chemistry.

I have been very fortunate to spend time working at external institutions during my project, namely with the groups of Prof. David Williams, Prof. Mark Reed, and Dr. Vandna Luthra. Thank you for making me feel so welcome in your respective countries, each secondment was a fantastic experience that I will never forget.

I wouldn't have made it through my first year in G15 without the gargantuan efforts of Emma Newton and Anupriya Naik, who dedicated significant proportions of their day to training, mentoring, and at one point first-aiding me; thank you for being so kind and patient. I have especially enjoyed the company of my lab mate Paula Tarttelin, with whom I have shared the ups and downs of the whole process. The same goes for David Buckley, whose own unique brand of guidance and friendship has led to a surprising amount of actual work, despite many Thursday afternoon brainstorming sessions, which I shall miss.

Whether in 320 or over a spot of karaoke, Monika, Nick, Emily, Will, Mike,

Helen, Carlos, Tom, Francesco and other UCL chemists have provided lots of good times; long may this continue. Likewise, I will miss daily potatoes with Alistair, Veronika, TRogers, Gibhawk, Guy, Alyson and other less frequent attendees to the Luncheon group, who have been a vital source of laughter and antics.

Thank you to Brydon Walk for reality check therapy, and to my Liverpool University friends who, despite my best efforts, keep in touch. I now have no excuse!

My extended family have been nothing but supportive and loving throughout, regardless of my boring PhD ramblings; I feel very lucky to have them. Thank you to Mum and Dad, who have always supported, encouraged, and been there for me whenever, wherever. I am grateful for the patience of Gareth and Michael, who continue to put up with my lecturing. To them, I apologise for being the favourite son.

And finally, to my worthiest adversary Anna SECReT, thank you, for everything.

"Even a broken clock is right twice a day". Dr S. Keptical.

"They say a little knowledge is a dangerous thing, but it's not one half so bad as a lot of ignorance." Terry Pratchett.

Contents

1 Introduction. 41

1.1 Motivation and objectives 41

1.2 Overview and summary 43

2 Background and literature review. 47

2.1 Introduction 47

2.2 Properties of carbon nanotubes and SWCNT networks 47

2.2.1 Historical Overview 47

2.2.2 Structure 49

2.2.3 Electronic properties 52

2.2.4 SWCNT networks for electronic applications 55

2.3 Carbon nanotube-based sensors 57

2.3.1 Chemiresistors and field effect transistors (FETs) 58

2.3.2 Chemicapacitiors 63

2.3.3 Mechanical resonators 65

2.3.4 Approaches to improve sensitivity and selectivity 65

2.3.5 Advantages and challenges 67

2.4 Mechanisms and models for SWCNT sensors 71

2.4.1 Gas adsorption 71

2.4.2 Mechanisms for conductive responses 73

2.4.3 Modelling SWCNT sensors 77

2.5 Gas sensing technologies 78

2.5.1 Defining figures of merit 79

2.5.2 Gas sensing methods 81
2.5.3 Zeolites for gas sensing 84
2.6 Thesis rationale based on literature review 86

3 Material characterisation theory and experimental methods. 93
3.1 Material characterisation theory 93
3.1.1 Raman spectroscopy 94
3.1.2 UV-Vis-NIR absorption spectroscopy 98
3.1.3 Scanning electron microscopy 100
3.1.4 Transmission electron microscopy 101
3.1.5 Thermal gravimetric analysis 101
3.1.6 Attenuated total reflectance-Fourier transform infrared spectroscopy 102
3.1.7 Energy dispersive X-ray spectroscopy 103
3.2 Electronic characterisation 103
3.2.1 Current-voltage device characteristics 103
3.2.2 Conductance-temperature measurements 104
3.2.3 Hot-probe method 105
3.3 Experimental methods 106
3.3.1 Sample preparation, SWCNT solution processing and surfactant functionalisation 106
3.3.2 Device fabrication 108
3.3.3 SWCNT-zeolite composite 109
3.3.4 Gas sensing experimental setup 110
3.3.5 Measurement circuit 114
3.3.6 Testing procedure and protocol 116
3.4 Determination of errors 117
3.4.1 Gas sensing errors 117
3.4.2 Characterisation errors 119

4 Study I: Changes in SWCNT network conductance on exposure to water vapour. 120

4.1 Introduction . . . 120

4.2 Experimental . . . 122

4.2.1 Device fabrication . . . 122

4.2.2 Material and device characterisation . . . 125

4.2.3 Humidity testing procedure . . . 127

4.3 Results . . . 128

4.3.1 Material characterisation . . . 128

4.3.2 Bidirectional conductance switching . . . 134

4.3.3 Functionalised SWCNT networks for humidity sensing . . . 146

4.4 Conclusion . . . 147

5 Study II: Water-assisted regeneration (WAR) of SWCNT networks for NO_2 gas sensing. 149

5.1 Introduction . . . 149

5.2 Experimental . . . 150

5.2.1 Device fabrication . . . 150

5.2.2 Characterisation techniques . . . 151

5.2.3 Water-assisted regeneration (WAR) testing procedure . . . 151

5.3 Results . . . 152

5.3.1 Material characterisation . . . 152

5.3.2 SWCNT sensor drift due to irreversible adsorption of NO_2 . 158

5.3.3 Water-assisted regeneration (WAR) of SWCNT networks . . 161

5.3.4 Applying the irreversible adsorption model . . . 162

5.3.5 Figures of merit for SWCNT network sensors . . . 167

5.3.6 NO_2 sensing calibration curves . . . 180

5.4 Conclusion . . . 182

6 Study III: Sensing NO_2 in humid environments with SWCNTs. 184

6.1 Introduction . . . 184

6.2 Experimental . . . 185
6.2.1 Device fabrication . . . 185
6.2.2 Material characterisation . . . 186
6.2.3 Current-voltage device characterisation . . . 186
6.2.4 NO_2 testing procedure . . . 187
6.3 Results . . . 187
6.3.1 Material characterisation . . . 187
6.3.2 Conductive responses to NO_2 in humid conditions . . . 194
6.3.3 Response and recovery rates . . . 199
6.3.4 Thickness dependent responses . . . 205
6.4 Conclusion . . . 206

7 Study IV: Reducing cross-sensitivity of SWCNT networks to water vapour using zeolites. 209

7.1 Introduction . . . 209
7.2 Experimental . . . 211
7.2.1 Device fabrication . . . 211
7.2.2 Material characterisation . . . 212
7.2.3 Cross-sensitivity testing procedure . . . 213
7.3 Results . . . 215
7.3.1 Material characterisation . . . 215
7.3.2 SWCNT-Zeolite composites . . . 218
7.3.3 Mixed layer sensor configuration . . . 222
7.3.4 Top layer sensor configuration . . . 231
7.3.5 SWCNT-Zeolite sensor characteristics and regeneration . . . 232
7.4 Conclusion . . . 234

8 Conclusion 236

8.1 Conclusions . . . 236
8.1.1 Introduction . . . 236

8.1.2 Summary of SWCNT network conductance-humidity behaviour . . . 236
8.1.3 Summary of NO_2 sensing in humid conditions . . . 238
8.1.4 Summary of SWCNT-Zeolite composites for gas sensing . . 239
8.1.5 Thesis overview conclusions . . . 239
8.2 Future work . . . 241

Appendices **244**

A Motivation for the experiments carried out in the project **244**

B Method for extraction of key SWCNT sensing parameters from sensor data **250**

B.1 Testing implementation of method by calculating S_{max} and k values reported in the literature . . . 250
B.1.1 (a) DNA functionalised SWCNT sensors detecting the analyte $SOCl_2$ . . . 250
B.1.2 (b) SDS functionalised SWCNT sensors detecting the analyte DMMP . . . 252
B.1.3 Root finding algorithm to find k numerically . . . 254

C Curve fitting procedure using Origin Pro 2017 to extract sensing parameters from data. **255**

C.1 NO_2 sensing responses for SWCNT-based sensors fitted using the Origin Pro 2017 fitting tool and the irreversible model. . . . 255
C.2 NO_2 sensing responses for SWCNT-based sensors fitted using the Origin Pro 2017 fitting tool and the partially reversible model. . . . 256
C.3 Using the Origin Pro 2017 fitting tool to fit sensor desorption curves. 260

D Potentiostat measurement circuit **262**

E Papers published from this thesis. **263**

Bibliography **282**

List of Figures

2.1 (a) A representation of a graphene lattice, showing the defined chiral vector $\mathbf{C}_h$, the unit vectors $\mathbf{a}_1$ and $\mathbf{a}_2$ and the translational vector $\mathbf{T}$ for an un-rolled (*6,3*) SWCNT. The so called armchair (red) and zig-zig (blue) vectors are shown. (b) the (*n,m*) index condition determining whether a m-SWCNT or a sc-SWCNT is obtained from the rolled up graphene lattice and an armchair (red), zig-zig (blue) or chiral nanotube structure. (c) Carbon atom in graphene lattice with three in plane σ (s, p_x, p_y) orbitals and the π (p_z) orbital perpendicular to the sheet. Figure is adapted from [53] and [54]. 51

2.2 Schematic representation of band theory depicting the position of the Fermi level in (a) insulating, (b) semiconducting or (c) conducting materials relative to the energy of the valance and conduction bands in a crystalline solid. 52

2.3 (a) A schematic representation of the density of states (DOS) for metallic and semiconducting nanotubes. The black arrows denote the allowed transitions between the van Hove singularities (vHS), where E_{11}^{M} denotes the lowest energy transition between energy levels in a m-SWCNT, and E_{22}^{S} denotes the second transition for a sc-SWCNT. For a metallic nanotube, the density of states at the Fermi level (E_F) is non-zero, whereas an energy band gap exists between transitions for semiconducting nanotubes in which $E_F = 0$. (b) A Kataura plot showing the transition energy as a function of nanotube diameter for sc-SWCNTs (• and ∘) and m-SWCNTs (⋆). This can be used to identify SWCNT species from optical spectra. Figure is adapted from [58] and [56] 54

2.4 (a) Optical image of top gated SWCNT thin film transistor printed on flexible Kapton, adapted from [68]. (b) An example of a macroscopic CNT wire used to bridge copper connectors adapted from [35]. (c) A flexible electroluminescent device formed using an ink-jet printed CNT film, adapted from [69]. 56

2.5 (a) A schematic diagram of a carbon nanotube field-effect transistor device (CNTFET). A SWCNT network connects the source and drain electrode, which is separated from the back Si gate used to control conduction by an insulating SiO_2 layer. (b) A plot of applied gate voltage (V_{Gate}) *vs* normalised conductance G/G_0, showing the changes in conductance and curve shape observed from the baseline conductance (black line) to increasing concentrations of NO_2 or NH_3, adapted from [75]. 59

2.6 (a) A schematic diagram of a SWCNT network chemiresistor. SWCNTs are deposited across interdigitated gold electrodes on an insulating Al_2O_3 substrate, across which the device conductance is measured with an applied bias of 0.1 V. A molecule such as NO_2 present on the tube surfaces causes an increase in measured conductance. Top-left inset shows a scanning electron microscope (SEM) image of the SWCNT network. 61

2.7 (a) Schematic diagram of the dual operation SWCNT network chemiresistor/ chemicapacitor setup and (b) the concurrent normalised conducive (green) and capacitive (red) responses to injections of DMMP vapour, adapted from the work by Snow *et al.* [91]. 64

2.8 A diagram depicting a cross-sectional view of a SWCNT bundle with potential gas adsorption sites (gas molecules represented by black circles). Figure is adapted from [126]. 73

2.9 A schematic diagram depicting three potential gas sensing mechanisms for SWCNTs depending on m-SWCNT percolation and network density. (i) Charge transfer directly changing the number of charge carriers in the SWCNTs, (ii) Modulation of the Schottky barrier between m-SWCNTs and sc-SWCNTs (iii) Change in Schottky barrier height between individual SWCNTs and metallic contacts. The mechanisms depicted are based on those summarised by Mittal *et al.* [135] and the energy band diagram for the Schottky barrier is based on a description by Suehiro *et al.* [136]. E_f indicates the Fermi level, E_v the valance band, E_c the conduction band, E_g is the band gap, ϕ_B the Schottky barrier height, ϕ_B is the work function of the metal required to remove an electron in a vacuum and χ_s is the electron affinity for the sc-SWCNT. 75

2.10 Faujasite type zeolite with an aluminosilicate framework viewed along the [111] direction [164]. (b) Faujasite type zeolite framework viewed along the [110] direction [164] with pore diameter of 8.0 $\AA$ [165].(c) Schematic diagram of MOS/zeolite composite film sensor [163]. 85

3.1 Raman spectra showing the intensity of the Raman signal for HiPco DOC SWCNTs deposited on a glass slide. The key spectral features include (i) the radial beathing modes (RBMs), (ii) the defect mode (D-band), (iii) the graphite mode (G-band), (iv) the G′ (2D-band). Some of the features change with laser wavelength (here λ = 532 nm). 95

3.2 Raman spectra showing the difference in G^+ and G^- features for (a) HipCo and (b) CoMoCat SWCNTs. Typically, a higher proportion ($\approx$ 90%) of sc-SWCNTs are found in the raw CoMoCat sample compared to HiPco samples ($\approx$ 66%), resulting in the difference in spectral features. Laser wavelength λ = 488 nm. 97

3.3 UV-Vis-NIR absorption spectra, displaying the range of metallic and semiconducting tube species present in a HiPco DOC SWCNT solution (diluted to 0.003 mg ml^{-1}). 99

3.4 (a) A schematic diagram of the hot-probe setup in which a soldering iron is used to heat the positive DMM probe, inducing a negative change in potential across the SWCNT network indicating *p*-type character. (b) An adapted setup to expose a segment of the film to water vapour, further changing the measured surface potential to investigate the effect of anionic and cationic surfactants in the film. . 105

3.5 The chemical structure of the surfactants used for the non-covalent functionalisation of SWCNTs in the current thesis. (a) Sodium deoxycholate (DOC), (b) Sodium cholate (SC), (c) Hexadecyltrimethylammonium bromide (CTAB), (d) Hexadecyltrimethylammonium p-toluenesulfonate (CTAT), (e) Triton X-100. Chemical structures are adapted for the figure from the RSC ChemSpider database [211] 107

3.6 Photographs of a SWCNT aqueous solution before and after the addition of sodium deoxycholate (DOC) and ultrasonication. The various possible arrangements of surfactants forming micelles around the SWCNTs to aid dispersion in water is also shown (a-c), adapted from [214]. 108

3.7 Example photographs of the fabrication process for the SWCNT network devices used in the current thesis. (i) Deposition of the SWCNT solution *via* drop coating with a removable mask covering the gold electrodes. (ii) After drying at 50 °C in air on a hot plate for 30 minutes, the mask is removed and the exposed electrodes are cleaned with ethanol. (iii) To form the SWCNT-Zeolite top layer devices steps (i) an (ii) are repeated using the zeolite ethanol solution. (iv) The devices (3 × 3 mm) are wire bonded to the sensor housing to complete the fabrication process. 109

3.8 A photograph of AA-Rig showing the controlled flow delivery setup, as well as the testing cell and various components. The rig was built and designed by Dr. Ayo Afonja [226], and has been adapted to include an internal humidity meter and additional flow meters. 112

3.9 A schematic of AA-Rig showing the flow delivery configuration for mixing of gases and generation of different testing chamber humidity levels. The rig was designed and built by Dr. Ayo Afonja [226], and has been adapted to include an internal humidity meter and additional flow meters. 113

3.10 A plot of the percentage change in resistance (left axis) of HiPco SWCNT DOC sensors when the flow rate (right axis) is reduced from 1 L min^{-1} to 0.75 L min^{-1}, 0.5 L min^{-1} and then to 0.25 L min^{-1} on AA-Rig. A 0.1 % change in resistance is observed. 114

3.11 The humidity level (RH %) as measured by an internal humidity meter when the mixing ratios of dry to wet air are varied between 100:0, 75:25, 50:50 and 25:75 on AA-Rig. 115

3.12 Inverting operational amplifier element of the potentiostat circuit. The probe voltage (V_{SD}), known negative feedback resistor (R_{fb}) and measured potential across the sensor (V_{out}) are used to calculate the resistance (R_{sensor}) of the sensor as per equation 3.5. Adapted from [226]. 116

4.1 Optical image of (a) a side on view of a thick HiPco DOC SWCNT network deposited on an alumina chip, (b) a thick HiPco DOC SWCNT network deposited on an alumina chip between interdigitated gold electrodes of 175 μm separation and (c) a thin HiPco DOC SWCNT network deposited on an alumina chip between interdigitated gold electrodes of 175 μm separation. 122

4.2 Schematic representation of (a) the surfactant functionalised HiPco SWCNTs deposited on an alumina substrate between interdigitated gold electrodes. The conductance (G) across the formed percolating network is measured in both dry and humid conditions. An SEM image of a typical SWCNT network is inset top-left. A representation of the induced electrostatic potential upon exposure to water vapour is shown in (b) for cationic and (c) anionic surfactant containing networks, with the respective increase (+ΔG) and decrease (-ΔG) in conductance indicated when the relative humidity (RH) increases. 128

4.3 SEM micrographs at (a) ×1,000 (b) ×20,000 (c) ×30,000 (d) ×50,000 magnification showing gold coated SWCNT bundles from a sample of raw HiPco powder. 129

4.4 UV-Vis absorption spectra obtained using an Elmer Lambda 950 spectrophotometer for aqueous solutions of HiPco SWCNTs non-covalently functionalised with (a) DOC, (b) SC, (C) CTAB and (d) CTAT. The inset top-right plot shows the shift in the 705-775 nm range peaks for the respective samples relative to (e) dry HiPco DOC on a quartz slide. (a)-(d) are offset by 0.05 absorbance for clarity and were 100 X dilutions of the initial concentrated solutions. 130

4.5 UV-Vis-NIR absorbance data for (a) HiPco DOC, (b) HiPco CTAB, (c) HiPco Triton X-100, (d) HiPco SC, (e) HiPco CTAT and (f) HiPco control (surfactant free) solutions. The legend indicates the volume of 1 X concentrated HiPco SWCNT solution added to 3.5 ml of deionised water to achieve the dilutions required to measure absorbance over a range of concentrations. A linear fit was applied to the Absorbance vs HiPco SWCNT volume data in accordance with the Beer-Lambert law to calculate the concentration of the concentrated 1 X HiPco SWCNT solutions. 131

4.6 Raman spectroscopy data for the dry (▪) and wet (•) HiPco control (surfactant free) samples. (a) The ratio of the G^+-bands at 1594 cm^{-1} to D-band at 1295 cm^{-1} indicates good sample purity. (b) The radial breathing modes (RBMs) in the range 100 cm^{-1} to 500 cm^{-1} suggest that nanotubes of different chirality and thus electronic type are also present in the deposited layer.(c) G′-band feature (2600 cm^{-1}). Laser wavelength λ = 785 nm at 1 mW power. 132

4.7 Raman spectroscopy data for the dry (▪) and wet (•) HiPco DOC samples. (a) The ratio of the G^+-bands at 1594 cm^{-1} to D-band at 1295 cm^{-1} indicates good sample purity. (b) The radial breathing modes (RBMs) in the range 100 cm^{-1} to 500 cm^{-1} suggest that nanotubes of different chirality and thus electronic type are also present in the deposited layer.(c) G′-band feature (2600 cm^{-1}). Laser wavelength λ = 785 nm at 1 mW power. 133

4.8 Raman spectroscopy data for the dry (▪) and wet (•) HiPco CTAB samples. (a) The ratio of the G^+-bands at 1594 cm^{-1} to D-band at 1295 cm^{-1} indicates good sample purity. (b) The radial breathing modes (RBMs) in the range 100 cm^{-1} to 500 cm^{-1} suggest that nanotubes of different chirality and thus electronic type are also present in the deposited layer.(c) G′-band feature (2600 cm^{-1}). Laser wavelength λ = 785 nm at 1 mW power. 134

4.9 The normalised Raman spectra of dry and wet SWCNT networks containing (a) anionic DOC, (b) cationic CTAB and (c) no surfactant. The differences in line-shape of the G^+ (at 1593 cm^{-1}) and G^- (at 1565 cm^{-1}) band before and after wetting are highlighted in (a)-(c) by grey shading. The error bars represent the standard deviation between measurements of 3 different spots on the SWCNT film after normalisation of intensity. The percentage decrease in full width at half maximum (FWHM) of the G^+ band before and after wetting is shown in (d), where the error bars represent the error on the measurement of the peak FWHM. Raman spectroscopy was performed using a Renshaw inVia Raman microscope with laser wavelength λ = 785 nm and 1 mW power. 135

4.10 Real time changes in HiPco SWCNT control network conductances (where G_0 is the baseline conductance at RH = 0% and G is the conductance at higher RH levels) as the relative humidity of the testing chamber is modulated between 0% RH and higher humidity (in the 20% to 70% RH range, as indicated by the top x-axis and blue shaded regions) for (a) thick (thickness = 19 ± 5 μm, dense) and (b) thin (thickness < 1 μm, lower-density) networks of HiPco control SWCNTs. 137

4.11 Real time changes in SWCNT network conductances (where G_0 is the baseline conductance at RH = 0% and G is the conductance at higher RH levels) as the relative humidity of the testing chamber is modulated between 0% RH and higher humidity (in the 20% to 70% RH range, as indicated by the top x-axis and blue shaded regions) for thick (thickness = 19 ± 5 μm, dense) networks of (▪) HiPco DOC, (•) HiPco SC, (▲) HiPco CTAB, (▼) HiPco CTAT, (+) HiPco Triton X-100 and (★) HiPco control samples. Results for thin (thickness < 1 μm, lower-density) networks are plotted without a symbol at the same y-axis offset as their respective sample type. Plots are offset for clarity. 138

4.12 The potential difference induced by the application and removal of a soldering iron to the positive measurement probe (hot-probe) in contact with the HiPco SWCNT control (surfactant free) network. The progressively larger negative change in potential difference across the SWCNT network between the positive and negative measurement probes upon heating of the positive probe (hot-probe, to 160°C, 200°C and 240°C) suggests that the semiconducting nanotubes in the network are *p*-type. 141

4.13 The potential difference across the SWCNT networks induced by the application of the hot-probe method whilst additionally delivering H_2O to the (a) HiPco DOC SWCNT network and (b) HiPco CTAB SWCNT network. At (i) the potential difference across the films is recorded using a Keithley 2100/230-240 digital multimeter in a flow of dry air. At (ii) the soldering iron is applied to the positive probe (hot-probe) in contact with the SWCNT network, inducing *p*-type negative increase in voltage. At (iii) wet air is delivered to a partitioned portion of the film so that the wet air cannot contact the hot-probe, inducing another change in potential difference, the direction of which is dependent on the type of surfactant present in the network. At (iv) the wet air is turned off and dry air flow resumes. The process is repeated with wet air on at (v) and (vii) and wet air off at (vi) and (viii). At (ix) the hot-probe is turned off and the potential difference across the film returns to initial levels in dry air at (x). 142

4.14 Current-voltage characteristics across the SWCNT network (source to drain, -1 V to 1 V single sweep) when dry (black ▪) and after wetting (red ▲) with 1 μL of H_2O for the (a) control film (b) the SWCNT network containing DOC surfactant (c) the SWCNT network containing DOC surfactant at different scale to show non-linearity after wetting and (d) the SWCNT network containing CTAB surfactant. 143

4.15 Current-voltage characteristics across the SWCNT network (source to drain) when dry (black ▪) and after wetting (red •) with 1 μL of H_2O for the (a) thin control film (dry) (b) thin control film (wet) (c) the thin SWCNT network containing DOC surfactant (dry) (d) the thin SWCNT network containing DOC surfactant (wet) (e) the thin SWCNT network containing CTAB surfactant (dry) (f) the thin SWCNT network containing CTAB surfactant (wet). A bias across the source-drain electrodes was applied as a duel sweep from -5 V to + 5V as indicated by the arrows, inducing a hysteresis in the I-V curve for the wetted films. 144

4.16 Magnitude and direction of conductance change for SWCNT network humidity sensors. (a) (▪) HiPco CTAB thick (dense) network, (•) HiPco CTAB thin (lower-density) network and (▲) thick HiPco control sample containing no surfactant. (b) (▪) HiPco DOC thick (dense) network, (•) HiPco DOC thin (lower-density) network and (▲) thin surfactant free HiPco control sample. The error bars represent the standard deviation of responses from two identical humidity sensors of the same type. 147

5.1 SEM micrographs at (a) ×3,300 (b) ×40,000 (c) ×100,000 magnification showing gold coated bundles of HiPco SWCNTs non-covalently functionalised with DOC and deposited as a film from aqueous solution. Cracks are present in the film surface across which SWCNT bundles are suspended as shown in (a). Networks of interconnected SWCNT bundles are formed as shown in (b) and (c). 153

5.2 (a) A side on SEM micrograph at ×3,000 magnification showing a HiPco DOC layer of ≈ 10 μm thickness deposited on an alumina substrate, as indicated by the black arrows. (b) SEM micrograph at ×2,000 magnification showing roughness of alumina (Al_2O_3) sensor substrate. 154

5.3 TEM micrographs showing (a) interconnected bundles of HiPco SWCNTs, with blue markings highlighting the100 sampled bundles used to calculate an average bundle diameter of 9 ± 6 nm. Individual SWCNTs within the bundles are visible in (b) and (c), with examples of the bundle sampling areas highlighted in light blue, used to generate the line intensity profile for estimation of individual SWCNT diameter shown in (d). 155

5.4 TEM micrographs showing (a) the presence of multiple residual iron impurities in the HiPco sample, with the dots marked in blue used to calculate the diameter of these particles (3 ±1 nm). (b) and (c) show the decoration of the SWCNT walls and bundles with iron impurities. 156

5.5 Raman spectroscopy data for HiPco DOC SWCNTs collected using a Renishaw inVia Raman microscope. The samples were deposited from aqueous solution to glass slides and heat treated at 100 °C, 150 °C, 200 °C or 250 °C in air using a thermostat controlled furnace prior to data collection. Laser wavelength λ = 514.5 nm. 157

5.6 (a) TGA profile of the HiPco SWCNTs in dried powder form at a ramp rate of 5 °C min^{-1} to 750 °C. (b) TGA profile of the surfactant wrapped HiPco SWCNTs in aqueous DOC solution at a ramp rate of 15 °C min^{-1} to 750 °C 158

5.7 (a) An example of a conductive response from a HiPco DOC sensor when exposed to 6 × 10 ppm pulses of NO_2 gas for 600 s, each followed by a recovery period of 1200 s. The slope of the response is reduced after subsequent NO_2 pulses, as well as the magnitude of the conductance change *DeltaG* as shown in (b). 159

5.8 A schematic based on real-time data highlighting the conductive response and recovery periods for a HiPco DOC sensor after exposure to 3 × 10 ppm NO_2 pulses. The real-time conductive responses to the 3 × NO_2 pulses (black line) form segments of a modelled response curve based on a continuous pulse of NO_2 (blue line). Each new NO_2 pulse generates an "up-shifted" change in conduction that is effectively a continuation of the previous sensing response, due to irreversible adsorption of NO_2. Therefore, seemingly different response slopes and magnitudes are observed for the same analyte concentration, problematic for the accurate quantification of NO_2 levels. 160

5.9 A real-time response plot for a HiPco DOC sensor demonstrating the recovery of baseline conductance G_0 after exposure to NO_2 using the WAR technique in the 2 ppm to 6 ppm concentration range. After each 600 s NO_2 pulse, the relative humidity of the chamber is increased from 0% to 50% RH by mixing dry air with wet for 600 s. Based on the response curve, the NO_2 rapidly desorbs from the SWCNT sensor surface and the baseline conductance of the device is re-established when the humidity is reset to 0% RH. 161

5.10 Application of the water-assisted regeneration technique (WAR) to HiPco DOC sensor 1 to recover responses after exposure to increasing concentrations of NO_2 in the 20 ppm to 120 ppm range. The grey dotted line indicates a pause in testing to change to a NO_2 gas cylinder of higher concentration. 162

5.11 Application of the water-assisted regeneration technique (WAR) to HiPco DOC sensor 2 to recover responses after exposure to increasing concentrations of NO_2 in the 20 ppm to 120 ppm range. The grey dotted line indicates a pause in testing to change to a NO_2 gas cylinder of higher concentration 163

5.12 The conductive response of a HiPco DOC sensor to 3 × 10 ppm NO_2 pulses for 600 s (timings indicated by the black dotted lines) each separated by 1200 s of dry air in the recovery period. After the 3 pulses, WAR was used to regenerate the sensor as marked in the blue shaded region, with the baseline conductance recovered with the switch back to 0% RH. This mode of operation could be used to periodically refresh the SWCNT-based sensors. 163

5.13 (a) A plot of the real-time responses of a HiPco DOC sensor to NO_2 gas in the 1 ppm to 120 ppm concentration range using the WAR technique to recover baseline conductance. (b) the same responses plotted against NO_2 dose ($C_a \times t$), showing the data collapses to a single curve as expected for irreversible adsorption of NO_2 [14]. . . 167

5.14 (a) A plot of the real-time responses of a HiPco DOC sensor to NO_2 gas in the 1 ppm to 6 ppm concentration range without using the WAR technique to recover baseline conductance. Due to a lack of baseline recovery, responses to higher concentrations are smaller in magnitude. (b) the same responses plotted against NO_2 dose ($C_a \times t$), showing the data does not collapse to a single curve or fit the irreversible NO_2 adsorption model, as was observed using the WAR technique for testing. This is because the model assumes an initially clean SWCNT array for each NO_2 pulse, which is not the case for the testing performed without WAR. 168

5.15 The baseline conductance G_0 of a HiPco DOC sensor *vs* the conductance change ΔG observed to multiple 10 ppm NO_2 pulses plotted (a) on log-log scale with a slope of 0.95. The intercept c of the straight line through the data can be used to estimate the adsorption constant k using the analysis described in section 5.3.5 and described in previous work [129]. (b) a plot of G_0 *vs* ΔG on a linear scale. 170

5.16 (a) A plot of G_0 *vs* ΔG on a log-log scale for 3 HiPco DOC sensors at different NO_2 concentrations, to provide the intercept value c for estimation of the adsorption constant k and maximum conductive response S_{max} using equation 5.17, based on the procedure described by Strano *et al*. (b)-(d) The real time responses of 3 HiPco DOC sensors plotted with the modelled response curves generated from equation 5.9 using the calculated S_{max} and k values, based on the irreversible adsorption model. 172

5.17 (a) Real-time conductive response plots to 60 ppm NO_2 for 3 HiPco DOC sensors with a line fit generated from the irreversible adsorption model (equation 5.9) to replicate the shape of the curve using the Origin Pro 2017 fitting tool, as outlined in appendix C. (b) An example of the improved curve fit to the same data, achieved by applying the partially reversible adsorption model [15] in the form of equation C.5. 179

5.18 Non-linear calibration curves for 3 HiPco DOC sensors, demonstrating the expected conductive responses upon exposure to NO_2 in the 1 ppm to 120 ppm concentration range using the WAR procedure. The error bars represent the standard deviation in responses between three repeated experiments. The y-offset of responses in the 80 ppm to 120 ppm range are attributed to a change of NO_2 gas cylinder between testing cycles for the higher concentrations. 180

5.19 Calibration curves for 3 HiPco DOC sensors, plotted on a log-log scale to generate a linear equation for the prediction of the expected conductive responses per NO_2 concentration in the 1 ppm to 120 ppm range using the WAR procedure. The variations in gradient and intercept values suggest that device to device variation in sensor responses must be reduced before general predictions based on a linear fit can be made accurately across multiple SWCNT-based sensors. The error bars represent the standard deviation in responses between three repeated experiments. 181

6.1 Raman spectroscopy was performed using a Renishaw inVia Raman microscope with a laser of wavelength λ = 785 nm at 1 mW power. (a) Raman spectra of the HiPco SWCNT networks containing anionic surfactant (i) DOC (G/D = 18.8) and (ii) SC (G/D = 13.4), cationic surfactant (iii) CTAB (G/D = 19.77) and (iv) CTAT (G/D = 7.02), non-ionic surfactant (v) Triton X-100 (G/D = 8,84), and no surfactant (vi) control (G/D = 6.875) showing the G-band (1594 cm^{-1}), D-band (1295 cm^{-1}) and G′-band (2600 cm^{-1}). (b) The radial breathing modes (RBMs) in the range 100 cm^{-1} to 300 cm^{-1} corresponding to nanotubes of different chirality for each aforementioned sample. Plots are y-offset for clarity. 189

6.2 (a) UV-Vis-NIR absorption spectra obtained using an Elmer Lambda 950 spectrophotometer for HiPco SWCNTs non-covalently functionalised with DOC, deposited from an aqueous solution on to a quartz slide using and Eppendorf pipette and dried. 400 μL of solution (diluted by 250 X from the initial concentrated solutions) was deposited successively after each drying and measurement cycle, so that the total amount of solution deposited on the quartz slide ranged from 600 to 2200 μL from the first to last step. (b) Linear increase in absorbance per 400 μL deposition. . . . 190

6.3 A Keithley 4200 semiconductor characterisation system was used to measure the DC (▪) resistance and (•) conductance across the source and drain electrodes for (a) HiPco DOC and (b) HiPco CTAB devices for a given amount of carbon deposited between the gold electrodes on the device, with a 0.2 V bias applied. The error bars represent the standard deviation in the measurement between two identical devices. 191

6.4 A Keithley 4200 semiconductor characterisation system was used to measure the DC (▪) resistance and (•) conductance across the source and drain electrodes for (a) HiPco DOC and (b) HiPco CTAB devices as a function of the number of layers (1 μL depositions) of SWCNT solution made across the gold electrodes, with a 0.2 V bias applied. The ×1000 diluted solutions (from aqueous stock solution) of DOC and CTAB functionalised SWCNTs were of concentration 0.00159 ± 0.0002 mg mL^{-1} and 0.00161 ± 0.0002 mg mL^{-1} respectively. The error bars represent the standard deviation in the measurement between two identical devices. 192

6.5 The DC (▪) resistance and (•) conductance across the source and drain electrodes of (a) a thick HiPco DOC device formed from a solution of 1.59 ± 0.2 mg mL^{-1} concentration and (b) a thin HiPco DOC device formed from a solution of 0.0108 ± 0.001 mg mL^{-1} concentration as a function of temperature (K). Data was collected by Zak Kobos of the Reed group, Yale, using a semiconductor analyser system and a cryostat setup utilising liquid nitrogen and an inbuilt heater to control the temperature of the device in the 96 K to 300 K temperature range. 193

6.6 The (i) conductive responses of thin film (a) HiPco DOC, (b) HiPco CTAB and (c) HiPco control devices to NO_2 gas in the 0.1 ppm to 0.6 ppm concentrations at 0%, 25%, 50%, and 75% atmospheric relative humidity. (ii) The corresponding drift after each injection of NO_2 as a % of the conductance before each pulse. 195

6.7 The real-time conductive responses of the thin film HiPco control sensors to concentrations of NO_2 in the 0.1 ppm to 0.6 ppm range (indicated by the right axis) at different levels of background relative humidity. The NO_2 pulses were 600 s in duration followed by a recovery period of 1200 s in air, with constant chamber humidity maintained at 0%, 25%, 50% or 75%. 196

6.8 The real-time conductive responses of the thin film HiPco DOC sensors to concentrations of NO_2 in the 0.1 ppm to 0.6 ppm range (indicated by the right axis) at different levels of background relative humidity. The NO_2 pulses were 600 s in duration followed by a recovery period of 1200 s in air, with constant chamber humidity maintained at 0%, 25%, 50% or 75%. 196

6.9 The real-time conductive responses of the thin film HiPco CTAB sensors to concentrations of NO_2 in the 0.1 ppm to 0.6 ppm range (indicated by the right axis) at different levels of background relative humidity. The NO_2 pulses were 600 s in duration followed by a recovery period of 1200 s in air, with constant chamber humidity maintained at 0%, 25%, 50% or 75%. 197

6.10 The approximately linear conductive responses in the initial stages of exposure (first 60 s) to 100 ppb of NO_2 gas at (▪) 0% and (•) 75% relative humidity for (a) HiPco control networks, (b) HiPco DOC networks and (c) HiPco CTAB networks. 200

6.11 The change in conductive response ΔS s^{-1} for the initial 60 s of exposure to NO_2 in the 100 ppb to 600 ppb range at either 0%, 25%, 50% or 75% background relative humidity. The rates are displayed for 6 HiPco thin film sensors with functionalisation as indicated. The error bars represent the standard deviation in the measured rates over two experiments. 201

6.12 The average time required for the SWCNT sensor conductances to reach 50% of the maximum possible change in conductance ($t_{1/2}$) upon exposure to 300 ppb of NO_2 for 600 s at 25%, 50% and 75% background relative humidity for the (a) reversible and (b) irreversible components of the response, extracted using the partially reversible adsorption model [15]. The error bars represent the standard deviation between times calculated for two identical devices. . 202

6.13 A visualisation of the proposed (dash) reversible and (dot) irreversible components of the experimental NO_2 conductive response curve, based on real data for the HiPco control sensor exposed to 300 ppb of NO_2 at (a) 25% background relative humidity and (b) 75% background relative humidity. The components are based on the application of the partially reversible adsorption model developed in ref [15] and detailed in Chapter 5 section 5.3.5. 203

6.14 The average time required for the SWCNT sensors to recover 50% of their initial baseline conductance in the recovery period for the (a) fast and (b) slow components of the curve (τ_1 and τ_2 half-life) after exposure to 300 ppb NO_2 for 600 s with 25%, 50% or 75% background relative humidity. The data from the recovery period was fitted using a two-phase exponentially decreasing curve as by Rigoni *et al.* [290]. The error bars represent the standard deviation between times calculated for two identical devices. 204

6.15 The real-time conductive responses for the thin film (solid line) and thick film (dashed line) HiPco sensors to concentrations of NO_2 in the 0.1 ppm to 0.5 ppm range (indicated by the right axis) at (a) 0% RH and (b) 50% RH. different levels of background relative humidity. The NO_2 pulses were 600 s in duration followed by a recovery period of 1200 s in air, with constant chamber humidity maintained at (a) 0%, or (b) 50%. 205

7.1 Schematic of a 3 x 3 mm Alumina substrate with interdigitated gold electrodes. Arrangement (a) consists of a HiPco SWCNT base layer with a top layer of porous zeolite. Arrangement (b) represents HiPco SWCNTs deposited over a zeolite to form a mixed layer and (c) a side on SEM micrograph at X10,000 magnification showing a H-Zeolite-Y layer of ≈ 7 μm thickness. 216

7.2 SEM micrographs of SWCNT-Zeolite mixed sensing layers showing bundles of HiPco SWCNTs distributed across the surface at (a) X10,000 (b) X20,000 and (c) X20,000 magnification using a 5 kV probe voltage. 217

7.3 TEM micrographs (200 kV) indicating the range of particle sizes present in the (a) Silicalite-1 and (b) H-Zeolite-Y ethanol dispersed samples, drop coated onto a holey copper grid. 219

7.4 Raman spectra showing the normalized intensity of the D band (1338 cm^{-1}) and G band (1593 cm^{-1}) for HiPco SWCNT DOC bundles before and after heating sample to 100°C, with radial breathing modes inset. G/D ratio before heating was 17.2 and 12.2 after heating, indicating an increase in the number of bundle defects after heat treatment. Laser wavelength $\lambda = 514.5$ nm. 220

7.5 A plot of the typical percentage change in conductance at room temperature (where $\Delta G = G_{Gas} - G_{Air}$) upon exposure to various combinations of NO_2 and H_2O for a blank SWCNT, a SWCNT sensor with a Silicalite-1 mixed layer and a SWCNT sensor with a H-Z-Y mixed layer. Region (a) displays the baseline conductance for each sensor type whilst operating in dry synthetic air, whilst in region (b) 10 ppm of NO_2 is additionally introduced to the testing chamber. Region (c) contains the desorption step in which the NO_2 pulse is turned off and H_2O is turned on resulting in a relative humidity of 75% inside the testing chamber, aiding NO_2 desorption from the sensor surface. In region (d) H_2O is turned off to return the relative humidity of the chamber to 0% and recover baseline conductance. Region (e) shows the response of each sensor type to 10 ppm of NO_2 whilst operating at 75% chamber humidity. Finally, in region (f) the NO_2 is turned off and relative humidity set at 75% for the desorption cycle. 222

7.6 Example of real time sensor responses to changes in the relative humidity levels within the sensing chamber, varying the relative humidity between 0% and 25% , 50% or 75%. Plot (a) shows the decrease in conductance observed for HiPCo SWCNT based devices, (b) shows the smaller changes for zeolite mixed layer devices with lower zeolite content (0.033 mg of zeolite per 1 μL drop of HiPco DOC solution) and (c) shows the increase in conductance for zeolite mixed layer devices with higher zeolite content (0.2 mg of zeolite per 1 μL drop of HiPco DOC solution), with changes still smaller in magnitude than the SWCNT control sensors. 224

7.7 Typical percentage change in conductance per sensor type (where Δ G = G_{Gas} − G_{Air}) as relative humidity in testing chamber is increased from 0 % to 25 %, 50 % and 75 % for SWCNT control sensors, SWCNT H-Zeolite-Y and SWCNT Silicalite-1 zeolite mixed layer type sensors. M.layer.1 indicates a mixed layer with lower zeolite content (0.033 mg of zeolite per 1 μL drop of HiPco DOC solution), M.layer.2 indicates a mixed layer with higher zeolite content (0.2 mg of zeolite per 1 μL drop of HiPco DOC solution). . . . 225

7.8 Example of real time sensor responses to 10 ppm NO_2 in both dry and wet air following testing procedure 3 for (a) Silicalite-1 mixed layer sensors (b) HZY mixed layer sensors (c) HipCo SWCNT sensors and (d) zeolite overlayer sensors. The timing of the 10 ppm pulse of NO_2 is indicated by the dashed black line and the humidity of the sensing chamber is denoted by the dashed grey line (right axis). 227

7.9 Average percentage change in conductance per sensor type (where Δ G = G_{Gas} − G_{Air}) upon exposure to both 10 ppm NO_2 in dry synthetic air and 10 ppm NO_2 in wet air at 75 % relative humidity over 6 testing cycles (mean responses of four identical sensors from each sensor type, taken over six repeated tests, presented with standard error). 228

7.10 ATR - FTIR spectra for the (a) HiPco SWCNT H-Zeolite-Y sample (b) HiPco SWCNT Silicalite-1 sample when exposed to (1) dry air for 30 minutes (2) 50 ppm NO_2 in dry air for 30 minutes and (3) 50 ppm NO_2 in wet air for 30 minutes at 50% RH, transferring the samples to the spectrometer after exposure. A Brucker ALPHA FTIR spectrometer with a diamond crystal and an ATR attachment was used, averaging 64 scans at a resolution of 4 cm^{-1}. Five repeated measurements were made per exposure cycle on each sample type, plots are offset for clarity. 230

7.11 Example of real time sensor responses to 40 ppm NH_3 in dry air for (a) Silicalite mixed layer sensors and (b) H-Z-Y mixed layer sensors. The timing of the 40 ppm pulse of NH_3 is indicated by the dashed black line. 231

7.12 An example of regenerating a Silicalite-1 mixed layer type sensor (a) and a HZY mixed layer sensor (b) after the zeolites begin to water saturate. After 10 consecutive cycles of testing for Silicalite-1 and 7 cycles for HZY, the water begins to interfere with the sensor responses to 10 ppm NO_2 at 75% RH, changing the shape of the response curve and beginning to cause the decrease in conductance that is observed for the SWCNT control sensors upon exposure to water vapour. By heating the sensing layer to 150°C in air via a platinum heater track on the underside of the chip (schematic (c)) in between cycles, the responses to NO_2 in both dry and wet air (the dotted orange line on each plot shows responses after regeneration step) can be recovered and the cross-sensitivity reduction is preserved. 234

C.1 Fitting of data extracted from ref [14] for exposure of polyethyleneimine (PEI) coated carbon nanotubes to 5 ppb NO_2 using the Origin Pro 2017 fitting tool to the "ExpDec1" function as highlighted in bold on the plot. The units of the displayed k are converted for comparison with literature values using equation C.1 so that $k = 1.45\times10^{-6}$ ppt $^{-1}$ s^{-1}. 256

C.2 Fitting of data extracted from ref [15] based on the partially reversible adsorption model for exposure of a SWCNT micro resistive chemical sensor to 0.5 ppm NO_2 using the Origin Pro 2017 fitting tool to the "ExpDec2" function, as highlighted in bold on the plot. The displayed value of irreversible $t_{1/2}$ = 2125.26 s and reversible $t_{1/2}$ = 147.99 s compare well with those reported in Table 1, ref [15]. 257

C.3 Fitting of data from ref [290] to extract desorption time constants from literature data using a double exponential curve as described in the paper by Rigoni *et al* ([290], Figure 6) for exposure of a SWCNT chemiresistive sensor to 10 ppm NH_3 for 60 s. The displayed desorption time constants τ_1 = 13.3 s and τ_2 = 111.2 s, associated with fast and slower desorption processes respectively compare well with those extracted using the same method by Rigoni *et al*. 261

D.1 The potentiostat measurement circuit. (a) shows the control circuit that supplies the probe voltage and (b) the measurement circuit. The sensor is connected between points C and S. The probe voltage is set and measured between Vp and ground, where as the voltage across the sensing element is measured between Vs and ground. (c) shows the circuit diagram for the power rail to the unit. The diagram has been adapted from the thesis of Dr. Ayo Afonja [226], which was based on a triple potentiostat unit designed by Dr. K F E Pratt [307]. 262

List of Tables

2.1 Mechanical, electronic and thermal properties of carbon nanotubes. . 48

2.2 A comparison table of the advantages and disadvantages of each gas sensing technology surveyed with carbon nanotube (CNT) or single-walled carbon nanotube (SWCNT)-based sensors. Each subclass of carbon nanotube-based sensor is included and marked as reviewed. Adapted from multiple sources [17, 118, 95, 168, 154, 159, 162] 86

4.1 Parameters of the HiPco SWCNT networks and their conductance behaviour when exposed to water vapour. 124

5.1 Adsorption rate (k) and maximum conductive response (S_{max}) extracted from the HiPco DOC sensor responses to NO_2 using the water-assisted recovery (WAR) procedure with the log-log plot or curve fitting method. Parameters from the literature are included using different sensor types and analytes for comparison with those from the current study (marked with a star*). 174

7.1 Testing procedure 1 is listed below detailing the time duration, gas type present, and the relative humidity of the testing chamber per testing step. Procedure 1 was used to establish the qualitative sensing behaviour for each sensor type. The flow rate was set to 1 litre per minute using MKS 1179A general purpose mass flow controllers. 213

7.2 Testing procedure 2 is listed below detailing the time duration, gas type present, and the relative humidity of the testing chamber per testing step. Procedure 2 was used to establish the sensitivity to changes in relative humidity within the sensing chamber for each sensor type. The flow rate was set to 1 liter per minute using MKS 1179A general purpose mass flow controllers. Different mixing ratios of dry and wet air were used to control humidity levels. 214

7.3 Testing procedure 3 is listed below detailing the time duration, gas type present, and the relative humidity of the testing chamber per testing step. Procedure 3 was used to investigate variations in the sensor responses to 10 ppm NO_2 gas whilst changing the relative humidity of the sensing chamber. The flow rate was set to 1 litre per minute using MKS 1179A general purpose mass flow controllers. . 214

7.4 Elemental analysis using energy dispersive X-ray spectroscopy (EDS) to confirm the silicon to aluminum ratio of the Silicalite-1 and H-Zeolite-Y layers investigated (calculated as the ratio of each elemental % weight) along with the Carbon content on the surface of each sensor type. Sensors were gold coated for EDS. 218

7.5 Example response times for each analyte and sensor type. Response time t_{90} is defined as the time required for sensor responses to reach 90 % of their maximum value. Recovery time Rec is defined as the time taken for the sensors to re-establish a baseline resistance. 223

A.1 The motivation for the experiments described in this thesis, along with section references. 244

Glossary

ATR-FTIR spectroscopy Attenuated total reflectance-Fourier transform infrared spectroscopy.

CNT Carbon nanotube.

CO_2 Carbon dioxide.

CTAB Hexadecyltrimethylammonium bromide.

CTAB Hexadecyltrimethylammonium p-toluenesulfonate.

DOC Sodium deoxycholate.

EDS Energy dispersive X-ray spectroscopy.

FET Field-effect transistor.

H_2O Water.

HNO_3 Nitric acid.

MWCNT Multi-walled carbon nanotube.

NH_3 Ammonia.

NO_2 Nitrogen dioxide.

SC Sodium cholate.

SEM Scanning electron microscopy.

SWCNT Single-walled carbon nanotube.

TEM Tunnelling electron microscopy.

TGA Thermal gravimetric analysis.

UV-Vis-NIR spectroscopy Ultra-violet visible near infrared spectroscopy.

VOC Volatile organic compound.

WAR Water-assisted regeneration.

Chapter 1

Introduction.

1.1 Motivation and objectives

Society has become accustomed to easily accessible data in the public domain, with the demand for continuous monitoring of chemicals across a broad range of environments increasing. For instance, air quality monitoring networks have been installed in our cities [1], where long-term exposure to nitrogen dioxide (NO_2) has contributed to respiratory disease rates in urban populations. Other examples include the development of personal glucose sensors for diabetes patients [2], the monitoring of ammonia gas (NH_3) in agricultural industries, or devices that track the degradation of perishable goods [3]. To meet the operational requirements of such exciting applications, sensors that are more portable, more energy efficient, and more selective towards the chemical species of interest must be designed. The development of new functional materials that can interact appropriately with the chosen chemical environment, is of critical importance to realising such devices.

In the year 2000, Kong *et al*. [4] reported the use of individualised single-walled carbon nanotubes (SWCNTs) for highly sensitive chemical sensing. Through their incorporation into carbon nanotube field effect transistors (CNT-FETs), exposure to gaseous analytes such as NO_2 or NH_3 was shown to induce an equivalent change in SWCNT conductance of up to three orders of magnitude at room temperature. Due to the combination of hollow geometry, high aspect ratio and the unique material characteristics of these molecular wires, a similarly timed

study by Collins *et al.* [5] communicated the important finding that the electronic properties of SWCNTs were extremely sensitive to their gas exposure history and chemical environment.

Further pioneering work by groups at Stanford [6] and the NASA Ames Research Centre [7] prompted numerous investigations into many types of SWCNT-based chemical sensors over the following years. In recent work, exciting applications such as breath analysis [8] and cancerous tissue diagnostics [9] for disease detection have been proposed, along with wireless food spoilage sensors [3] and glucose monitoring devices [2] fabricated from functionalised, low-powered SWCNT sensor arrays. The existence of recently founded start-ups [10, 11, 12] suggests the commercialisation of SWCNT-based sensors may be viable.

Despite the promise of such applications and the extensive research progress made, some of the fundamental challenges facing the development of SWCNT-based sensors remain unsolved. For example, most practical chemical sensing applications involve fluctuating measurement parameters, such as changing air flow rate or atmospheric relative humidity. Cross-sensitivity to molecules such as water vapour or oxygen can obscure sensing responses. The effects of such interferents on non-functionalised or functionalised SWCNT devices are poorly understood, with often conflicting results and few studies reported in the literature.

Furthermore, the recovery of the baseline sensing signal after exposure to strongly interacting molecules such as NO_2 or NH_3 is slow (of the order of 12 hours), making accurate quantification of the target analyte difficult. Strategies used to expediate the desorption of the target analyte (UV illumination, sensor heating, current stimulated desorption) can often degrade the SWCNT sensing material and increase the power requirements of the device.

The combined promise and challenges facing the development of SWCNT-based sensors provided the motivation for the current project. The aim of this thesis was to establish the effect that adsorbed water vapour had on the conductance of SWCNT networks, the resulting impact on sensing responses of SWCNT-based chemiresistors to NO_2, along with analyte adsorption processes. Based on this

insight, an additional aim was to develop a composite material that demonstrated reduced sensitivity to cross-interference from H_2O. Therefore, the objectives of the study were to:

(1) Determine if HiPco SWCNT networks display *n*-type or *p*-type behaviour when exposed to water vapour.

(2) Establish whether adsorption of water to conductively responsive sites on SWCNT networks is reversible.

(3) Investigate the effect that non-covalent surfactant functionalisation has on the conductance-humidity behaviour of SWCNT networks.

(4) Assess the suitability of the water-assisted regeneration (WAR) technique to regenerate SWCNT-based sensors after exposure to NO_2.

(5) Study the influence of atmospheric humidity levels on NO_2 adsorption/desorption kinetics and sensor response magnitudes for SWCNT network chemiresistors.

(6) Evaluate the use of Zeolites to reduce the cross-sensitivity of SWCNT networks to water vapour.

1.2 Overview and summary

This thesis is structured to guide the reader through the current study of SWCNT networks and related composite materials for gas sensing applications. Chapter 2 provides a background to SWCNTs, along with a review of the relevant sensing literature. Chapter 3 details the general experimental techniques, theory and procedures used for the acquisition of material characterisation and gas sensing data. Chapters 4 to 7 provide experimental results and discussion, with conclusions to be taken from the study presented in Chapter 8. A synopsis of each chapter is provided below. In appendix A, Table A.1 details the motivation for the experiments carried out in the project with section references. Published work is indicated at the begin-

ning of the relevant chapters and is appended to this thesis in appendix E.

Chapter 2: Background and literature review.

The unique chemical, physical and electronic characteristics of single-walled carbon nanotubes (SWCNTs) are introduced. A historical context is provided to summarise the exciting properties of SWCNTs, along with the challenges to be addressed in order to realise their many potential technological applications. Types of carbon nanotube-based gas sensors are discussed, along with previously adopted approaches to improve sensor sensitivity and selectivity. Mechanisms and models of SWCNT gas sensing behaviour from the literature are reviewed to guide analysis and the interpretation of results in subsequent chapters. Important performance metrics for chemiresistive SWCNT-based gas sensors are identified, and the state of the art at the time of writing is compared with other gas sensing devices. Finally, the potential applications of SWCNT-based gas sensors and the challenges facing their development are considered to provide rational for the topics investigated throughout this thesis.

Chapter 3: Experimental techniques and theory.

The experimental techniques used to characterise the physical and chemical properties of the as received, treated and processed HiPco SWCNTs used in this study are detailed. The methods for electronic device characterisation are described, along with the gas sensing apparatus and experimental procedure used to obtain the gas sensing results for the SWCNT network devices.

Chapter 4: Changes in SWCNT network conductance on exposure to water vapour.

Sensitivity of the SWCNT networks to water vapour is reported from humidity testing experiments. Non-covalent surfactant functionalisation, widely used in SWCNT processing, is shown to affect the conductance-humidity behaviour of the SWCNT networks. A reversible model of H_2O adsorption, proposed by Strano *et*

at[13], was found to qualitatively describe the conductive response curves. Complimentary Raman spectroscopy data is used to suggest a possible mechanism for the bi-directional conductance changes observed in the surfactant functionalised SWCNT networks. This work was published in *Nanoscale* as detailed in the statement at the beginning of the chapter.

Chapter 5: Water-assisted regeneration (WAR) of SWCNT networks for NO_2 gas sensing.

A partially irreversible change in conductance upon adsorption of NO_2 is observed for the SWCNT network sensors, resulting in significant baseline signal drift. The impact of humidity on the SWCNT device conductance, reported in Chapter 4, is manipulated to regenerate the SWCNT network sensors after exposure to known concentrations of NO_2 gas. This water-assisted regeneration (WAR) enables the extraction of key figures of merit from gas sensing experiments, along with the acquisition of sensor calibration curves by minimising baseline drift. Possible mechanisms for the removal of surface bound NO_2 using WAR are discussed. The irreversible adsorption model, proposed by Strano *et al.* [14], and the partially reversible adsorption model developed by Kumar *et al.* [15] for NO_2 on SWCNT networks were assessed for their applicability to the experimental sensing data.

Chapter 6: Sensing NO_2 in humid environments with SWCNTs.

Following on from the use of WAR in Chapter 5, the influence of atmospheric humidity levels on the SWCNT network sensor responses to NO_2 was investigated. At different levels of relative humidity, changes in the response and recovery rates of the sensors were observed, as well as in the magnitudes of the conductive responses. The effects were dependent on surfactant functionalisation and the thickness of the SWCNT network films. A model for partially reversible adsorption of NO_2 in humid conditions was applied to the data to aid interpretation of the results.

Chapter 7: Reducing cross-sensitivity of SWCNT networks to water

vapour using Zeolites.

Zeolites were incorporated into the SWCNT sensing layers to reduce cross-sensitivity to water vapour, facilitating the detection of NO_2 despite rapidly fluctuating atmospheric humidity levels. Two different layer configurations were investigated. While the cross-sensitivity to water vapour was reduced, completely irreversible adsorption of NO_2 was observed, resulting in diminishing sensor responses over repeated testing cycles. Regeneration of responses was achieved using an *in situ* substrate heat treatment. This work was published in *ACS applied materials and interfaces* as detailed in the statement at the beginning of the chapter.

Chapter 8: Conclusion.

The results from the study chapters are summarised, presented in a wider chemical sensing context as a whole and future work is proposed.

Chapter 2

Background and literature review.

2.1 Introduction

Carbon nanotubes have been found to possess extraordinary electronic, mechanical and optical properties [16]. Sensitivity of their electronic properties to gases present on their surface, combined with a porous and cylindrical geometry, makes them particularly promising candidates for use in gas sensing applications [17, 18]. In this section, the properties, gas sensing mechanisms and potential applications of SWCNTs and SWCNT networks are introduced, beginning with a historical overview of their development.

2.2 Properties of carbon nanotubes and SWCNT networks

2.2.1 Historical Overview

The first carbon fibers, macroscopic analogs of carbon nanotubes, were prepared by Thomas Edison (around 1892) to provide filaments for an early model of the electric light bulb [19]. Increased research efforts after World War II, driven by the need for light yet strong materials for space and aircraft components, were undertaken into the synthesis of carbon based materials *via* chemical vapour deposition (CVD) and other processes. This lead to the synthesis of higher quality carbon fibers, along with the discovery of fullerenes by Kroto and Smalley [20].

Smalley speculated (after discussions with Mildred Dresselhaus and Huff-

man, prompting further research) that carbon nanotubes of dimensions similar to Buckminsterfullerene may exist, stimulating direct study of small diameter carbon filaments, which had occasionally been observed in the synthesis of carbon fibers previously [21]. In 1991, Iijima reported a breakthrough experimental observation of carbon nanotubes using transmission electron microscopy (TEM) [22].

Since this discovery of carbon nanotubes, their study has progressed rapidly, along with the number of papers published in the field [23]. Single, double or multiwalled carbon nanotubes can be synthesised displaying a range of properties and dimensions. They possess remarkable mechanical, thermal, structural and electronic properties, displayed in Table 2.1.

Table 2.1: Mechanical, electronic and thermal properties of carbon nanotubes.

Properties	**Comments**
Youngs modulus: 1 TPa [24]	>Diamond
Tensile strength: 150 GPa [25]	100 times the strength of steel
Carrier mobility: 79000 cm^2/Vs (at room temp.) [26]	>Hole mobility in Si
Maximum electrical current density: 10^9 A/cm^2 [27]	100 times greater than copper wires
Thermal Conductivity: 6600 W m^{-1} K^{-1} [28]	>Diamond

Due to these extraordinary properties, many potential applications have been suggested for carbon nanotubes; photovoltaics [29], drug delivery [30], electronic components (transistors [31], touch screens [32]), energy storage (fuel cells [33], batteries [34]), electrical cabling [35], water treatment [36], composite strength re-enforcement [37], mechanical actuators [38] and chemical sensing [39].

The sensitivity of SWCNT electronic properties to surface adsorbed molecules, combined with their high surface area, stimulated investigation into their use for chemical sensing. Early pioneering work performed by groups at Stanford [4, 6] and the NASA Ames Research Centre [7] in the early 2000's, showed that sensitive detection of target analytes was possible with low-powered nanotube devices

operating at room temperature. Further work from the Star [40] and Swager [41] groups, prompted a plethora of attempts from researchers worldwide to develop carbon nanotube based sensors for applications in defence [42], space [43], environmental monitoring [44] and health [8].

Despite the promise that carbon nanotubes demonstrate for new technologies, there are still many challenges to be to be resolved. The impressive properties of individual SWCNTs do not necessarily translate to bulk materials, and the separation of SWCNTs by chirality, required for many electronic applications, remains challenging [23]. While methods for scalable production [45] and device processing have improved [46, 47], the cost of these processes must be reduced and further research into the toxicity of SWCNTs must be conducted [48, 49]. However, many in the field believe that the aforementioned applications of carbon nanotubes will be realised with continuing research effort [50].

Chemical sensing using carbon nanotubes is a particularly promising area, as evidenced by recent well funded start-ups commercialising the technology [10, 11, 12]. An understanding of the physical and chemical structure of SWCNTs, which facilitate such potential applications, is required to tailor SWCNT properties for specific use cases. These structures are described in the following section.

2.2.2 Structure

SWCNT structures can be visualised as a sheet of graphene rolled up into a cylinder. They exist in a one-dimensional (1-D) system, with a wall thickness of one atom and a circumference of a few tens of atoms. SWCNTs can be up to many micrometers in length and are highly anisotropic due to their 1-D nature, allowing them to carry high currents with negligible heating effects [16].

Each carbon atom is covalently linked to three neighbours by in plane σ-bonds. The remaining p orbitals for each carbon atom form weak, delocalised, out-of plane π bonds to form a sp^2 hybridised system, the properties of which govern the low energy electronic and optical properties of SWCNTs (Figure 2.1) [51].

The direction in which this single layer of graphene is rolled impacts upon the properties of a carbon nanotubes. The nanotube is specified by the chiral vector $\mathbf{C}_h$ [52]:

$$\mathbf{C}_h = n\mathbf{a}_1 + m\mathbf{a}_2 = (n,m) \tag{2.1}$$

This vector can be described by a pair of (n,m) indices, denoting the number of real space unit vectors $n\boldsymbol{a_1}$ and $m\boldsymbol{a_2}$ in the hexagonal honeycomb lattice contained in the vector $\mathbf{C}_h$. Figure 2.1a shows a representation of the un-wrapped carbon honeycomb lattice for a given SWCNT. $\mathbf{C}_h$ is the circumferential direction in which the sheet is rolled, connecting points O and O′, to form the SWCNT. Therefore, the length of the chiral vector ($\mathbf{C}_h$) is equivalent to the circumference of the tube. The translation vector, $\mathbf{T}$, shown on the pink line connecting from O to P, is in the direction along the longitudinal nanotube axis. It is the shortest repeat distance along the nanotube, and it's magnitude corresponds to the length of the *(n,m)* SWCNT unit cell. The "armchair" vectors are seen when $m = n$, and "zig-zag" vectors when $m = 0$, as depicted in Figure 2.1b. These SWCNTs are known as achiral, since their mirror image is identical to the original image.

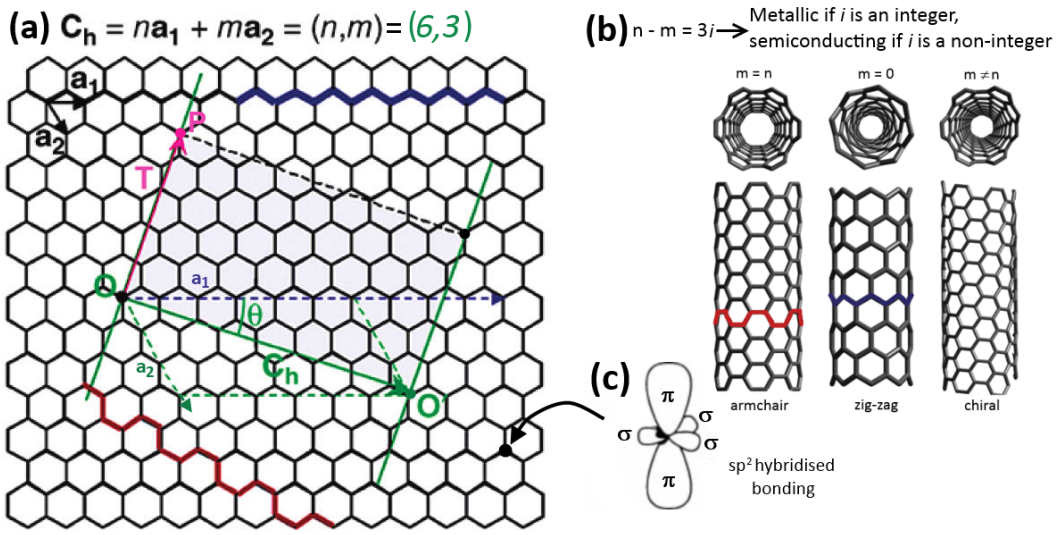

Figure 2.1: (a) A representation of a graphene lattice, showing the defined chiral vector $\mathbf{C}_h$, the unit vectors $\mathbf{a}_1$ and $\mathbf{a}_2$ and the translational vector $\mathbf{T}$ for an un-rolled *(6,3)* SWCNT. The so called armchair (red) and zig-zig (blue) vectors are shown. (b) the *(n,m)* index condition determining whether a m-SWCNT or a sc-SWCNT is obtained from the rolled up graphene lattice and an armchair (red), zig-zig (blue) or chiral nanotube structure. (c) Carbon atom in graphene lattice with three in plane σ (s, p_x, p_y) orbitals and the π (p_z) orbital perpendicular to the sheet. Figure is adapted from [53] and [54].

Between the chiral vector ($\mathbf{C}_h$) and $\mathbf{a}_1$ is the angle θ, known as the chiral angle. The chiral angle for the zig-zag direction corresponds to θ = 0 °, whereas an armchair nanotube axis corresponds to θ = 30 °. The chiral nanotube axis corresponds to 0 °<θ <30 ° (Figure 2.1b). Once the *(n,m)* indices are specified, (such as the *(6,3)* nanotube in Figure 2.1a) other structural properties such as the chiral angle (θ) and the nanotube diameter (d_t) can be determined. In terms of the integers *(n,m)*, the diameter of nanotubes can be described as [52]:

$$d_t = \frac{C_h}{\pi} = \frac{3^{1/2} a_{CC} (m^2 + mn + n^2)^{1/2}}{\pi} \tag{2.2}$$

where a_{CC} is the nearest neighbour C-C distance (1.421 Å in graphite). Therefore the chiral angle is given by [52]:

$$\theta = tan^{-1}\left[\frac{3^{1/2} m}{(m + 2n)}\right] \tag{2.3}$$

Nanotubes can be defined by either their *(n,m)* indicies or equivalently by d_t

and θ [52].

2.2.3 Electronic properties

The conducting, semiconducting or insulating behaviour of a crystalline solid can be understood in terms of band theory. Instead of the discrete energy levels that are available for free atoms, those bound in a crystalline structure are able to exist over a range of many energy levels, known as energy bands, due to inter-atomic interactions. To contribute to conduction, valance electrons (those occupying the highest bound electron energy level in an outer electron shell) must be able to populate the conduction band. As depicted in Figure 2.2, depending on the energy separation between these bands, a material can either be an insulator, a semiconductor or a conductor [55].

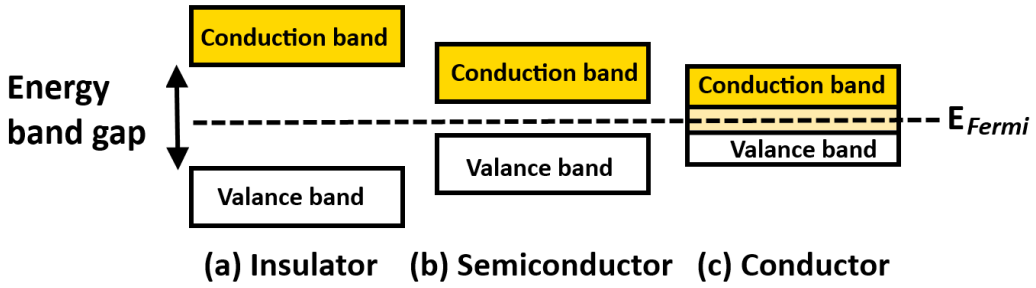

Figure 2.2: Schematic representation of band theory depicting the position of the Fermi level in (a) insulating, (b) semiconducting or (c) conducting materials relative to the energy of the valance and conduction bands in a crystalline solid.

An insulator requires a large amount of energy to facilitate electron transfer to the conduction band, due to the large energy spacing from the valance band. Semiconducting materials have a smaller band gap, with promotion to the conduction band possible at a finite temperature resulting in an increase in charge carrier concentration. In conductors, the valance and conduction bands overlap, with electrons easily existing in the conduction band. The Fermi level (the highest occupied energy state at T= 0 K) exists between the valance and conduction bands for semiconductors, and in the conduction band for conducting materials [55]. The range of

structural arrangements that are possible for SWCNTs, as discussed in the previous section, can alter the electronic band structure of the material.

When rolling up the graphene sheet to obtain 1-D SWCNTs, electronic propagation is quantized in the circumferential direction of the tube [56], as the diameter of the nanotube is of the order of the de Broglie wavelength of an electron in the system. Electrons can only propagate along the nanotube axis and are confined by the graphene monolayer of one atom in thickness. Due to this quantisation, only certain electronic states are allowed, dependent on the structure and nanotube diameter [52].

The density of states (DOS) describes the number of available states in which the electron can exist per energy interval, averaged over space and time. A high DOS at a specific energy level means there are many states available for occupation. If the DOS = 0, then an electron can not exist at that specific energy level [57].

Depending on the way in which the graphene lattice is rolled, denoted by the (*n,m*) indices, there can be differences in the electronic interband transition energies and population of energy levels [58]. An example of the available DOS at a certain energy is shown in Figure 2.3a. The sharp energy peaks found in the electronic DOS are known as van Hove singularities (vHs), and can be probed using optical techniques such as ultraviolet-visible-near infrared spectroscopy (UV-Vis-NIR), as detailed in Chapter 3 [58]. E_{11}^{M} denotes the first transition between energy levels for a m-SWCNT, and E_{22}^{S} denotes a transition for sc-SWCNTs. For a metallic nanotube, the density of states at the Fermi level (E_F) is non-zero, whereas an energy band gap exists between transitions for semiconducting nanotubes in which $E_F = 0$.

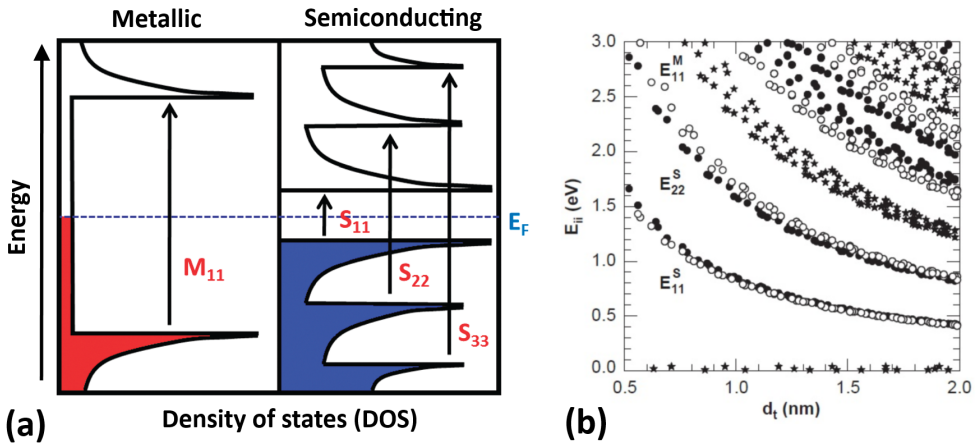

Figure 2.3: (a) A schematic representation of the density of states (DOS) for metallic and semiconducting nanotubes. The black arrows denote the allowed transitions between the van Hove singularities (vHS), where E_{11}^{M} denotes the lowest energy transition between energy levels in a m-SWCNT, and E_{22}^{S} denotes the second transition for a sc-SWCNT. For a metallic nanotube, the density of states at the Fermi level (E_F) is non-zero, whereas an energy band gap exists between transitions for semiconducting nanotubes in which $E_F = 0$. (b) A Kataura plot showing the transition energy as a function of nanotube diameter for sc-SWCNTs (• and ∘) and m-SWCNTs (⋆). This can be used to identify SWCNT species from optical spectra. Figure is adapted from [58] and [56]

Therefore, SWCNTs can be either metallic or semiconducting, governed by the condition of their specific (*n*,*m*) indices, so that [53]:

- if $\frac{n-m}{3} = i \rightarrow$ the SWCNT is metallic at room temperature, where i is an integer.

- if $\frac{n-m}{3} \neq i \rightarrow$ the SWCNT is semiconducting, where i is an integer.

As a result, raw carbon nanotube samples contain 1/3 metallic nanotubes, and 2/3 semiconducting [59]. However, this can vary through modification of the growth method [60] or post synthesis treatments [61], in which samples are enriched with a certain electronic species or nanotube chirality. A plot of energy state separation vs nanotube diameter, known as a Kataura plot [62] (Figure 2.3b), can be used to determine if an individual nanotube is semiconducting or metallic [63].

Unlike isolated 1-D SWCNTs, collections of multiple SWCNTs in bundles

and 2-D films can exhibit collective behaviour [64]. Whilst the individual electronic characteristics of the nanotubes in such arrangements are often still measurable, the electronic properties of devices based on SWCNT bundles and networks are averaged over those of the constituent SWCNTs. The interesting properties of SWCNTs, whether metallic or semiconducting, have resulted in attempts to obtain highly homogeneous samples, required for many potential applications of SWCNTs, which are reviewed in the following section.

2.2.4 SWCNT networks for electronic applications

The electronic properties that arise from the physics of carbon nanotubes, combined with their unique dimensions and high aspect ratio, have led to much research effort internationally, focusing on the integration of SWCNTs with existing or newly developed technologies [65].

Much attention has focused on the potential of SWCNTs to address scaling issues in the semiconductor industry for electronic components. The fabrication limits using lithographic techniques, combined with heat dissipation issues and quantum effects predicted to limit the downsizing of silicon technology, have resulted in 20 years of research effort into developing SWCNT based transistors or complimentary structures which may overcome these limitations [66, 31, 67]. Thin film SWCNT transistors have been printed on flexible substrates (see Figure 2.4a) [68]. Existing challenges for SWCNT-based transistors include elimination of hysteresis in the devices, controlled positioning of the SWCNTs and obtaining SWCNT networks with a very high (>99.99%) proportion of sc-SWCNTs in the network [66, 31].

Similarly, networks of SWCNTs have been used to develop transparent conducting films (TCFs), required for many common components found in consumer electronics products such as touch screens and light-emitting displays (Figure 2.4c) [69]). These electrodes are currently fabricated using indium tin oxide (ITO), which has a high associated material cost, poor mechanical robustness, high reflectivity and limited production capacity (i.e a dwindling supply of indium) [32]. Carbon nanotubes present an exciting opportunity to replace metal oxides with transparent

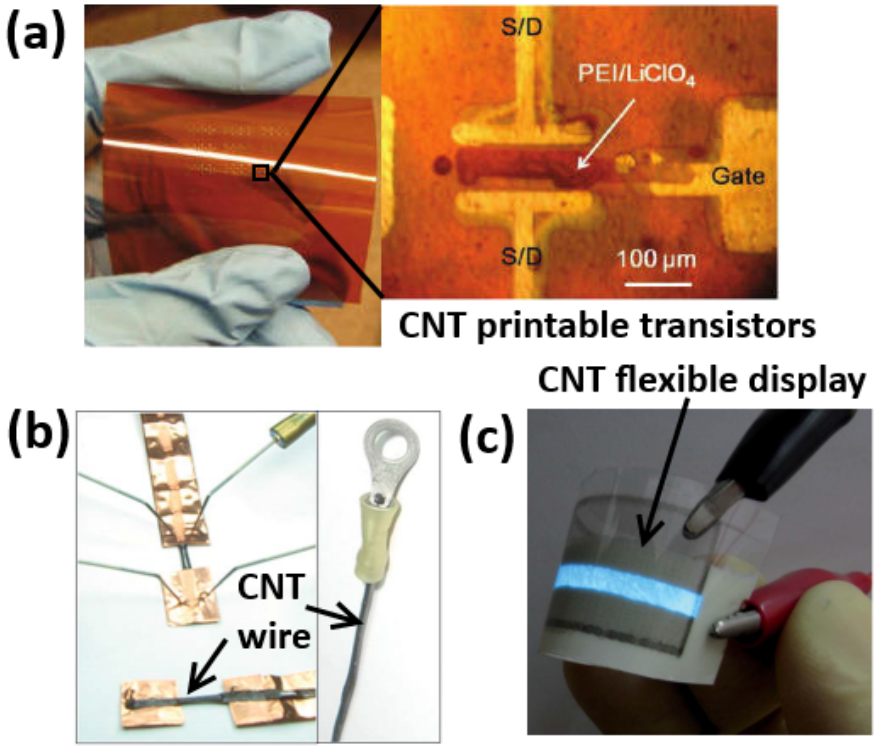

Figure 2.4: (a) Optical image of top gated SWCNT thin film transistor printed on flexible Kapton, adapted from [68]. (b) An example of a macroscopic CNT wire used to bridge copper connectors adapted from [35]. (c) A flexible electroluminescent device formed using an ink-jet printed CNT film, adapted from [69].

conducting films consisting of nanotube networks that have higher current carrying ability and robust mechanical properties, as well as a potentially plentiful supply of raw material being available to manufacturers. Furthermore, scalable techniques for the printing of SWCNT-based TCFs have been demonstrated, along with the ability to deposit the networks on to flexible substrates [32, 69]. There are barriers which need to be overcome to enable use of SWCNT TCF technology. These include the ability to incorporate SWCNT printing processes into existing fabrication procedures for consumer electronics products, and increasing SWCNT sample homogeneity to achieve screens of sufficient quality repeatedly.

SWCNTs may in the future form an integral component for energy storage technologies. The high surface area of SWCNT electrode materials has attracted interest in their use for improving the performance of hydrogen fuel cells [33]. Work from the Haddon group, in which the SWCNTs act as a support for the platinum (Pt) catalyst, reportedly reduces the amount of Pt required in a proton exchange

membrane fuel cells, approaching the 2017 targets set by the US Department of Energy for Pt use reduction [70]. SWCNTs are also being applied for stabilisation of the sulfur cathode for enhancement of rechargeable Lithium-sulfur (Li-S) batteries [34].

Macroscopic arrangements of CNTs, processed into wires and ribbons, may potentially offer an alternative to copper cabling in the future for both power and data transfer [35]. The CNT structures potentially offer savings *via* weight reduction and cost, as well as demonstrating dramatically improved resilience to environmental stresses such as mechanical bending and acidic corrosion (see Figure 2.4b). However, to advance their utility as functional cabling, the relatively poor conduction observed for macroscopic arrangements of CNTs must be improved towards that observed on the micro and nano-scale.

SWCNT networks can be used as a conducting scaffold for TiO_2 semiconductor based photoelectrochemical cells. TiO_2 nanoparticles are dispersed throughout the SWCNT films which facilitate charge transport and collection in the photovoltaic device, improving the photo conversion efficiency of the solar cell by a factor of 2 [29].

Finally, SWCNTs have been investigated as the functional sensing element in low-cost, portable chemical sensors, one of the most promising potential electronic applications [39]. Many of the technological barriers discussed above also apply to the development of SWCNT-based sensors for practical applications. As this is the topic of the current thesis, an in depth review of the CNT-based sensor literature is now provided in the following section.

2.3 Carbon nanotube-based sensors

The properties of carbon nanotubes have been exploited for use in a wide range of sensors, with different transduction types and sensing principles. Devices based on changes in conductance (resistance), capacitance and shift in resonant frequency have been reported in the literature, all with the ability to operate at room temperature [65]. This section provides an overview of the operating principles for these

sensor types, along with a discussion of their comparative advantages and disadvantages.

2.3.1 Chemiresistors and field effect transistors (FETs)

The most reported sensing principle for carbon nanotube-based sensors is a change in conductance (resistance) upon introduction of a target molecule. Carbon nanotubes are commonly incorporated into field effect transistors (FET) or chemiresistive devices [71].

Carbon nanotube FET (CNTFET) sensors utilise individualised, networks or bundles of carbon nanotubes as the gas sensitive element. For CNTFET sensors, SWCNTs are typically deposited [72, 73] or grown directly [74] onto an insulating (SiO_2) substrate, top, side or back gated with silicon. An example of the resulting CNTFET back gated configuration is shown in Figure 2.5a, in which charge flows through the SWCNT channel between a voltage source and drain electrode. A voltage gate is used to control the current flow through the SWCNT layer, which is altered when target molecules impinge on the nanotube surfaces. Typically, enriched samples of semiconducting SWCNTs are desired for FET devices, as this permits control over the sensor operating regimes *via* the gate voltage.

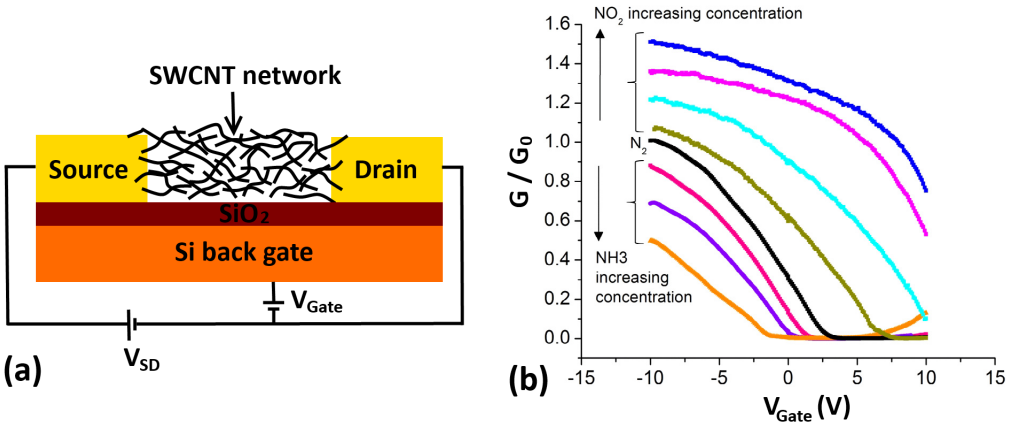

Figure 2.5: (a) A schematic diagram of a carbon nanotube field-effect transistor device (CNTFET). A SWCNT network connects the source and drain electrode, which is separated from the back Si gate used to control conduction by an insulating SiO_2 layer. (b) A plot of applied gate voltage (V_{Gate}) *vs* normalised conductance G/G_0, showing the changes in conductance and curve shape observed from the baseline conductance (black line) to increasing concentrations of NO_2 or NH_3, adapted from [75].

Early work on the use of CNTFETs for molecular sensing was reported by Kong *et al.* [4] and Collins *et al.* [5]. Kong *et al.* observed that the conductance of CNTFET devices utilising individualised sc-SWCNTs could increase or decrease by up to three orders of magnitude, when exposed to 200 ppm of NO_2 or NH_3 respectively [4]. This was consistent with the observed *p*-type transistor characteristics, induced by the application of various gate voltages.

Collins *et al.* demonstrated that the electronic properties (e.g resistance, thermoelectric power, density of electronic states) of both SWCNT films and isolated SWCNTs can be reversibly "tuned" by simply exposing them to oxygen [5]. As a consequence, the electronic properties of SWCNTs are dependent on their gas exposure history, as well as diameter and chirality. Oxygen saturated SWCNT films were found to have a higher electrical conductance, and the sign of the thermoelectric power switches from negative to positive after exposure to dry air. This is again consistent with *p*-doped SWCNTs. It was also suggested that the presence of defects could facilitate charge transfer between the tubes and surface adsorbed O_2, as is the case for graphite [5].

Enhanced CNTFET molecular sensing has recently been reported by Jeon *et*

al. [76] using SWCNT networks enriched with 99.9% sc-SWCNTs. The back gated transistors exhibited excellent"on/off"' ratios allowing use of the device in distinct operating regimes, providing a good platform to investigate and optimise the sensing responses to NO_2 and H_2. The work also suggested that the physical dimensions of the SWCNT network can influence the sensing performance of the devices.

In CNTFET devices, the conductive behaviour in different gaseous environments can be investigated over a range of applied gate voltages almost simultaneously [77]. Firstly, changes in the I_{SD}-V_{gate} characteristics may provide additional information to discriminate between different target analytes [39]. Secondly, any changes in the slope of the I_{SD}-V_{gate} curve (dI/dV, known as transconductance) can be indicative of the introduction of scattering sites due to molecular adsorption, which may provide information on the gas sensing mechanism [17]. Such changes are displayed in Figure 2.5b, adapted from [75].

Hysteresis in the I-V characteristics and sensing responses have been reported in the literature for CNTFETs [78]. This was attributed to ionic species in the SWCNT films, and can be influenced by functionalisation of the SWCNTs. The effect is further enhanced in humid atmospheres, but can be drastically reduced *via* vacuum baking treatments.

CNTFETs can also be applied for the sensing of biomolecules [79, 80]. In these devices, SWCNTs are exposed to analytes in solution and are liquid-gated. Chen and co-workers demonstrated that SWCNTs embedded into an FET architecture are not only sensitive to their chemical environment, but also to surrounding electrostatic charges. Therefore, they can be used to investigate surface-protein and protein binding interactions in aqueous mediums [79].

The benefits of using CNTFETs for gas sensing include higher sensitivity and faster response times than polymer based sensors, due to the high percentage of surface located atoms available for material-analyte interactions [81]. The devices can also be operated at room temperature, an advantage over metal oxide semiconducting (MOS) sensors which require operating temperatures in the 250 °C to 400

°C range [81]. This could potentially unlock applications in which high operating temperature are unsuitable (e.g medical, space or defence settings) or distributed monitoring networks in which the devices should be low-powered.

However, as described by Meyyappan in a recent review [39], the aforementioned hysteresis in CNTFETs, along with drift in the baseline signal of the devices, can make the accurate quantification of analyte concentration challenging. The CNTFET devices must be highly enriched with sc-SWCNTs to achieve the desired high sensitivities to target molecules. In addition, the three terminal operation, combined with extensive fabrication steps to construct the CNTFET devices, make the design a relatively more expensive option than the simple chemiresistor platform [39].

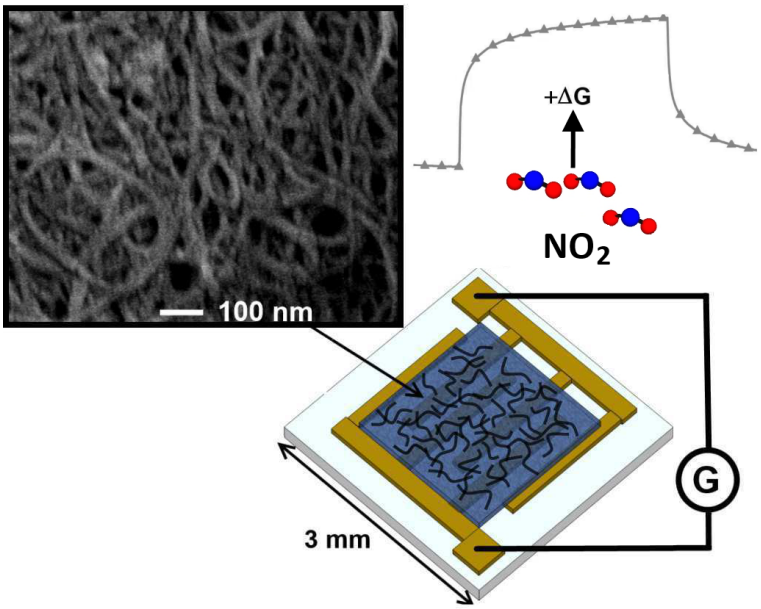

Figure 2.6: (a) A schematic diagram of a SWCNT network chemiresistor. SWCNTs are deposited across interdigitated gold electrodes on an insulating Al_2O_3 substrate, across which the device conductance is measured with an applied bias of 0.1 V. A molecule such as NO_2 present on the tube surfaces causes an increase in measured conductance. Top-left inset shows a scanning electron microscope (SEM) image of the SWCNT network.

Chemiresistive devices consist of SWCNTs grown or deposited between metallic electrodes to form a conductive network, as depicted in Figure 2.6. A change

in conductance is measured between the source and drain electrodes when gases interact chemically with the SWCNTs.

Snow and co-workers have published extensively in the area of SWCNT-based chemiresistors, demonstrating that sensing of a wide range of target analytes is possible, including those considered toxic (NH_3), simulants for chemical warfare agents (DMMP) and relevant to medical diagnosis (VOC's) [82]. Their work focused on the use of SWCNT networks, rather than individualised SWCNTs. If many SWCNTs form an interconnected network that is electrically continuous over macroscopic dimensions, then the electronic properties of such a network represents the aggregate behaviour of the randomly orientated SWCNTs. Device to device variation can be largely reduced with this approach [82].

Schnorr *et al.* report that functionalised SWCNTs can be used to develop chemiresistors that are sensitive to vapour signatures of materials used for the production of commercial or home made explosive devices. Examples include nitromethane, a common solvent used for the formation of explosive mixtures, along with cyclohexanone, which us used to recrystallize explosive RDX. The specificity can be tailored for a variety of other target molecules. Although several techniques are capable of detecting trace quantities of these analytes, such as ion mobility spectrometry (IMS) and mass spectrometry (MS), low-cost SWCNT-chemiresistors may in the future offer a complimentary route for detection using portable devices [42].

As with CNTFETs, the geometric dimensions of the SWCNT network can influence the sensing characteristics of the chemiresistors. Described by Battie *et al.* [83], the thickness (or density) of the SWCNT layer in the film can dictate whether it exhibits a metallic or semiconducting character. This is due to the availability of a complete or incomplete path for conduction through the m-SWCNTs in the film respectively, across the source and drain electrodes. In the case of low-density films, sc-SWCNTs contribute significantly towards conduction and thus the sensing response, whereas they do not contribute in dense SWCNT networks with complete metallic pathways. As a result, the thickness (density) of the SWCNT layer in the chemiresistive device can alter the sensing responses [83].

Due to the simple device structure, the fabrication of SWCNT-chemiresistors is possible using flexible substrates, such as textiles and plastics (e.g polyethylene terephthalate, PET). Routes to flexible sensor fabrication include spray-layering onto fibers [84, 85], spinning processes [86] and printing [87] for the same wide variety of analytes traditionally detectable with SWCNT-based sensors. The Swager group have even reported a process in which SWCNT-chemiresistors are drawn mechanically by hand on paper using compressed SWCNT powders [88], highlighting the simplicity of the devices. The low-mass and flexibility of such substrates may lead to the incorporation of SWCNT-based sensors into clothing or packaging.

Chemiresistors can also been easily integrated into wireless technology, also demonstrated by the Swager group, who have incorporated them into existing near field communication (NFC) tags, for wireless transmission of chemical sensing data to smart-phones [89].

Alternative device architectures and sensing principles using SWCNTs have been investigated in numerous studies, as are now discussed.

2.3.2 Chemicapacitiors

In addition to their work on SWCNT-chemiresistors, the use of randomly aligned SWCNTs in a capacitor type setup has been demonstrated by Snow and co-workers for gas sensing, referred to as chemicapacitors. Using changes in the capacitance of the SWCNT network upon introduction of a target molecule, SWCNT capacitors offer an alternative transduction mechanism for the detection of a broad class of chemical vapours [90].

In the presence of chemical vapour, analytes adsorbed to the tube surfaces become polarized by the applied alternating electric fields (e.g 0.1 to 1 V, 30 kHz) radiating from the surface of the SWCNT network, causing an increase in the measured capacitance. The slow response times usually associated with chemicapacitor type sensors are not observed using SWCNTs, due to the thin sensing layer and careful functionalisation with a hydrogen-bonding molecular monolayer [90].

The common problem of slow analyte desorption, observed for SWCNT chemiresistors, is reduced when using SWCNT chemicapacitors. Average re-

sponses are reported as completely reversible within 30 seconds for certain analytes (e.g acetone, 60 ppm) [90]. However, desorption issues arise with exposure to other molecules, such as NH_3, which are more strongly bound to the SWCNTs [91].

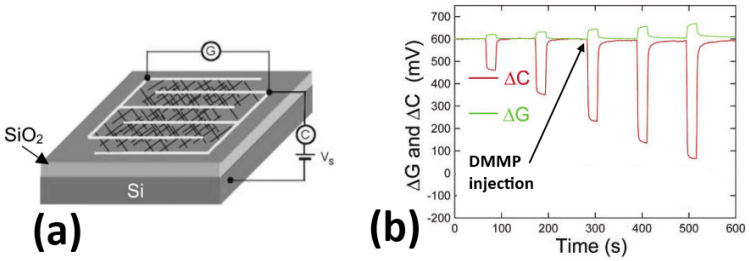

Figure 2.7: (a) Schematic diagram of the dual operation SWCNT network chemiresistor/ chemicapacitor setup and (b) the concurrent normalised conducive (green) and capacitive (red) responses to injections of DMMP vapour, adapted from the work by Snow *et al.* [91].

The noise in the sensing signal can limit the minimum concentration of target analyte it is possible to detect. A significant portion of the noise in CNTFET type devices has been attributed previously to random charge fluctuations in the device, giving rise to $1/f$ noise. Conductance through a material is more dependent on charge fluctuations than it's capacitance. Therefore, chemicapacitors were found to display much lower signal noise, permitting more sensitive and reliable chemical detection than CNTFETs [92].

There are potential drawbacks of using capacitance based sensors. As is the case for CNTFETs, the SWCNT-chemicapacitor setup is more complex than the chemiresistive analogue. The biggest potential barrier to the adoption of capacitance type sensors, is the requirement for more complex electronic readout components, such as a lock-in amplifier, to measure the change in capacitive sensing response. An AC power supply is also a disadvantage, as many of the potential applications for which SWCNT-based sensors are suited require extremely portable devices.

Further work by Snow *et al.* demonstrated that a network of SWCNTs can be used in dual operation mode, simultaneously measuring the conductance and capacitance across the network [91]. This was an interesting development, as it allowed

the measurement of two distinct physiochemical properties of the adsorbate; charge transfer and polarisability. A schematic representation of this device, as well as examples of the simultaneously measured conductive and capacitive responses, is shown in Figure 2.7. The ratio of the capacitive response to the conductive response was found to be independent of analyte concentration. It was suggested this could be used to assist in the identification of a chemical vapour.

2.3.3 Mechanical resonators

Mechanical SWCNT-based resonance sensors offer an alternative to those using a change in SWCNT network electrical properties as the detection principle. For this type of sensor, an isolated SWCNT is made to oscillate at it's resonant frequency in an environmentally controlled chamber. When a vapour or molecule is present on the surface of the SWCNT, a shift in resonant frequency occurs, which is correlated with the mass of the atoms impinging on the surface of the SWCNT [93].

Lassagne *et al*. reported ultra-sensitive mass detection using this technique, with masses of 25 $\times 10^{-21}$ g of evaporated chromium atoms detected at room temperature [94]. Detection of a wide range of other gases and molecules has also been reported [93].

However, ultra-sensitive mass detection using this technique is limited to one type of analyte per experiment. The detection of distinct sets of molecules in a mixed gas environment remains challenging, which could hinder further developments using this detection principle [93].

2.3.4 Approaches to improve sensitivity and selectivity

Lack of selectivity towards a specific target molecule is a universal problem for many of the more affordable, portable gas sensing devices introduced in the previous section. This can prevent analyte of interest detection in complex, real world sampling environments, consisting of many chemical components. To improve the sensing response towards a specific gas, three complementary approaches are often adopted:

- Functionalisation/chemical modification of the active sensing material.
- Incorporation of sensing element into a composite matrix.
- Using a range of sensors in a discriminatory array with statistical classification methods.

A good review is provided by Zhang *et al.* on the subject of functionalisation methods for carbon nanotube-based sensor devices [95]. Routes such as the attachment of metallic nanoparticles [40, 96], polymers [97, 98, 99], DNA [100] and functional groups [101, 41, 102] to the surface of the SWCNTs have been explored to increase sensor selectivity towards certain target molecules.

Star *et al.* decorated the SWCNT networks in the sensing channel of CNT-FETs with 18 different metals/metal oxides *via* electrodeposition. By incorporating them into a sensory array on a single chip, the differing catalytic activity of each individual device resulted in variable sensing responses to five different gases at room temperature, providing a method to increase the selectivity and discriminatory power of a SWCNT network based device [40].

Further work by Ding and co-workers demonstrated non-covalent functionalisation of SWCNTs with polyaniline (PAni) for gas sensing. The PAni formed a shell around the SWCNTs to form a composite sensing material with higher sensitivity and stability than sensors based on either material alone [98].

In a recent report from the Swager group, polymer wrapping of SWCNTs enabled detection of the nerve agent simulant DMMP. The selectivity of the poly(3,4-ethylenedioxythiophene) (PEDOT) polymer functionalised SWCNT sensors was further modified with the addition of a hexafluoroisopropyl group (HFIP). The non-covalently functionalised sensor, in which swelling induces a change in the electrical conductivity of the SWCNT network, exhibited superior temporal durability and performance [97]. A range of other covalent methods have been investigated by the group for defence applications, highlighting the wide range of options for SWCNT sensor functionalisation [41, 42].

For functionalisation of SWCNT-based chemicapacitors, Snow *et al.* coated

SWCNT networks with a chemoselective polymer, known as HC [90]. The acidic, strong-hydrogen-bonding layer increased the magnitude of capacitive responses observed using the HC functionalised SWCNT networks by 100 and 500 times for acetone and DMMP respectively. These large gains in response magnitude were not observed for water and chloroform, thus the selectivity of the SWCNT device was increased.

There have also been many efforts to incorporate carbon nanotubes directly into composite matrices to improve sensor selectivity [103, 104, 105, 106, 107, 108, 109, 110]. The composite may act as a pre-concentrator of the target vapour, or a catalyst for surface reactions. Whilst some of these methods have proved partially successful, they often result in the dampening of the excellent electronic properties of the carbon material and come at the cost of increased operating temperature or reducing the reproducibility of responses.

Varying the fabrication process, operating conditions, or detection mechanism can also offer a certain degree of differentiation between sensors using the same active material [111, 112, 82]. Arrays of functionalised sensors of carbon nantubes have been reportedly used to good effect, distinguishing between different types of target molecules [113, 114]. Techniques such as principle component analysis (PCA) and support vector machines (SVM) have been retrospectively applied to data from sensory arrays to achieve classification of the target molecule [115, 42, 116].

2.3.5 Advantages and challenges

The research and literature to date suggests that the use of SWCNTs in solid state chemical sensors may prove advantageous. The ability to detect target analytes at ambient temperature offers opportunities for the development of extremely low-powered sensor devices for large scale monitoring and data collection applications. Prototype SWCNT sensors have been integrated into portable technologies, such as smart-phones [89], medical devices [2, 8], and have even been deployed directly to living plant matter [117].

Room temperature sensing also presents new opportunities in areas in which

gas sensors operating at high temperature may not be suitable, such as sensing in potentially explosive environments or where non-destructive sampling of the target molecule and it's surroundings may be required.

The ease of chemiresistor fabrication and the simplicity of the required measurement hardware relative to other SWCNT device types allows fast prototyping of SWCNT network arrays with different functionalisations or physical properties [118]. This expedites the investigation of methods to improve SWCNT-based sensor selectivity and sensitivity.

SWCNT chemiresistors can also be incorporated into flexible structures, which are suitable for mass production *via* printing or deposition methods. The ability to incorporate SWCNTs on to flexible substrates may one day lead to the development of low-powered devices embedded in unconventional mediums, such as biological systems [117] or packaging [3].

Compared to non-functionalised chemiresistors or chemicapacitors, CNTFETs can display a much larger change in device conductance when exposed to the target analyte. For example, the conductance of a CNTFET sensor was reported to change by three orders of magnitude for 200 ppm of NO_2 [4], whereas the typical expected change for a SWCNT-chemiresistor would be approximately 4 × that of the original baseline conductance pre-exposure to 100 ppm NO_2 [7]. This is advantageous, as larger conductive responses result in an increased signal to noise ratio and a smaller minimum detectable concentration of target vapour.

All of the SWCNT-based sensor types demonstrate similar response times, so that a change in signal due to molecules impinging on the SWCNT sensing element is detectable above baseline signal [44]. The actual response time depends on the species and concentration of the target molecule interacting with the SWCNTs, with 10 s being the typical time taken for a detectable change in the conductance to occur for a SWCNT chemiresistor exposed to 10 ppm of NO_2.

Reports of part per trillion (ppt) limits of detection have been reported previously for SWCNT-based sensors to NO_2 gas, which would be within in the concentration range required for reporting of pollutant levels in city environments [6].

However, at such low concentrations, the sensitivity and limit of detection for the sensor is often limited by the ability of the sampling configuration to deliver such low concentrations of vapour to the sensor surface. Problems such as analyte adsorption to the surrounding sensor casing or tubing must be considered when designing the sampling system for such applications.

Due to the simple fabrication procedures available for SWCNT-based chemiresistors, they are a cost-effective option compared to the more complex device architectures and measurement systems. However, what the CNTFET or chemicapacitive type SWCNT sensors lose with increased fabrication difficulty, they gain with additional measures by which to discriminate between target gases, such as a change in the slope of I-V characteristics or reversible capacitive responses respectively [18]. Therefore, the operational requirements of the final application should determine which device architecture is adopted.

Despite the promising characteristics of SWCNTs for chemical sensing, first reported over 15 years ago [4], many of the original challenges inhibiting their use in real-world applications remain.

For devices based on the change in conductance of the SWCNT sensing element (chemiresistors and CNTFETs), poor recovery of the baseline conductance post exposure to the target gas or vapour makes the accurate quantification of analyte concentration difficult [44]. Repeated measurement of the same molecular quantity yields different magnitudes of sensing response and adsorption kinetics, due to incomplete desorption of the target analyte from previous exposures. While this may allow the application of SWCNT-based devices as disposable chemical dosimeters, it is problematic for scenarios in which the sensors are required to remotely report data and cannot be replaced easily or cost effectively.

Techniques such as UV-illumination [119], sensor heating [120] and electrically stimulated desorption [121] have been proposed and tested as methods to recover the baseline conductance of SWCNT-based sensors. Such methods could potentially prevent the saturation of the sensing response and facilitate the reliable measurement of sensing figures of merit per concentration of target analyte. How-

ever, they require more complex device architectures, have a higher power consumption and in some cases the methods can degrade the sensing material over time, resulting in diminuation of the sensing response.

The sensitivity of SWCNT-based sensors to many different analytes suggests promise for a wide variety of applications, facilitating many previous experimental investigations. However, outside of a controlled testing environment, it is also a nuisance, as a sensing signal may be generated by an analyte of no relevance to the desired application. Fortunately, the large scale investigation of SWCNTs over the past 20 years has revealed many methods for their functionalisation, which can be utilised to increase selectivity towards the target species for gas sensing applications [122].

In a broader sense, carbon is generally a good absorber of many chemical species including volatile organic compounds (VOC's), hence it is commonly used in protective respiratory equipment and air conditioning systems. Thus, specificity along with selectivity for carbon based sensors is an issue. To date, there are no methods that completely prevent all cross-interfering molecules from inducing a sensing response in SWCNT-based sensors. Water is a particularly troublesome interferent [123], as it is present in most practical sensing environments, with atmospheric humidity levels varying temporally and spatially. Furthermore, cross-sensitivity to oxygen (O_2) [5], ammonia gas (NH_3), carbon monoxide (CO) and other common molecular species may necessitate a controlled flow of carrier gas to the sensor and filtering of unwanted contaminants in many situations.

Data processing and classification techniques, such as principle component analysis (PCA) and support vector machines (SVM), have been applied previously to negate the effects of cross-interference and successfully identify the target in mixed analyte systems [124, 42, 114, 116]. Such techniques typically require an array of sensors to be deployed, where predictive models can only be developed after calibration data has been obtained in an experimental setting, a time consuming process. It is also unclear if these data processing methods can always be implemented and adjusted on the fly after a predictive model has been established, a requirement

for many real-world applications.

Previous studies have suggested that carbon nanotubes may be toxic to human beings and the environment [48, 49]. Closer investigation has revealed that this may be dependent on the type (e.g SWCNT or MWCNT) and form (e.g airborne or in solution) of nanotube that is under consideration. While guidelines for the safe use of SWCNTs in devices are being continuously developed, it should be noted that any toxicity or future regulation may impact upon their suitability for use in applications in which the user may come in to direct contact with the sensing element.

Finally, one disadvantage to the use of carbon nanotube-based sensors is that the raw material often contains impurities, defects and a range of SWCNT species that can vary between production batches [122]. The heterogeneity of samples used to fabricate SWCNT-based sensors can result in large discrepancies in conductive response magnitudes from otherwise identical devices. Therefore, sensors need to be calibrated and results normalised to derive meaningful conclusions from results. New synthesis methods and post-production processing techniques are being continually developed to alleviate this problem, moving towards more homogeneous SWCNT materials for use in device applications.

2.4 Mechanisms and models for SWCNT sensors

The chemical sensing mechanisms behind the electrical responses of SWCNT networks are not fully understood. There has been much theoretical and experimental work investigating the interaction of gases such as NO_2, NH_3 and H_2O with the surface of tubular carbon nanotube structures. The type of gas adsorption taking place to the SWCNT network was first considered for the current thesis, followed by the potential mechanisms responsible for the observed sensing responses and appropriate models able to describe the sensing results, as are now detailed.

2.4.1 Gas adsorption

In networks of single-walled carbon nanotubes, Zhao *et al* studied molecular adsorption computationally at room temperature [125]. It was found that NO_2, O_2,

NH_3, H_2O, CH_4, CO_2, H_2, N_2 and Ar molecules are all weakly adsorbed onto the surface of SWCNTs. Further studies corroborating this, show that physisorption can occur at surface, groove, pore and interstitial sites in carbon nanotube bundles, as shown in Figure 2.8 [126]. However, weak adsorption was not consistent with experimental gas sensing results or temperature-programmed desorption (TPD) experiments, as highlighted by Andzelm *et al*. [127]. Explaining large, semi-permanent changes in SWCNT network conductance upon exposure to low concentrations (1 to 100 ppm range) of oxidising or reducing molecules, such as NO_2 and NH_3 respectively, required significant charge transfer, formation of surface complexes and strong adsorption [127].

Due to this inconsistency between theory and experimental results, it was established through further investigation that chemisorption of gases can also occur due to sample impurities, deliberate functionalisation of the SWCNT network, or *via* mediators such as adsorbed water or oxygen [127, 128]. However, the semi-permanent binding of NH_3 and NO_2 is sometimes not apparent for other polar molecules, such as H_2O. This indicates that a mixture of physical and chemical adsorption is possible, depending on the gaseous species.

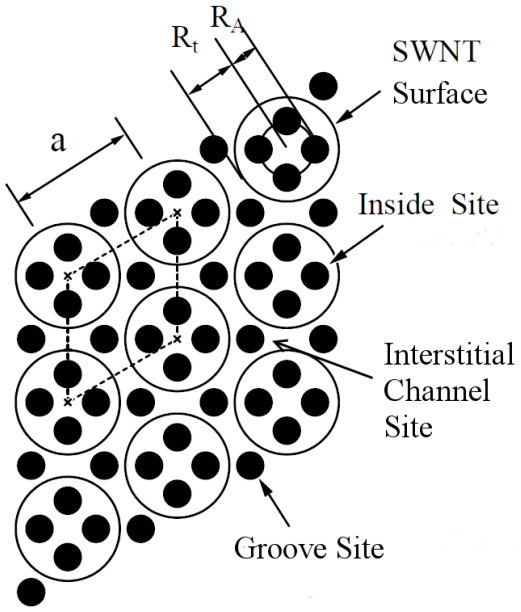

Figure 2.8: A diagram depicting a cross-sectional view of a SWCNT bundle with potential gas adsorption sites (gas molecules represented by black circles). Figure is adapted from [126].

Due to the low dimensionality and high electronic sensitivity of CNTs, it is widely believed that subsequent charge transfer after strong molecular adsorption is the mechanism responsible for the measured change in conductance (resistance) of the carbon material, facilitating a sensing response. Many further studies were conducted to explore the potential mechanisms in greater depth, as are now introduced.

2.4.2 Mechanisms for conductive responses

There are many factors that influence the electrical responses of carbon nanotube based sensors when surface adsorption of gases and vapours from the surrounding environment takes place. These include the nanotube type [129], surface morphology [130], film thickness and density [83], applied potential [121], operating temperature [120], structural defects [131], impurities and chemical functionalisation [112]. Thus, there are often variations in measured responses between sensors, despite the use of a common sensing material, as concluded by Lee *et al.* [132] .

SWCNT networks in chemiresistive devices are reported to show *p*-type responses when exposed to gases such as NO_2 and NH_3 [17]. Their *p*-type nature

is thought to arise from the pre-adsorption of oxygen from the surrounding atmosphere in ambient conditions, resulting in hole doping of the nanotubes [5]. The *p*-type responses are consistent with the idea that charge transfer from an oxidising molecule (NO_2) induces an increase in SWCNT network conductance, with a decrease in conductance observed upon adsorption of a reducing molecule (NH_3) (see Figure 2.9 (i)).

It is known that the conductance (resistance) of devices using singular nanotubes (such as individual nanotube CNTFETs) is dominated by Schottky barriers that form at the metal-nanotube contact junction, as depicted in Figure 2.9 (iii) [133]. However, in SWCNT networks, the contact resistance becomes small when compared to the resistance between connecting m-SWCNTs or sc-SWCNTs, thus the main contributor to the electrical resistance of the device is at nanotube-nanotube junctions [134]. Therefore, modulation of the contact resistance between the SWCNTs is expected to dominate the conductive responses in SWCNT network based chemiresistors Figure 2.9 (ii).

Past work has shown the resistance of networks containing sc-SWCNTs decreases as operating temperature is increased, consistent with semiconducting behaviour [120]. SWCNT networks also contain a metallic portion of tubes. This is seen in powdered samples grown using the high pressure carbon monoxide disproportionation (HiPCo) process, in which approximately one third of tubes are metallic [137]. For the purposes of gas sensing, semiconducting nanotubes are amenable to larger changes in conductance due to charge transfer modulation of the bandgap [76]. Other growth processes, such as the silica supported cobalt molybdenum catalyst method (CoMoCAT) produces high yields (≈95%) of semiconducting SWNT samples, along with various selective techniques [138, 58]. However, it is not possible to fabricate chemiresistors using a high proportion (>99.0%) of sc-SWCNTs, as charge cannot flow across the network without an applied gate potential, only available with the CNTFET type devices.

Randomly orientated SWCNT network devices are thought to behave analogously to random 2-D resistor networks, studied using percolation theory [139].

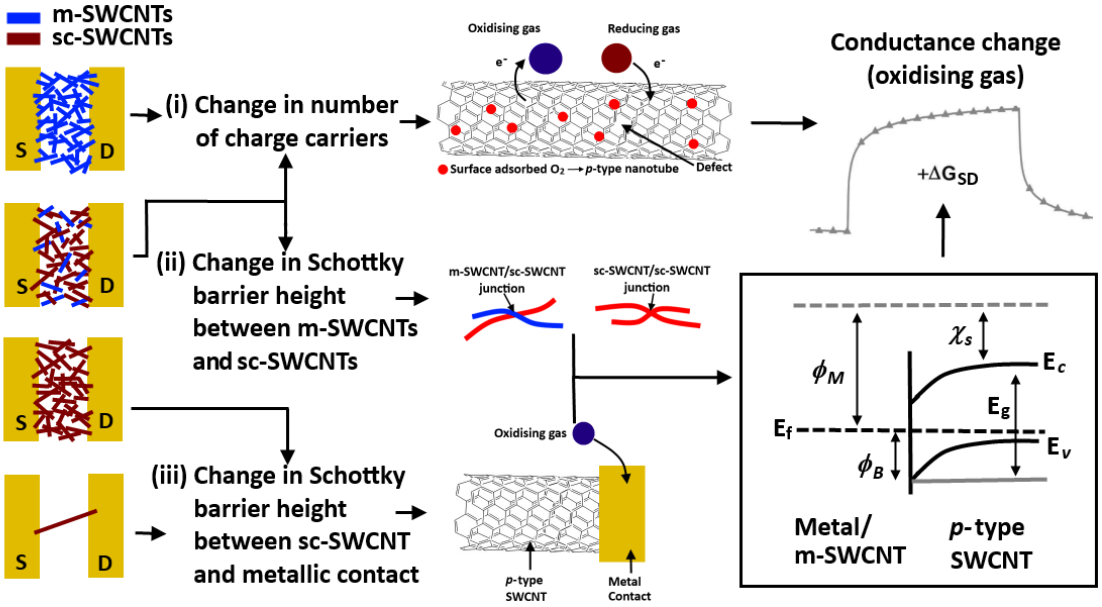

Figure 2.9: A schematic diagram depicting three potential gas sensing mechanisms for SWCNTs depending on m-SWCNT percolation and network density. (i) Charge transfer directly changing the number of charge carriers in the SWCNTs, (ii) Modulation of the Schottky barrier between m-SWCNTs and sc-SWCNTs (iii) Change in Schottky barrier height between individual SWCNTs and metallic contacts. The mechanisms depicted are based on those summarised by Mittal *et al.* [135] and the energy band diagram for the Schottky barrier is based on a description by Suehiro *et al.* [136]. E_f indicates the Fermi level, E_v the valance band, E_c the conduction band, E_g is the band gap, ϕ_B the Schottky barrier height, ϕ_B is the work function of the metal required to remove an electron in a vacuum and χ_s is the electron affinity for the sc-SWCNT.

Conduction across these resistor networks takes place so long as the density of connected resistors (SWCNTs) exceeds the percolation threshold. For the devices used in this study, electrode spacing ($\approx$ 0.2 mm) is much larger than the length L of the nanotube bundles ($\approx$ 500 nm to 2000 nm), so a percolating network is necessary for a complete conduction path. Previous studies have shown that two semiconducting SWNTs (sc-SWCNTs) form a good electrical contact as well as two metallic SWCNTs (m-SWCNTs) [139]. At sc-SWCNT/m-SWCNT junctions, a Schottky barrier is formed with a barrier height approximately half that of the sc-SWCNT bandgap [140]. Therefore, it is thought that highly interconnected networks of SWCNTs will be electrically continuous and have properties that depend on the level of interconnectivity and SWCNT type [141].

As a result, the gas sensing mechanism for a SWCNT network film containing

both m-SWCNTs and sc-SWCNTs is expected to vary depending on the thickness and areal density of the nanotubes. Battie *et al.* investigated these parameters using CNTFET devices [83]. They found that below the metallic percolation threshold, modulation of the Schottky barrier resistance at m-SWCNT/sc-SWCNT junctions and sc-SWCNT/metallic contacts was the dominant sensing mechanism. Above the percolation threshold in which a continuous conduction path is present *via* m-SWCNTs, which can be confirmed by measuring Ohmic conduction (where the I_{SD}-V_{SD} characteristics are linear) across the device, the gas detection mechanism was solely attributed to charge transfer between the SWCNTs and adsorbed molecules. Therefore, it is likely that for chemiresistive devices (which display a measurable conductance without an applied gate voltage, thus having a connected m-SWCNT conduction path), charge transfer between the tubes and impinging molecules is the dominant sensing mechanism.

Salehi-Khojin *et al.* observed that the conductance through networks of highly defective nanotubes (as confirmed by Raman spectroscopy) was influenced only by a change in the resistance of the nanotubes themselves, whilst conductance through pristine nanotube networks was modulated at the junctions [111]. In addition to the study by Robinson *et al.* on the role of defects in SWCNT chemical sensors, it would therefore appear that increased defectiveness results in different sources of conductance change induced by SWCNT-gas interactions [112]. This is in line with the gas adsorption studies discussed in the previous section, in which strong chemisorption took place at defect sites. As a consequence, the possible influence of defects should be evaluated when proposing mechanisms for SWCNT gas sensor results. A summary of the possible sensing mechanisms for SWCNT networks containing different amounts of m-SWCNTs and sc-SWCNTs is presented in Figure 2.9.

Recently, doubt has been cast on the adequacy of the charge transfer mechanism to describe the changes in electrical conductance of SWCNT networks upon exposure to H_2O. Bell *et al.* suggested that water does not significantly dope carbon nanotubes [142]. Instead, the conductive responses are attributed to charge

redistribution in the SWCNT network, due to induced polarisation by the dipole moment of the surface-bound water molecules. The alternative mechanism may explain the discrepancy between *p*-type [143, 123, 144, 145] and *n*-type [146, 147] responses observed in the literature, with doping used previously to explain the induced conductance changes for carbon nanotubes when exposed to water vapour. This was considered in Chapter 4 of the current thesis.

Along with considering the mechanisms behind the conductive responses, the application of models to describe the gas sensing data can add weight to and distinguish between the proposed pathways for conductance modulation upon molecular adsorption. They can also be used to extract useful metrics from the sensing responses, as is now detailed.

2.4.3 Modelling SWCNT sensors

In order to probe the understanding of the mechanisms responsible for the change in electrical properties induced by analytes present on the sensor surface, as well as to extract key sensing parameters, Lee *et al*. used a simple model for irreversible adsorption of NO_2 to fit SWCNT chemiresistor response curve data [14].

The total number of NO_2 interaction sites on the SWCNT network ($T\theta$) was assumed to be correlated with the baseline conductance of the sensor, since this in turn is determined by the number of SWCNTs on the device. Due to this, they observed a strong linear relationship between the change in conductance (ΔG) measured upon introduction of an analyte with the baseline conductance (G_0).

It was suggested that the adsorption constant (k) and maximum possible conductive responses (S_{max}) were useful figures of merit to compare the performance of SWCNT based chemiresistors. Therefore, using the linear relationship of ΔG *vs* G_0, a method was developed to extract these two parameters from experimental data. The good fit of the irreversible adsorption model suggested that chemisorption of the target molecule had taken place at sites on the tube surfaces, with subsequent charge transfer altering the measured conductance across the device.

In this sense, the irreversible responses observed indicated that the SWCNT

based sensors could be thought of as doismeters. It was highlighted that for completely irreversible sensing responses, it was inappropriate to report a limit of detection (LOD) for the sensor, as given enough time the build up of any vanishingly small concentration of gas could induce a change in device conductance.

In further work, the Strano group described a fully reversible adsorption model for detection of dimethyl methylphosphonate (DMMP) with SWCNT networks [148]. Extracting the thermodynamic parameters from the results, they were able to calculate the Gibbs free energy of adsorption for the system under study. This could potentially be useful for other target analytes, such as H_2O, which are often easily desorbed from the sensor surface.

However, many of the SWCNT based sensors reported in the literature actually demonstrate partially reversible conductive responses to target analytes. This suggests that adsorption of, for example NO_2, takes place at multiple distinct interaction sites, with different associated desorption constants. Kumar *et al*. developed a model which described both reversible and irreversible adsorption of NO_2 to the surface of the SWCNTs [15]. They found that this adapted model better fitted the SWCNT chemiresistor response data for different concentrations of NO_2. Using this approach, it was also possible to calculate the extent to which the total conductive response curve was composed of irreversible or reversible type adsorptions.

The mathematical formulation of these models is described in Chapters 5 and 6. The ability of these models to describe the sensing responses observed in the current thesis was assessed, and the methods proposed were used to extract figures of merit from the sensing data to enable comparison with those reported in the literature.

2.5 Gas sensing technologies

While the current thesis focuses on the use of SWCNT-based chemiresistors for chemical vapour sensing, it is necessary to draw comparisons with other existing gas sensing technologies to benchmark performance and assess suitability for

real-world applications. Therefore, the figures of merit used to draw comparisons between the different techniques are defined, and the wide range of analytical methods available for gas sensing are reviewed.

2.5.1 Defining figures of merit

The use of various figures of merit allows the comparison of performance metrics for different gas sensing technologies, aiding evaluation of their suitability for the wide range of potential applications that exist. The parameters and figures of merit used in this study to draw comparisons with the literature are based on those suggested by both Senesac *et al*. [149] and Strano *et al*. [14], as are now described.

Magnitude of conductive response (S): The ratio of the change in conductance ΔG of the sensor upon introduction of the target analyte to the baseline conductance G_0 in the analyte free carrier gas , so that $S = \frac{\Delta G}{G_0}$.

Maximum conductive response (S_{max}): The maximum possible ratio of change in conductance to baseline conductance upon exposure to the target analyte, limited by the total number of gas-surface interaction sites.

Sensitivity: The slope of the calibration curve or change in unit sensor response with change in unit analyte concentration.

Selectivity: The ability to detect a specific analyte in the presence of other interfering molecules.

Response time (t_{90}): The time required to reach 90 % of the maximum conductive response upon introduction of the target analyte.

Recovery time (t_{-1}): The time required to recover 90 % of the original baseline conductance G_0 as before introduction of the target analyte.

Reversibility: The ability of the sensor to return back to its original baseline resistance value when the analyte is removed. A sensor response is defined as reversible if it can recover at least 50 % of it's original baseline conductance G_0 within 60 s.

Baseline drift (G_0 *drift*): The total change in the baseline conductance (G_0) of the sensor from the beginning of the experimental test to the end. This quantifies the amount of drift to be expected after a full experimental test with repeated exposure to the target analyte.

Signal drift (ΔG_0): The difference in the conductance of the sensor immediately before each pulse of target gas in experimental testing. This quantifies the level of drift to be expected after one injection of the target analyte of a certain concentration.

Adsorption constant (k): This parameter communicates the ability to transduce a given concentration of analyte within a pre-defined time, with units of parts per trillion per second (ppt^{-1} s^{-1}) used in the current study for comparison with other values communicated in the literature.

Desorption constant (k_{-1}): The rate at which an analyte is desorbed from the surface of the sensor.

Limit of detection (LOD): The lowest analyte concentration value that can be detected, often limited by the noise in the baseline signal of the sensor. The LOD can be calculated as the y-intercept value of a linear calibration plot of concentration *vs* response (if available), or 3 × the standard deviation of the average baseline signal, whichever is largest.

Dynamic range: The analyte concentration from minimum to maximum concentration that can be reliably detected before signal loss or saturation respectively.

Linearity: The range in which sensor response linearly proportional to the analyte concentration.

Hysteresis: The difference in sensor characteristics for increasing and decreasing analyte concentrations.

2.5.2 Gas sensing methods

Metal oxide semiconducting (MOS) sensors, first extensively reported by Seiyama *et al.* [150] and Taguchi *et al.* [151] in 1962, are a well established, commercially produced gas sensor technology. They have been used to detect a wide range of analytes for many industrial and commercial applications [152].

As the metal oxides used for gas sensing are insulating at room temperature, they must be heated, typically in the 200 °C to 500 °C temperature range, to facilitate electrical measurement of their conductivity. The principle of operation is *via* modulation of the charge carriers on the surface of a semiconducting metal oxide in the presence of a contacted reactive gas [153]. In an *n*-type semiconductor, such as SnO_2, oxygen adsorbed from the air to the surface upon heating acts as an electron acceptor state. Reactions at the surface result in a change in the surface coverage of oxygen, and thus a measurable change in the conductivity of the metal oxide.

MOS sensors are low-cost, extremely portable, have high sensitivity to low-concentrations of the target gas and demonstrate fast response times [154]. This has lead to their use in a wide variety of industrial monitoring applications [152], as well as in potable electronic nose (e-nose) systems [155].

However, selectivity is poor and functional layers must be added to MOS sensors to increase discrimination in atmospheres of mixed composition, or even to minimise the effect of atmospheric humidity on the sensing signal [154]. High

operating temperatures have limited their use in ultra low-powered applications, such as remote environmental monitoring or consumer electronics. Additionally, the low-cost of the sensor is often dwarfed by the cost of the complete sensing unit. Efforts for complete integration of metal oxide sensors into complementary metal-oxide-semiconductor (CMOS) circuitry, combined with the use of micro-hotplate technology may help to address power consumption issues and reduce the total price of the gas sensing systems [156].

Other forms of carbon are suitable for low powered gas sensing devices. These include carbon black, carbon nanofibres and graphene [157]. In particular, low noise can be achieved using graphene in sensing devices, with the dimensionality of the 2-D crystalline structure meaning that all atoms are exposed to the environment, resulting in high interaction surface area per unit volume and sensing responses at room temperature. Therefore, graphene has attracted considerable interest of late for chemical sensing. The level of defects or dopants, deliberately introduced in the graphene or otherwise, has been shown to modulate the change in resistance across the material during a sensing event, with an increased response observed using a more defective layer [157]. As with SWCNT based sensors, baseline drift can be an issue, and selectivity needs to be increased via chemical functionalisation to move towards commercially viable graphene sensors.

Both conducting polymers and non-conducting polymers have found utility in gas sensing devices [158]. Alteration of the electrical conductivity of conducting polymers is induced through exposure to a diverse range of organic and inorganic gases [159]. Examples of such polymers include polypyrrole (PPy), polyaniline (PAni) and polythiophene (PTh) [158].

The conductivity of conducting polymer based gas sensors must often be improved so that they are conducting or semiconducting *via* redox reactions or protonation, before electrical measurements can be carried out. The level of doping can then be altered by chemical reactions on the surface of the polymer, inducing a change in the measured conductance.

Non-conducting polymers are used as functional coatings for gas sensors to

aid adsorption of the target analyte [160]. Instead of measuring a change in conductance, mass sensitive (e.g quartz crystal microbalance, QCM), surface acoustic wave (SAW), capacitive or calorimetric sensor devices are employed.

Polymer-based gas sensors also demonstrate high sensitivity and fast response times to many molecules of interest. They have the added advantage of being operable at room temperature, reducing device complexity, power consumption and allowing them to be more easily used in integrated silicon circuitry. Unfortunately, they suffer from long-term instability, sometimes irreversible sensing responses and poor selectivity [158, 159].

Electrochemical gas sensors are a mature and important sensor class for environmental monitoring applications, displaying a large dynamic range of detection (over 10 orders of magnitude in some instances) [161]. Two or three electrode devices are commonly employed, where the open circuit potential across an electrolyte located between the electrode is monitored upon exposure to a target gas. The electrolyte, which transports charge within the sensor for detection at the electrodes, can be made from an ionically conducting solid (Nafion,yttria-stabilized zirconia) or aqueous electrolytes (sulfuric acid, sodium hydroxide, and potassium chloride) [161].

Electrochemical gas sensing responses can be linearly proportional, or proportional to the logarithm of the analyte concentration, depending on whether amperometric or potentiometric type devices are used. Detection down to the low ppb range has been reported, as has sensitivity to a wide range of gases (H_2, CO, O_2, NO_2, NO, H_2S SO_2).

Gas sensing using optical methods can introduce a high degree of selectivity towards the required gas, which is sometimes lacking in CNT, MOS and polymer based sensors [162]. Optical methods such as differential absorption DOAS, intracavity absorption spectroscopy (ICAS), Fourier Transform Infrared Spectroscopy (FTIR) and Raman light detection and ranging (Raman LIDAR) are capable of real-time, on-line monitoring of gaseous mixtures. Optical methods are often superior in performance to the sensors described previously. However, they have high asso-

ciated build and maintenance costs, with applications restricted due to the size/lack of portability of the instruments [162].

Acoustic methods using the speed, attenuation or impedance of sound can be used for reliable detection of gases. Typically, changes in the propagation of an ultrasonic wave through a gas sample is compared to a reference signal, which can be used to deduce the concentration of the test sample. Again, high power consumption and non-portable instrumentation limits the application of this technique, but it is considered reliable and to have a long lifetime [162].

As described above, each of the gas sensing technologies has associated advantageous and disadvantages, listed in Table 2.2. In most cases, a trade off must be made between cost and portability *vs* selectivity and long term reliability. Therefore, the suitability of each type of gas sensor depends on the operational requirements of the final desired application. As this study concerns SWCNT-based chemiresistors, which reportedly suffer from a lack of selectivity and cross-interference effects, strategies previously implemented to increase selectivity using Zeolites are introduced as a possible solution in the next section.

2.5.3 Zeolites for gas sensing

To increase the selectivity of the low-cost, low-powered sensors described in the previous section, functional layers are often added to the sensing element. One approach is to incorporate Zeolites, also referred to as molecular sieves, into the sensing layer. They are also used in a range of other applications, such as water purification, separation membranes and catalyst beds for the petrochemical industry [163].

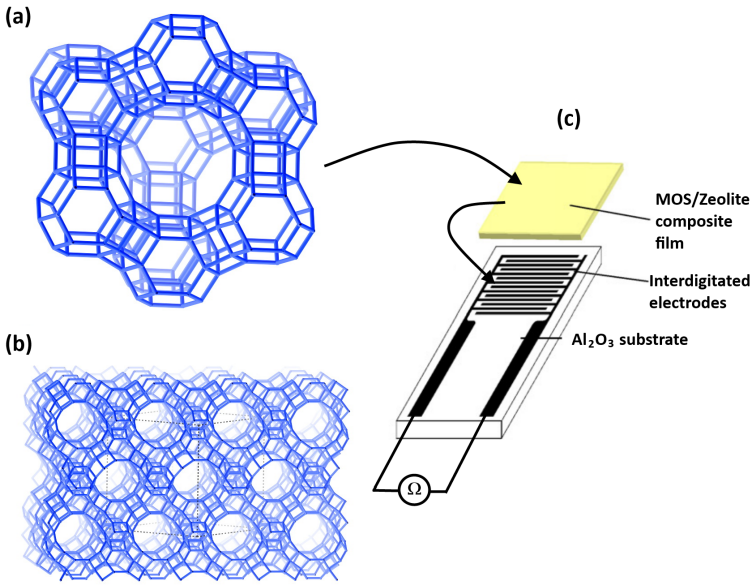

Figure 2.10: Faujasite type zeolite with an aluminosilicate framework viewed along the [111] direction [164]. (b) Faujasite type zeolite framework viewed along the [110] direction [164] with pore diameter of 8.0 *Å* [165].(c) Schematic diagram of MOS/zeolite composite film sensor [163].

Zeolites are 3-dimensional (3D) porous aluminosilicate frameworks which selectively exclude molecules from adsorption to pores (Figure 2.10a and b). They are composed of corner sharing AlO_4 and SiO_4 tetrahedra joined into 3-D structures [165], The ratio of silicon to aluminum in the zeolite material is an important quantity, as it dictates the number of cationic centers that are distributed throughout the framework, and thus it's acidity and hydrophobicity.

The high-surface area, absorptivity, porosity and catalytic activity of zeolite type materials make them attractive for chemical sensing applications. Zeolites are normally electrically insulating, often displaying ionic (but not electronic) conductivity in which mobile cations move between binding sites. Therefore, their use outright as a gas sensitive material requires an impedance based measurement system [166]. Sahner *et al.* report that water and a range of polar organic vapours can be detected using such methods in the 40 °C to 110 °C operating temperature range [163].

Zeolites can also be used as an auxiliary element to increase discrimination in an array of MOS type sensors [167]. This is achieved through a combination

of selective adsorption of the target gases to the framework and increased catalytic activity facilitating secondary reactions on the sensor surface, as depicted in Figure 2.10c. In other work, molecular sieves have been adopted as adsorptive layers in quartz crystal microbalance (QCM), surface acoustic wave (SAW) and attenuated total reflectance (ATR) type sensors [166]. As an interesting option for modification of SWCNT sensor responses and adsorption characteristics, they are investigated as a an auxiliary functional element in chapter 7.

2.6 Thesis rationale based on literature review

After surveying the carbon nanotube and gas sensing literature, a comparison between the different performance metrics, advantages, disadvantages and suitability for practical applications was possible. These quantities are displayed in Table 2.2 for each type of the carbon nanotube based sensor reviewed, as well as other existing alternative gas sensing technologies.

Table 2.2: A comparison table of the advantages and disadvantages of each gas sensing technology surveyed with carbon nanotube (CNT) or single-walled carbon nanotube (SWCNT)-based sensors. Each sub-class of carbon nanotube-based sensor is included and marked as reviewed. Adapted from multiple sources [17, 118, 95, 168, 154, 159, 162, 161]

Sensor type	**Advantages**	**Disadvantages**	**Applications**
Carbon nanotube [*i*] SWCNT chemiresistor [*ii*] CNTFET [*iii*] SWCNT chemicapacitor [*iv*] CNT resonator	(a) Room temperature operation[*i,ii,iii,iv*] (b) Low power consumption[*i,ii,iii*] (c) Fast response times[*i,ii,iii,iv*] (d) High sensitivity[*i,ii,iii,iv*] (e) High surface to volume ratio[*i,ii,iii,iv*] (f) Portable[*i,ii,iii*] (g) Functionalisation for application tailoring[*i,ii,iii,iv*] (h) Possible CMOS integration[*i,ii,iii*] (i) Printable[*i,ii,iii*] (j) Simple design[*i*]	(a) Cross-sensitivity to humidity[*i,ii,iii,iv*] (b) Poor selectivity without functionalisation[*i,ii,iii,iv*] (c) Poor response recovery[*i,ii,iii,iv*] (d) Increased device complexity[*ii,iii,iv*] (f) Device-to-device variability[*ii*] (g) Higher cost[*ii,iii,iv*]	(a) Health monitoring / diagnosis (b) Pollution monitoring (c) E-nose (d) Flexible devices (e) Embedded sensor systems (f) Wireless, low-powered applications

Table 2.2: A comparison table of the advantages and disadvantages of each gas sensing technology surveyed with carbon nanotube (CNT) or single-walled carbon nanotube (SWCNT)-based sensors. Each sub-class of carbon nanotube-based sensor is included and marked as reviewed. Adapted from multiple sources [17, 118, 95, 168, 154, 159, 162, 161]

Sensor type	Advantages	Disadvantages	Applications
Metal Oxide Semiconductor (MOS)	(a) High sensitivity (b) Fast response time (c) Low cost (d) Responsive to wide range of gases (e) Good response recovery (f) Portable	(a) Poor selectivity (b) High operating temperature (c) Long term stability issues (poisoning) (d) Humidity interference	(a) Industrial monitoring (b) E-nose (c) Pollution monitoring
Polymer	(a) Low cost of fabrication (b) Simple device (c) Low energy consumption	(a) Irreversible responses (b) Poor selectivity (b) Long term instability	(a) Chemical storage monitoring (b) Air quality monitoring (c) Portable devices

Table 2.2: A comparison table of the advantages and disadvantages of each gas sensing technology surveyed with carbon nanotube (CNT) or single-walled carbon nanotube (SWCNT)-based sensors. Each sub-class of carbon nanotube-based sensor is included and marked as reviewed. Adapted from multiple sources [17, 118, 95, 168, 154, 159, 162, 161]

Sensor type	Advantages	Disadvantages	Applications
Electrochemical	(a) High sensitivity (b) Large dynamic range (c) Well understood mature technology (d) Low cost (e) Responsive to wide range of gases	(a) Poor selectivity (b) Limited life span (electrode drying) (c) Long term stability issues (poisoning) (d) Minimum size of cell required	(a) Industrial monitoring (b) Automotive industry (c) Environmental monitoring Medical applications
Optical methods	(a) Highly accurate quantification via calibration (b) Long lifetime (c) Selective (d) Resilient to cross-interference	(a) High cost (b) Device maintenance (c) Non-portable (d) High power consumption	(a) Gas leak detection (b) Security (c) Air quality monitoring (d) Quality control
Acoustic methods	(a) Long lifetime	(a) Low sensitivity (b) Sensitivity to environmental change	(a) Wireless sensor network

The higher sensitivity of carbon nanotube-based sensors, due to their hollow, 1-D structure, along with faster response times to gases of interest, may make them

favourable to polymer sensors. This is accompanied by the added benefit of many possible nanotube functionalisation routes to explore for specific applications, combined with room temperature operation capability, lacking in MOS type sensors and potentially allowing nanotubes to be incorporated into CMOS technology.

In terms of portability, the carbon nanotube devices are clearly superior to the less portable, bulky, optical or acoustic methods, associated with relatively high power requirements. Furthermore, commercially produced gas sensing technologies utilising solid-state materials as the sensing element (MOS and polymer type sensors) are traditionally more affordable. Given the similarities in sensor design, this is also expected to be the case for carbon nanotube-based sensors.

The potential benefits of improving the current state of the art of carbon nanotube sensor technology largely depends on use cases. Bearing in mind that operational requirements will commonly dictate the optimal choice of sensor for a specific application, carbon nanotube based sensors appear to be best suited to portable, low-powered device applications. The wide range of possible use cases for extremely low-powered, affordable and selective gas sensing justifies the efforts to improve the performance and viability of current carbon nanotube sensors.

Substantiated by the literature review, further research is required and many challenges must be overcome to move towards carbon nanotube-based sensors which are viable for real-world applications. It is clear from the reports of both *n-type* and *p*-type sensing responses for SWCNT networks to H_2O that the interaction of water vapour and the subsequent changes in measured electrical conductance are not fully understood. An understanding is important for the development of SWCNT-based devices in general, thus this was investigated in Chapter 4, along with the effect of SWCNT functionalisation on the conductance-humidity behaviour.

Irreversible carbon nanotube conductive responses are commonly reported in the literature, limiting accurate quantification of target gases and vapours. The current techniques used to improve the characteristically slow signal recovery after exposure to analytes such as NO_2 or NH_3, either degrade the sensing material over

time, require more power or increase device complexity. In Chapter 5 an alternative method, referred to as the water-assisted regeneration technique (WAR), is applied and evaluated to improve baseline signal recovery.

A further implication of functionalised SWCNT network sensitivity to water vapour was the potential for it to impact upon and alter sensing responses to NO_2, which has not been studied previously in the literature. This effect is important because of it's relevance to the varying atmospheric conditions encountered for real-world pollution monitoring. Therefore, Chapter 6 describes the effect of atmospheric humidity levels on SWCNT chemiresistor conductive responses to NO_2 gas.

The cross-sensitivity of SWCNT-based gas sensors to water vapour is often overlooked in the literature when considering potential applications. Accordingly, Chapter 7 details the development of a novel SWCNT-Zeolite composite material, which reduces the impact of changes in atmospheric humidity levels on the conductance of SWCNT-based sensors when incorporated into the sensing layer.

Within the carbon nanotube sub-class of gas sensor, chemiresistors, chemicapacitors, CNTFETs and mechanical resonator type devices were reviewed. Due to the difficulty in fabricating multiple, characteristically consistent devices with individual single-walled carbon nanotubes, networks of SWCNTs, which display the aggregate properties of the constituent SWCNTs, were chosen for use throughout this study.

In terms of the sensor sub-classes available, SWCNT chemiresistors were chosen as the sensor type for study in the current thesis. Firstly, this decision was made due the simplicity of the fabrication method, enabling the controlled assembly and investigation of many devices with similar sensing characteristics, key in understanding and solving some of the current SWCNT-based sensor challenges.

Secondly, the ability to incorporate widely used solution processing techniques, combined with minimal required on chip circuitry for the sensing measurement, facilitated the use of established gas sensing apparatus and methods to investigate the SWCNT chemiresistor sensing properties. The compatibility of the

solution processing methods with the SWCNT chemiresistor fabrication route also allowed the exploration of different SWCNT functionalisations to increase selectivity and performance. With a view to exciting future applications, such as sensors embedded in fabrics or food packaging, the device architecture was deemed the simplest for incorporation of SWCNTs into wireless, printed, or flexible devices.

Finally, the wealth of literature available on SWCNT-based chemiresistors offered an opportunity to compare reported data with results from the functionalised SWCNT devices used in the current study. Furthermore, models previously developed to extract key figures of merit from SWCNT chemiresistor sensing data could then be applied to the modified SWCNT devices in the current thesis, aiding understanding and reasoning.

Chapter 3

Material characterisation theory and experimental methods.

In this chapter, the first section describes the theory required for the material characterisation techniques used throughout the studies reported later in this thesis. The experimental procedures and methods used to fabricate the SWCNT devices are introduced in the following sections, along with the apparatus used for the gas sensing studies. Finally, the methodology used to determine errors in the quantities reported throughout the thesis are explained.

3.1 Material characterisation theory

A wealth of literature exists describing the characterisation of SWCNTs. Due to the heterogeneity of as-produced SWCNT powders, often containing a variety of SWCNT species, electronic types and impurities, a range of techniques are commonly applied to establish the physical and electronic properties of the sample [169]. Changes in these quantities can be monitored to evaluate subsequent processing and functionalisation methods, ultimately used to tailor SWCNTs for applications such as chemical sensing.

In this section, the theories behind the material characterisation techniques used throughout the study are introduced. These methods were used to characterise the properties of the raw SWCNT powders, the functionalised samples and the SWCNT network devices. Additionally, they were employed to investigate the

potential mechanisms behind the chemical sensing results reported in the current study. The methods, along with justifications for their use, are now discussed.

3.1.1 Raman spectroscopy

Raman scattering, the inelastic scattering of light, occurs when the electric field of an incident photon interacts with a molecule. Due to Coulomb's law, a displacement of the electrons and nuclei will occur, inducing a dipole moment [55]. In a scattering event, an electron is excited from the valance electron band to the conduction energy band by photon absorption. This excited electron is scattered by emitting or absorbing phonons, where a phonon is defined as the collective, quantised vibration of atoms, and can be treated as a quasi-particle [55]. The electron relaxes to the valance band by emitting a photon of lesser or greater energy than the incident photon.

The Raman spectra is a plot of the intensity of the scattered light as a function of energy change (frequency shift). This provides information on a material's phonon frequencies [56], since the shift in frequency is related to the amount of energy gained or lost during the scattering of the incident photon with a phonon. Raman scattering can occur for phonon emission or by phonon absorption, known as the Stokes and Anti-Stokes process respectively. In the current work, Stokes scattering is used due to the temperature dependence of Anti-Stokes scattering [170].

Raman spectroscopy is a powerful tool for the characterisation of SWCNTs. It can be used to confirm the presence of carbon nanotubes in powder form, solution or composite materials, as well as providing a measure of tube defectiveness [56]. The determination of SWCNT diameter, and therefore electronic type, is possible using Raman spectroscopy, an important indicator of their suitability for device applications [171]. Changes in the Raman spectra of bulk SWCNT samples can also be related to varying environmental conditions, such as temperature or atmospheric composition.

The phonon structure of a SWCNT, which is unique for each different chirality, determines it's response to the Raman effect. The main features of the Raman spectra for a HiPco SWCNT sample are highlighted in Figure 3.1. The G-band of

a SWCNT spectra is composed of several peaks. It is also known as the graphite band, centered at 1580 cm^{-1}, and results from vibrations of the carbon atoms tangential to the tube surface [172].

The G-band can be used to distinguish between semiconducting (sc-

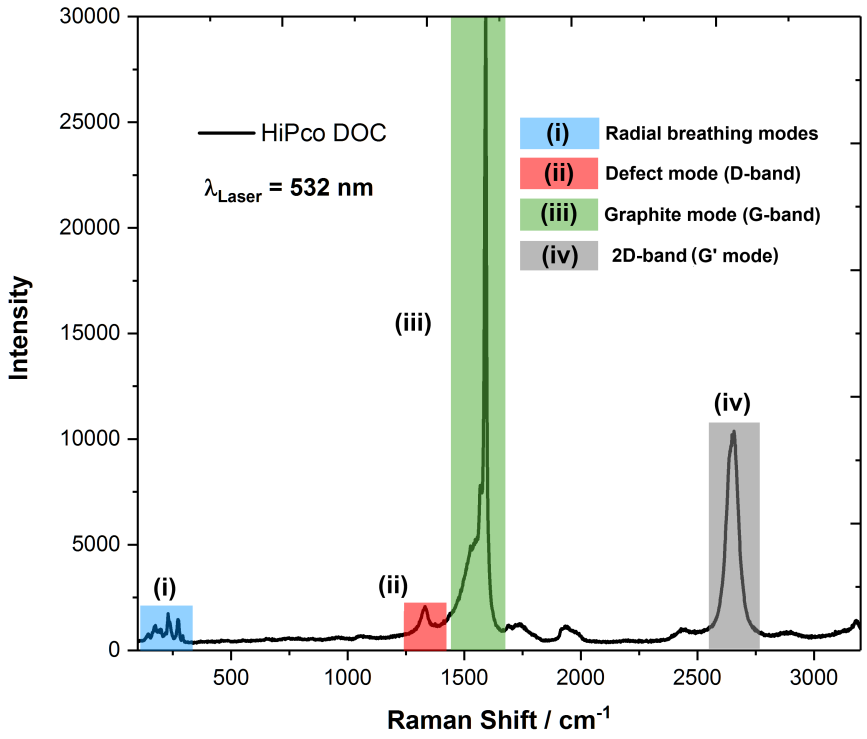

Figure 3.1: Raman spectra showing the intensity of the Raman signal for HiPco DOC SWCNTs deposited on a glass slide. The key spectral features include (i) the radial beathing modes (RBMs), (ii) the defect mode (D-band), (iii) the graphite mode (G-band), (iv) the G′ (2D-band). Some of the features change with laser wavelength (here λ = 532 nm).

SWCNTs) and metallic (m-SWCNTs) nanotubes. Splitting of the band, due to symmetry breaking effects associated with the curvature of the tubes [56], takes the form of the G^+ band (at $\approx$ 1591 cm^{-1}) and a G^- band (at $\approx$ 1567 cm^{-1}) as is seen in Figure 3.2 for SWCNTs grown using the (a) HiPco and (b) CoMoCat methods. The G^+ feature is associated with the vibration of carbon atoms along the nanotube axis. The frequency at which it appears is sensitive to charge transfer from donors interacting with the SWCNTs (the frequency at which the peak is observed shifts

up for electron acceptors, and down for electron donor type dopants) [56].

The G^- feature is associated with vibrations of carbon atoms along the circumferential direction of the SWCNT. The line shape is highly sensitive to whether the nanotubes are semiconducting or metallic, as well as the nanotube diameter. The intensity and line shape of the G^- band can also decrease or increase due to charge transfer from a dopant material [173].

The radial breathing modes (RBMs, observed at 100-550 cm^{-1}) are unique to carbon nanotubes and their observation provides direct evidence that a sample contains SWCNTs [56]. Their frequency can be used to determine the diameter of the nanotubes present in a sample. The RBM modes are due to coherent vibrations of C atoms in the radial direction (out of plane from the tube surface) [172], and the frequency at which they appear is inversely proportional to tube diameter [174]:

$$\omega_{RBM} = \frac{A}{d_t} + B \tag{3.1}$$

where the proportionality constant A = 227.0 cm^{-1} nm and B = 0 cm^{-1} for an ideal vibrating isolated SWCNT [174]. In practice, the measurement of ω_{RBM} is up-shifted by B, which factors in an offset of the RBM frequency caused by environmental factors such as bundling with other tubes, substrate interactions or chemical surroundings (e.g adsorption of water vapour or oxygen) [175]. This dependency arises from the fact that the masses of all carbon atoms along the circumferential direction are proportional to the diameter. A typical range of RBMs for a HiPco sample are shown in Figure 3.1. From these RBM modes, an estimation of corresponding diameters can be made using equation 3.1.

An experimentally determined Kataura plot (as displayed in Figure 2.3b from Chapter 2) can be used to translate the observed RBM frequencies into tube diameters. However, the aforementioned environmental effect on the RBM frequency must be considered before assuming accurate assignment of the chirality to the tubes present in the sample [176].

The intensity of the D-mode (also known as the disorder band, observed in the 1250 cm^{-1} to 1350 cm^{-1} range depending on laser wavelength [177]) is dependent

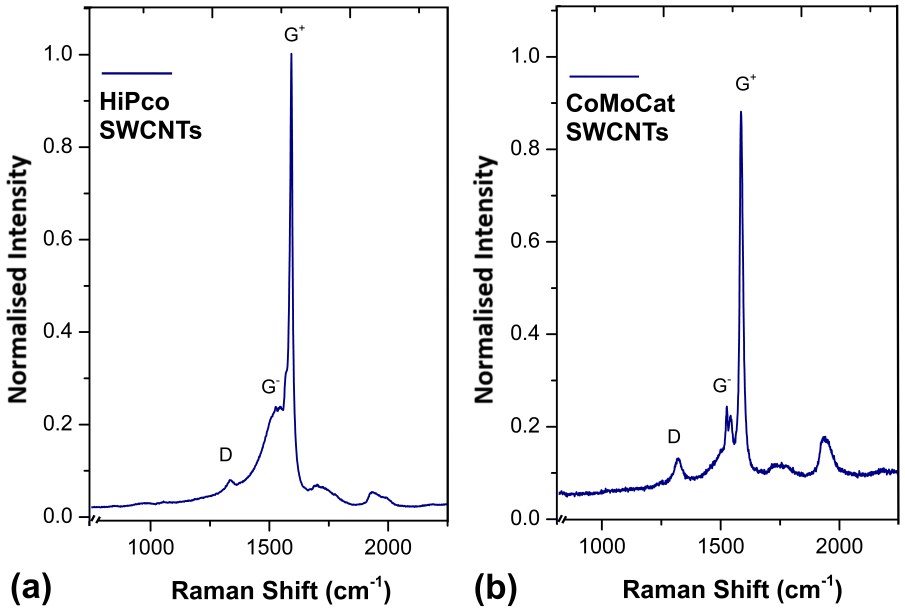

Figure 3.2: Raman spectra showing the difference in G^+ and G^- features for (a) HipCo and (b) CoMoCat SWCNTs. Typically, a higher proportion ($\approx 90\%$) of sc-SWCNTs are found in the raw CoMoCat sample compared to HiPco samples ($\approx 66\%$), resulting in the difference in spectral features. Laser wavelength $\lambda = 488$ nm.

on the breaking of sp^2 symmetry found throughout the rolled up graphene lattice, which can be caused by the end of the nanotube, defect sites, functionalisation or the presence of residual metallic impurities. Therefore, it can be used as a qualitative guide to the purity of the sample. The intensity of the G^+-band to the D-band (I_G / I_D ratio) is commonly reported to provide an indication as to the defectiveness of the sample after processing treatments [178].

Diameter dependent assignments of the G^- peak can only be performed at the single nanotube level, which can then be used in combination with measured RBM frequencies to assign (n,m) structure of the nanotube. Due to the range of species observed in bulk HiPco SWCNT powders, individual assignments of nanotube chirality is not possible, although the RBMs can provide an indication to the range of SWCNT types present [171].

The 2D-mode (also sometimes referred to as the G′-mode), is an overtone of the D-mode, so that $\omega_{2D} = 2\omega_D$, is found in the 2500 cm^{-1} to 2900 cm^{-1} range. Charge transfer due to doping or an applied gate voltage induces a frequency up/down shift of the 2D feature in SWCNTs. It's position is also dependent on in-

cident photon energy [172].

Raman spectroscopy is applied in Chapter 4 to aid interpretation of the humidity effect on the conductance of the SWCNT networks. In Chapters 5 and 7 it is used to assess the influence of heat treatment on the SWCNT sensing films, and to investigate the effect of surfactant functionalisation in Chapter 6. However, the Raman effect is most effectively used for characterisation of SWCNT samples and devices in conjunction with other techniques. UV-Vis-NIR absorption spectroscopy can provide data complementary to Raman studies, as is now detailed.

3.1.2 UV-Vis-NIR absorption spectroscopy

The absorption of ultraviolet (UV, λ=10 nm to 390 nm range) visible (Vis, λ= 390 nm to 700 nm range) and near-infrared (NIR, λ= 700 nm to 2400 nm range) light by matter causes the energy content of the molecule (or atom) to increase, which in some cases can induce transitions between different electronic energy levels. The energy of light absorbed corresponds to the energy required to excite an electron to a higher energy level, thus different absorbing species will absorb light at different wavelengths [179].

The energy of an incident photon of light is given by $E = \frac{hc}{\lambda}$, where the energy E is given in Joules, h is Planck's constant (6.63×10^{-34} J s) and the wavelength of the incident light λ in meters is given by $c = f\lambda$, where $c = 3 \times 10^{8}$ ms^{-1} and f is the frequency of the light wave (Hz) . Therefore, incident photons of shorter wavelength carry more energy when interacting with a molecule.

When incident light passes through a sample, the absorbance over a range of wavelengths can be measured, characteristic of the samples chemical composition and structure. UV-Vis-NIR absorption spectroscopy has been applied previously to characterise SWCNTs in both solution and deposited films. It is a useful tool to assess the range of m-SWCNTs and sc-SWCNTs that exist in a sample. This, in turn, is important for their use in future technologies, since a high number of metallic SWCNTs may be desirable or detrimental, depending on electronic application.

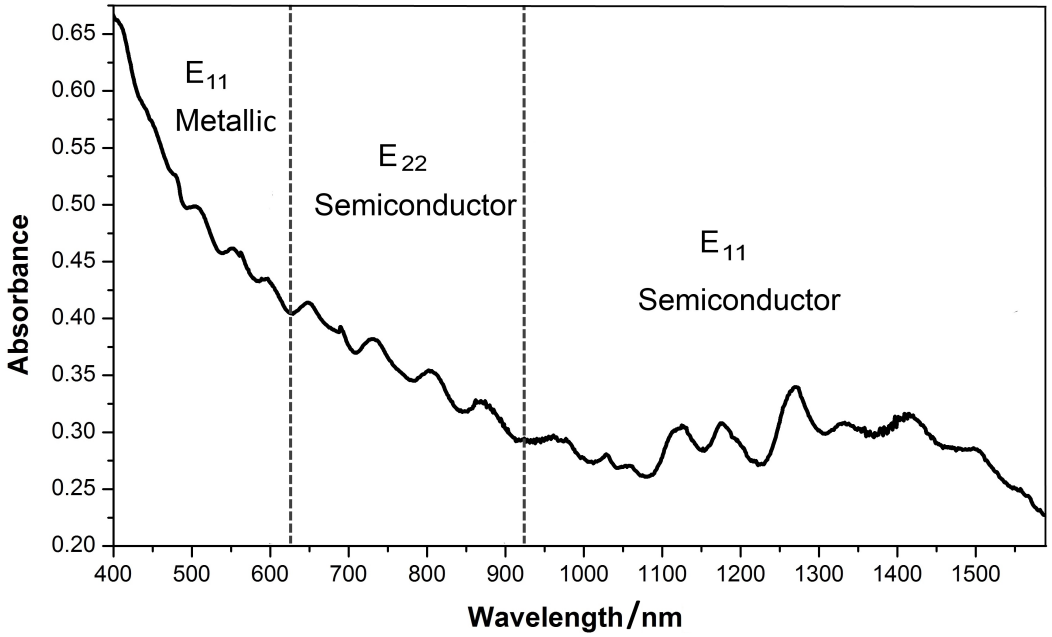

Figure 3.3: UV-Vis-NIR absorption spectra, displaying the range of metallic and semiconducting tube species present in a HiPco DOC SWCNT solution (diluted to 0.003 mg ml^{-1}).

Figure 3.3 demonstrates a typical adsorption spectra for HiPco SWCNTs suspended in a D_2O sodium deoxycholate (DOC) solution. The incoming photons, of controlled energy, pass through the a cuvette containing the solution, where individualised SWCNTs absorb the photons at wavelengths specific to their chirality.

Sharp peaks in the electronic spectra of one dimensional nanomaterials, referred to as van Hove singularities (vHs), correspond to allowed transitions between energy levels in the nanotube electronic density of states (DOS, the allowed energy levels for electron occupation) [53]. SWCNTs strongly absorb when the energy of the incident photon matches that of a specific vHs energy transition, denoted E_{ii}. These diameter dependent singularities appear due to the 1-D nature of nanotube electronic structure [58]. The energy at which absorption takes place can be matched with a specific tube diameter using a Kataura plot, as described in section 3.1.1.

As depicted in Figure 3.3, regions of the spectra can be assigned to m-SWCNTs or sc-SWCNTs [58], as well as to peaks from functionalisation agents and solvent (in this case DOC in D_2O, chosen to minimise overlap with SWCNT

absorption bands). The absorption peaks can be broadened by bundling of the SWCNTs in solution [180] or the micelle interaction with chosen surfactant [59].

The concentration of SWCNT solutions can be determined using the Beer-Lambert law, describing the linear relationship between absorbance and concentration of particles in a solution [179]:

$$C = \frac{A_\lambda}{\varepsilon_\lambda l}, \tag{3.2}$$

where A_λ, ε_λ and l are absorbance, extinction coefficient at a specific wavelength λ and optical path length of the cuvette used respectively. The extinction coefficient can vary depending on functionalising agent and the homogeneity of the sample, so should only be used as a guide for concentration calculations [181].

UV-Vis-NIR absorption spectroscopy was used in Chapter 4 to calculate the concentration of the HiPco SWCNT solutions used to fabricate the SWCNT-based devices and to confirm the mixture of m-SWCNTs and sc-SWCNTs present in the sample. An attempt was made in Chapter 6 to estimate the thickness of a solid HiPco SWCNT film, used to fabricate SWCNT-based sensors to detect NO_2 in a range of different background atmospheric humidities. The morphology of these films was revealed through use of scanning electron microscopy (SEM), as is now discussed.

3.1.3 Scanning electron microscopy

Scanning electron microscopy (SEM) is a material characterisation technique in which high resolution images (up to 100 nm in the case of the current study) can be obtained to provide qualitative topological information, as well as to estimate the size of surface features and structures [182]. An electron beam is raster scanned across the surface of a sample in a vacuum (10^{-6} Torr), ionizing specimen atoms and ejecting electrons to a distance of a few nanometers above the surface, known as secondary electrons. These are accelerated using a high voltage ($\approx$ 10 kV) towards a detector, where the contrast and topological image is determined by the number

of incident electrons [183]. To avoid charging of the material (and a degradation in image quality) the samples in the current study were gold coated and attached to a metal stub for imaging.

SEM can qualitatively enable assessment of SWCNT network topology, as well as estimates of SWCNT bundle sizes present in the sample, reported in Chapters 4 and 6. Furthermore, it is useful to visualise the surface structure of SWCNT-composite materials, such as the SWCNT-Zeolite sensing elements described in Chapter 7. Transmission electron microscopy (TEM) was also used for imaging of the nanotubes used in the current study, as is now discussed.

3.1.4 Transmission electron microscopy

Transmission electron microscopy (TEM) can be used to provide images of nanoscale features, with sub-nanometer resolution possible. Typically, specimens are deposited from solution on to a copper grid coated with carbon or holey carbon, so that a specimen layer of thickness < 100 nm is formed. The specimen is loaded into a vacuum chamber and an electron beam focused on to the sample using lenses. The beam passes through the sample, with electrons interacting with the sample to produce a modified beam, which is collected and subsequently focused on to an imaging device (such as a fluorescent screen or a charge-coupled device) to image nanoscale features of the sample [184].

Due to the high resolution achievable, TEM can be used to approximate the diameter of SWCNT bundles and individual SWCNTs in the sample, as is described in Chapter 6. A qualitative assessment of carbonaceous or metallic impurities present on the tube walls can also be made [169]. Finally, TEM was used to establish the size of particles present in the SWCNT-Zeolite composites described in Chapter 7.

3.1.5 Thermal gravimetric analysis

Thermal gravimetric analysis (TGA) is a fast and effective technique, able to quantify the amorphous carbon, catalytic metals and graphitic structures, such as SWCNTs or MWCNTs, within a bulk sample without requiring extensive sample perpetration. It can be used to characterise as-produced SWCNT samples or to track the

effects of subsequent processing techniques [185].

Samples are placed into an alumina crucible and positioned on a calibrated microbalance. The sample is then heated (in the case of the current study from room temperature to 750 °C) at a specified ramp rate in air, whilst the mass change of the sample is recorded. Mass change can then be related to the oxidation of constituent particles in the sample due to heating in air. TGA can also be used to determine the stability of the sample against degradation *via* oxidation when heated in air. Performing the technique can cause metallic impurities to convert to metal oxides, as well as any carbon content to form CO or CO_2.

The maximum derivative of the TGA curve provides the average oxidation temperature of the bulk material. Lower oxidation temperatures can be indicative of multiple forms of carbon in the material, such as amorphous carbon, smaller diameter SWCNTs, SWCNT bundles or defective SWCNTs, which oxidise faster at defect sites [186]. The curve can also be altered by surfactant functionalisation [187].

The technique was used in Chapter 6 to investigate the effects of heat treatment on surfactant functionalised SWCNTs and estimate the level of impurities present in the bulk raw sample.

3.1.6 Attenuated total reflectance-Fourier transform infrared spectroscopy

Attenuated total reflectance-Fourier transform infrared (ATR-FTIR) spectroscopy has been applied previously to study the adsorption of H_2O to zeolite frameworks [188]. Other FTIR studies have examined the adsorption of NO_2 to zeolites, as well as the subsequent formation of reaction products [189, 190, 191].

In Chapter 7, ATR-FTIR was used to study the adsorption of NO_2 to the zeolite frameworks used for the top layer and mixed layer type SWCNT-zeolite composite sensors in both dry an humid conditions. The results were used to infer possible reactions that take place upon the co-adsorption of water and NO_2, or the adsorption of NO_2 in an already water saturated layer. The full experimental details are outlined in Chapter 7.

3.1.7 Energy dispersive X-ray spectroscopy

In conjunction with SEM, energy dispersive X-ray spectroscopy (EDS) was used to confirm the silicon to aluminum ratio in the zeolite composite materials, along with the carbon content on the surface of each sensor type. In EDS, the inelastic interaction of the incident high energy electron beam with atoms in the sample causes the ejection of inner shell electrons. The hole left behind is filled by an outer shell electron, in the process emitting an X-ray with energy equivalent to the difference between the higher and lower energy levels. The energy of the emitted X-ray is detected and is characteristic of the constituent element in the sample [184].

Hydrophobic zeolites, such as Silicalite-1, have a high silicon to aluminium framework ratio, whilst the silicon to aluminium ratio of hydrophilic H-Zeolite-Y is low. Therefore, EDS is a useful tool for the current study, as the hydrophobicity of a zeolite depends on its silicon to aluminium framework ratio[192]. It is applied in Chapter 7.

3.2 Electronic characterisation

3.2.1 Current-voltage device characteristics

Current-voltage (I-V) characterisation facilitates the calculation of DC conductance (DC resistance) for a given device, as well as revealing how direct current is influenced by an applied voltage bias across the functional electronic element [193]. A voltage is applied (V_{SD}) in finite steps across the source/drain electrodes and the current (I_{SD}) is measured. The conductance, G_{SD}, is given by:

$$G_{SD} = \frac{I_{SD}}{V_{SD}} \tag{3.3}$$

where the resistance measured across the device R_{SD} is inversely proportional to the conductance:

$$R_{SD} = \frac{1}{G_{SD}} \tag{3.4}$$

Linear or non-linear variation of induced current *vs* applied voltage can reveal

joule heating [194, 195, 196] or charging effects in the device [197], which may be related to fabrication processes or the surrounding environment, potentially affecting suitability and performance for desired applications.

In the current study, two-point I-V characterisation was used to investigate the dependency of device conductance on the amount of carbon (SWCNTs) incorporated into the device, as detailed in Chapter 6, using a Keithley 4200 semiconductor characterisation system. The effect of SWCNT functionalisation was also studied in Chapter 4, along with the variation of device I-V characteristics for wetted SWCNT networks. I-V characterisation over a range of temperatures can also provide useful information on the properties of SWCNT networks, as is now detailed.

3.2.2 Conductance-temperature measurements

Electronic transport measurements can be used to investigate how the DC conductance (DC resistance) of a device varies with temperature [198]. The conductivity of metallic materials (charge carriers are electrons) decreases as the temperature of the material increases, whereas the conductivity of semiconducting materials (charge carriers are *n*-type electrons or *p*-type holes) increases with increasing temperature [198]. Therefore, obtaining data on the conductance-temperature relationship observed for SWCNT networks can indicate whether the sc-SWCNTs contribute towards conduction, and consequently gas sensing responses.

To obtain data on the conductance of the SWCNT networks as a function of temperature, a cryostat with an in-built sample heater and liquid nitrogen supply for cooling was used to control the temperature of the device in the 96 K to 300 K range. A semiconductor analyser setup was used to obtain I-V curves for the sample in two-terminal contact mode.

Many mechanisms are reported to describe conduction through the SWCNT networks in the literature, such as three dimensional variable-range hopping (3D-VRH) [199, 200], fluctuation-assisted tunnelling (FAT) [201, 202], Schottky [134, 203] and Poole-Frenkel conduction [197, 204, 205]. Whilst it is beyond the scope of this thesis to study the SWCNT network conduction mechanisms in depth, conductance- temperature data was obtained by Zak Kobos of the Reed group, Yale,

to enable comparison of the conductive properties of the SWCNT networks used in this study with those elsewhere. These results are reported in Chapter 6.

3.2.3 Hot-probe method

The Hot-probe method provides a simple way to distinguish between *n*-type and *p*-type semiconductors, using a two-terminal multimeter and a heated probe (typically heated using the tip of a soldering iron). The soldering iron is applied to the positive probe (termed the hot-probe) connected to the multimeter, and the cold probe is connected to the negative terminal (as shown in Figure 3.4a). When the hot and cold probes are contacted to a semiconductors surface (with sufficient spatial separation such that the temperature of the cold probe is not initially increased by the hot), a positive voltage reading is measured for *n*-type semiconductors and a negative voltage readout is observed for *p*-type semiconductors. The majority charge carriers (electrons or holes) become thermally excited at the hot-probe terminal, diffusing throughout the rest of the semiconductor to the cold probe. This induces a potential difference across the semiconductor, the sign of which is measured using a multimeter, corresponding to the sign of the minority charge carriers remaining at the hot-probe [206].

The hot-probe method has been applied previously to confirm *p*-type con-

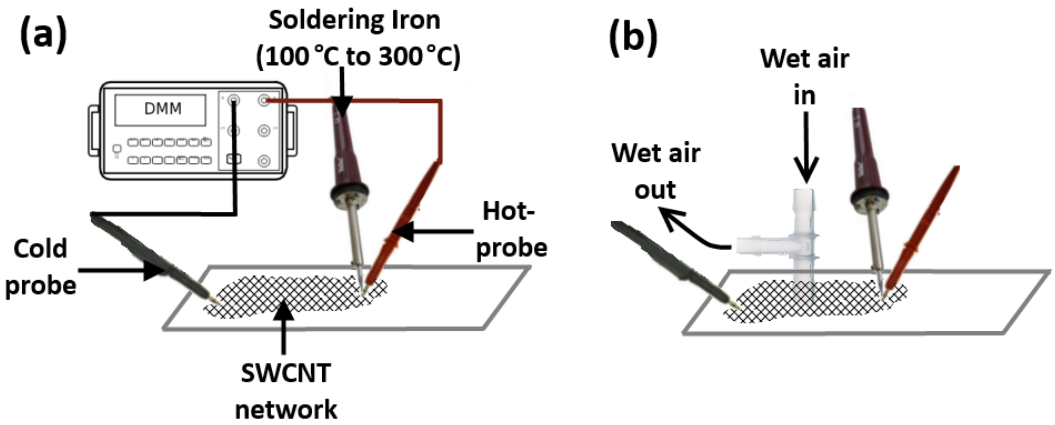

Figure 3.4: (a) A schematic diagram of the hot-probe setup in which a soldering iron is used to heat the positive DMM probe, inducing a negative change in potential across the SWCNT network indicating *p*-type character. (b) An adapted setup to expose a segment of the film to water vapour, further changing the measured surface potential to investigate the effect of anionic and cationic surfactants in the film.

ductivity in SWCNT networks [207]. A similar study was performed in Chapter 4 for the DOC and CTAB functionalised SWCNT networks deposited on glass. This confirmed the *p*-type nature of the sc-SWCNTs in the film. The experiment was further adapted to investigate the effect of surface adsorbed water vapour on the charge carriers across the SWCNT films (Figure 3.4b). This revealed a difference in behaviour between the networks containing anionic or cationic surfactant.

3.3 Experimental methods

3.3.1 Sample preparation, SWCNT solution processing and surfactant functionalisation

There have been many studies devoted to the development of procedures to enable fabrication of SWCNT-based devices from raw samples. Two approaches dominate; the growth of SWCNTs directly on to the device, or solution processing methods, each with associated advantages and disadvantages. In the current work, HiPco SWCNT powders were obtained externally and a solution processing route was adopted to allow an experimental approach to the characterisation of the SWCNTs and versatile fabrication of SWCNT-based sensors. These methods are now described in this section.

The dispersion of raw SWCNT powders in solution for processing is difficult due to their hydrophobicity and tendency to form hexagonally packed bundles [208]. Covalent [209] and non-covalent functionalisations [210] have been applied previously to add functional groups to the walls of SWCNTs and aid their dispersion in aqueous solution. In the current study, non-covalent functionalisations using a range of anionic, cationic and non-ionic surfactants (depicted in Figure 3.5) were used to disperse the HiPco produced SWCNTs in H_2O, enabling material characterisation and fabrication of the SWCNT-based sensors.

In surfactant-nanotube aqueous solutions, the surfactant forms micelle structures around the tubes (wrapping), inhibiting re-aggregation and aiding efficient dispersion, as depicted in Figure 3.6 [212]. For anionic (DOC, SC) or cationic surfactants (CTAB, CTAT), the hydrophobic tail of the molecule is orientated towards

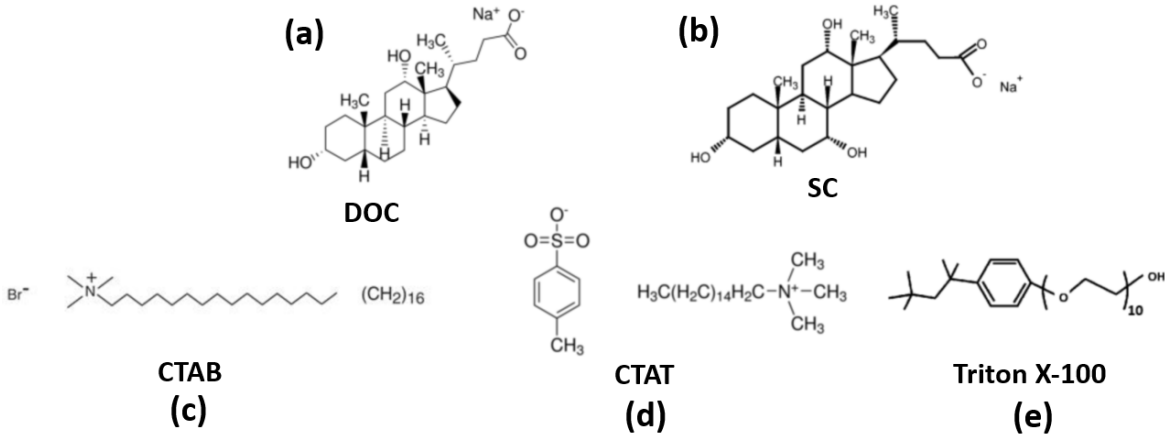

Figure 3.5: The chemical structure of the surfactants used for the non-covalent functionalisation of SWCNTs in the current thesis. (a) Sodium deoxycholate (DOC), (b) Sodium cholate (SC), (c) Hexadecyltrimethylammonium bromide (CTAB), (d) Hexadecyltrimethylammonium p-toluenesulfonate (CTAT), (e) Triton X-100. Chemical structures are adapted for the figure from the RSC ChemSpider database [211] .

the nanotube and the hydrophilic, charged head group, interacts with water forming a micelle like structure around the tube bundles [213]. When this process is combined with an external energy input to overcome the strong van der Waals (vdW) interactions that cause tube bundling, such as that from an ultrasonic probe, the SWCNTs become isolated and form a stable dispersion of individualised nanotubes [208]. Ultrasonication of SWCNT solutions should be carried out with caution and used in tandem with sample characterisation, as excessive use is known to shorten or damage the SWCNTs in the sample [212].

Surfactant functionalisation, ultrasonication and centrifugation was employed in this thesis to achieve individualised SWCNT solutions of varying concentration that were suitable for deposition as described in the literature previously [208, 212, 215]. The exact solution processing experimental parameters relevant to each study are outlined in the experimental sections for Chapters 4, 5, 6 and 7. The fabrication of devices from these SWCNT solutions to form SWCNT-chemiresistive sensors is now described.

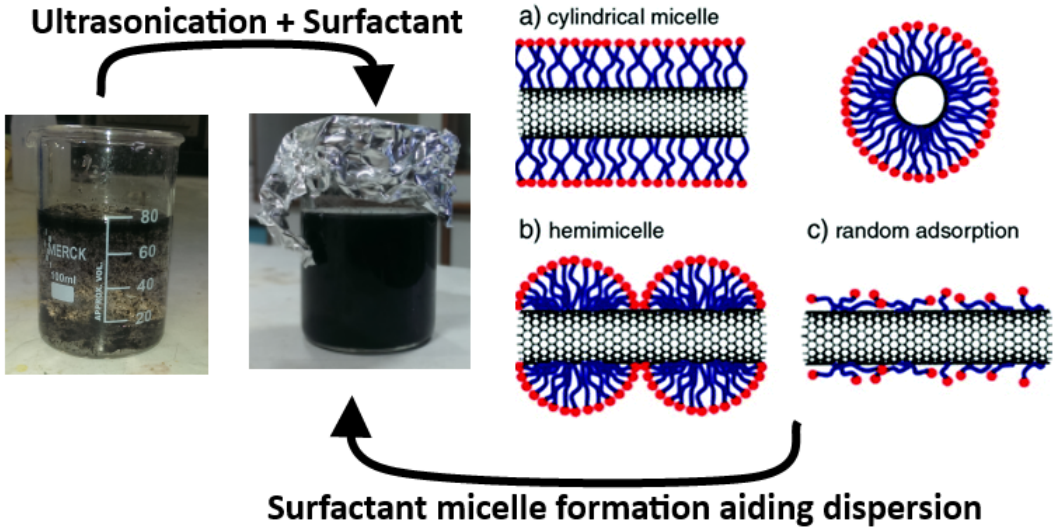

Figure 3.6: Photographs of a SWCNT aqueous solution before and after the addition of sodium deoxycholate (DOC) and ultrasonication. The various possible arrangements of surfactants forming micelles around the SWCNTs to aid dispersion in water is also shown (a-c), adapted from [214].

3.3.2 Device fabrication

Fabrication techniques to form carbon nanotube based devices are divided into either dry or wet processes [216]. Dry methods include chemical vapour deposition [217] and spinning of carbon nanotube yarns [218] directly on to device architectures. However, the following discussion focuses on wet processes, due to their relevance to the current thesis.

Films of SWCNTs can be fabricated from SWCNT solutions using drop coating, self-assembly, AC dielectrophoresis, rod coating, filtration, spin coating, ink-jet and screen printing [73]. The deposited SWCNT networks can then be modified *via* chemical doping, heat treatments, functionalisation, washing or etching to suit the final application. Metallic contacts can be deposited using sputtering before or after deposition of the film, with the choice of metal affecting the device contact resistance [219].

In the current thesis, drop coating was used to fabricate SWCNT devices due to the simplicity of the technique, the ability to deposit a known concentration of carbon to the substrate and to control layer thickness (see Figure 3.7). A mild heat treatment (at 50 °C in air) was used to minimize the coffee ring effect during deposi-

tion steps [220]. Surfactant present in the SWCNT network can alter the electronic characteristics of the film, the effects of which are investigated in Chapters 4 and 6. The exact fabrication procedures for each type of SWCNT based sensor are detailed in the experimental sections of Chapters 4, 5, and 6, as they are specific to each study.

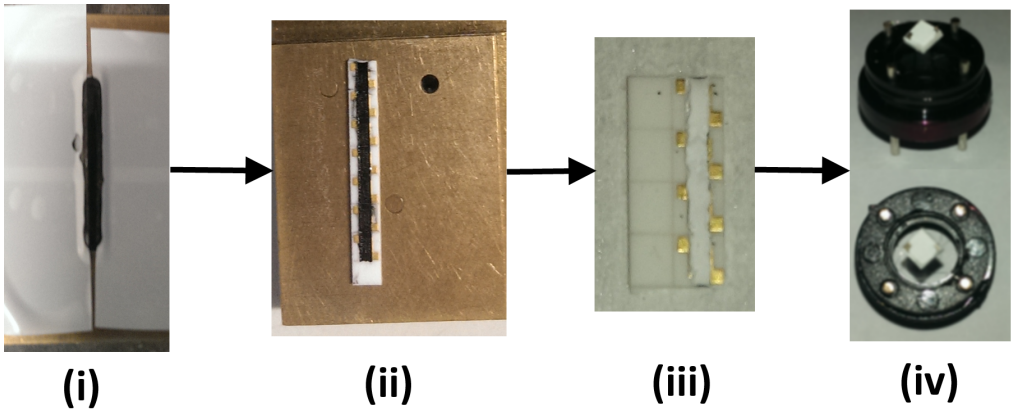

Figure 3.7: Example photographs of the fabrication process for the SWCNT network devices used in the current thesis. (i) Deposition of the SWCNT solution *via* drop coating with a removable mask covering the gold electrodes. (ii) After drying at 50 °C in air on a hot plate for 30 minutes, the mask is removed and the exposed electrodes are cleaned with ethanol. (iii) To form the SWCNT-Zeolite top layer devices steps (i) an (ii) are repeated using the zeolite ethanol solution. (iv) The devices (3 × 3 mm) are wire bonded to the sensor housing to complete the fabrication process.

3.3.3 SWCNT-zeolite composite

Zeolites, due to their ability to selectively adsorb molecules and catalyse surface reactions, are an interesting class of materials with a view to gas sensing applications [166]. They have previously been used as a growth template for small diameter (4 Å) carbon nanotubes in the pores of the aluminosilicate structure [221]. Conversely, MWCNT samples have also been used for the templated growth of mesoporous zeolite single crystals [222, 223, 224].

Zeolites have also found application as auxiliary functionalisation layers in gas sensors, increasing selectivity and sensitivity [163]. A Zeolite-MWCNT composite material has also been reported for electrochemical sensing of copper (II) ions

[225].

In Chapter 7, SWCNT-zeolite composite sensing layers were formed. After achieving the HiPco DOC dispersions described in the previous sections, two types of SWCNT-zeolite composite sensor were fabricated; a top layer or a mixed layer configuration. Zeolites were dispersed in ethanol using a magnetic stirrer bar at a concentration of 0.2 g ml^{-1}. For the top layer configuration, 1 μL of the dispersed zeolite was deposited on top of the pre-formed HiPco DOC SWCNT network, forming a filter layer of approximately 10 μm in thickness (see Figure 3.7, the thickness was established in Chapter 7).

The mixed layer sensor configuration was achieved by first depositing the insulating zeolite across the gold electrodes before any SWCNTs had been deposited on to the substrate. 1 μL of the initial HiPco DOC SWCNT solution was then drop coated on to the zeolite, filtering through to connect the gold electrodes whist also forming a percolating mixed layer from which an electrical measurement could be made. A final drying step was carried out in air using a furnace at 100 °C for 1 hour. This procedure was repeated for multiple sensors and different zeolite types, as outlined in Chapter 7. Characterisation of the raw and functionalised materials was used to study the effect of the fabrication procedure, as well as gas sensing experiments, on the SWCNTs. This is described in the following section.

3.3.4 Gas sensing experimental setup

In order to conduct controlled gas sensing experiments, an experimental system that enabled control of gas flow rate, mixing and testing chamber humidity was required.

Simultaneously, a measurement circuit which facilitated recording of the electrical sensing responses for multiple SWCNT-based devices, detailed in the previous section, was needed. These are described in the following section, along with appropriate testing protocols.

Figure 3.8 shows a labelled photograph of the gas sensing experimental setup (known as AA-Rig, designed previously by Dr. Ayo Afonja [226]). The main components of the gas sensing rig, corresponding to Figure 3.8, are:

- A gas delivery system; a series of mass flow controllers, flow meters and

solenoid valves connected with Polytetrafluoroethylene (PTFE) tubing to control the test humidity, flow and mixing of the required concentration of analyte gas (supplied from pressurised, BOC certified gas cylinders).

- A sealed testing chamber; A gas-tight container with an inlet and outlet that houses the gas sensors for controlled exposure to a flow of the analyte under investigation.
- An electrical measurement system; the measurement circuitry that facilitates the accurate measurement of the electrical conductance of the sensing element, utilising data acquisition (DAQ) instruments for recording and storage of the experimental data.
- A sensor heating circuit; a circuit connected to the integrated platinum heater track on a sensor substrate to obtain an elevated operating temperature if required.
- Power supply; units to provide the required voltage/current for all of the components.

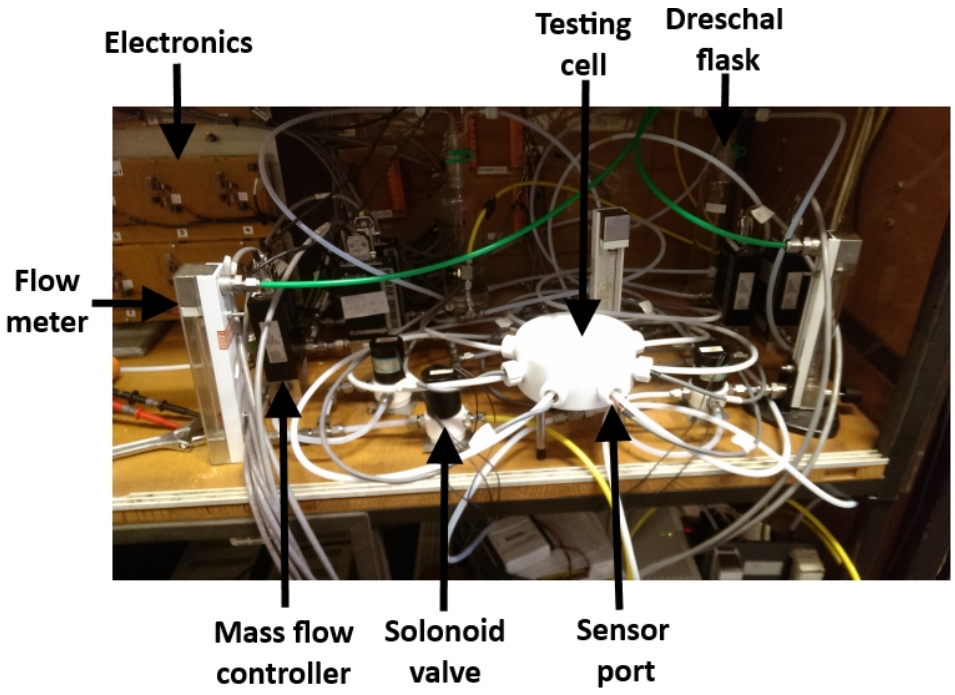

Figure 3.8: A photograph of AA-Rig showing the controlled flow delivery setup, as well as the testing cell and various components. The rig was built and designed by Dr. Ayo Afonja [226], and has been adapted to include an internal humidity meter and additional flow meters.

A schematic of the multichannel gas flow system is depicted in Figure 3.9. The air-tight testing cell was designed in a cylindrical shape with the inlet to the cell equidistant from each of the 8 sensors housed in the perimeter. The out-flow of gas was extracted through outlets behind each of the 8 sensor ports to ensure equal exposure to the target gas. The internal testing chamber flow volume was minimised to reduce the time taken for the target analyte to reach the sensor, permitting short measurement time scales.

The test cell is made from solid Polytetrafluoroethylene (PTFE) material as it is chemically inert. Sensors were secured around the perimeter of the 8-channel test cell *via* a screw-in holder to a hollow air-tight grove port. The holders were also designed to allow air-tight external electrical connections to the sensors.

Dry synthetic air (BOC, synthetic grade, 200 bar, CAS number: 132259-10-0) is delivered to the mass flow control system *via* a regulator connected gas cylinder (regulator pressure 1 bar), with a total flow rate of 1 L min^{-1} measured

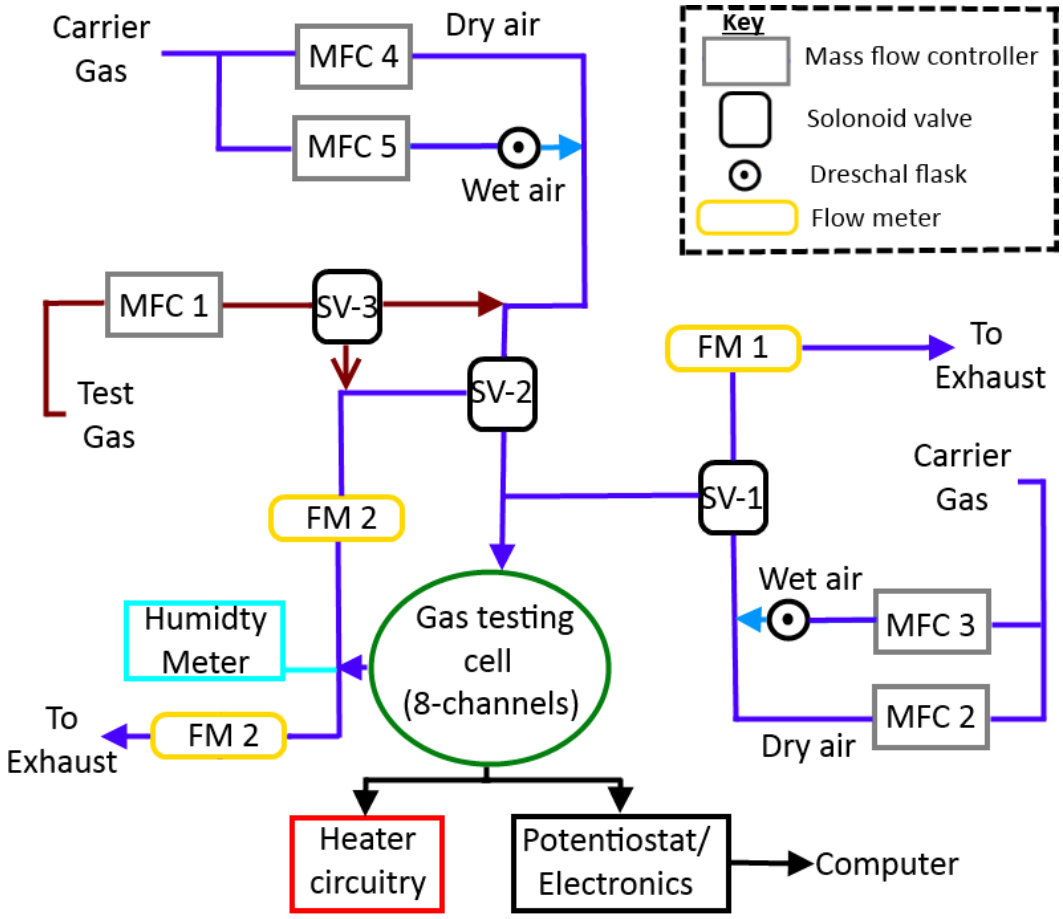

Figure 3.9: A schematic of AA-Rig showing the flow delivery configuration for mixing of gases and generation of different testing chamber humidity levels. The rig was designed and built by Dr. Ayo Afonja [226], and has been adapted to include an internal humidity meter and additional flow meters.

at the inlet and outlet of the testing cell. The sensitivity of the HiPco SWCNT sensor resistances to changes in the air flow was quantified and is shown in Figure 3.10. This air flow calibration suggests that after an initial period of 1200 s, a consistent baseline resistance is established. It also demonstrates that changes in air flow account for less than a 0.1% change in sensor resistance when switching from 100% to 25% air flow rate.

Depending on the testing requirements and setup configuration, a portion of this dry air was directed through a Dreschal flask filled with 500 mL of de-ionised water to generate atmospheric humidities in the 10% to 90% range in the testing chamber. To confirm that this mixing procedure was able to generate the desired atmospheric humidity within the testing cell, an internal humidity meter was used.

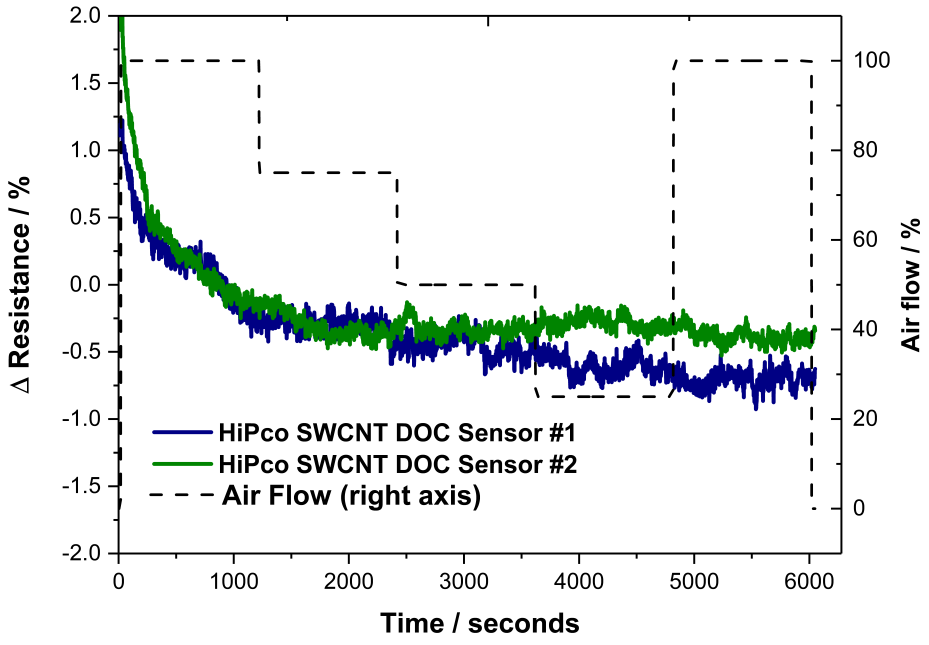

Figure 3.10: A plot of the percentage change in resistance (left axis) of HiPco SWCNT DOC sensors when the flow rate (right axis) is reduced from 1 L min^{-1} to 0.75 L min^{-1}, 0.5 L min^{-1} and then to 0.25 L min^{-1} on AA-Rig. A 0.1 % change in resistance is observed.

The results are shown in Figure 3.11, suggesting that equilibrium RH for lower values (RH< 50%) is more quickly established than higher RH (RH> 50%). The calibration step also suggests that a 5% error in the actual value of generated relative humidity should be assumed.

The test gas (cylinder) under consideration (specific to each study) is connected to a separate mass flow control line as depicted in Figure 3.9, then mixed with the carrier gas after the required relative humidity is established.

3.3.5 Measurement circuit

The electrical measurements were made using a potentiostat type circuit, adapted from previous designs [226]. The entire system consists of eight potentiostats, a digital multimeter (DMM, National Instruments (NI) 7-digit, model PXI-4071), multiplexer unit (MUX, NI PXI-2503 Switch) and a computer with LabVIEW software. Potentiostat type circuits permit a wide conductance measurement range, required

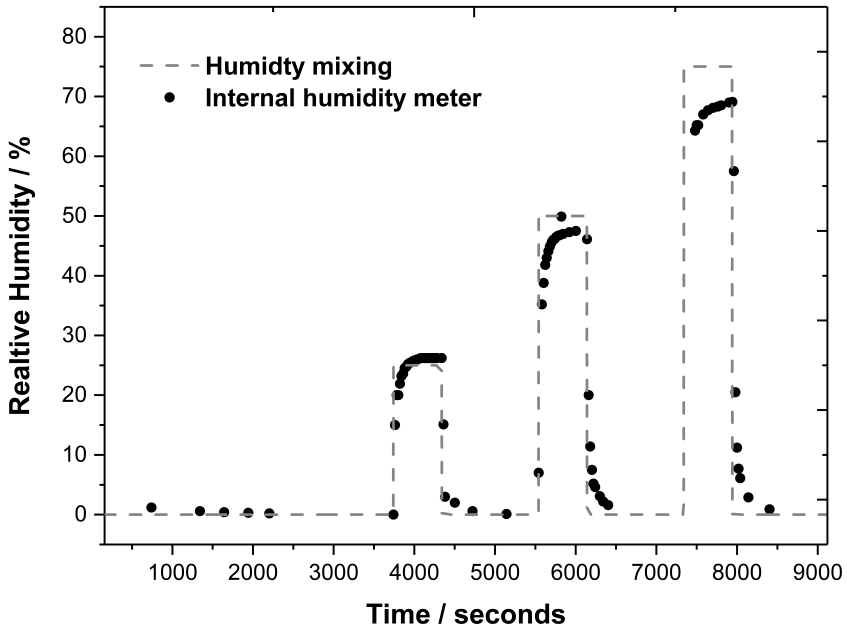

Figure 3.11: The humidity level (RH %) as measured by an internal humidity meter when the mixing ratios of dry to wet air are varied between 100:0, 75:25, 50:50 and 25:75 on AA-Rig.

for the current study, as well as control of the surface potential applied across the sensing material.

A constant 100 mV bias (w.r.t ground) is applied across the sensing element using a control circuit throughout the experiment to enable current flow through the device. Another circuit was connected, so that the voltage required to supply the current to maintain a constant 100 mV bias was measured, using a DMM with two-point contacts. The presence of analyte on the sensor surface induces a change in the amount of current required to maintain a constant 100 mV bias. Potentiostat outputs for all of the sensors were sampled using the NI DMM and the multiplexer unit (MUX), providing a multichannel DAQ system.

Changes in the supplied potential to alter the current, ΔI, required to maintain a constant potential, V_{SD}, were measured across the sensing elements (the SWCNT network layer) and the interdigitated gold electrodes (source-drain electrodes), which is then converted into a DC conductance value, ΔG, for each sensor

using the relationship:

$$V_{out} = -V_{SD} \times \frac{R_{fb}}{R_{sensor}} \tag{3.5}$$

where V_{out} is the measured voltage, V_{SD} is the probe voltage (100 mV), R_{fb} is the feedback resistor value and R_{sensor} is the unknown sensor resistance to be calculated. The diagram depicting the elements of the circuit which allow the calculation of the resistance across the sensor surface is shown in Figure 3.12. The full potentiostat circuit diagram, adapted from the work of Dr. Ayo Afonja [226], can be found in appendix D.

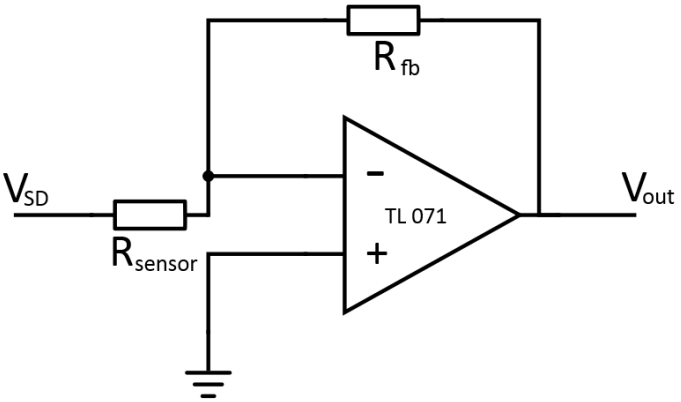

Figure 3.12: Inverting operational amplifier element of the potentiostat circuit. The probe voltage (V_{SD}), known negative feedback resistor (R_{fb}) and measured potential across the sensor (V_{out}) are used to calculate the resistance (R_{sensor}) of the sensor as per equation 3.5. Adapted from [226].

The change in sensor conductance, ΔG, can then be calculated from:

$$\Delta G = \frac{1}{\Delta R_{sensor}} \tag{3.6}$$

3.3.6 Testing procedure and protocol

The total combined flow rate entering and exiting the testing cell was always maintained at 1 L min^{-1}. For each experiment, gas leak tests were performed at the cylinder regulator connections, with the gauge set to achieve a pressure of 1 bar

before entry to the mass flow system. At the beginning of each test, the flow meters (placed up and down stream of the carrier gas flow w.r.t the testing cell) were checked for consistency and equivalence to a 1 L min^{-1} flow rate.

Unless explicitly stated in the experimental sections of the results chapters, the sensor baseline conductances were stabilised in an initial flow of 100% carrier gas for 3600 s. Each exposure to a certain concentration of target analyte in the carrier gas was for a duration of 600 s, followed by a 1200 s recovery period in carrier gas only. In some instances, the amount of water vapour in the carrier gas was varied to alter background chamber humidity temporarily or throughout the entire experiment.

The Dreschal flask, containing 500 mL of de-ionised water, was replenished after 3 testing runs. Periodically, an internal humidity meter was used to confirm the relative humidity of the testing chamber, typically accurate to within 5% of the desired value.

The exact testing parameters (such as analyte concentrations and testing chamber humidity levels) were variable between studies (detailed in the experimental sections of Chapters 4, 5, 6 and 7). However, the above protocols were adhered to in all test cases.

3.4 Determination of errors

3.4.1 Gas sensing errors

Significant variations in the conductive responses of SWCNT-based chemiresistors have been reported previously, outlined in Chapter 2. As a result, it is important that the error associated with the measurement of such responses is communicated to quantify the variation observed alongside the magnitude of sensing response. Two types of response variation, with distinct causes, may be observed in the gas sensing experiments conducted in the current study:

(1) Run to run variation of the conductive response magnitudes observed for a specific sensor over repeated experiments.

(2) Variation in the conductive responses recorded for identical sensors of the

same SWCNT type, functionalisation and layer thickness within the same experiment.

The errors reported for type (1) are potentially due to the incomplete desorption of previously adsorbed analyte gas from the sensor surface, sensor poisoning, or changes in the temperature of the testing environment (typically between 18 °C and 23 °C depending on time of year). To quantify this error, the standard deviation between recorded sensor responses was calculated from three repeated experiments. Error bars communicate this quantity in the response magnitude figures as detailed in the relevant figure captions.

The sources of error for type (2) are likely to arise from the heterogeneous nature of randomly orientated SWCNT networks, which may contain a different arrangement of m-SWCNTs or sc-SWCNTs. Variations in the thickness of the sensing layer, deposited using drop casting, may also contribute to the discrepancy in recorded conductive responses between identical devices. To quantify this error, the standard deviation of average responses over three repeated experiments between two identical sensors was calculated to provide an indication of device to device variation in sensor responses. This is indicated in figure captions reporting conductive response magnitudes per sensor type (e.g thick or thin network, functionalised or non- functionalised). The type (2) error is typically larger than type (1).

As stated in the previous section and articulated in Figure 3.11, the mixing procedure between wet and dry air to maintain a constant atmospheric humidity resulted in a chamber humidity within 5% of the desired value (confirmed by an internal humidity meter).

Changing the air flow rate from 1 L min^{-1} to 0.25 L min^{-1} typically resulted in a 0.1% change in sensor baseline resistance (see Figure 3.10). Therefore, resistance variations induced by changes in the MFC air flow rate throughout the experiment (<5% variation in flow rate, based on manufacturer specification) were considered to be negligible for the SWCNT-based sensors. The maximum error associated with the delivered concentration of test gas was estimated to be 10%, limited by the read-out scale on the flow meters. The consistent readings taken from inlet and out-

let flow meters between experiments suggested any error in test gas concentration due to flow mixing would have been systematic throughout the studies.

3.4.2 Characterisation errors

For electrical characterisation of the SWCNT devices, a Keithley 4200 semiconductor characterisation system was used to investigate how the conductance across the devices varied with film thickness and the concentration of the deposited solution. Due to the random arrangement of the SWCNTs in the deposited layer, the largest uncertainty in the measurement of conductance arose from device to device variations, thus the standard deviation in conductance values between two identical devices was presented as the error associated with the measurement.

The maximum resolution of the Renishaw inVia Raman microscope was 1 cm^{-1}, the limiting factor in determining positional peak shifts in the Raman spectra. In Chapter 4, the Raman results are presented with the mean, normalised intensity of measurements gathered from at least three different points on the material. The standard deviation is then presented *via* the error bars on the plot.

In Chapter 4, the concentrations of the SWCNT-surfactant solutions were estimated using UV-Vis-NIR spectroscopy and the Beer-Lambert law. Due to the limited quantity of available HiPco sample, multiple batches of solution from different raw samples could not be prepared. Also, variations in repeat measurements of the UV-Vis-NIR spectra on the same solution at the same concentration were not detectable. Therefore, an alternative technique, the vacuum filtration method, was used to provide a secondary estimation of the concentration for the HiPco DOC solution. The error in estimated concentration (14%) was taken to be the standard deviation between the concentration measured using the UV-Vis-NIR technique and the vacuum filtration method for the DOC sample.

Where possible, the physical dimensions estimated from microscopy images are averaged over multiple features in the image. For example, in the TEM data presented in Chapter 5, the diameter of 50 SWCNT bundles are measured from the image (based on the scale bar and using the software package ImageJ) and the mean bundle diameter along with standard deviation is presented.

Chapter 4

Study I: Changes in SWCNT network conductance on exposure to water vapour.

The work in this chapter was published in *Nanoscale*. I conceptualised the study, carried out the experimental investigations, performed the analysis and wrote the manuscript. Dr. D. J. Buckley assisted with the sample preparation and interpretation of the materials characterisation data. Prof. N. T. Skipper and Prof. I. P Parkin proof read the manuscript and contributed experimental guidance. The paper is appended to this thesis in appendix E.

Associated Publications: Evans, G. P., Buckley, D. J., Skipper, N. T., & Parkin, I. P. (2017). Switchable changes in the conductance of single-walled carbon nanotube networks on exposure to water vapour. *Nanoscale*, 9(31), 11279-11287.

4.1 Introduction

As highlighted in the literature review from Chapter 2, the electrical properties of SWCNT networks are sensitive to the surface adsorption of water vapour from the surrounding environment. Although measurable changes in the conductance of SWCNTs have been reported, both increases [146, 147] and decreases [143, 123, 144, 145] have been observed, with different mechanisms proposed to

explain the findings. For SWCNT-based chemical sensors and other electronic components, the necessary interaction with external operating environments suggests that an understanding of the conductance-humidity behaviour of SWCNT networks is required to optimise performance for specific applications.

In this chapter, the sensitivity of SWCNT networks to water vapour was investigated. Firstly, the effect that residual surfactant has on the conductance of SWCNT networks when exposed to water vapour, in comparison with surfactant free samples, was studied. This is a critical consideration for many applications of SWCNTs, including touch screen displays[32] and environmental sensors, as changes in the relative humidity of the operating environment may interfere with device performance. While useful for liquid processing and the deposition of SWCNTs, the electrical properties of the fabricated devices can be significantly altered by the presence of surfactant[227], due to the blocking of inter-nanotube connections in the network and increased contact resistance[228, 229]. Non-covalent functionalisation using a wide variety of surfactant molecules is applied as a route to disperse inherently hydrophobic nanotubes in water for sorting processes[230, 61, 231], as well as for a wide variety of SWCNT device fabrication methods[216, 232, 233, 234, 235]. The removal of this residual surfactant is possible by washing[227], annealing[236, 187] or acid treatment[237, 229]. The properties of deposited SWCNT networks are significantly dependent on the success and ramifications of such treatments.

For the current study, SWCNT networks were deposited after non-covalent functionalisation with a range of anionic (DOC, SC), cationic (CTAB, CTAT) and non-ionic (Triton X-100) surfactants. The magnitude and direction of the change in conductance of the SWCNT networks upon exposure to water vapour was used to explore the contrasting *p*-type or *n*-type behaviour reported in the literature. The reversibility of H_2O adsorption and the associated conductive response curves were probed. Finally, based on this insight, the water sensitive properties of the surfactant containing films were manipulated to develop and evaluate humidity sensors using the SWCNT networks.

4.2 Experimental

4.2.1 Device fabrication

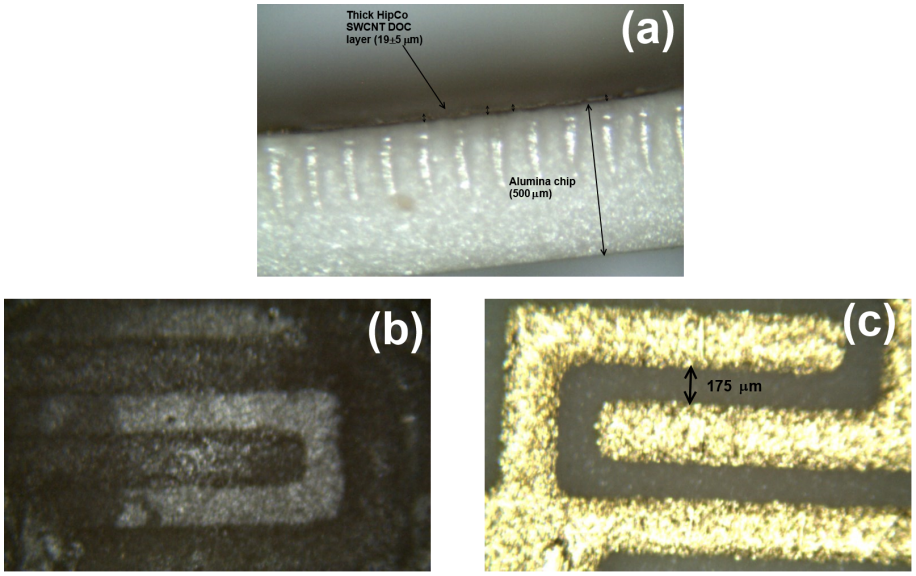

Figure 4.1: Optical image of (a) a side on view of a thick HiPco DOC SWCNT network deposited on an alumina chip, (b) a thick HiPco DOC SWCNT network deposited on an alumina chip between interdigitated gold electrodes of 175 μm separation and (c) a thin HiPco DOC SWCNT network deposited on an alumina chip between interdigitated gold electrodes of 175 μm separation.

SWCNTs produced via the high pressure carbon monoxide disproportionation (HiPco) process [137] (purchased from Nanointegris, batch number: R1-831) were dried in air at 120°C to remove moisture from the bundles and stored under vacuum.

For the HiPco SWCNT control sample, the black powder was added to water (H_2O, CAS Number: 7732-18-5, HPLC grade) at a concentration of approximately 2 mg mL^{-1}. To prepare the test samples, the SWCNTs were added to aqueous solutions containing the following surfactants at 0.5 wt.%: Sodium deoxycholate (DOC, CAS Number: 302-95-4 , 97%), sodium cholate (SC, CAS Number: 206986-87-0, 97%), hexadecyltrimethylammonium bromide (CTAB, CAS Number: 57-09-0, 98%), Hexadecyltrimethylammonium p-toluenesulfonate (CTAT, CAS Number: 138-32-9) or Triton X-100 (CAS Number: 9002-93-1) purchased from Sigma-Aldrich. The initial carbon concentration was approximately 2 mg mL^{-1} for the HiPco SWCNT surfactant solutions. Surfactant molecules form micelle like struc-

tures around the nanotubes allowing dispersion in water. To aid efficient solubilisation and de-bundling of the tubes *via* surfactant wrapping, the solution was sonicated using a tip sonication probe at a power of 225 W for 15 minutes, with the container placed in an ice bath for cooling.

The surfactant treatment resulted in well dispersed solutions, whilst the carbon in the control sample was highly agglomerated. The samples were centrifuged at 4000 g for 30 minutes and the upper 80% of the supernatant was decanted to limit the presence of carbonaceous impurities and highly bundled SWCNTs in the final concentrated solution. Diluted samples were also obtained by dilution of the concentrated solutions in deionised water.

3 x 3 mm alumina tiles with patterned gold electrodes of 175 μm separation (as shown in Figure 4.1 and Figure 4.2) were used as the substrate to facilitate measurement of the conductance across the SWCNT networks. The HiPco SWCNT solutions were deposited across the interdigitated gold electrodes using a calibrated Finnpipette novus electronic single-channel micro pipette (drop volume 1 μL per sensor) and left to dry in air at 23 °C for 24 hours to form chemiresistor type devices.

Thick network devices were formed using the concentrated solutions detailed in Table 4.1, with a thickness of 19 ± 5 μm estimated first using a side on view from a microscope (see Figure 4.1). Due to the difficulty in focusing on the deposited film using an optical microscope, side on SEM was used in Chapter 5 to confirm the film thickness to be in the 10 μm to 20 μm range (Figure 5.2). Typically, thick network device resistance was of R_{thick} = 200 Ω to 500 Ω. Thin films were formed using the diluted solutions displayed in Table 4.1, with a thickness < 1 μm and a device resistance of R_{thin} = 50 kΩ to 200 kΩ.

Table 4.1: Parameters of the HiPco SWCNT networks and their conductance behaviour when exposed to water vapour.

Surfactant type (ionicity)	**DOC (anionic)**	**SC (anionic)**	**CTAB (cationic)**	**CTAT (cationic)**	**Triton X-100 (non-ionic)**	**Control (surfactant free)**
Solution concentration (concentrated / diluted, mg mL^{-1})	1.59 ± 0.2 / 0.0108 ± 0.001	0.51 ± 0.05 / 0.004 ± 0.0004	1.61 ± 0.2 / 0.0102 ± 0.001	0.91 ± 0.1 / 0.00453 ± 0.001	0.46 ± 0.05 / 0.00496 ± 0.001	0.64 ± 0.1 / 0.531 ± 0.07
Network conductance change (ΔG) upon exposure to H_2O (thick / thin networks)	decrease/ decrease	decrease/ decrease	increase/ increase	decrease/ increase	increase/ decrease	increase/ decrease
Conductance sensitivity ($\Delta G\%\ \Delta RH\%^{-1}$) to H_2O (thick / thin networks)	-0.49/ -0.11	-	0.057/ 0.17	-	-	0.016/ -0.041

4.2.2 Material and device characterisation

The UV-Vis-NIR absorption spectra for each of the decanted SWCNT surfactant solutions were obtained using a PerkinElmer Lambda 950 spectrophotometer to estimate the concentration of carbon in the aqueous solutions. The initial decanted solution was diluted (between 1000 X and 50 X dilution from the initial solution with deionised H_2O) to enable experimental measurement of absorbance. Multiple spectra were recorded in the 180 nm to 1300 nm range for dilutions of each SWCNT surfactant solution, using a quartz cuvette with a path length 1 cm. The background absorbances for the blank H_2O surfactant solutions were subtracted. The relevant extinction coefficients (ε_λ) experimentally determined by Goak *et al.* [238] (SWCNTs stabilised with CTAB : ε_λ = 34.5 mL mg^{-1} cm^{-1} , SWCNTs stabilised with SC: ε_λ = 33.6 mL mg^{-1} cm^{-1}) at a wavelength of 700 nm were used to approximate the carbon concentration for each of the diluted solutions.

A linear relationship between the volume of decanted SWCNT solution present in the diluted aqueous solution vs the absorbance was observed. The Beer-Lambert law,

$$C = \frac{A_\lambda}{\varepsilon_\lambda l}, \tag{4.1}$$

where A_λ, ε_λ and l are absorbance, extinction coefficient at a specific wavelength λ and optical path length respectively, was used to calculate the concentration of the diluted and concentrated SWCNT solutions as displayed in Table 4.1. The surfactant free SWCNT control sample values are included to enable an approximate comparison, although the carbon agglomerated in the control solutions formed without the use of surfactant, decreasing the accuracy of the UV-Vis concentration measurement. The approximate carbon concentration of the concentrated decanted SWCNT solutions were calculated using a linear fit to the diluted absorbance data.

The mass filtration method was applied to obtain a secondary comparison with the estimated UV-Vis-NIR concentration. A mass balance with 0.01 mg sensitivity was used to obtain the mass of a PTFE filter membrane before and after 600 μL

of the HiPco DOC suspension was deposited and dried *via* vacuum filtration. The difference in mass after the deposition was calculated and the mass of the surfactant (derived from the molecular weight of DOC) subtracted to estimate the mass of carbon deposited on the membrane. Three HiPco DOC samples were prepared, with the average carbon concentration calculated as 1.4 ± 0.2 mg mL^{-1}, in good agreement with the UV-Vis-NIR based calculations displayed in Table 4.1.

A Renishaw inVia Raman microscope with laser wavelength λ = 785 nm and 1 mW power was used to perform Raman spectroscopy on each of the surfactant wrapped HiPco SWCNT thick films after deposition and drying on 3 x 3 mm alumina substrates. Wet measurements were obtained by depositing 1 μL of deionised water (H_2O, CAS Number: 7732-18-5, HPLC grade) on top of the SWCNTs and re-obtaining the Raman spectra.

A Jeol JSM-6700F field emission scanning electron microscope (SEM) was used in secondary electron imaging mode using a 10 kV probe voltage at a working distance of 7.9 mm to obtain micrographs of the SWCNT networks.

The hot probe method (as described by Golan *et al.* [206]) was used to confirm that the networks contained sc-SWCNTs and displayed *p*-type behaviour. Either the HiPco control sample, the HiPco DOC or HiPco CTAB containing films were deposited on a glass substrate. The potential difference across the films was measured using a Keithley 2100/230-240 digital multimeter. A positive probe was heated to a set temperature while in contact with the SWCNT network using a soldering iron tip and the induced change in potential was recorded. A negative voltage at the heated probe indicates that holes are the majority charge carrier in the semiconducting portion of the network as described previously[206].

The current-voltage characteristics across the SWCNT network (source to drain) were measured using a Keithley 4200 semiconductor characterisation system when dry and after wetting with 1 μL of de-ionised H_2O for the control films, the SWCNT networks containing DOC surfactant and the SWCNT networks containing CTAB surfactant.

4.2.3 Humidity testing procedure

The SWCNT networks (deposited on alumina substrates between interdigitated gold electrodes) were placed in electrical read out ports within a cylindrical testing chamber to measure the change in device conductance as a function of relative humidity (RH). The circular arrangement of the devices, along with the extraction of air behind each individual port location, ensures that each device is exposed to an equal flow of dry or humid air. The air flow rate of dry synthetic air (BOC certified synthetic air, 20% pure oxygen, 80% pure nitrogen, CAS number: 132259-10-0) was controlled using digital mass flow controller 1 (MFC 1). Wet air was generated by flowing dry synthetic air through a Drechsel flask (controlled using MFC 2) containing 500 mL of deionised water (HPLC grade, CAS Number: 7732-18-5). Dry air and wet air were mixed at different ratios using the mass flow controllers and delivered to the testing chamber *via* a central inlet to achieve between 0% and 90% RH in the testing chamber, confirmed using an internal humidity meter. A potentiostat setup[239] was used to measure the room temperature device conductance with a 100 mV bias applied throughout the testing procedure.

Prior to the experiments, dry synthetic air was passed over the sensors for 2 hours to obtain a baseline conductance (G_0) for each device and achieve 0% relative humidity in the chamber. A mixture of dry and wet air was then introduced to the chamber for 600 s to achieve to the required humidity level and the new device conductance was measured (G). This was followed by a 1200 s intermediary step in which the relative humidity was re-adjusted to 0% and G_0 was re-established before the next incremental humidity testing step (in the range of 20% to 90% RH).

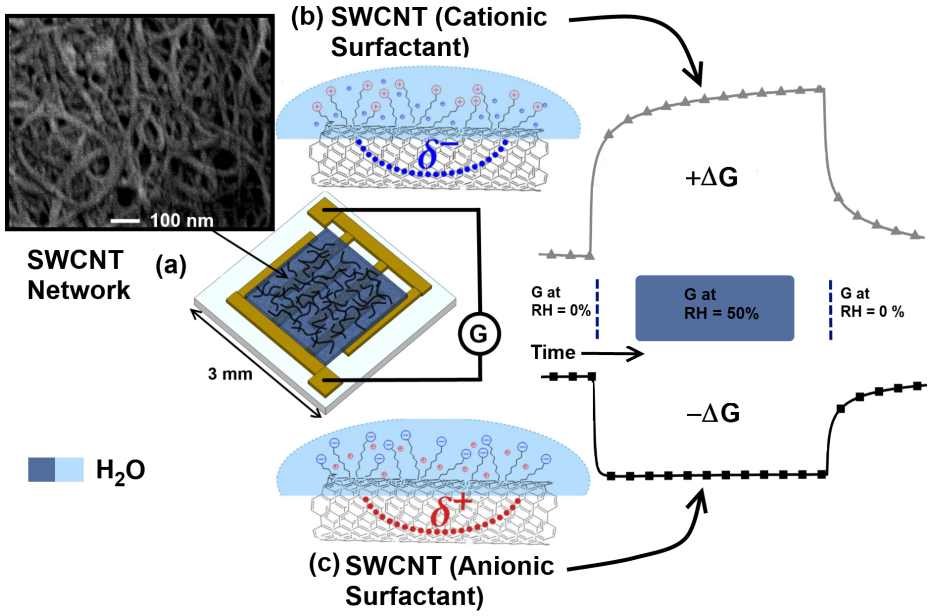

Figure 4.2: Schematic representation of (a) the surfactant functionalised HiPco SWCNTs deposited on an alumina substrate between interdigitated gold electrodes. The conductance (G) across the formed percolating network is measured in both dry and humid conditions. An SEM image of a typical SWCNT network is inset top-left. A representation of the induced electrostatic potential upon exposure to water vapour is shown in (b) for cationic and (c) anionic surfactant containing networks, with the respective increase (+ΔG) and decrease (-ΔG) in conductance indicated when the relative humidity (RH) increases.

4.3 Results

4.3.1 Material characterisation

The topology of the raw SWCNT sample is displayed in Figure 4.3. A highly interconnected SWCNT network structure is revealed by scanning electron microscopy (SEM) of the gold coated as received HiPco sample. Individual SWCNTs are not visible, instead forming bundles estimated to be 10 nm to 30 nm in diameter from the SEM micrographs in Figure 4.3c and d. The constituent SWCNTs become separated and individualised to a greater degree during the aqueous dispersion of the raw sample *via* ultrasonication.

The aqueous solutions of HiPco SWCNTs, non-covalently functionalised with the range of surfactants detailed in Table 4.1, were then characterised using UV-Vis-NIR absorption spectroscopy. Multiple peaks in the 400 nm to 1000 nm range

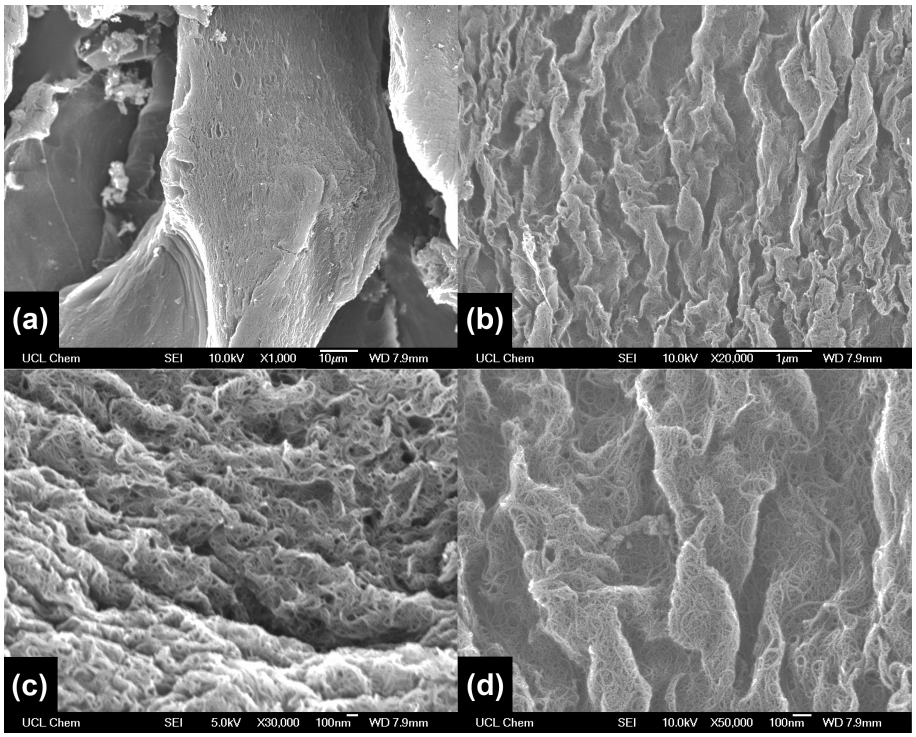

Figure 4.3: SEM micrographs at (a) ×1,000 (b) ×20,000 (c) ×30,000 (d) ×50,000 magnification showing gold coated SWCNT bundles from a sample of raw HiPco powder.

of the UV-Vis-NIR absorption spectra (Figure 4.4) indicate a mixture of metallic SWCNTs (m-SWCNTs) and semiconducting SWCNTs (sc-SWCNTs) in each of the aqueous solutions [240] at high (0.5 to 1.8 mg mL^{-1}) and low (0.004 to 0.01 mg mL^{-1}) concentrations, as to be expected for non-sorted HiPco SWCNTs [169].

The peaks are red or blue shifted at various wavelengths if dispersed using a cationic or anionic surfactant, compared with a dry sample of SWCNTs on quartz. This effect has previously been attributed to the varying charge imparted on the tubes when surfactant wrapped in aqueous solution, as well as to nanotube bundling in poorly dispersed samples [173].

The approximate concentrations of the SWCNT solutions are detailed in Table 4.1. These were calculated from the UV-Vis-NIR data for the aqueous HiPco DOC, HiPco SC, HiPco CTAB, HiPco CTAT, HiPco Triton X-100 and HiPco control (surfactant free) solutions at different dilutions (data presented in Figure 4.5). The carbon concentration of the initial surfactant solution (blank) was increased

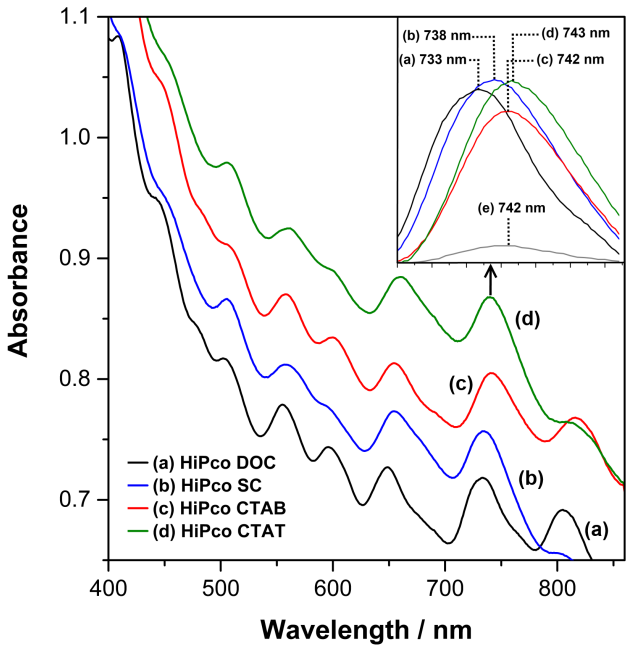

Figure 4.4: UV-Vis absorption spectra obtained using an Elmer Lambda 950 spectrophotometer for aqueous solutions of HiPco SWCNTs non-covalently functionalised with (a) DOC, (b) SC, (C) CTAB and (d) CTAT. The inset top-right plot shows the shift in the 705-775 nm range peaks for the respective samples relative to (e) dry HiPco DOC on a quartz slide. (a)-(d) are offset by 0.05 absorbance for clarity and were 100 X dilutions of the initial concentrated solutions.

stepwise by the addition of the 1 X concentrated SWCNT solution for each respective surfactant. The added volume of 1 X solution, specified in Figure 4.5, resulted in an increase in absorbance.

The absorbance at wavelength $\lambda \approx 730$ nm was used to calculate the carbon concentration of the diluted solutions using the Beer-Lambert law. The relevant extinction coefficients (ε_λ) experimentally determined by Goak *et al.* [238] (SWCNTs stabilised with CTAB : ε_λ = 34.5 mL mg^{-1} cm^{-1}, SWCNTs stabilised with SC: ε_λ = 33.6 mL mg^{-1} cm^{-1}) were used to approximate the carbon concentration for each of the diluted solutions.

The 1 X solutions were too concentrated to obtain UV-Vis-NIR measurements. Therefore, the concentration of the concentrated HiPco SWCNT solutions

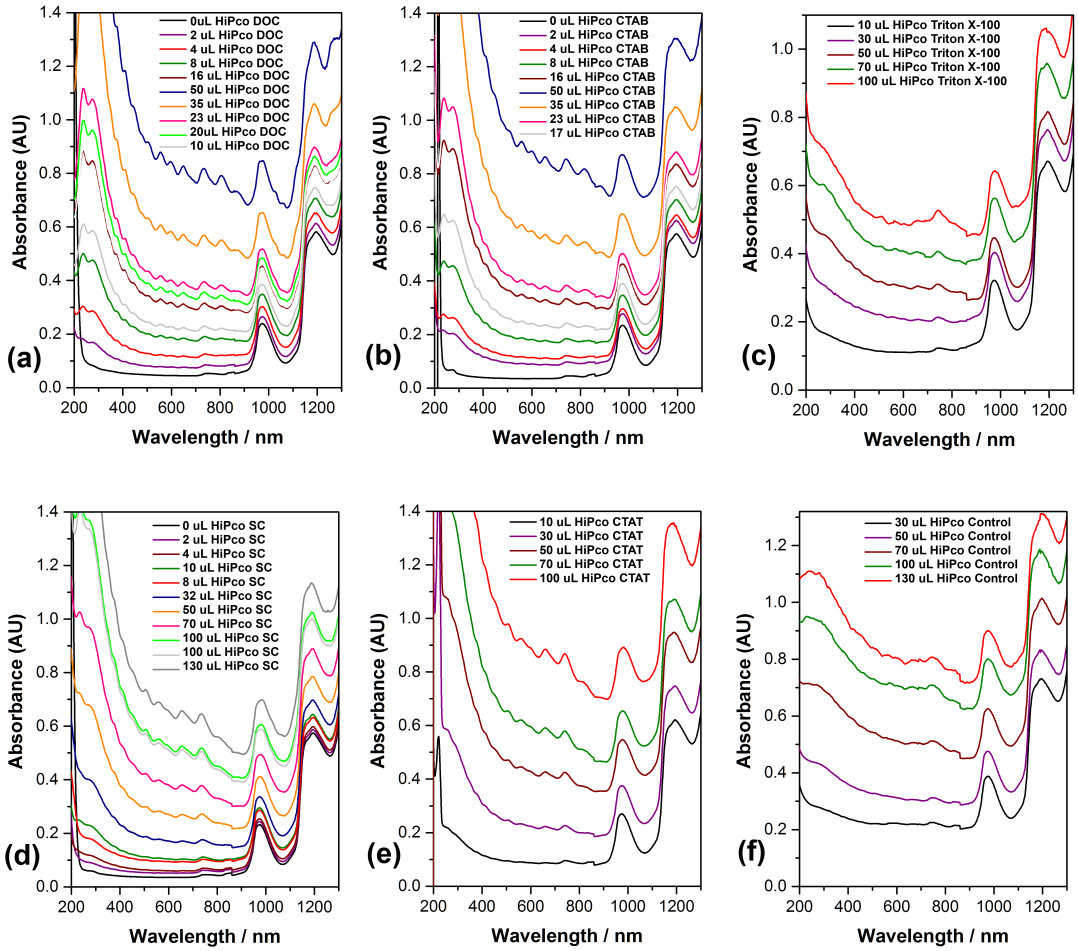

Figure 4.5: UV-Vis-NIR absorbance data for (a) HiPco DOC, (b) HiPco CTAB, (c) HiPco Triton X-100, (d) HiPco SC, (e) HiPco CTAT and (f) HiPco control (surfactant free) solutions. The legend indicates the volume of 1 X concentrated HiPco SWCNT solution added to 3.5 ml of deionised water to achieve the dilutions required to measure absorbance over a range of concentrations. A linear fit was applied to the Absorbance vs HiPco SWCNT volume data in accordance with the Beer-Lambert law to calculate the concentration of the concentrated 1 X HiPco SWCNT solutions.

was determined by applying a linear fit to the absorbance data to obtain the predicted absorbance for the concentrated 1 X solution and calculating the concentration in accordance with the Beer-Lambert law.

The mass filtration method was used to compare and confirm the concentration of the concentrated HiPco DOC SWCNT solutions calculated from the UV-Vis measurements. Three HiPco DOC samples were prepared, with the average carbon concentration calculated as 1.4 ± 0.2 mg mL^{-1}, in good agreement with the concen-

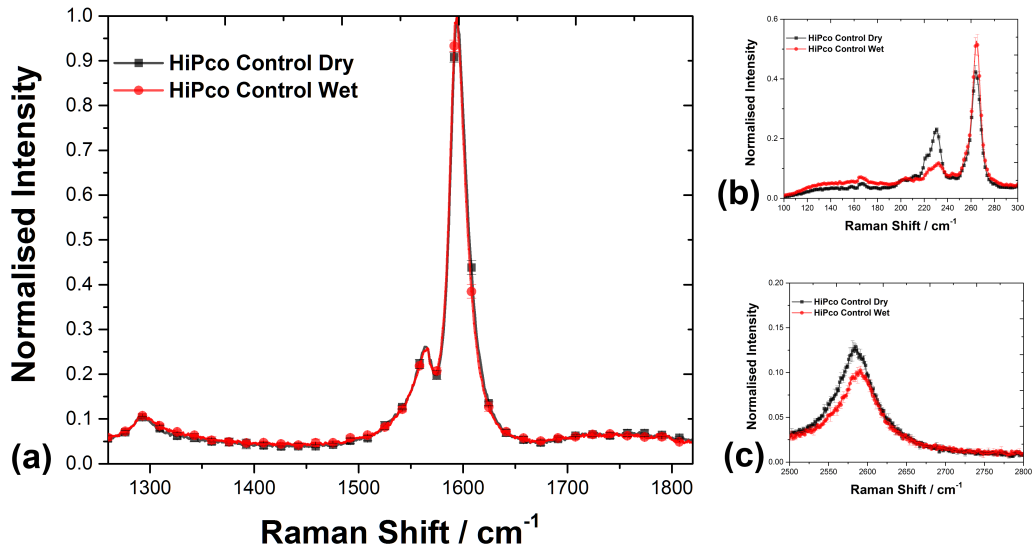

Figure 4.6: Raman spectroscopy data for the dry (▪) and wet (•) HiPco control (surfactant free) samples. (a) The ratio of the G^+-bands at 1594 cm^{-1} to D-band at 1295 cm^{-1} indicates good sample purity. (b) The radial breathing modes (RBMs) in the range 100 cm^{-1} to 500 cm^{-1} suggest that nanotubes of different chirality and thus electronic type are also present in the deposited layer.(c) G′-band feature (2600 cm^{-1}). Laser wavelength λ = 785 nm at 1 mW power.

trations calculated using the UV-Vis-NIR data (as displayed in Table 4.1).

Raman spectroscopy was performed on the thick SWCNT networks (thickness = 19 ± 5 μm) after deposition on to the alumina substrates, firstly in ambient conditions (room temperature = 23°C, relative humidity = 45%). Figure 4.6, 4.7 and 4.8 show the G-bands (1560 cm^{-1} to 1620 cm^{-1}), D-band (1295 cm^{-1}), G′-band (2600 cm^{-1}) and radial breathing modes (RBMs, 100 cm^{-1} to 500 cm^{-1}) for the samples under investigation.

The ratio of the G^+-bands at 1594 cm^{-1} to D-bands at 1295 cm^{-1} indicates good sample purity (see Figure 4.6, 4.7 and 4.8)[56]. The radial breathing modes (RBMs) in the range 100 cm^{-1} to 500 cm^{-1} suggest that nanotubes of different chirality and thus electronic type are also present in the deposited layer[56], in agreement with the UV-Vis-NIR data.

Each of the samples was then wetted with 1 μL of deionised water and Raman measurements were re-acquired as detailed in the experimental section. The full width at half maximum (FWHM) of the G^+ band decreases significantly for the wet

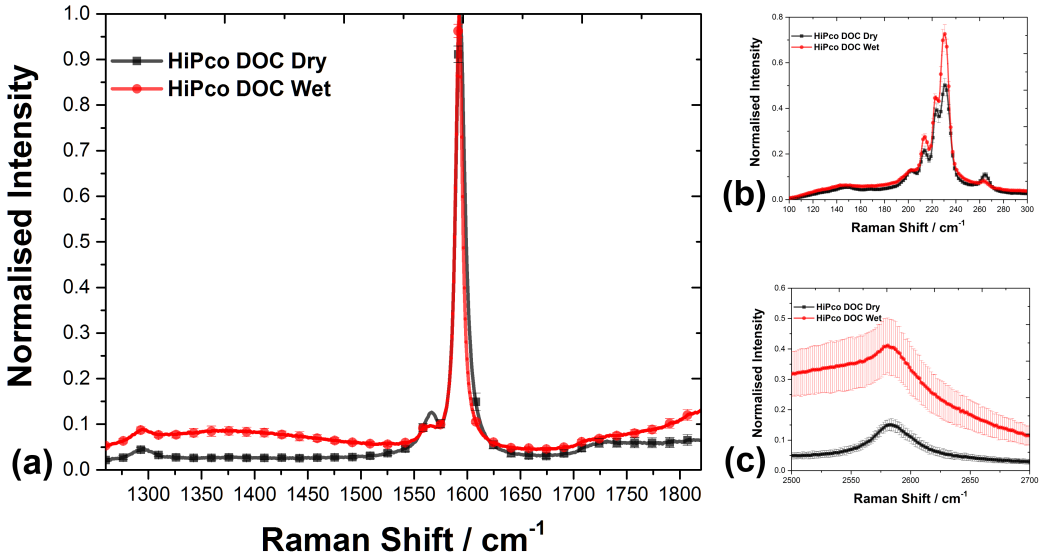

Figure 4.7: Raman spectroscopy data for the dry (▪) and wet (•) HiPco DOC samples. (a) The ratio of the G^+-bands at 1594 cm^{-1} to D-band at 1295 cm^{-1} indicates good sample purity. (b) The radial breathing modes (RBMs) in the range 100 cm^{-1} to 500 cm^{-1} suggest that nanotubes of different chirality and thus electronic type are also present in the deposited layer.(c) G′-band feature (2600 cm^{-1}). Laser wavelength λ = 785 nm at 1 mW power.

surfactant containing networks (see Figure 4.9). Previous studies have found that the Breit-Wigner-Fano (BWF) component of the G^--band is suppressed for some surfactant m-SWCNTs aqueous systems compared to the dry equivalent[173]. As an intrinsic feature of bundled m-SWCNTs, perturbation of the SWCNT electronic charge by the charged groups present in the surfactant molecule is thought to be partially responsible for the change in the BWF feature. Also, the intensity, FWHM and frequency of the G^+ band for sc-SWCNTs can be altered by the application of a gate voltage[241, 242], suggesting that any additional potential difference due to water-surfactant interactions should induce changes in the G^+-band line-shape.

In the current study, the decrease in FWHM of the G^+ band, along with the suppression of the G^-, is treated as a proxy for a change in the gate/charge sensitive G^+ band and BWF component respectively. Therefore, the different G-band line-shapes highlighted in Figure 4.9 suggest that exposure to water alters the interaction between the charged groups present in the SWCNT-surfactant system. This in turn implies that the electronic properties of SWCNT based devices containing residual

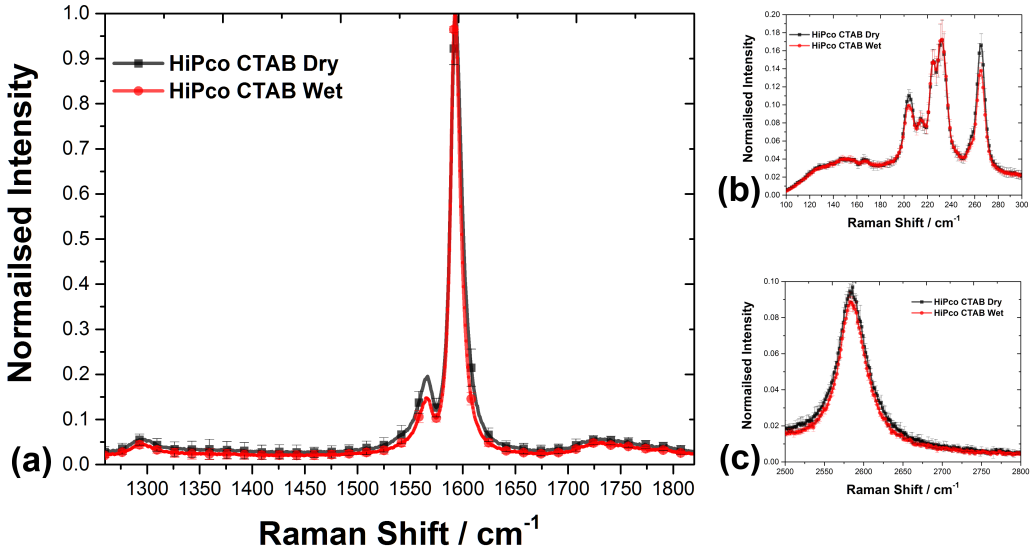

Figure 4.8: Raman spectroscopy data for the dry (▪) and wet (•) HiPco CTAB samples. (a) The ratio of the G^+-bands at 1594 cm^{-1} to D-band at 1295 cm^{-1} indicates good sample purity. (b) The radial breathing modes (RBMs) in the range 100 cm^{-1} to 500 cm^{-1} suggest that nanotubes of different chirality and thus electronic type are also present in the deposited layer.(c) G′-band feature (2600 cm^{-1}). Laser wavelength λ = 785 nm at 1 mW power.

surfactant could be altered due to electrostatic interactions upon exposure to water vapour.

From Figures 4.6, 4.7 and 4.8, changes in the intensity of various RBM modes are observed for the wetted films. A similar effect has been previously reported for sc-SWCNTs in CNTFETs, in which the application of a gate voltage alters the intensity of the RBM mode [243]. For the control and DOC samples, changes in the G′ peak shape and intensity also occur, which has previously been observed by Zaumseil *et al.* for electrolyte gated CNTFET devices [241].

4.3.2 Bidirectional conductance switching

It has been previously reported that water induces *n*-type[146, 147] or *p*-type[143, 123, 144, 145] responses from carbon nanotubes, causing a change in the conductance of ropes and bundles. Whether the change in conductance is due to electrostatic gating or chemical doping is debated within the literature.

The study by Bell *et al.* suggested that this effect is attributable to electrostatic

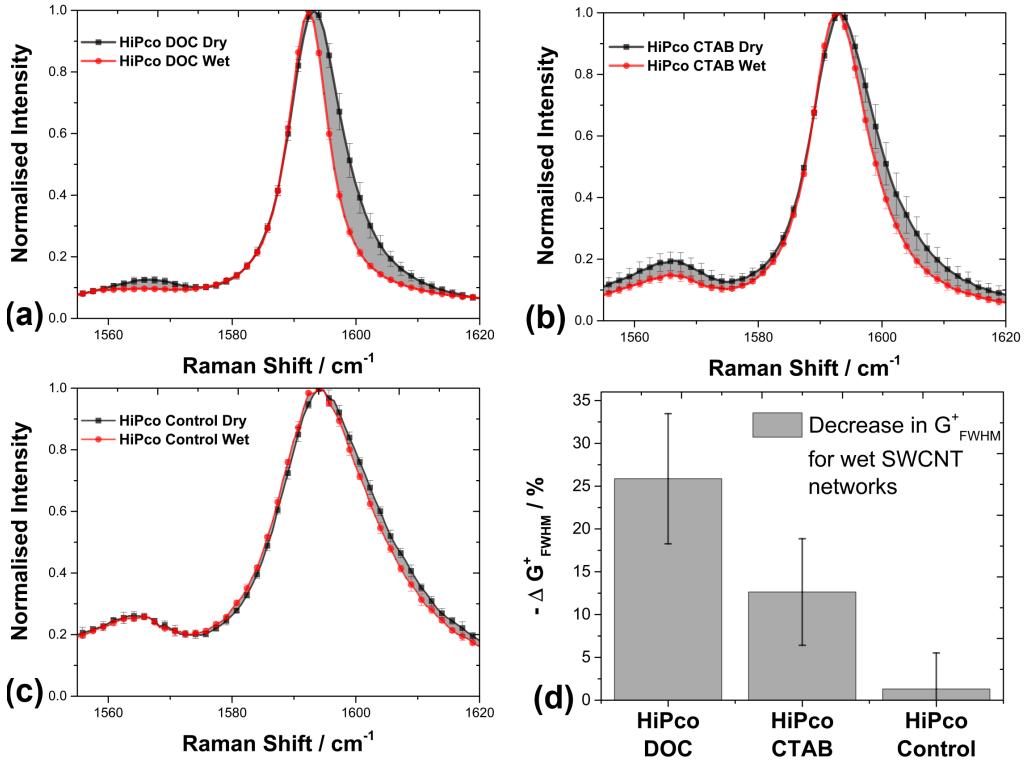

Figure 4.9: The normalised Raman spectra of dry and wet SWCNT networks containing (a) anionic DOC, (b) cationic CTAB and (c) no surfactant. The differences in lineshape of the G^+ (at 1593 cm^{-1}) and G^- (at 1565 cm^{-1}) band before and after wetting are highlighted in (a)-(c) by grey shading. The error bars represent the standard deviation between measurements of 3 different spots on the SWCNT film after normalisation of intensity. The percentage decrease in full width at half maximum (FWHM) of the G^+ band before and after wetting is shown in (d), where the error bars represent the error on the measurement of the peak FWHM. Raman spectroscopy was performed using a Renshaw inVia Raman microscope with laser wavelength λ = 785 nm and 1 mW power.

interactions [142]. The permanent dipole moment of water induces a polarisation of electronic charge density in the nanotube over a long range (3 nm). Lekawa-Raus *et al.* [244] also suggested that chemical doping does not occur in carbon nanotube fibres, with water vapour instead interacting with the nanotubes at CNT-CNT junctions. If this is the case, then it is to be expected that residual charged species in the network, such as ionic surfactants, increase the polarisation of charge upon exposure to water vapour and thus the magnitude of the conductance change observed.

Networks of HiPco SWCNTs functionalised with the range of surfactants listed in Table 4.1 were deposited between gold electrodes and their electrical conductance was recorded in a humidity controlled chamber (described in the ex-

perimental section). The thickness and density of randomly orientated SWCNT films is important when considering gas sensing mechanisms[245, 111] and charge transport in the network[246]. Previous work by Battie *et al.* [83] has shown that SWCNT sensing behaviour changes with a reduction in the number of m-SWCNTs in the film.

Randeniya *et al.* [145] found that thinner networks of SWCNTs are increasingly influenced by the substrate and a higher proportion of SWCNTs in the film contribute towards sensing behaviour[145]. Furthermore, contact resistance between SWCNTs[140], bundling and electrostatic environment[141] influence charge transport in macroscopic networks. In low-density networks of non-sorted SWCNTs below the m-SWCNT percolation threshold, conductance is increasingly dominated by Schottky barrier modulation at the interface between sc-SWCNT and the electrodes or m-SWCNTs, while thick networks have complete metallic conduction paths with the resistance of the film dominated by nanotube-nanotube junctions[83].

Surfactant functionalised SWCNT devices based on both thick films (thickness = 19 ± 5 μm, device resistance R_{thick} = 200 Ω to 500 Ω) and thin films (thickness < 1 μm, device resistance R_{thin} = 50 kΩ to 200 kΩ) were therefore fabricated to investigate how these quantities affect the conductance behaviour in humid conditions. The effect of residual surfactant and water vapour was found to differ in thin (and thus lower density) networks.

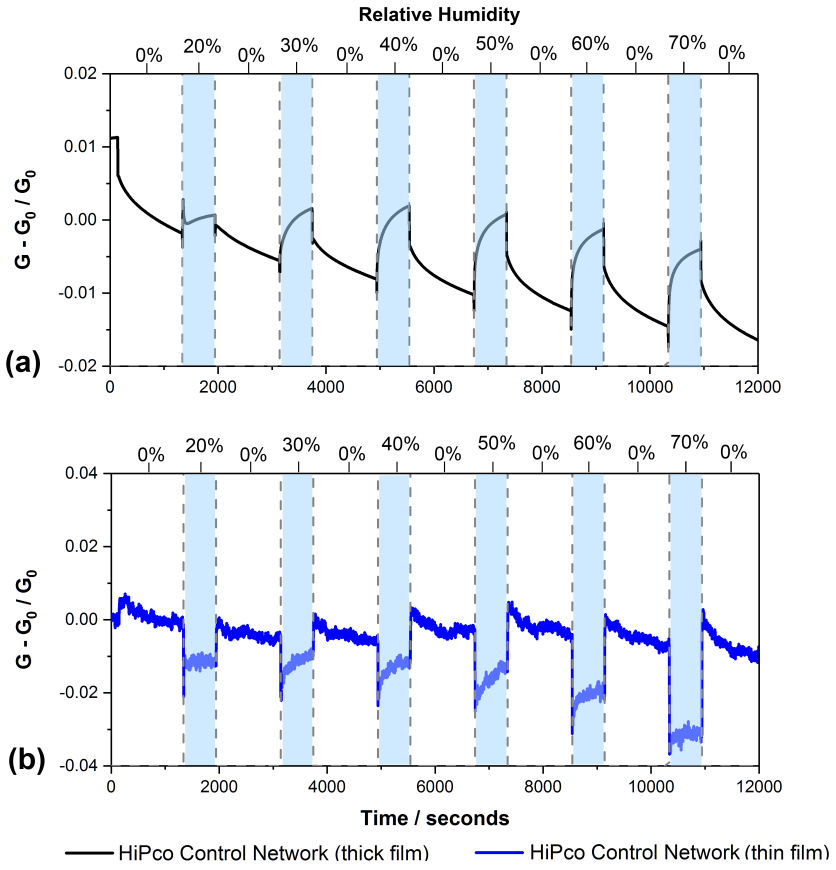

Figure 4.10: Real time changes in HiPco SWCNT control network conductances (where G_0 is the baseline conductance at RH = 0% and G is the conductance at higher RH levels) as the relative humidity of the testing chamber is modulated between 0% RH and higher humidity (in the 20% to 70% RH range, as indicated by the top x-axis and blue shaded regions) for (a) thick (thickness = 19 ± 5 μm, dense) and (b) thin (thickness < 1 μm, lower-density) networks of HiPco control SWCNTs.

As is displayed in Figure 4.10, the conductance of a control SWCNT network (containing no surfactant) is sensitive to water vapour. At certain time intervals, the relative humidity of the testing chamber is increased and a new steady state conductance value (G) for the network is reached after time t_{90}. The chamber humidity is then reset to 0% and the conductance returns to baseline value (G_0).

The conductance of the control SWCNT device (containing no surfactant) is increased by the presence of water vapour in the sensing chamber (see Figure 4.10a). Reducing the thickness of the SWCNT control sample switches the direction of the conductive response so that conduction through the network is instead

reduced after exposure to water vapour (Figure 4.10b). Veeramasuneni *et al.* [247] found that an alumina substrate is positively charged at pH 7 upon wetting. If this is the case, the net positive charge may impede electron conduction in the thinner SWCNT control sample.

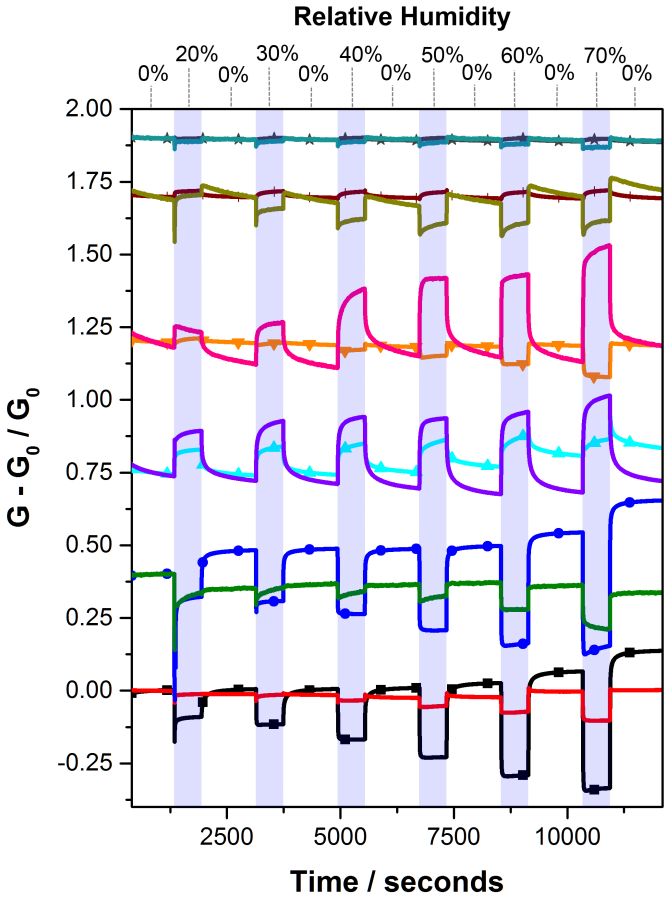

Figure 4.11: Real time changes in SWCNT network conductances (where G_0 is the baseline conductance at RH = 0% and G is the conductance at higher RH levels) as the relative humidity of the testing chamber is modulated between 0% RH and higher humidity (in the 20% to 70% RH range, as indicated by the top x-axis and blue shaded regions) for thick (thickness = 19 ± 5 μm, dense) networks of (■) HiPco DOC, (●) HiPco SC, (▲) HiPco CTAB, (▼) HiPco CTAT, (+) HiPco Triton X-100 and (★) HiPco control samples. Results for thin (thickness < 1 μm, lower-density) networks are plotted without a symbol at the same y-axis offset as their respective sample type. Plots are offset for clarity.

Figure 4.11 demonstrates that the magnitude and direction of the change in conductance is strongly dependent on the type of surfactant present in the network. When surfactants possessing charged groups are present in the films, the

change in conductance is one order of magnitude larger than those without surfactant (the control HiPco SWCNT sample). For the SWCNTs non-covalently functionalised with anionic surfactant (DOC, SC), the conductance decreases upon exposure to water vapour. However, those functionalised with cationic surfactant (CTAB, CTAT) show an increase in conductance when the humidity of the chamber is increased. This is evidence that the head groups and counterions of the ionic surfactants contribute significantly to the electrical properties of the SWCNT networks when exposed to water vapour.

Electrolyte solutions have been utilised to gate SWCNT FETs[248, 249]. An applied potential causes a re-distribution of charges in the solution, imparting a potential on the nanotubes and causing changes in the intensity, position and line-shape of the SWCNT Raman bands[241]. Such changes in the G^+ and G^- bands are observed for the wetted SWCNT networks containing surfactant in the current study (Figure 4.9). The previous use of liquid gated devices, along with the change in line-shape of the G^+ and G^- bands, indicates that the interaction of the surfactant molecule and counterions with the nanotubes (upon wetting) modulates conduction, effectively gating the SWCNT networks under investigation.

Goak *et al*. [238] proposed that for anionic surfactants such as SC, the Na^+ counterion interacts with both m-SWCNTs and sc-SWCNTS electrostatically in dry network films. When such a film is wetted, re-orientation of the surfactant molecules on the surface takes place (in this case the surface of the SWCNTs in the network)[250]. Therefore, the re-arrangement of the hydrophilic, negatively charged head groups away from the tubes upon wetting would increase the density of positive charges (Na^+ for DOC and SC) interacting electrostatically with the nanotubes. This would explain the decrease in conductance through the networks containing residual anionic surfactant.

Conversely, the same re-arrangement of the positively charged, hydrophillic head group for the CTAB containing films would increase the density of Br^- counterions interacting with the tubes, inducing a distributed negative charge (δ^-) and increasing electron conduction (or decreasing hole density) through the SWCNTs.

This proposed mechanism for the respective decrease or increase in conduction for the anionic/cationic surfactant containing films is represented schematically in Figure 4.2. The red or blue shifts seen in the SWCNT-surfactant UV-Vis data with respect to the dry samples (Figure 4.4, inset), further suggests a change in electrostatic potential, depending on the surfactant-nanotube interaction in water.

Bernardes *et al*. [251] measured a humidity dependent electrostatic potential on the surface of ionic surfactant films, which supports the hypothesis that atmospheric water can change the imparted potential on the SWCNTs in the surfactant containing networks. Additionally, positively charged species (such as the Na^+ counterion present in SC and DOC) have previously been found to reduce DC conductance through SWCNTs suspended in liquid water[252].

It is not expected that swelling of the surfactant functionalised SWCNT film is solely responsible for the change in network conductance. Although swelling is expected to occur in surfactant films upon exposure to water vapour[253, 254, 255, 256], it would always decrease the number of nanotube-nanotube conductive pathways (decreasing film conductance), thus does not account for the increase in conductance of films containing residual cationic agents.

As a higher proportion of SWCNTs are exposed to the analyte in a thin network, a larger ΔG was expected for thinner SWCNT films. This was the case for the SWCNT control, non-ionic and cationic samples. However, the real time humidity response plots in Figure 4.11 show that the opposite is true for thin anionic SWCNT films. Fewer metallic pathways exist in the thinner samples, with the conduction properties of the network increasingly dominated by Schottky barrier modulation between the sc-SWCNTs and m-SWCNTs or the gold electrodes. As chemiresistor type devices are used, there is no applied gate voltage to activate conduction through the sc-SWCNTs in the dry state. However, in a way analogous to electrolyte gated SWCNT transistors, wetting of the film and re-arrangement of surfactant counterions may activate (or reduce, depending on the counterion) conduction through the sc-SWCNTs. Thus, the differences in conductance-humidity behavior of thick vs thin networks (thickness = 19 ± 5 μm, thickness < 1 μm respectively) containing

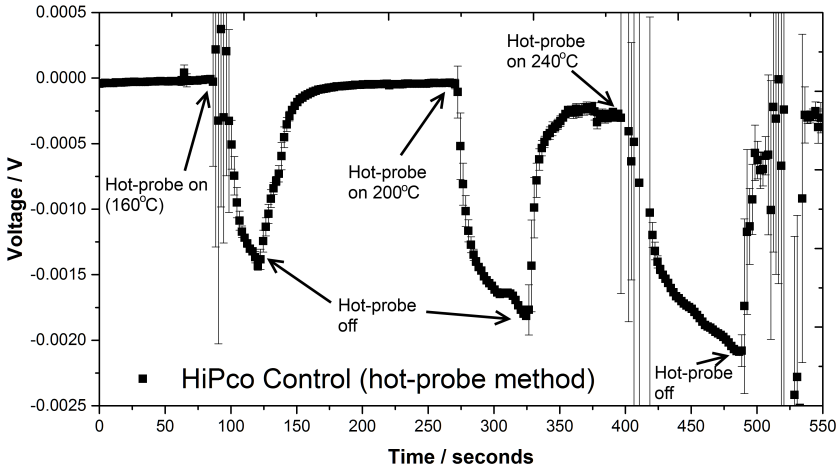

Figure 4.12: The potential difference induced by the application and removal of a soldering iron to the positive measurement probe (hot-probe) in contact with the HiPco SWCNT control (surfactant free) network. The progressively larger negative change in potential difference across the SWCNT network between the positive and negative measurement probes upon heating of the positive probe (hot-probe, to 160°C, 200°C and 240°C) suggests that the semiconducting nanotubes in the network are *p*-type.

anionic or cationic surfactant may be caused by the increasing influence of the counterion on the sc-SWCNTs in the mixed chirality films.

From Figure 4.11, differences in the peak shapes were recorded. When conductance increases (as for the cationic surfactant containing films), a "shark fin" shaped response curve was observed, in which the saturation time for the response was extended compared to the cases in which conductance decreased upon exposure to water vapour. This may be attributable to different adsorption kinetics associated with the different SWCNT-surfactant films.

The hot probe method has been applied previously to determine the charge carrier type in sc-SWCNT networks[207]. The recorded negative voltage upon probe heating (as shown in Figure 4.12 and Figure 4.13) indicates that the semiconducting nanotubes in the DOC, CTAB and control (surfactant free) networks are *p*-type, in line with previous studies of SWCNTs exposed to ambient conditions. The *p*-type change in potential for the CTAB containing SWCNT network after application of the hot probe (as shown in Figure 4.13) is approximately one order of magnitude

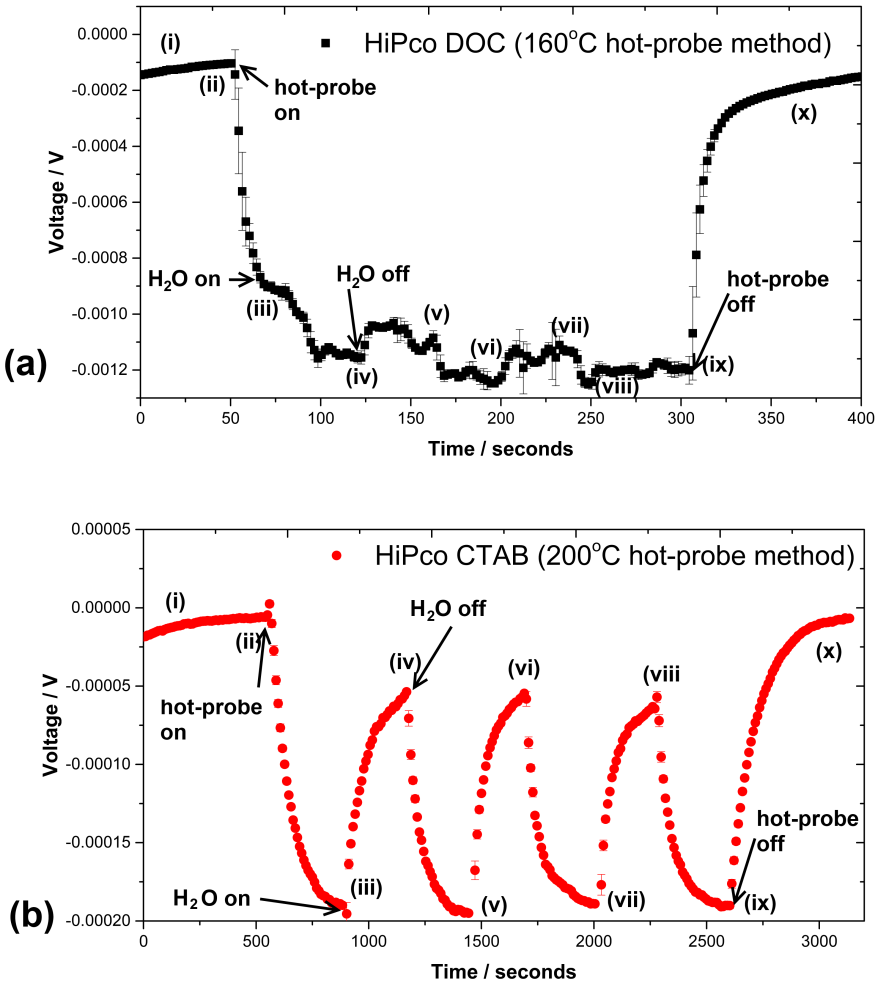

Figure 4.13: The potential difference across the SWCNT networks induced by the application of the hot-probe method whilst additionally delivering H_2O to the (a) HiPco DOC SWCNT network and (b) HiPco CTAB SWCNT network. At (i) the potential difference across the films is recorded using a Keithley 2100/230-240 digital multimeter in a flow of dry air. At (ii) the soldering iron is applied to the positive probe (hot-probe) in contact with the SWCNT network, inducing *p*-type negative increase in voltage. At (iii) wet air is delivered to a partitioned portion of the film so that the wet air cannot contact the hot-probe, inducing another change in potential difference, the direction of which is dependent on the type of surfactant present in the network. At (iv) the wet air is turned off and dry air flow resumes. The process is repeated with wet air on at (v) and (vii) and wet air off at (vi) and (viii). At (ix) the hot-probe is turned off and the potential difference across the film returns to initial levels in dry air at (x).

lower than the change for the DOC or control network, suggesting the CTAB containing film is less *p*-type.

As detailed in the experimental section, the setup was adapted so that a seg-

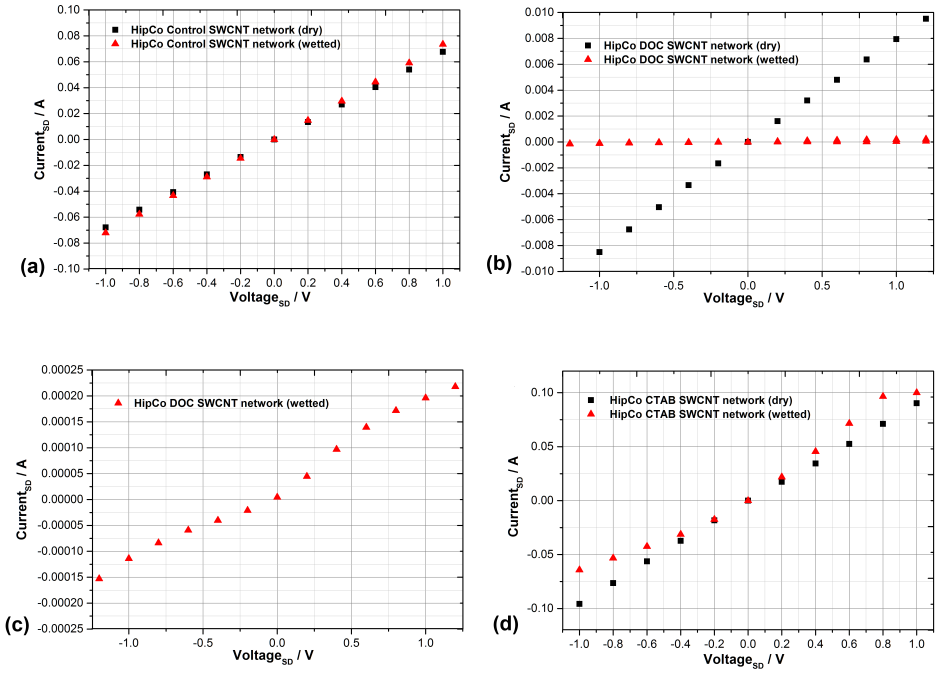

Figure 4.14: Current-voltage characteristics across the SWCNT network (source to drain, -1 V to 1 V single sweep) when dry (black ■) and after wetting (red ▲) with 1 μL of H_2O for the (a) control film (b) the SWCNT network containing DOC surfactant (c) the SWCNT network containing DOC surfactant at different scale to show non-linearity after wetting and (d) the SWCNT network containing CTAB surfactant.

ment of the thick (dense) network film could be exposed to water vapour without contacting the hot probe, held at a temperature in the range of 160°C to 200°C. The change in potential, firstly due to the application of the hot probe and then due to increasing humidity, was recorded. The potential difference across the DOC containing film increases in magnitude and remains negative when more water vapour is present, whereas the potential across the CTAB film increases in magnitude upon application of the hot probe, but decreases and moves towards a positive value when H_2O is introduced (see Figure 4.13a and Figure 4.13b). This indicates that in the CTAB containing networks, exposure to water vapour decreases the *p*-type behaviour of the sc-SWCNTs in the semiconducting portion of the film. A decrease in the *p*-type character of sc-SWCNTs would decrease inter-tube resistances between metallic and *p*-type semiconducting nanotubes, which may explain

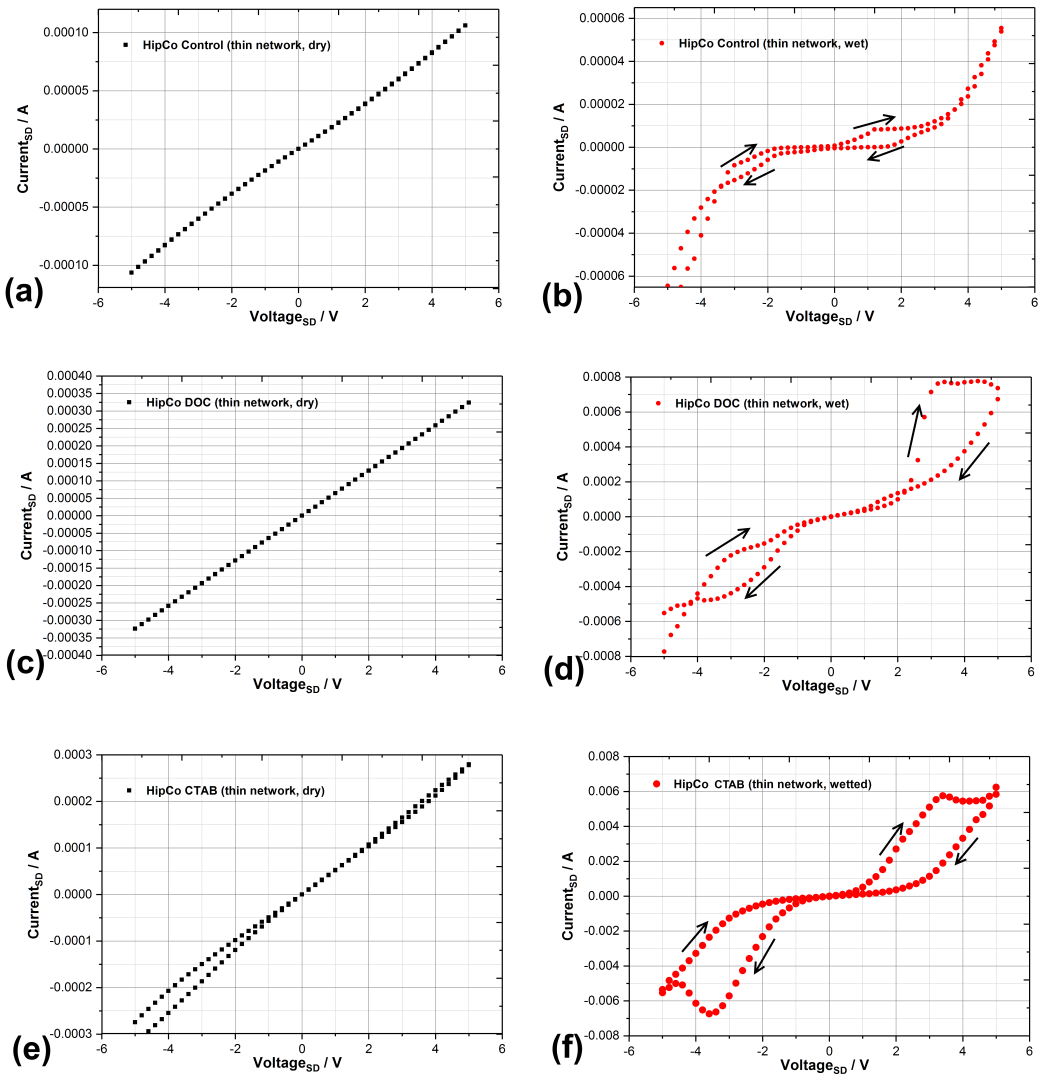

Figure 4.15: Current-voltage characteristics across the SWCNT network (source to drain) when dry (black ▪) and after wetting (red •) with 1 μL of H_2O for the (a) thin control film (dry) (b) thin control film (wet) (c) the thin SWCNT network containing DOC surfactant (dry) (d) the thin SWCNT network containing DOC surfactant (wet) (e) the thin SWCNT network containing CTAB surfactant (dry) (f) the thin SWCNT network containing CTAB surfactant (wet). A bias across the source-drain electrodes was applied as a duel sweep from -5 V to + 5V as indicated by the arrows, inducing a hysteresis in the I-V curve for the wetted films.

the overall increase in conductance for the SWCNT-CTAB films upon exposure to water. Correspondingly, the increase in *p*-type nature of the sc-SWCNTs in the DOC network results in an overall conductance drop, potentially due to increased inter-tube resistances.

A similar approach was adopted by Adu *et al*, who employed a method to measure the change in thermoelectric power of SWCNT mats to He, N_2, H_2 NH_3 and O_2 [257]. They inferred that the changes in thermoelectric power were due to the increase or decrease in *p*-type nature of the sample, in line with the above reasoning for exposure to water vapour.

The humidity testing experiments discussed thus far were conducted at a constant source-drain bias of 100 mV (performed on AA-Rig). Investigation of the I-V characteristics under dry and wet conditions were then undertaken to reveal any dependence of the conductance-humidity behaviour on the applied potential across the network.

A linear relationship between applied voltage and induced current flow was observed for all of the dry SWCNT network devices over the - 1 V to +1 V range (single sweep mode, Figure 4.14) and the -5 V to + 5 V range (dual sweep mode, Figure 4.15). This suggested Ohmic conduction through the dry SWCNT network at room temperature. In Figure 4.15e for the dry CTAB film, a small discrepancy between the up sweep (-5 V to 5 V) and down sweep (from 5 V to -5 V) was observed, which may be due to a build up of charge in the film.

When the SWCNT films were wetted (with a 1 μL drop of de-ionised H_2O), the current-voltage relationship across the SWCNT network was altered (Figure 4.14), becoming non-linear at higher applied bias, as shown in Figure 4.15. This could be due to charging effects which are enhanced when the film is wetted.

The presence of surfactant seems to introduce a more extreme hysteresis in the up and down sweep I-V measurements, as displayed in Figures 4.15b, d and f. One potential explanation for this effect is that the counterions, more mobile due to the wetting of the film, impart or remove a partial potential on the SWCNTs in a fashion analogous to electrolyte gating of CNT network FETs [241]. The charged species in the surfactant film may act as an additional applied potential which alters current flow through the device, causing non-linear I-V characteristics. While the Raman bands also display similar changes to line shape observed for electrolyte gated CNT devices [241], further work is required to confirm this hypothesis. How-

ever, it may explain the differences between the conductance-humidity relationship for the control, anionic and cationic surfactant containing SWCNT films.

4.3.3 Functionalised SWCNT networks for humidity sensing

Monitoring of humidity is important for industrial processes, commercial and domestic technologies [258, 259]. The high sensitivity and reversibility of the SWCNT network conductances upon adsorption and desorption of water vapour indicates that the chemiresistors may be useful as humidity sensors. The conductance-humidity behaviour is predictable and repeatable between multiple identical devices, as shown in Figure 4.16, with the chemiresistors containing ionic surfactant functionalised SWCNTs showing the largest ΔG. The percentage change in conductance per percentage change in relative humidity, as displayed in Table 4.1, compares well with values for carbon nanotube based humidity sensors in the literature (-0.5% $RH\%^{-1}$ from Liu *et al.* [260] and -0.7% $RH\%^{-1}$ by Han *et al.* [261]). Some signal drift was observed after exposure to higher levels of relative humidity, which could be attributed to the re-arrangement of charged species in the film upon wetting, as described in the previous section. This may be addressed by optimising the SWCNT to surfactant ratio and the thickness of the sensing layer.

The devices are low-powered (operating at room temperature), affordable and could be easily incorporated into a sensing array. Furthermore, industrially viable solution based fabrication techniques, such as screen printing or spray coating, could be used for large scale manufacture of such sensors.

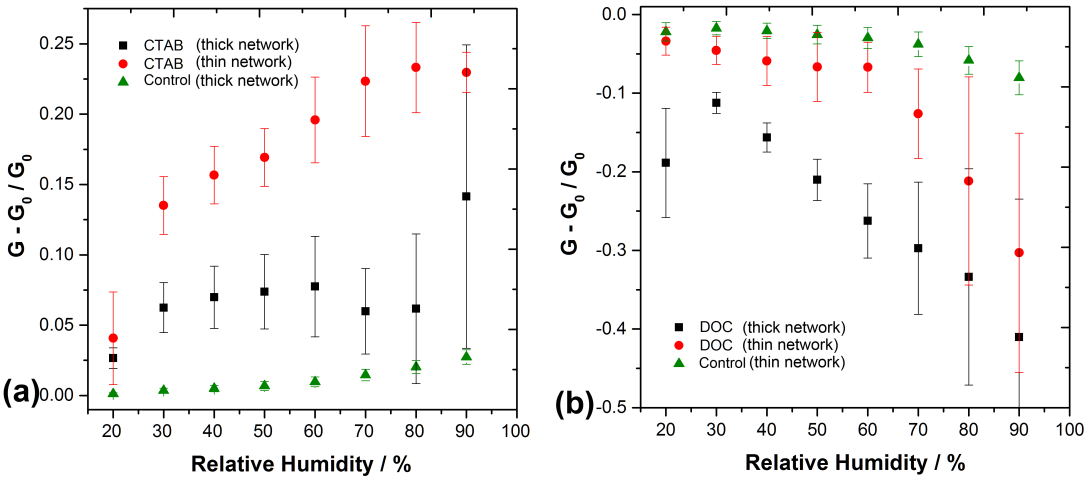

Figure 4.16: Magnitude and direction of conductance change for SWCNT network humidity sensors. (a) (■) HiPco CTAB thick (dense) network, (●) HiPco CTAB thin (lower-density) network and (▲) thick HiPco control sample containing no surfactant. (b) (■) HiPco DOC thick (dense) network, (●) HiPco DOC thin (lower-density) network and (▲) thin surfactant free HiPco control sample. The error bars represent the standard deviation of responses from two identical humidity sensors of the same type.

4.4 Conclusion

In this chapter, the adsorption or desorption of water vapour from the surrounding atmosphere to the surface of SWCNTs was shown to alter the conductance through SWCNT networks. It was proposed that electrostatic interactions of water molecules with the SWCNTs in the network induce the reversible change in conductance of surfactant containing samples, rather than permanent chemical doping of the film.

An enhanced conductance change measured for the SWCNT films (compared to the control, enhanced by a factor of 10) was attributed to the ionic surfactants in the sample. SWCNTs functionalised with cationic surfactants (CTAB and CTAT) demonstrate an increase in conductance upon exposure to water vapour (*n*-type increase), whereas anionic agents (DOC and SC) have the opposite effect, causing the conductance to decrease (*p*-type decrease). It was suggested that this behaviour is due to the interaction of polar water with the charged head groups and counterions associated the ionic surfactants, which impart a partial potential

on the SWCNTs. Similar causes, such as charged substrate-SWCNT interactions or other chemical functionalisation routes, could be the source of the discrepancies previously reported for the conductance-humidity behaviour of SWCNTs [146, 147, 143, 123, 144, 145].

It was suggested that the substrate influences the SWCNT - analyte interaction, enhancing the humidity induced conductance change for thin SWCNT control (surfactant free) networks. Moreover, differences in conductance-humidity behavior of thin vs thick networks containing anionic or cationic surfactant were attributed to the varying contribution of sc-SWCNTs to conduction across the wetted films.

The functionalisation of SWCNT networks with ionic surfactants produced fast and reversible humidity sensing behaviour. By optimising the thickness and type of ionic surfactant in the film, the future development of low powered humidity sensors based on SWCNT networks may be possible. In addition, this study provides a method to evaluate the success of various surfactant removal strategies, through investigation of the SWCNT network conductance-humidity behaviour. The observed intrinsic sensitivity to water vapour demonstrates the importance of assessing the characteristics of SWCNT based devices in humid environments, especially for SWCNT-based chemical sensors.

After establishing the conductance-humidity behaviour for the range of functionalised networks described in this study, the sensitivity to water vapour was harnessed to improve the NO_2 sensing characteristics of SWCNT networks, as described in the following chapter.

Chapter 5

Study II: Water-assisted regeneration (WAR) of SWCNT networks for NO_2 gas sensing.

5.1 Introduction

In this chapter, the NO_2 gas sensing characteristics of HiPco SWCNT networks were investigated. Preliminary experiments revealed that significant baseline signal drift occurred after repeated exposure to NO_2 gas, also observed in other studies [7]. As a consequence, the accurate quantification of NO_2 concentrations was challenging, due to the deterioration of the sensing response after sequential exposures.

To address this issue, the water-assisted regeneration (WAR) technique was applied [145]. By exploiting the interaction of water vapour with the surfactant functionalised SWCNTs, as detailed in Chapter 4, the sensor surface was regenerated after exposure to NO_2 gas. This is the first reported study to explore the WAR technique with surfactant functionalised SWCNTs, which typically display an order of magnitude larger sensitivity to H_2O than non-functionalised SWCNT networks.

It was possible to extract key parameters (such as the adsorption rate, k, and maximum conductive response, S_{max}) from the SWCNT DOC network real-time response plots using two previously reported methods [14, 15]. Calibration curves were generated for NO_2 sensing, with minimal baseline signal drift occurring using

the WAR technique.

The irreversible adsorption model proposed previously by Strano *et al.* [14] was fitted to the results, providing a rational for the proposed NO_2 sensing mechanism, yet not completely describing the sensor responses. Rather, the shape of the transient conductive response curves to NO_2 were better modelled by considering a balance of both irreversible and reversible adsorption processes as suggested by Kumar *et al.* The two distinct adsorption processes are potentially related to different NO_2 adsorption sites on the SWCNTs.

5.2 Experimental

5.2.1 Device fabrication

SWCNTs produced via the high pressure carbon monoxide disproportionation (HiPco) process [137] (purchased from Nanointegris, batch number: R1-831) were dried in air at 120 °C to remove moisture from the bundles and stored under vacuum.

To prepare the test samples, the SWCNTs were added to aqueous solutions containing 2 wt.% Sodium deoxycholate (DOC, CAS Number: 302-95-4 , 97%) purchased from Sigma-Aldrich. The initial carbon concentration was approximately 2 mg mL^{-1} for the HiPco SWCNT surfactant solutions.

To aid efficient solubilisation and de-bundling of the tubes *via* surfactant wrapping, the solution was sonicated using a tip sonication probe at a power of 225 W for 15 minutes, with the container placed in an ice bath for cooling. The samples were centrifuged at 4000 g for 30 minutes and the upper 80% of the supernatant was decanted to limit the presence of carbonaceous impurities and highly bundled SWCNTs in the final concentrated solution. Diluted samples were also obtained by dilution of the concentrated solutions in deionised water.

3 x 3 mm alumina tiles with patterned gold electrodes of 175 μm separation were used as the substrate to facilitate measurement of the conductance across the SWCNT networks. The HiPco DOC SWCNT solutions were deposited across the interdigitated gold electrodes using a calibrated Finnpipette novus electronic

single-channel micro pipette (drop volume 1 μL per sensor) and dried in air at 100 °C in a thermostat controlled furnace for 2 hours to form chemiresistor type devices.

5.2.2 Characterisation techniques

A JEOL JSM-6700F field emission scanning electron microscope (SEM) was used in secondary electron imaging mode to image the HiPco DOC surface using a 2, 5 or 10 kV probe voltage at a working distance between 5 and 14 mm. A rotatable sample holder was used to obtain side on SEM images of the HiPco DOC sensors. Samples were gold coated for imaging.

Transmission electron microscopy (TEM) was performed using a JEOL 200 kV transmission electron microscope in imaging mode. The HiPco DOC solution was drop coated onto a holey-carbon coated copper TEM grid purchased from Agar Scientific for the measurement.

A Renishaw inVia Raman microscope with laser wavelength 514.5 nm and 1 mW power was used to perform Raman spectroscopy on the surfactant wrapped HiPco DOC samples (deposited on a glass substrate after heating to 100 °C, 150 °C, 200 °C or 250 °C in air using a thermostat controlled furnace).

Thermo gravimetric analysis (TGA) profiles were obtained using a Netsch TA45 DSC/TGA. Either dried HiPco or HiPco DOC aqueous solution was placed into an alumina crucible and heated to a temperature of 750 °C in air, using a ramp rate of 5 or15 °C min^{-1}.

5.2.3 Water-assisted regeneration (WAR) testing procedure

Sensors were placed in ports within a circular testing chamber. The synthetic air flow rate (1 L min^{-1}), chamber humidity and gas mixing was controlled using digital mass flow controllers, being delivered at a determined concentration through a central inlet. The circular arrangement of the devices, along with the extraction of gas behind each individual port location, ensures that each sensor is exposed to an equal flow and concentration of gas. A potentiostat setup was used to derive the room temperature sensor conductance throughout the testing run.

Prior to the experiments, dry synthetic air was passed over the sensors for 2 hours to obtain a baseline conductance (G_{Air}) and achieve 0 % relative chamber humidity (confirmed using an internal humidity meter). Four testing procedures were employed for this study, outlined below.

In procedure 1, 6 × 10 ppm concentration of NO_2 were introduced to the testing chamber with dry air for 600 s, with 1200 s of dry air flow only separating each pulse to highlight the lack of sensor recovery and diminishing responses. In procedure 2, 600 s pulses of NO_2 gas (in the 2 ppm to 6 ppm range) were followed by a flow of only wet air (50% RH in the chamber) for 600 s and then dry air for 600 s to demonstrate the recovery of the baseline signal after WAR. Procedure 3 was similar to procedure 2, but NO_2 concentrations in the 20 ppm to 120 ppm range were investigated. Finally, procedure 4 followed that of procedure 1, but a 1200 s flow of wet air is introduced at the end of the test to demonstrate the recovery of baseline conductance after sequential NO_2 pulses.

5.3 Results

5.3.1 Material characterisation

Scanning electron microscopy (SEM) of the of the HiPco DOC sensors qualitatively revealed the surface structure of the deposited film. The micrograph shown in Figure 5.1a shows the cracks that formed in the film after the 100 °C drying step in air. Smaller bundles of SWCNTs bridge the cracks in the film, separating densely packed areas of larger bundles.

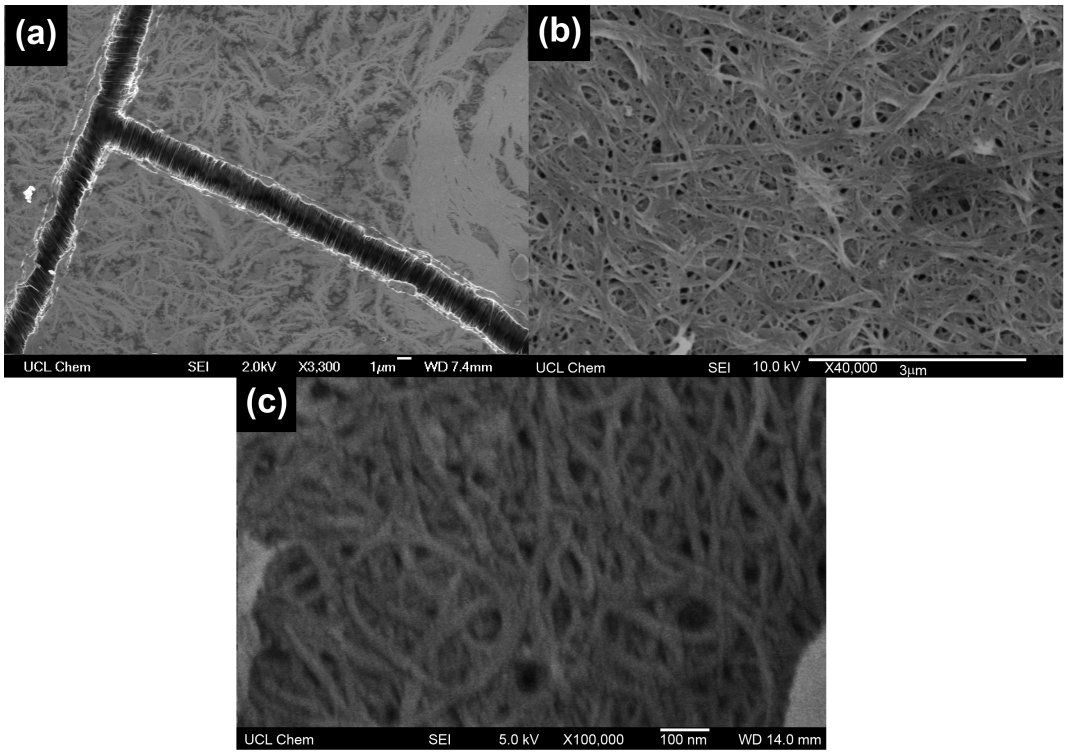

Figure 5.1: SEM micrographs at (a) ×3,300 (b) ×40,000 (c) ×100,000 magnification showing gold coated bundles of HiPco SWCNTs non-covalently functionalised with DOC and deposited as a film from aqueous solution. Cracks are present in the film surface across which SWCNT bundles are suspended as shown in (a). Networks of interconnected SWCNT bundles are formed as shown in (b) and (c).

At higher magnification (×40,000) in Figure 5.1b, the interconnected network structure of the SWCNT film, with high reported surface area [262] is displayed. From Figure 5.1c, the approximate diameters of the SWCNT bundles present on the surface of the sensors were between 10 nm and 50 nm. Imaging of individual SWCNTs (typically of order 1 nm in diameter) was not possible due to the maximum resolution of the SEM instrument. Partial re-bundling of the nanotubes after deposition to the sensor substrate is expected due to the drying of the surfactant film and the re-emergence of Van der Waals interactions between individual SWCNTs [52].

The HiPco DOC films were estimated to be 10 μm in thickness. This is shown in Figure 5.2a, in which side on SEM was used to estimate the distance between the substrate and surface of the SWCNT network, as indicated by the black arrow. The

rough morphology of the alumina substrate is shown in Figure 5.2b using conventional SEM at ×2,000 magnification.

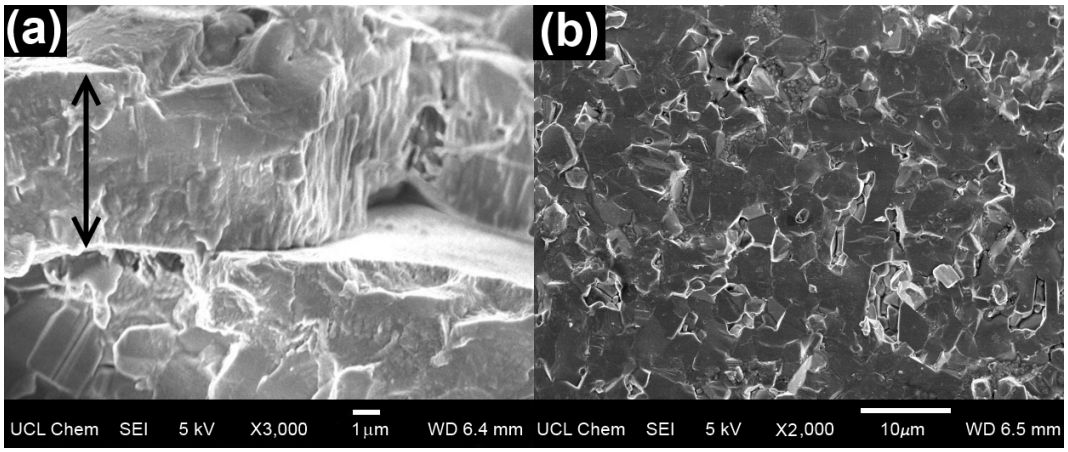

Figure 5.2: (a) A side on SEM micrograph at ×3,000 magnification showing a HiPco DOC layer of ≈ 10 μm thickness deposited on an alumina substrate, as indicated by the black arrows. (b) SEM micrograph at ×2,000 magnification showing roughness of alumina (Al_2O_3) sensor substrate.

Imaging *via* transmission electron microscopy (TEM) is of higher resolution, enabling the qualitative estimation of SWCNT and SWCNT bundle dimensions. Figure 5.3a shows interconnected bundles of HiPco SWCNTs deposited on a copper holey-carbon TEM grid. The average diameter of 100 different bundles (as marked in blue in Figure 5.3a) was calculated as 9 ± 6 nm. At higher magnification, individual constituent SWCNTs of these bundles are observable, as displayed in Figures 5.3b and 5.3c. This permits the estimation of the diameter of individual SWCNTs in the sample, by drawing a line profile across the image of the bundles and calculating the separation between intensity peaks in the profile. Figure 5.3d shows such a method, in which the diameter of the SWCNT is estimated to be in the 0.68 to 1.1 nm from it's bundle profile, in line with previously reported values for HiPco samples [263].

Impurities are present on the walls of the SWCNTs throughout the HiPco sample. These appear as black dots in Figure 5.4 and are highlighted in blue on Figure 5.4a. They have an average diameter of 3 ±1 nm and have previously been identified in the literature as residual iron impurities from the HiPco SWCNT synthesis

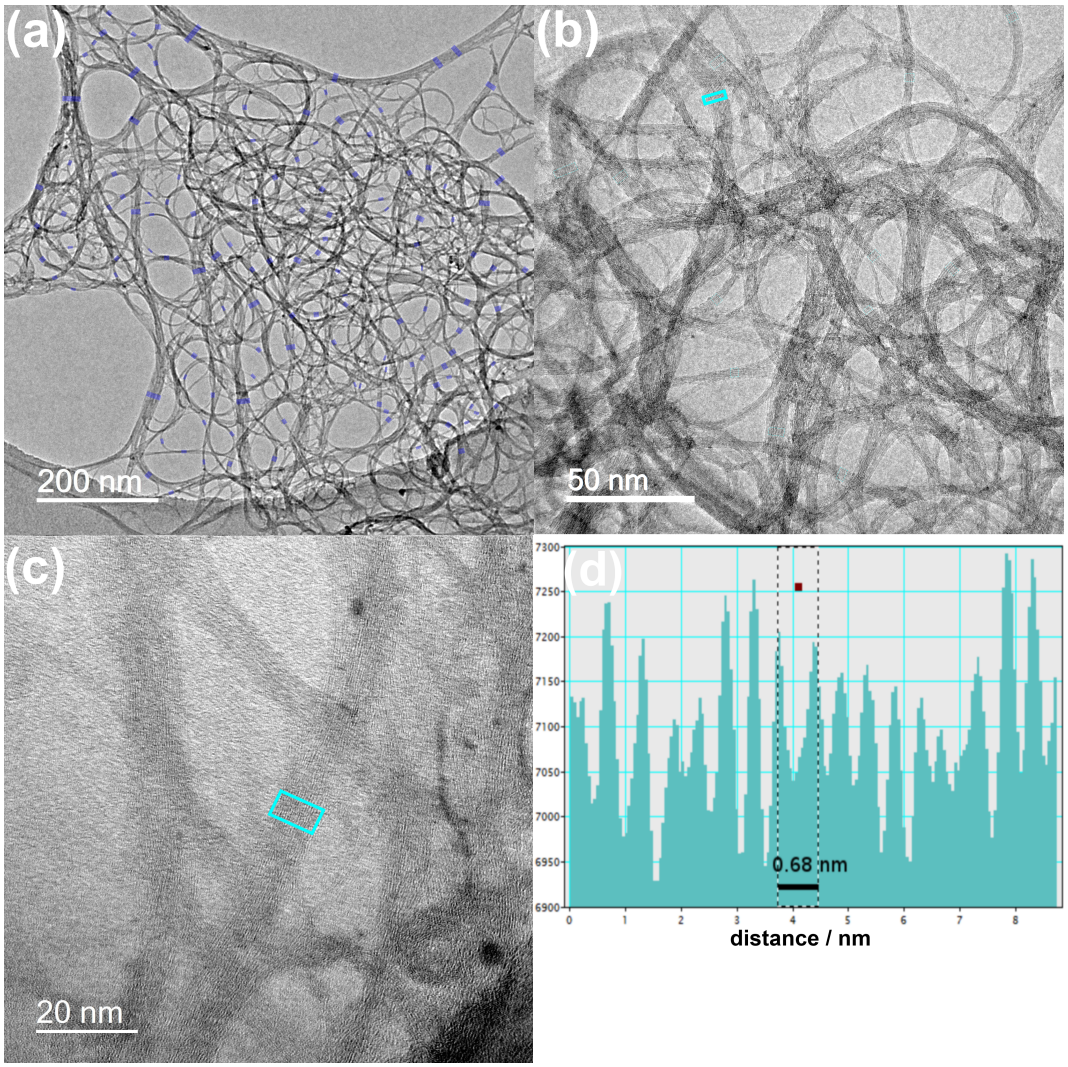

Figure 5.3: TEM micrographs showing (a) interconnected bundles of HiPco SWCNTs, with blue markings highlighting the100 sampled bundles used to calculate an average bundle diameter of 9 ± 6 nm. Individual SWCNTs within the bundles are visible in (b) and (c), with examples of the bundle sampling areas highlighted in light blue, used to generate the line intensity profile for estimation of individual SWCNT diameter shown in (d).

process [137].

Raman spectroscopy was performed on the surface of the HiPco DOC sensors before gas testing experiments were undertaken. The spectra obtained, as displayed in Figure 5.5 for the HiPco SWCNTs heat treated at 100 °C in air, contains the RBM, G-band, D-band and G′-band features expected using a laser wavelength of 514.5 nm, as reported previously in Chapter 4 Figure 4.7 and described elsewhere [56].

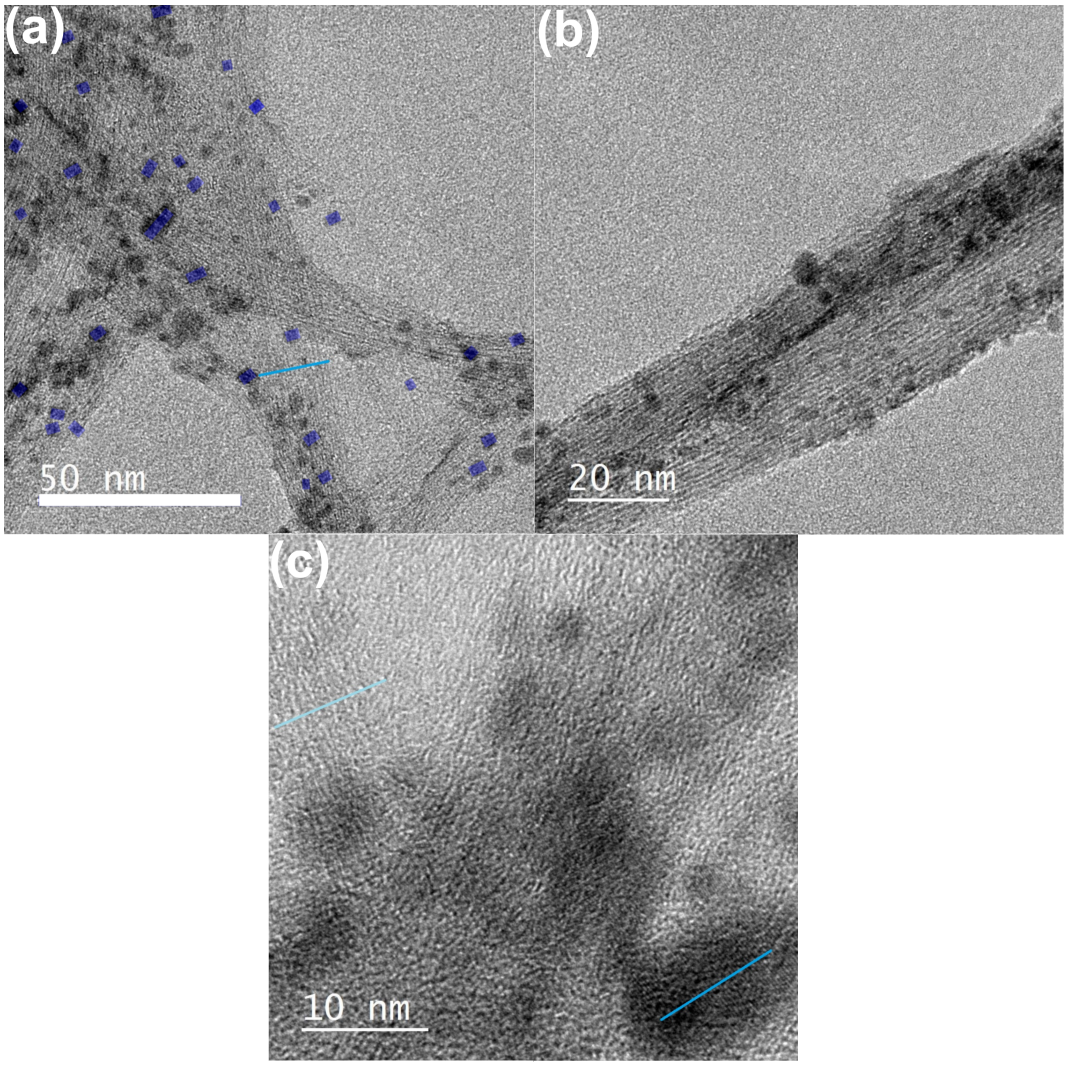

Figure 5.4: TEM micrographs showing (a) the presence of multiple residual iron impurities in the HiPco sample, with the dots marked in blue used to calculate the diameter of these particles (3 ±1 nm). (b) and (c) show the decoration of the SWCNT walls and bundles with iron impurities.

Heat treatment of the HiPco DOC material at higher temperatures was performed in 50 °C intervals up to 250 °C, and the Raman spectra was once again collected for each sample. Figure 5.5 shows that the D/G band ratio increases slightly as the heat treatment temperature increases, symptomatic of an increase in the number of defects in the sample [56]. The data for the 250 °C heat treated sample sits on a large background, which could be due to the deterioration of the SWCNTs into amorphous carbon, but may also be associated with degradation of

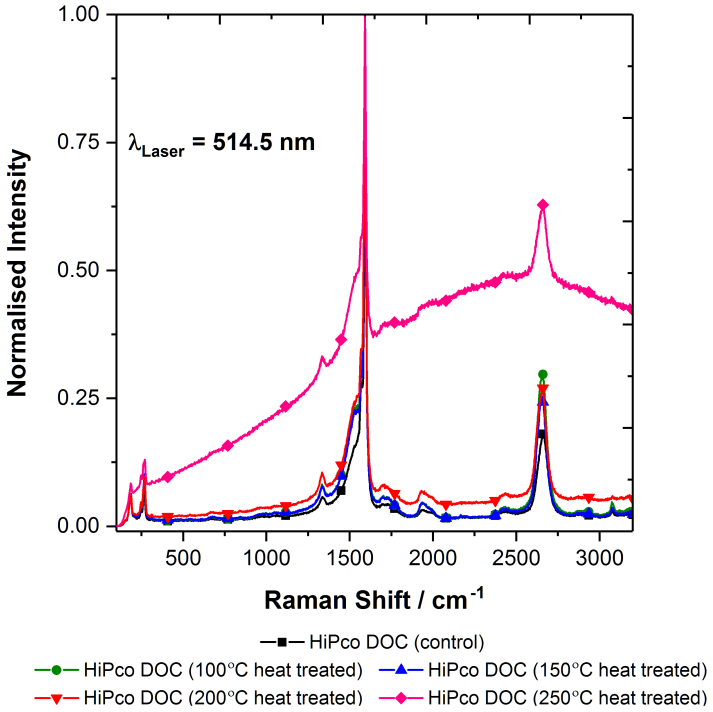

Figure 5.5: Raman spectroscopy data for HiPco DOC SWCNTs collected using a Renishaw inVia Raman microscope. The samples were deposited from aqueous solution to glass slides and heat treated at 100 °C, 150 °C, 200 °C or 250 °C in air using a thermostat controlled furnace prior to data collection. Laser wavelength λ = 514.5 nm.

the DOC surfactant molecule. Therefore, the data indicates that heat treatments in air over 200 °C may lead to significant deterioration of this sample.

This is further corroborated by thermo gravimetric analysis (TGA) of the sample. Figures 5.6a and 5.6b show the mass change of dry HiPco and aqueous HiPco DOC sample respectively as a function of temperature in air. The TGA profiles suggest that oxidation of the sample occurs over a broad temperature range (300 °C to 600 °C). The broadening of this range has previously been attributed to the existence of different carbon forms in the sample. This includes SWCNTs in bundles of different sizes, the presence of DWCNTs or MWCNTs, as well as amorphous carbon impurities which have different associated oxidation temperatures[185]. Furthermore, the step present at 450 °C and the broadening over this range has been

attributed to the surfactant used to disperse the SWCNT sample [187]. The mass remaining above 600 °C is due to metal oxide impurities (such as iron oxide, also detected in the TEM images) [264], approximately 15 % of the dry sample mass, which is reportedly removed by dispersion in solution and centrifugation [265].

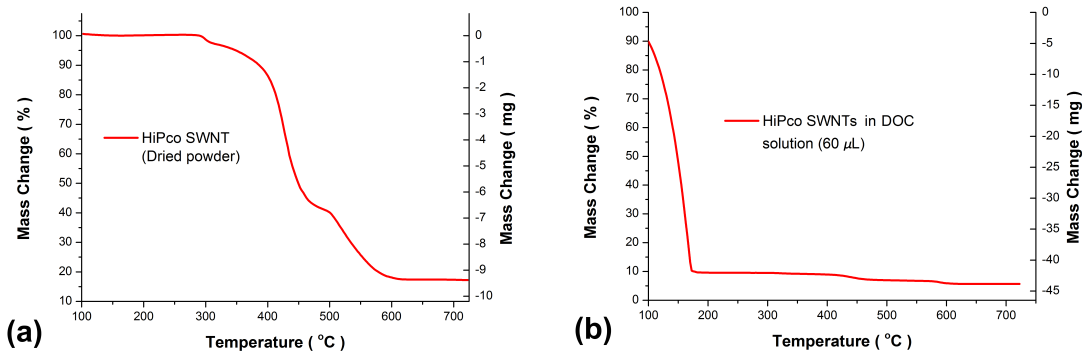

Figure 5.6: (a) TGA profile of the HiPco SWCNTs in dried powder form at a ramp rate of 5 °C min^{-1} to 750 °C. (b) TGA profile of the surfactant wrapped HiPco SWCNTs in aqueous DOC solution at a ramp rate of 15 °C min^{-1} to 750 °C

5.3.2 SWCNT sensor drift due to irreversible adsorption of NO_2

After characterisation of the SWCNT network chemiresistors, a preliminary study into the NO_2 gas sensing properties of the devices was conducted. Figure 5.7 demonstrates the substantial drift in baseline conductance when exposing the dry SWCNT layer to 6 × 10 ppm pulses of NO_2 gas. Diminishing conductive responses to the same concentration are also observed. It is thought that the drift in baseline conductance is caused by chemisorption of the molecule at binding interaction sites, with long desorption times over 10 hours reported in the literature [7, 17]. As there are only a finite number of interaction sites (which become occupied to an increasing extent after every pulse), the percentage change in conductance to repeat concentrations is altered, as shown in Figure 5.7b.

After each pulse of NO_2, the following conductive response is offset, resulting in what looks like a response curve of different magnitude and shape. In fact, the observed data is an "up-shifted" version of the response curve that would have been observed if the SWCNT network was clean initially, as articulated in Figure 5.8.

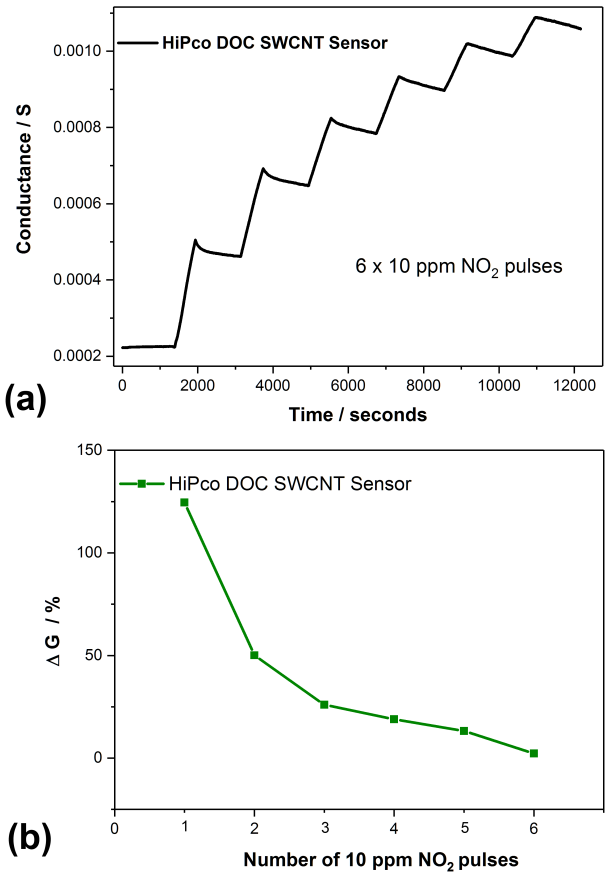

Figure 5.7: (a) An example of a conductive response from a HiPco DOC sensor when exposed to 6 × 10 ppm pulses of NO_2 gas for 600 s, each followed by a recovery period of 1200 s. The slope of the response is reduced after subsequent NO_2 pulses, as well as the magnitude of the conductance change *DeltaG* as shown in (b).

The surface reaction rate constant k also appears to decrease for later pulses, whereas it should be constant for a given SWCNT network at a certain concentration C_a [14]. This again is a result of the "up-shifted" response curve; the adsorption of NO_2 at later pulses begins with less available binding sites, akin to starting at a later time point on the response curve from an initially clean sensing layer (shown in Figure 5.8).

The drift and diminution of response prevents accurate quantification of NO_2 concentration, as the response magnitude changes for a constant number of impinging NO_2 molecules depending on exposure history, as shown in Figure 5.7b. To increase the rate of NO_2 desorption, k_{-1}, incident ultraviolet light, sensor heating

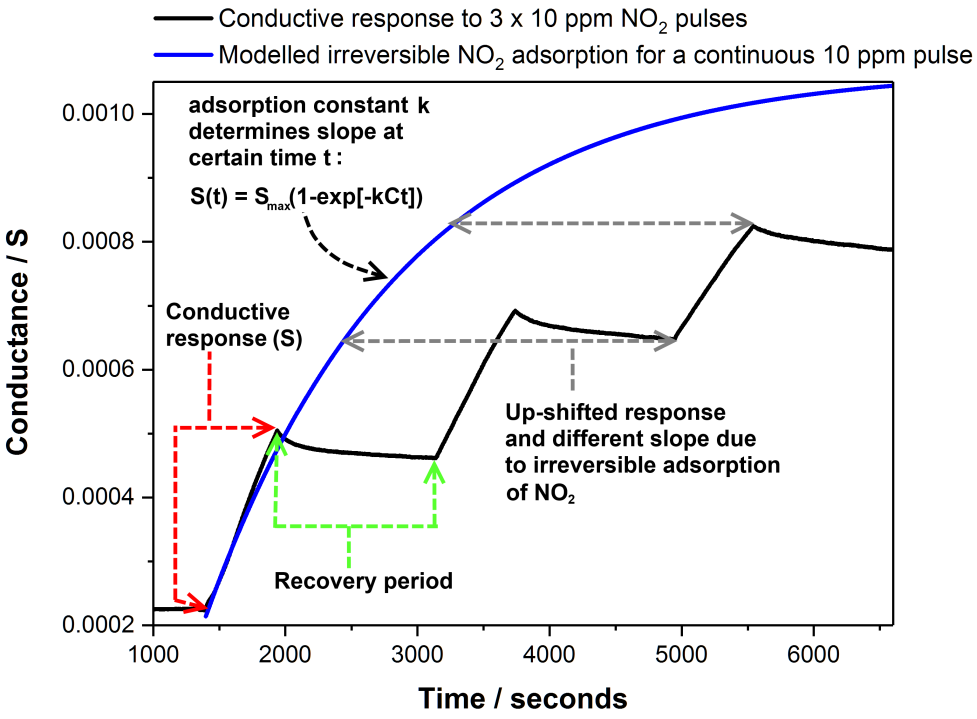

Figure 5.8: A schematic based on real-time data highlighting the conductive response and recovery periods for a HiPco DOC sensor after exposure to 3 × 10 ppm NO_2 pulses. The real-time conductive responses to the 3 × NO_2 pulses (black line) form segments of a modelled response curve based on a continuous pulse of NO_2 (blue line). Each new NO_2 pulse generates an "up-shifted" change in conduction that is effectively a continuation of the previous sensing response, due to irreversible adsorption of NO_2. Therefore, seemingly different response slopes and magnitudes are observed for the same analyte concentration, problematic for the accurate quantification of NO_2 levels.

and current-stimulated desorption have been applied previously. However, these techniques can degrade the sensing material over time, require more power or complicate the advantageously simple fabrication procedure for SWCNT network chemiresistors.

Randeniya *et al.* investigated the use of hydrolysis to recover the baseline resistance of SWCNT network based sensors. It was proposed that introducing water vapour to the sensing chamber weakens the bonding of NO_2 to the SWCNTs, encouraging desorption. An Al_2O_3 substrate is reported to partially facilitate the interaction, as the effect is not observed using free standing SWCNT films. Water-assisted regeneration (WAR) was explored as an alternative NO_2 desorption

stimulus for the surfactant functionalised SWCNT networks studied in this work, as is now discussed.

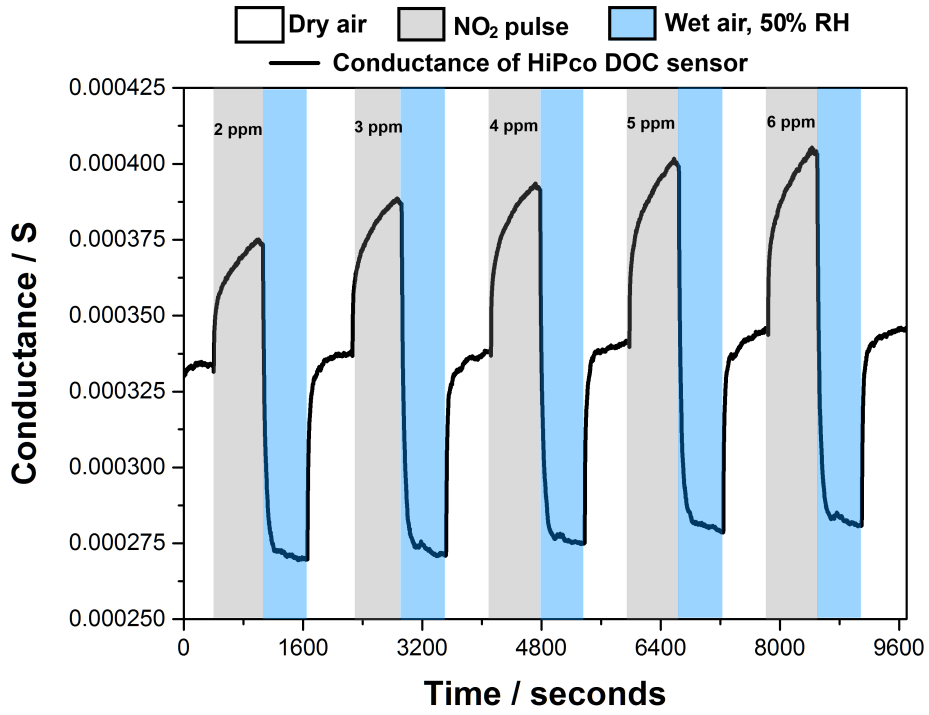

Figure 5.9: A real-time response plot for a HiPco DOC sensor demonstrating the recovery of baseline conductance G_0 after exposure to NO_2 using the WAR technique in the 2 ppm to 6 ppm concentration range. After each 600 s NO_2 pulse, the relative humidity of the chamber is increased from 0% to 50% RH by mixing dry air with wet for 600 s. Based on the response curve, the NO_2 rapidly desorbs from the SWCNT sensor surface and the baseline conductance of the device is re-established when the humidity is reset to 0% RH.

5.3.3 Water-assisted regeneration (WAR) of SWCNT networks

SWCNT networks deposited on the Al_2O_3 substrates used in this study were amenable to water-assisted regeneration. As shown in Figure 5.9, at the end of each 600 s pulse of NO_2, the conductance change does not reach a steady state. Introducing water vapour (wet air, 50% RH) to the sensing chamber after every testing pulse of NO_2 gas (in the 2 ppm to 6 ppm concentration range) aids desorption of the molecule and the conductance returns to the baseline value when a flow of dry air resumes. The responses do not deteriorate after each pulse and they increase as

the concentration of the NO_2 gas is increased throughout the experiment.

After establishing the effectiveness of the WAR method for 2 ppm to 6 ppm concentrations of NO_2, testing was performed with multiple devices over a wider concentration range (20 ppm to 120 ppm) using procedure 3 (as outlined in section 5.2). A good recovery of baseline conductance was still observed even at higher concentrations, as shown in Figure 5.10 and Figure 5.11. This suggests that water vapour is suitable to regenerate the active interaction sites on SWCNT-based sensors over a wide range of concentrations for gas sensing experiments. Assuming that the return to baseline conductance *via* WAR is equivalent to the removal of all of the previously adsorbed NO_2 from the SWCNTs, the number of available adsorption sites is constant for each new exposure to NO_2.

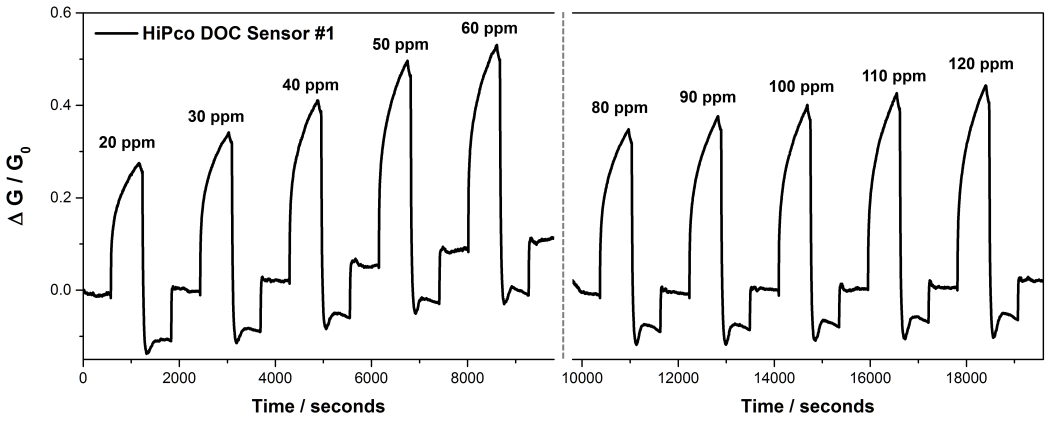

Figure 5.10: Application of the water-assisted regeneration technique (WAR) to HiPco DOC sensor 1 to recover responses after exposure to increasing concentrations of NO_2 in the 20 ppm to 120 ppm range. The grey dotted line indicates a pause in testing to change to a NO_2 gas cylinder of higher concentration.

The method can also be applied to regenerate SWCNT-based sensors after an entire testing cycle. Figure 5.12 shows the recovery of the baseline conductance after 3×10 ppm pulses of NO_2. This procedure may be used as a desorption step after a set amount of exposure time for the regeneration of practical devices for environmental monitoring.

5.3.4 Applying the irreversible adsorption model

Attempting to describe the gas sensing results with a model can help to shed light on the adsorption processes taking place on the surface. Therefore, the applicability

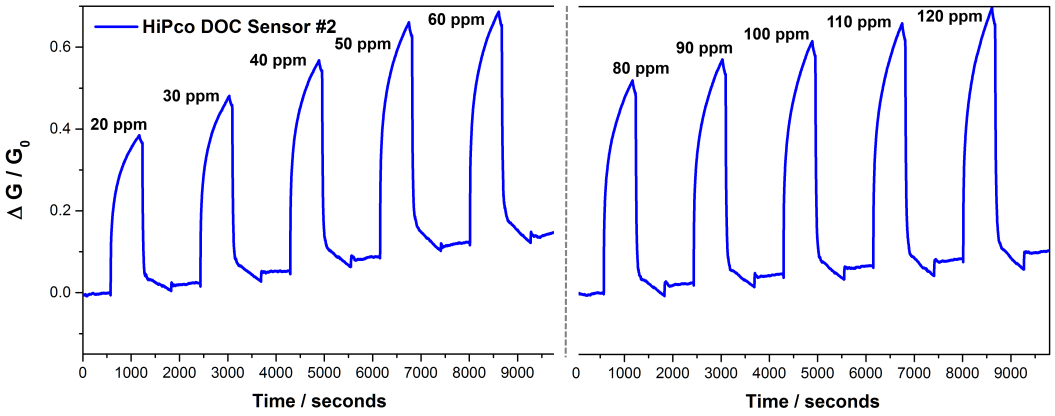

Figure 5.11: Application of the water-assisted regeneration technique (WAR) to HiPco DOC sensor 2 to recover responses after exposure to increasing concentrations of NO_2 in the 20 ppm to 120 ppm range. The grey dotted line indicates a pause in testing to change to a NO_2 gas cylinder of higher concentration

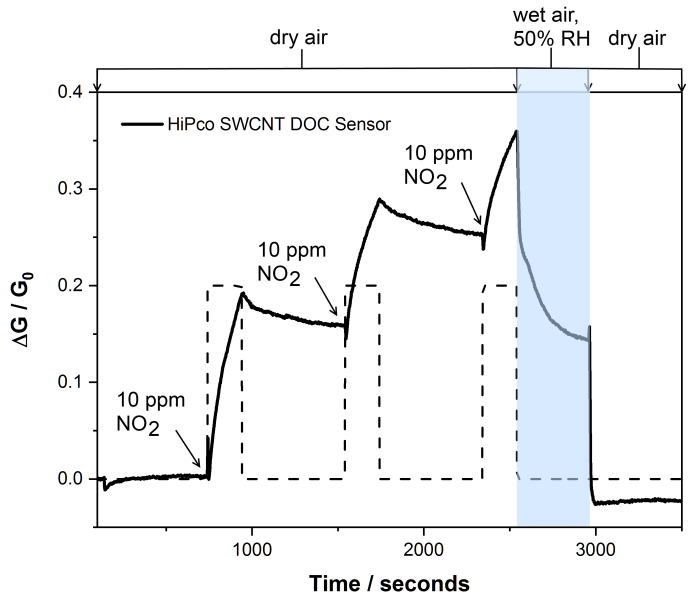

Figure 5.12: The conductive response of a HiPco DOC sensor to 3 × 10 ppm NO_2 pulses for 600 s (timings indicated by the black dotted lines) each separated by 1200 s of dry air in the recovery period. After the 3 pulses, WAR was used to regenerate the sensor as marked in the blue shaded region, with the baseline conductance recovered with the switch back to 0% RH. This mode of operation could be used to periodically refresh the SWCNT-based sensors.

of the irreversible adsorption model proposed by Strano *et al.* [14, 129] was investigated.

In the context of SWCNT-based sensors, it is useful to consider both irreversible adsorption (in which recovery of the baseline transduction signal does not

occur upon removal of the analyte from the sensing atmosphere, on a time scale within an order of magnitude of the detection period) and reversible adsorption (in which at least half of the baseline conductance is recovered within 60 s of removing the analyte from the atmosphere). Defining irreversible adsorption as the lack of recovery of 50% of the baseline conductance after 12 hours, adsorption of NO_2 to the SWCNT DOC sensors used in this study was considered to be irreversible (examples of irreversible adsorption are highlighted in Figure 5.7). Even using the WAR method, the adsorption of NO_2 was treated as irreversible, as the NO_2 was only desorbed from the surface on appropriate time scales after introduction of the water vapour.

To identify the process dominating the NO_2 responses in the current study, the model proposed by Strano *et al.* [14, 129] is now described from their publications on the topic.

The total number of available binding sites, $T\theta$, describes the total number sites accessible on the nanotube surfaces for molecular interactions. θ and $A\theta$ are the available and analyte occupied sites respectively. At a concentration C_a, the analyte molecule A reacts with unoccupied sites with the surface reaction:

$$\theta(surface) + A(gas) \xrightarrow{k} A\theta(surface) \tag{5.1}$$

The forward adsorption rate constant is k, with *gas* and *surface* indicating gas phase and surface bound species. The total number of sites on the sensor surface, $T\theta$, is conserved so that:

$$\theta(surface) + A\theta(surface) = T\theta(surface) \tag{5.2}$$

For a given SWCNT network, $T\theta$ is constant and should be proportional to the accessible surface area. The change in sensor conductance (ΔG) after exposure to a target gas is:

$$\Delta G = G - G_0 \tag{5.3}$$

where G is the new conductance after exposure to an analyte and G_0 is the baseline conductance. The sensor conductive response (S) is defined as:

$$S = \frac{\Delta G}{G_0} \tag{5.4}$$

If S is directly proportional to the number of sites occupied by an analyte, then

$$\frac{d^2S}{d(A\theta)^2} = 0 \tag{5.5}$$

The rate of sensor response is found by mass action using equation 5.1:

$$\frac{dA\theta}{dt} = k\theta C_a \tag{5.6}$$

using the site balance in equation 5.2

$$\frac{dA\theta}{dt} = k[T\theta - A\theta]C_a \tag{5.7}$$

If equation 5.7 is solved for the case of an initially clean SWCNT network at $t = 0$, then the number of occupied sites and sensor response as a function of time can be expressed as:

$$A\theta(t) = (T\theta)(1 - e^{-kC_at}) \tag{5.8}$$

$$S(t) = (S_{max})(1 - e^{-kC_at}) \tag{5.9}$$

where S_{max} is the maximum conductance change when the sensor is saturated. Equation 5.9 should then predict the conductive response curve over time, as articulated in Figure 5.8. The response rates can be found using:

$$\frac{dA\theta(t)}{dt} = (T\theta)kC_ae^{-kC_at} \tag{5.10}$$

$$\frac{dS}{dt} = (S_{max})kC_ae^{-kC_at} \tag{5.11}$$

Equations 5.10 and 5.11 indicate that there are three ways to increase the sensor response rates [14]:

(1) Increasing the total number of adsorption sites ($T\theta$) by using more SWCNTs in the sensing layer.

(2) Increase the surface reaction rate constant k by controlled doping of the sensing material.

(3) Using a functional material to pre-concentrate the target analyte, effectively increasing the concentration (C_a) to which the sensor is exposed.

Strano *et al.* point out that, assuming a completely irreversible response is observed, equation 5.9 provides a useful scaling for the real time response curve data at different concentrations (shown in Figure 5.13). If the responses are completely irreversible, then a plot of concentration multiplied by exposure time ($C_a \times t$) *vs* the response data at those concentrations, should collapse all of the data on to one curve. This is akin to plotting the expected response of the sensor *vs* NO_2 dose (where dose = $C_a \times t$), which, assuming all of the NO_2 remains in the sensing system, should lie on one curve. This collapsed plot can then be used to distinguish irreversible from reversible responses, as the latter will not collapse onto a single curve.

Figure 5.13 shows the real time response curves for a HiPco DOC SWCNT sensor with an exposure duration of 600 s for a range of NO_2 concentrations (1 ppm to 120 ppm) using the WAR procedure, along with the plot of $C_a \times t$ *vs* $\Delta G / G_0$. The NO_2 response data collapses to a single curve in Figure 5.13b using the above analysis, indicating that the adsorption of NO_2 to the HiPco networks is irreversible (using a lack of sensor recovery on a time scale within an order of magnitude of the detection period as a definition for irreversible adsorption).

The regeneration of the sensor surface after every pulse is necessary for this reasoning to provide insight to the nature of adsorption. Figure 5.14b shows the same analysis applied to a SWCNT HiPco sensor without using the WAR technique. As diminishing responses to increasing concentrations of NO_2 are observed,

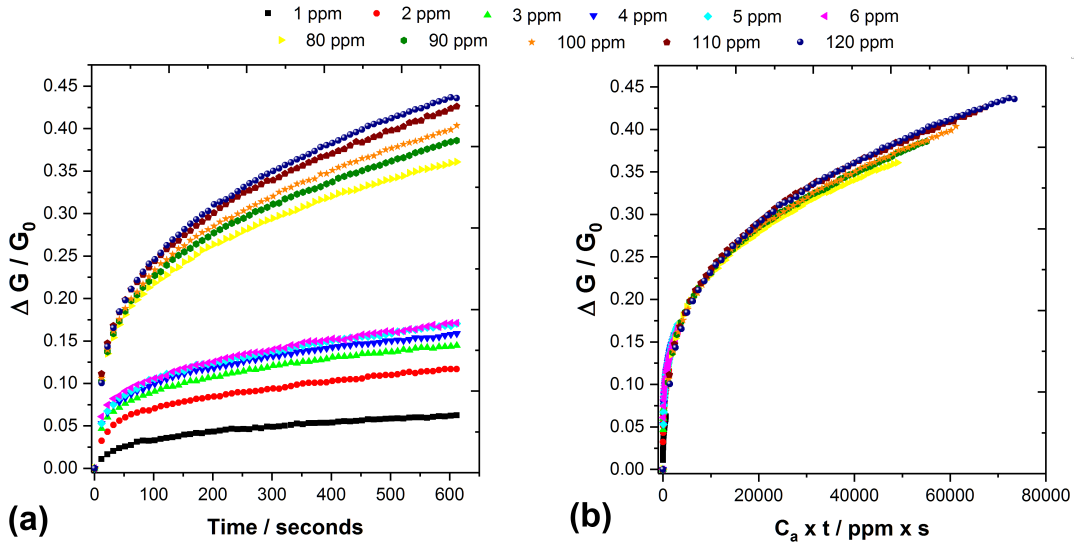

Figure 5.13: (a) A plot of the real-time responses of a HiPco DOC sensor to NO_2 gas in the 1 ppm to 120 ppm concentration range using the WAR technique to recover baseline conductance. (b) the same responses plotted against NO_2 dose ($C_a \times t$), showing the data collapses to a single curve as expected for irreversible adsorption of NO_2 [14].

the plot of concentration multiplied by exposure time ($C_a \times t$) *vs* the response data at those concentrations does not collapse onto one curve. This demonstrates the importance of recovering the baseline conductance signal before drawing conclusions from the data about the mechanisms contributing toward the SWCNT sensor responses, which the WAR technique facilitates.

After establishing the irreversible nature of NO_2 adsorption to the HiPco SWCNT networks used in the current study, it was possible to extract key sensing parameters from the sensor data using a method developed by Strano *et al.* from the aforementioned adsorption model. S_{max} and k were calculated using this procedure and compared with a standard curve fitting procedure using Origin Pro 2017 software, as is now detailed.

5.3.5 Figures of merit for SWCNT network sensors

In order to compare the sensing performance of SWCNT-based sensors, it is important to report standardised figures of merit. Strano *et al.* proposed a model for irreversible adsorption of NO_2 to metallic networks of SWCNTs. As pointed out in their work, a completely irreversible sensing response implies that reporting a limit

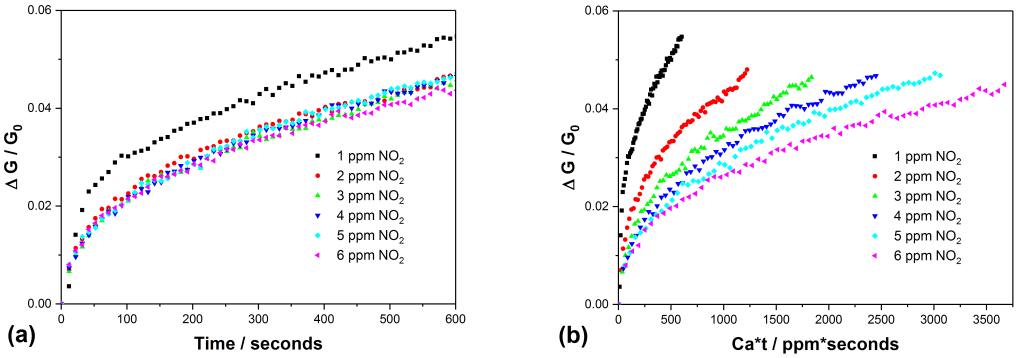

Figure 5.14: (a) A plot of the real-time responses of a HiPco DOC sensor to NO_2 gas in the 1 ppm to 6 ppm concentration range without using the WAR technique to recover baseline conductance. Due to a lack of baseline recovery, responses to higher concentrations are smaller in magnitude. (b) the same responses plotted against NO_2 dose ($C_a \times t$), showing the data does not collapse to a single curve or fit the irreversible NO_2 adsorption model, as was observed using the WAR technique for testing. This is because the model assumes an initially clean SWCNT array for each NO_2 pulse, which is not the case for the testing performed without WAR.

of detection (LOD) is inappropriate, since the build up of any concentration of gas on the sensor surface could be detected given enough time [14].

Instead, the surface reaction rate constant k was considered suitable, as it communicates the ability to transduce a specific concentration (C_a) within a predefined time [14]. k is expected to be independent of detector geometry and the number on nanotubes in the array for irreversible adsorption. The maximum conductive response at sensor saturation (S_{max}, limited by the number of available interaction sites) is also a useful quantity to report, as well as the calibration curve which describes the response of a sensor over a range of gas concentrations (with full desorption taking place, in this case *via* WAR, after each exposure to a known NO_2 concentration).

The baseline conductances of the HiPco SWCNT network devices, G_0, are proportional to the number of nanotubes bridging the gold electrodes that provide the current source and drain for the device [129]. As a consequence, G_0 is proportional to the total number of available adsorption sites ($T\theta$), and ΔG is proportional to the number of analyte molecules adsorbed on to the SWCNTs in the sensing layer ($A\theta$)

[129], so that:

$$T\theta = \alpha G_0 \tag{5.12}$$

and

$$A\theta = \beta \Delta G \tag{5.13}$$

where α and β are proportionality constants. Therefore, for a given concentration of gas, C_a, an identical HiPco SWCNT device containing more nanotubes in the sensing layer is expected to show a larger change in absolute conductance, ΔG. Taking the ratio of α to β by combining 5.12 and 5.13 gives:

$$\frac{\alpha}{\beta} = \frac{T\theta}{A\theta} \times \frac{\Delta G}{G_0} \tag{5.14}$$

The maximum conductive response, S_{max}, equivalent to the maximum conductance change $(\Delta G / G_0)_{max}$, is achieved when all of the possible adsorption sites are occupied with analyte molecules, so that $T\theta$=$A\theta$. Equation 5.14 then becomes:

$$S_{max} = \frac{\alpha}{\beta} = \left(\frac{\Delta G}{G_0}\right)_{max} \tag{5.15}$$

Equation 5.8 describes the relationship between the total number of available adsorption sites ($T\theta$) and sites occupied by analyte molecules ($A\theta$) over time. It can be re-written to relate the SWCNT network baseline conductance G_0 and the induced conductance change ΔG at a certain analyte concentration C_a for exposure time t, to the maximum possible conductive response and the adsorption constant k by substituting in equations 5.12 and 5.13 :

$$\frac{\Delta G}{G_0} = \frac{\alpha}{\beta}\left[1 - e^{-kC_a t}\right] \tag{5.16}$$

Substituting in equation 5.15 and taking the logarithm to the base 10 (log_{10} is used as the data is plotted on a on a log_{10}-log_{10} scale for the analysis procedure described below) gives:

$$log_{10}\Delta G = log_{10}\left\{S_{max}\left[1 - e^{-kC_a t}\right]\right\} + log_{10}G_0 \tag{5.17}$$

for a given concentration (e.g 1 ppm NO_2) and exposure time (t = 600 s) and where $S_{max} = \left(\frac{\Delta G}{G_0}\right)_{max}$.

Strano *et al.* observed a linear relationship between G_0 and ΔG, when plotted on a log-log scale with a slope ≈ 1, from their work on sensing arrays of metallic SWCNTs [129].

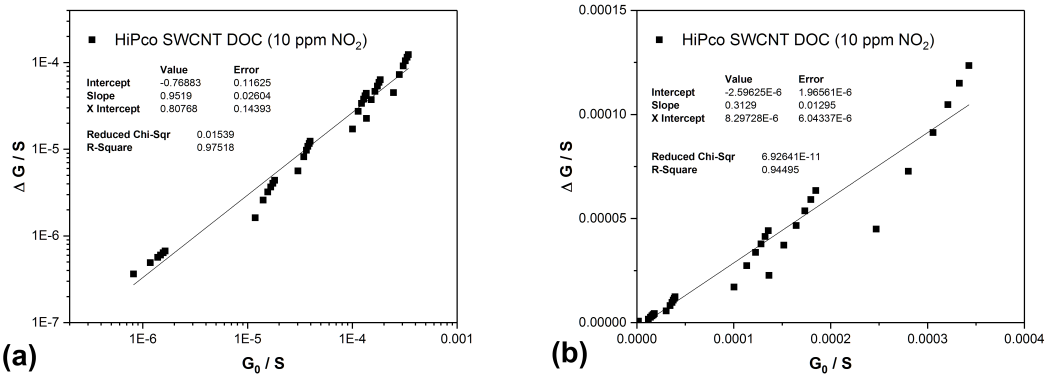

Figure 5.15: The baseline conductance G_0 of a HiPco DOC sensor *vs* the conductance change ΔG observed to multiple 10 ppm NO_2 pulses plotted (a) on log-log scale with a slope of 0.95. The intercept c of the straight line through the data can be used to estimate the adsorption constant k using the analysis described in section 5.3.5 and described in previous work [129]. (b) a plot of G_0 *vs* ΔG on a linear scale.

As shown in Figure 5.15a, this linear relationship is also observed for the HiPco SWCNT networks used in the current study (with a slope of 0.95 ± 0.026 observed in the log-log plot) . This suggests that equation 5.17 can take the form $y = mx + c$, where

$$y = log_{10}\Delta G,$$
$$x = log_{10}G_0,$$
$$m = 1$$
$$c = log_{10}\left\{S_{max}[1 - e^{-kC_at}]\right\}$$

Therefore, the intercept value, c, is related to the maximum conductive response possible for a given SWCNT network [129]. With equation 5.17 written in this form, a plot of $\log_{10}(G_0)$ *vs* $\log_{10}(\Delta G)$ at two different concentrations, such as shown for 3 different sensors using WAR in Figure 5.16a, allows the extraction of two key parameters; the adsorption rate k and S_{max}. This is described in the work by Strano *et al*. [129] and the procedural steps are as follows:

(1) Firstly, the intercept values, c_1 and c_2, are obtained from Figure 5.16a (tabulated in Table 5.1) at two different concentrations of NO_2, C_a = 60 ppm and 20 ppm respectively, with exposure time t = 600 s and set against the intercept of equation 5.17.

$$log_{10}\left\{S_{max}[1 - e^{-k\times60\times10^{-6}\times600}]\right\} = c_1, \tag{5.18}$$

$$log_{10}\left\{S_{max}[1 - e^{-k\times20\times10^{-6}\times600}]\right\} = c_2, \tag{5.19}$$

(2) This leaves equations 5.18 and 5.19 with two unknowns, k and S_{max}. Rearranging to eliminate S_{max}:

$$S_{max}[1 - e^{-k\times60\times10^{-6}\times600}] = 10^{c_1}, \tag{5.20}$$

$$S_{max}[1 - e^{-k\times20\times10^{-6}\times600}] = 10^{c_2}, \tag{5.21}$$

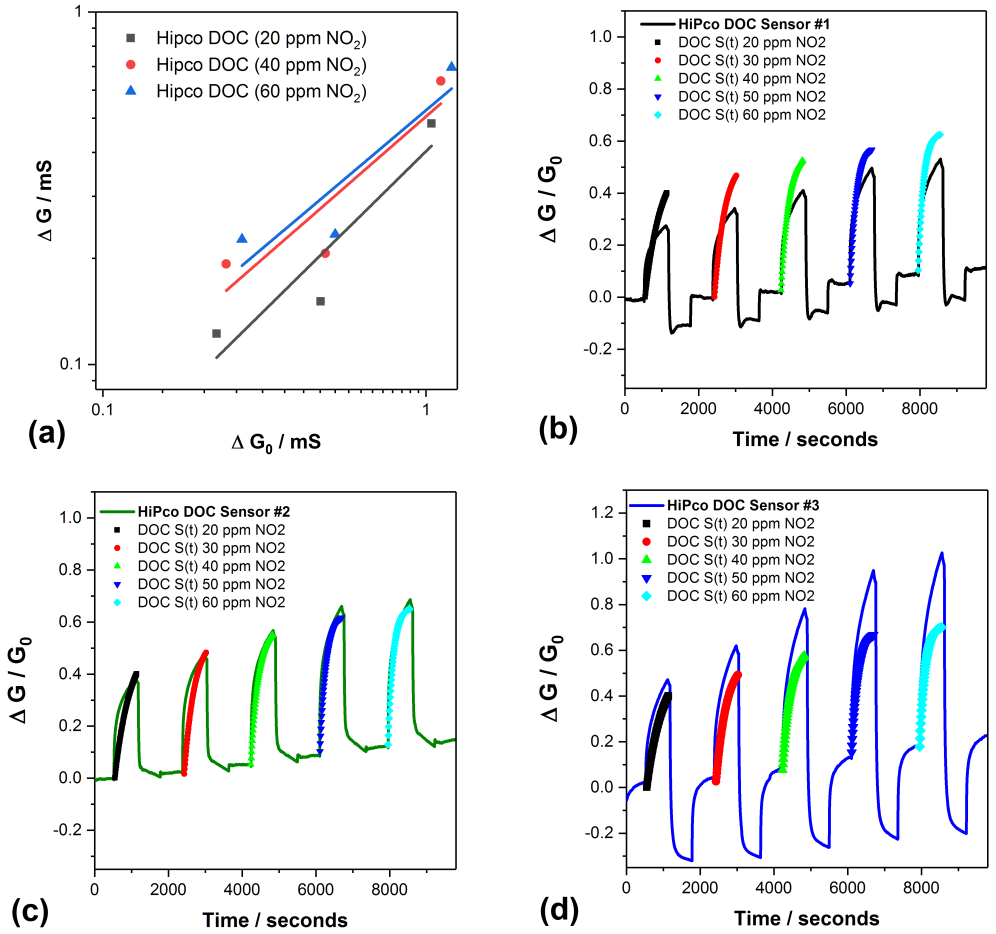

Figure 5.16: (a) A plot of G_0 *vs* ΔG on a log-log scale for 3 HiPco DOC sensors at different NO_2 concentrations, to provide the intercept value c for estimation of the adsorption constant k and maximum conductive response S_{max} using equation 5.17, based on the procedure described by Strano *et al.* (b)-(d) The real time responses of 3 HiPco DOC sensors plotted with the modelled response curves generated from equation 5.9 using the calculated S_{max} and k values, based on the irreversible adsorption model.

$$\frac{1-e^{-k\times 60\times 10^{-6}\times 600}}{1-e^{-k\times 20\times 10^{-6}\times 600}} = 10^{c_1-c_2} \tag{5.22}$$

(3) Equation 5.22 is then solved numerically for k using a root finding algorithm (a software package provided with OriginPro 2017 was used, details of which can be found in appendix B).

(4) Once k has been found, it can be input to equation 5.20 or 5.21 to calculate

the theoretical S_{max} for that SWCNT sensor type.

This procedure was tested using intercept values provided in ref [129] to calculate values of k and S_{max} quoted in the literature. Details of this testing is provided in appendix B, confirming the correct implementation of the method in the current study.

The parameters k =1.18 ± 0.05 $\times 10^{-10}$ ppt^{-1} s^{-1} and S_{max} = 0.533 were calculated for three of the HiPco DOC SWCNT sensors used in the WAR study using this method and are displayed in Table 5.1. They are similar to some of the adsorption rates previously observed in the literature for SWCNT-based NO_2 chemiresistors [15]. However, much higher adsorption rates for field-effect transistor (FET) devices were reported ([14, 6], see Table 5.1), which may indicate that the application of an adjustable gate potential alters the surface adsorption kinetics for SWCNT networks. The devices are also coated with various functional layers, which could explain differences in experimentally measured adsorption rates. As expected, a range of k values are reported for other analytes, also shown in Table 5.1.

Table 5.1: Adsorption rate (k) and maximum conductive response (S_{max}) extracted from the HiPco DOC sensor responses to NO_2 using the water-assisted recovery (WAR) procedure with the log-log plot or curve fitting method. Parameters from the literature are included using different sensor types and analytes for comparison with those from the current study (marked with a star*).

Sensor	Method	Anlayte	C_a (ppm)	intercept (c)	k (ppt^{-1} s^{-1})	S_{max}
HiPco (DOC)*, Chemiresistor	WAR (log-log plot)	NO_2	60	-0.2787	$1.18 \pm 0.05 \times 10^{-10}$	0.533
			40	-0.29638		
			20	-0.39515		
HiPco (DOC)*, Chemiresistor	WAR (irreversible curve fitting)	NO_2	60	n/a	$6.74 \pm 1.62 \times 10^{-9}$	0.569
HiPco (DOC)*, Chemiresistor	WAR (partially reversible curve fitting)	NO_2	60	n/a	$k_1 = 2.42 \pm 0.059 \times 10^{-11}$	0.534
					$k_2 = 7.77 \pm 1.74 \times 10^{-10}$	
HiPco (PEI [14, 6]), FET	UV recovery (regression)	NO_2	0.01	n/a	1.64×10^{-6}	0.43
HiPco (SDS [129]), FET	no recovery (log-log plot)	$SOCl_2$	50	-0.5486	2.69×10^{-9}	0.533
			10	-0.8838		
HiPco (DNA [129]), FET	no recovery (log-log plot)	$SOCl_2$	100	-0.8291	9.41×10^{-10}	0.243
			50	-1.04		
HiPco (SDS [129]), FET	no recovery (log-log plot)	DMMP	100	-1.479	3.29×10^{-9}	0.0345
			50	-1.556		
Arc-discharge SWCNTs (DMF, [15]), Chemiresistor	UV recovery (curve fitting)	NO_2	0.5	n/a	$k_1 = 1.51 \times 10^{-11}$	0.923
				n/a	k_2 1.68×10^{-8}	

The maximum conductive responses to NO_2 in the literature lie in the range of 0.44 to 1.73 × the baseline conductance (G_0) of the device, which are in line with the S_{max} calculated in the current study (Table 5.1). This is again expected to vary with different SWCNT functionalisations and also target analytes due to different binding affinities [13].

These parameters were then input into equation 5.9 to investigate how well the simple irreversible adsorption model resembles the response curves observed using the WAR method to detect a given concentration of NO_2 gas. The model fit is demonstrated in Figure 5.16b-d. It predicts the magnitude of the response for HiPco DOC sensor 2 (Figure 5.16c) to a good degree, but over predicts for HiPco DOC sensor 1 (Figure 5.16b) and under predicts for HiPco DOC sensor 3 (Figure 5.16d). Furthermore, the model, whilst capturing some of the shape of the experimental response curves, clearly do not completely describe the data at all NO_2 concentrations.

Therefore, using the fitting tool in Origin Pro 2017 (data analysis software), equation 5.9 was fitted to the response curves at 60 ppm NO_2 for the same three sensors to compare the fits achievable and evaluate the extent to which the irreversible adsorption model can describe the transient conductive responses. To validate this second fitting method used to extract k for each individual response curve, it was applied to data from the literature to calculate approximate values of k which were the correct order of magnitude, as outlined in appendix C.

From Figure 5.17a, it is clear that equation 5.9 does not fit the response curve well at initial time intervals. This suggests that an additional phenomenon contributes towards the sensing response alongside irreversible adsorption. Kumar *et al*. arrived at a similar conclusion in their study of NO_2 adsorption kinetics for SWCNT chemiresistors [15]. They developed a model (adapted from previous work by Strano *et al*) using coupled differential equations to simulate irreversible and reversible adsorption processes taking place simultaneously. Distinguishing between irreversible and reversible adsorption sites, they introduce an additional parameter, the equilibrium constant $K = \frac{k}{k_{-1}}$, to account for desorption of NO_2 from the sensor

surface in the case of the latter [15]. This model is now detailed below.

Adapting equation 5.2 to distinguish between irreversible and reversible adsorption sites:

$$A_1\theta + A_2\theta = A\theta, \tag{5.23}$$

$$\theta + A_1\theta + A_2\theta = T\theta \tag{5.24}$$

where $A_1\theta$ and $A_2\theta$ are the number of occupied irreversible and reversible adsorption sites respectively and θ is the number of unoccupied sites. The equilibrium constant of adsorption K is introduced to account for NO_2 desorption from reversible sites:

$$K = \frac{k_2}{k_{-1}} \tag{5.25}$$

where k_2 and k_{-1} are the adsorption and desorption constants for the reversible sites respectively. Using the law of mass action, the sensor response for occupied reversible sites $A_2\theta$ is given by:

$$\frac{dA_2\theta}{dt} = k_2\theta C_a - \frac{k_2}{K}A_2\theta \tag{5.26}$$

using equation 5.24, the change in number of occupied reversible sites over time is given by:

$$\frac{dA_2\theta}{dt} = k_2 T\theta C_a - k_2 A_1\theta C_a - A_2\theta\left(k_2 C_a + \frac{k_2}{K}\right) \tag{5.27}$$

and the change in number of occupied irreversible sites over time is given by substituting equation 5.24 into equation 5.6 :

$$\frac{dA_1\theta}{dt} = k_1 T\theta C_a - k_1 A_1\theta C_a - k_1 A_2\theta C_a \tag{5.28}$$

This provides two coupled differential equations, 5.27 and 5.28, which give the change in number of occupied sites over a period of time after exposure to an

analyte. If several assumptions are made, the solution to equations 5.27 and 5.28 can be found. These assumptions are:

(1) at $t = 0$, all irreversible adsorption sites $A_1\theta$ are unoccupied.

(2) at $t = 0$, all reversible adsorption sites $A_2\theta$ are unoccupied.

(3) as $t \to \infty$, all absorption states are filled so that $A\theta = T\theta$.

(4) The conductive response $S = 0$ when the sites are unoccupied.

(5) The maximum conductive response is achieved when $A\theta = T\theta$ and so $S = S_{max}$.

The solution to the coupled equations can be found by substituting the value of $A_1\theta$ from equation 5.28 into equation 5.27 and integrating. Set the conditions for the integration so that at $t = 0$, $A_1\theta = A_2\theta = 0$ and at $t \to \infty$, $A\theta = T$. The number of irreversible adsorption sites are:

$$A_1(t) = T\left\{1 - \frac{k_2 C_a}{m_1 - m_2} e^{m_1 t}\left(1 + \frac{1}{KC_a} + \frac{m_1}{k_2 C_a}\right) + \frac{k_2 C_a}{m_1 - m_2} e^{m_2 t}\left(1 + \frac{1}{KC_a} + \frac{m_2}{k_2 C_a}\right)\right\} \tag{5.29}$$

and the number of reversible sites are given by:

$$A_2(t) = T\frac{k_2 C_a}{m_1 - m_2}\left(e^{m_1 t} - e^{m_2 t}\right) \tag{5.30}$$

By substituting equation 5.29 and 5.30 into equation 5.23, then the total sum of occupied irreversible and reversible adsorption sites $A\theta$ is given by:

$$A(t) = T\left\{1 - \frac{k_2}{m_1 - m_2}\left(\frac{1}{K} + \frac{m_1}{k_2}\right)e^{m_1 t} + \frac{k_2}{m_1 - m_2}\left(\frac{1}{K} + \frac{m_2}{k_2}\right)e^{m_2 t}\right\} \tag{5.31}$$

where the roots m_1 and m_2 are given by equation C.4 in appendix C.2. If the conductive response, *S*, is proportional to the number of occupied adsorption sites, $A\theta$, then the conductive response as a function of time *S(t)* is given by:

$$S(t) = S_{max}\left\{1 - \frac{k_2}{m_1 - m_2}\left(\frac{1}{K} + \frac{m_1}{k_2}\right)e^{m_1 t} + \frac{k_2}{m_1 - m_2}\left(\frac{1}{K} + \frac{m_2}{k_2}\right)e^{m_2 t}\right\} \tag{5.32}$$

This equation can now be compared to the exponential function used to model the experimental data. The function used to fit the data in Origin Pro 2017 was of the form:

$$y = y_0 + (A_1)e^{-\frac{t}{\tau_1}} + (A_2)e^{-\frac{t}{\tau_2}} \tag{5.33}$$

If equation C.2 is compared to this form, then:

$$y_0 = S_{max}, \tag{5.34}$$

$$A_1 = S_{max}\left\{\frac{k_2}{m_1 - m_2}\left(\frac{1}{K} + \frac{m_1}{k_2}\right)\right\}, \tag{5.35}$$

$$A_2 = S_{max}\left\{\frac{k_2}{m_1 - m_2}\left(\frac{1}{K} + \frac{m_2}{k_2}\right)\right\}, \tag{5.36}$$

$$\frac{1}{\tau_1} = m_1, \tag{5.37}$$

$$\frac{1}{\tau_2} = m_2 \tag{5.38}$$

where τ_1 and τ_2 are the time constants for the irreversible and reversible adsorption components respectively.

The curve fitting applying equation C.2 is shown in Figure 5.17b. The model describes the data well at initial intervals, as well as the response curve overall. This adds weight to the suggestion that limited reversible adsorption of NO_2 takes place, with irreversible adsorption dominating the HiPco SWCNT DOC sensing responses as a first approximation observed in the current study.

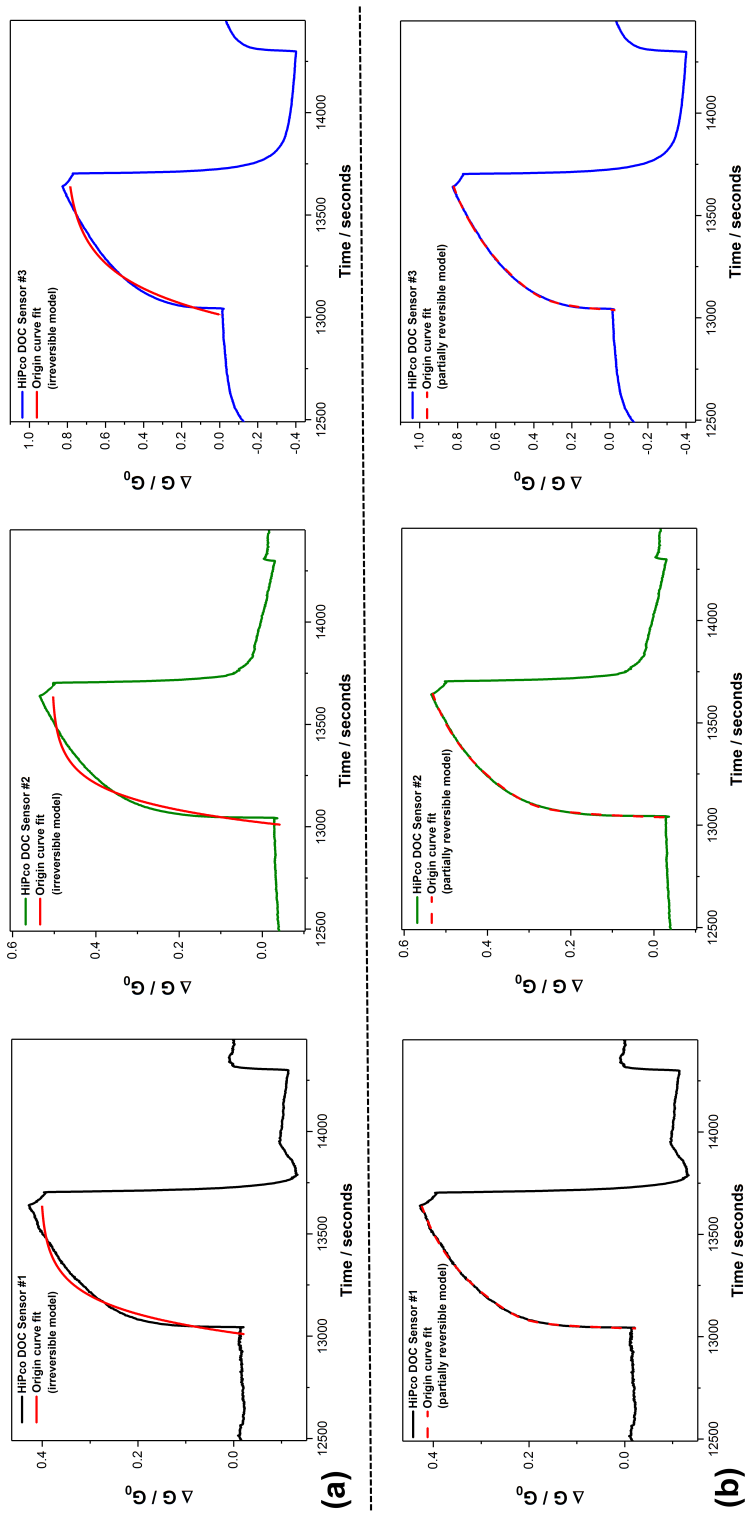

Figure 5.17: (a) Real-time conductive response plots to 60 ppm NO_2 for 3 HiPco DOC sensors with a line fit generated from the irreversible adsorption model (equation 5.9) to replicate the shape of the curve using the Origin Pro 2017 fitting tool, as outlined in appendix C. (b) An example of the improved curve fit to the same data, achieved by applying the partially reversible adsorption model [15] in the form of equation C.5.

The manifestation of different adsorption processes may be due to multiple factors. Firstly, adsorption could take place at different sites within the SWCNT network (such as at interstitial sites or grooves in the nanotube bundles, inside or on the outer surfaces of the nanotube surface [266, 126]). Secondly, defects or impurities in the sensing material could act as additional adsorption sites with different associated molecular affinities [112, 111] . Finally, any functional coating that can adsorb the target analyte and influence the conductance across the SWCNT network may also play a part in altering the NO_2 adsorption/desorption rates [42, 267, 268].

5.3.6 NO_2 sensing calibration curves

The WAR technique enables the generation of calibration curves for SWCNT sensors. These are shown in Figure 5.18, similar to NO_2 calibration curves found in the literature using WAR [105] and other regeneration techniques [269, 270, 83, 271, 130].

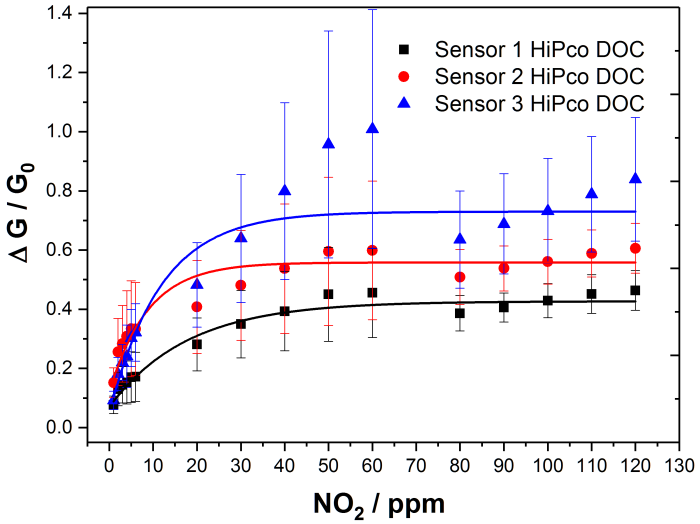

Figure 5.18: Non-linear calibration curves for 3 HiPco DOC sensors, demonstrating the expected conductive responses upon exposure to NO_2 in the 1 ppm to 120 ppm concentration range using the WAR procedure. The error bars represent the standard deviation in responses between three repeated experiments. The y-offset of responses in the 80 ppm to 120 ppm range are attributed to a change of NO_2 gas cylinder between testing cycles for the higher concentrations.

Throughout the NO_2 concentration range studied using the WAR technique (1 ppm to 120 ppm), the relationship between the conductive response S and concentration is non-linear, with the sensors reaching their saturation limit when the number of occupied interaction sites are equivalent to the total number of available interaction sites, so that $A\theta = T\theta$. The maximum possible conductive response (S_{max}) is observed at this point.

Each data point displayed Figure 5.18 is the average conductive response to a certain concentration of NO_2 gas, with the error bars representing the standard deviation from three repeated tests. The higher test concentrations (80 ppm to 120 ppm) appear to be negatively offset from the non-linear curve fitting the data compared to the 10 ppm to 60 ppm results. This is attributed to a change of NO_2 gas cylinder between testing cycles for the higher 80 ppm to 120 ppm range. Despite this, the data can be fit to an exponentially decaying function as shown by the fit lines in Figure 5.18.

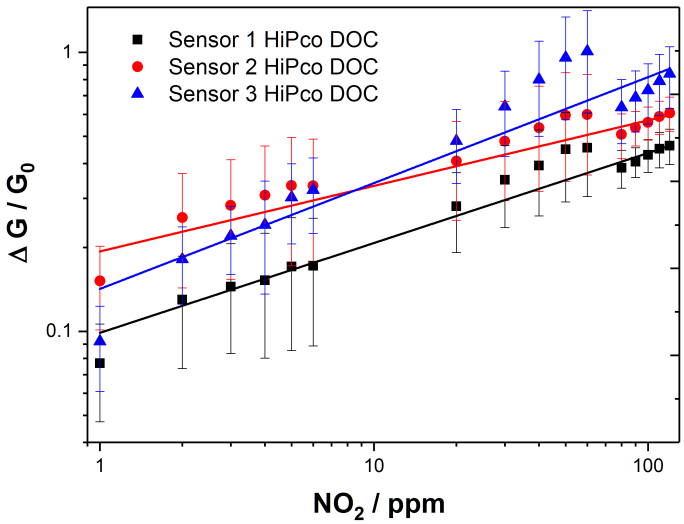

Figure 5.19: Calibration curves for 3 HiPco DOC sensors, plotted on a log-log scale to generate a linear equation for the prediction of the expected conductive responses per NO_2 concentration in the 1 ppm to 120 ppm range using the WAR procedure. The variations in gradient and intercept values suggest that device to device variation in sensor responses must be reduced before general predictions based on a linear fit can be made accurately across multiple SWCNT-based sensors. The error bars represent the standard deviation in responses between three repeated experiments.

Hu *et al.* [272] plot the calibration curve for an rGO based sensor on a log-log scale (as shown in Figure 5.19 for the current WAR study) to generate a linear equation (of the form $y = mx + c$), which enables prediction of unknown NH_3 concentrations. This is not straight forward for the current study for NO_2, as significant variations in gradient and intercept values between identical HiPco DOC sensors are observed (m = 0.322, 0.235, 0.378 and c = -1.00544, -0.71319, -0.84799, for responses from the HiPco DOC sensors 1, 2 and 3 respectively *vs* concentration on a log-log scale) . Device to device variation must be reduced before such an approach can be employed to predict unknown concentrations of NO_2 based on the conductive response.

5.4 Conclusion

The baseline conductance of HiPco SWCNT network sensors drifts substantially after the largely irreversible adsorption of NO_2 gas. The water-assisted regeneration (WAR) technique enables recovery of the baseline signal in surfactant functionalised SWCNT devices, aiding the desorption of the NO_2 molecule, potentially *via* mediated reactions as suggested by Randeniya *et al.*

The WAR method can be used to regenerate the sensor surfaces either in between gas pulses of NO_2, or periodically after testing cycles. It allows the generation of calibration curves for NO_2 sensing with SWCNTs, whilst also enabling the extraction of key figures of merit from the data, such as the adsorption constant, k, and the maximum possible conductive response, S_{max}.

While the HiPco DOC sensors exhibited similar qualitative sensing characteristics, there was a significant variation in electrical responses to NO_2 gas. This device to device variation must be overcome to facilitate the prediction of unknown NO_2 concentrations using methods such as those proposed by Hu *et al.* [272].

A model of irreversible NO_2 adsorption, proposed by Strano *et al.* [14], was able to capture features of the SWCNT network transient conductive response curves and allow calculation of k and S_{max} from the response data. However, it did not appropriately describe the responses of the SWCNT sensors in the initial stages

of gas exposure.

The partially reversible adsorption model, developed by Kumar *et al.* [15], provided the best fit to the experimental results and provided additional insight into the processes taking place on the SWCNT surfaces. The existence of both reversible and irreversible NO_2 adsorption sites across the SWCNT networks, with different associated adsorption kinetics and molecular affinities, may provide a rationale for the better match between the experimental sensing results and the partially reversible adsorption model.

Chapter 6

Study III: Sensing NO_2 in humid environments with SWCNTs.

6.1 Introduction

For real world environmental monitoring applications, such as street level pollution monitoring, measurement devices are exposed to a range of atmospheric humidities that can vary temporally and spatially. Sensors for pollutants such as NO_2 must be either insensitive to variations in relative humidity (RH) levels, or refinement of the data *via* calibration and analysis techniques must be possible post collection to account for any cross-interference effects on the sensing signal.

The use of SWCNT networks for the sensing of NO_2, introduced in Chapter 5, has been widely reported. It was demonstrated in Chapter 4 and elsewhere [146, 261, 273, 274, 275] that the electrical conductivity of SWCNT-based sensors can be altered by the adsorption of water vapour, and in Chapter 5 the introduction of water vapour to the sensor surface was shown to aid NO_2 desorption using the water-assisted regeneration (WAR) method [145]. This leads to a question which has not been fully resolved by previous studies; how does the presence of water vapour in the atmosphere affect the conductive responses of SWCNT-based sensors to NO_2 ?

In this chapter, the sensing characteristics of SWCNT chemiresistors for detection of NO_2 gas were investigated at different levels of background humidity.

Key parameters, such as the conductive response magnitude (S), adsorption rate (k) and desorption rate (k_{-1}), were altered by variations in the RH levels in the testing chamber. The dependency of these quantities on the presence of water vapour was also studied for SWCNT networks of different thicknesses and non-covalent functionalisations.

An attempt was made to apply a model for partially reversible adsorption of NO_2, previously developed in the literature [15], to rationalise the results. Coupled with the changes in sensing behaviour and characterisation of the sensor material, possible interactions between the SWCNTs in the network, NO_2 and H_2O were discussed, along with the usefulness of the findings to provide refinement of real world SWCNT sensor data post collection in the future.

6.2 Experimental

6.2.1 Device fabrication

For the HiPco SWCNT control, the raw sample was added to water (H_2O, CAS Number: 7732-18-5, HPLC grade) in powder form at a concentration of approximately 2 mg mL^{-1}. For the surfactant functionalised test samples, the SWCNTs were added to aqueous solutions containing the following surfactants at 0.5 wt.% also at a concentration of approximately 2 mg mL^{-1}: Sodium deoxycholate (DOC, CAS Number: 302-95-4 , 97%), hexadecyltrimethylammonium bromide (CTAB, CAS Number: 57-09-0, 98%), purchased from Sigma-Aldrich.

The solutions were sonicated using a tip sonication probe at a power of 225 W for 15 minutes (with the container placed in an ice bath for cooling) to form well dispersed solutions, whilst the carbon in the control sample was highly agglomerated. Centrifugation was used to (4000 g, 30 minutes) to limit the presence of carbonaceous impurities and highly bundled SWCNTs. The final concentrated solution were obtained by decanting the upper 80% of the supernatant, with less concentrated solutions achieved by dilution with deionised water.

The HiPco SWCNT solutions were deposited across pre-patterned interdigitated gold electrodes on 3 x 3 mm alumina substrates using a calibrated Finnpipette

novus electronic single-channel micro pipette (drop volume 1 μL per sensor) and left to dry in air at 23 °C for 24 hours to form chemiresistor type devices.

6.2.2 Material characterisation

A Renishaw inVia Raman microscope with laser wavelength λ = 785 nm and 1 mW power was used to perform Raman spectroscopy on each of the surfactant wrapped HiPco SWCNT thick films after deposition and drying on glass substrates. The spectras were obtained for the control, DOC, SC, CTAB, CTAT and Triton X-100 samples.

The UV-Vis-NIR absorption spectra for the deposited HiPco DOC SWCNTs (deposited on a quartz slide from the 250 X diluted stock solution) were obtained using a PerkinElmer Lambda 950 spectrophotometer to confirm the range of nanotube species present in the films. The spectra was obtained for an initial 600 μL deposition of the 250 X diluted HiPco DOC solution dried on to the quartz slide, after a blank reading was taken and subtracted. 4 additional depositions (+400 μL each) and drying steps were made with the absorbance spectra collected within the intervals to assess the repeatability of the deposition process.

6.2.3 Current-voltage device characterisation

A Keithley 4200 semiconductor characterisation system was used for current-voltage (I-V) characterisation of the chemiresistor devices. A voltage step size of 0.1 V in the -5 V to +5 V range was employed to measure the induced current from the applied voltage across the device source-drain electrodes. The conductance across the device was then calculated at a V_{bias}= 0.2 V using the relation conductance $G = I/V$.

The I-V characterisation at low temperature was performed by Zak Kobos of the Reed group, Yale. A semiconductor analyser system was used to obtain the I-V characteristics of the thick and thin film HiPco DOC SWCNT devices and a cryostat setup (Janis SVT-100 continuous vapor flow cryostat using liquid nitrogen) to control the temperature of the device in the 96 K to 300 K temperature range.

6.2.4 NO_2 testing procedure

The SWCNT sensors were placed in ports within a circular testing chamber. The synthetic air flow rate (1 L min^{-1}), chamber humidity and gas mixing was controlled using digital mass flow controllers, being delivered at a determined concentration through a central inlet. The circular arrangement of the devices, along with the extraction of gas behind each individual port location, ensures that each sensor is exposed to an equal flow and concentration of gas. A potentiostat setup was used to derive the room temperature sensor conductance throughout the testing run.

Prior to the experiments, either dry or wet air was passed over the sensors for 1 hour to obtain a baseline conductance (G_0) and achieve the required relative chamber humidity (in the 0% to 75% range, confirmed using an internal humidity meter). Wet air was generated by flowing dry synthetic air through a Drechsel flask containing 500 mL of deionised water (HPLC grade, CAS Number: 7732-18-5). Dry air and wet air were mixed at different ratios using the mass flow controllers and delivered to the testing chamber to achieve the required chamber humidity.

For the nitrogen dioxide (NO_2) - humidity experiments, a flow of NO_2 (BOC certified cylinder, 1 ppm NO_2 in dry synthetic air, CAS number: 10102-44-0) was diluted *via* mixing with a dry flow of synthetic air and introduced to the testing chamber in 600 s intervals to realise a NO_2 concentrations in the 0.1 to 0.6 ppm range, followed by 1200 s of air flow only in the signal recovery period. Conductive sensing responses to these concentrations of NO_2 were then recorded at 0%, 25%, 50% and 75% background levels of relative humidity.

6.3 Results

6.3.1 Material characterisation

Raman spectroscopy was performed on the HiPco control and the surfactant functionalised SWCNT samples, which were deposited and dried on a glass substrate. Figure 6.1 shows the expected radial breathing modes (RBMs), G-band, D-band and G′-band features are present for all of the samples studied, with the spectras

consistent with those observed previously in Chapter 4 Figure 4.9 and elsewhere [56]. The G/D ratios, calculated from Figure 6.1a and displayed in caption, were found to be in the range of 6.8 to 18.8 for all of the samples studied, indicating a low level of defects in the deposited samples.

Interestingly, the RBM peaks displayed in Figure 6.1b were found to vary in intensity with surfactant functionalisation. This would correspond to SWCNTs of different chirality (and thus electronic type) being present in different proportions for each sample. Previously, it was reported that certain aqueous surfactant systems produce solutions enriched with a specific SWCNT chirality [276, 277], which may lead to a disparity in the proportion of SWCNTs present in the different surfactant functionalised solutions. Also, bundling of nanotubes is thought to influence RBM peak intensity [278], which could be linked to how well each surfactant aids SWCNT dispersion in aqueous solution. The proportion of semiconducting SWCNTs (sc-SWCNTs) to metallic SWCNTs (m-SWCNTs), known to be the most important determinant of conductance through a SWCNT network film [279], can not be determined from analysis of the RBMs presented here, since the observed Raman RBM peaks change with incident laser wavelength.

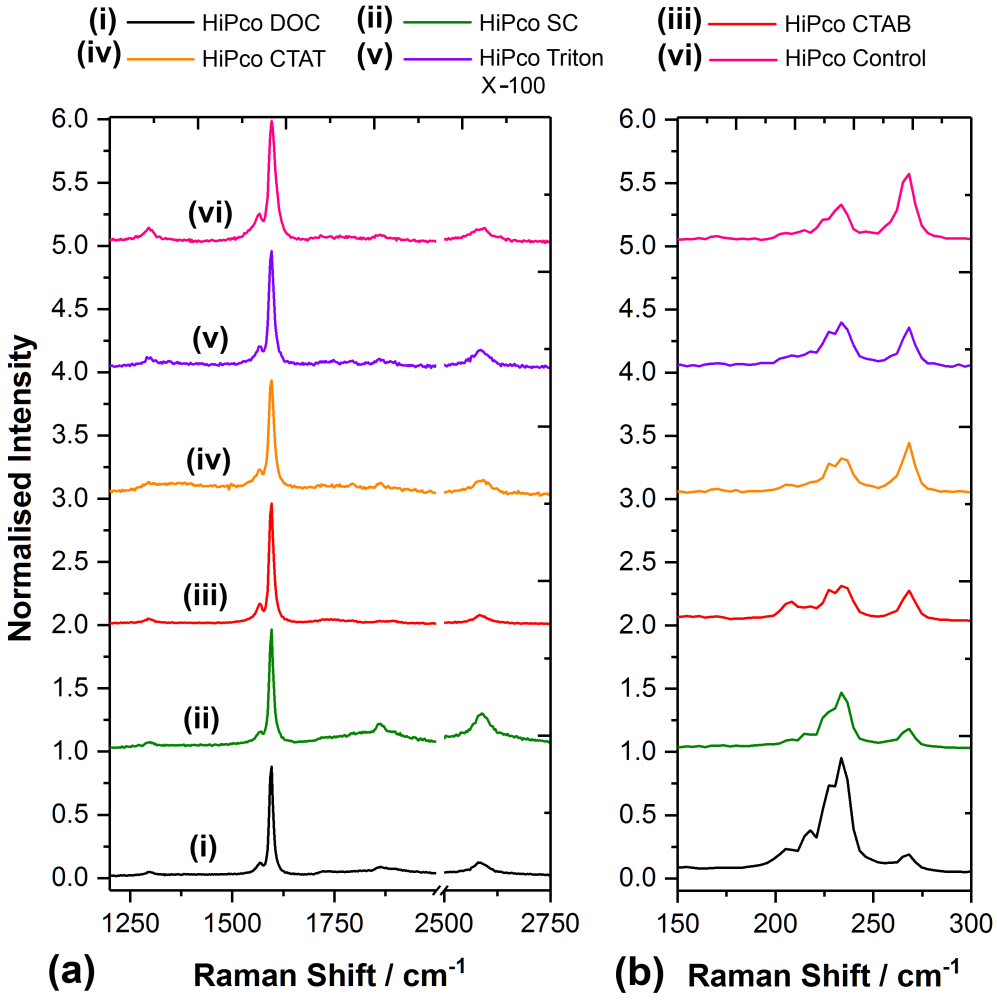

Figure 6.1: Raman spectroscopy was performed using a Renishaw inVia Raman microscope with a laser of wavelength λ = 785 nm at 1 mW power. (a) Raman spectra of the HiPco SWCNT networks containing anionic surfactant (i) DOC (G/D = 18.8) and (ii) SC (G/D = 13.4), cationic surfactant (iii) CTAB (G/D = 19.77) and (iv) CTAT (G/D = 7.02), non-ionic surfactant (v) Triton X-100 (G/D = 8,84), and no surfactant (vi) control (G/D = 6.875) showing the G-band (1594 cm^{-1}), D-band (1295 cm^{-1}) and G′-band (2600 cm^{-1}). (b) The radial breathing modes (RBMs) in the range 100 cm^{-1} to 300 cm^{-1} corresponding to nanotubes of different chirality for each aforementioned sample. Plots are y-offset for clarity.

However, UV-Vis analysis from Chapter 4 Figure 3.3 suggests the number of metallic to semiconducting SWCNTs in all of the surfactant functionalised samples remains constant. This would suggest that the changes in the RBM intensities, and thus the SWCNT chirality distribution, should not affect the overall gas sensing

responses observed described later in the study, though this can not be completely ruled out.

UV-Vis was also used in the current study to study confirm the presence of m-SWCNTs and sc-SWCNTs in the sensing films and indicate the reliability of the assumption that repeated depositions using the Eppendorf pipette resulted in approximately the same amount of carbon on the substrate. Figure 6.2 shows the measured absorbance of multiple layers of HiPco DOC SWCNT solution deposited and dried sequentially on a quartz slide. The absorbance increases linearly after repeated depositions of solution and thus the number of SWCNT present in the deposited films was assumed to be approximately constant for identical devices. As in Chapter 4 Figure 3.3, the peaks in the 400 nm to 800 nm range suggest a mixture of m-SWCNTs and sc-SWCNTs are found within the network [58].

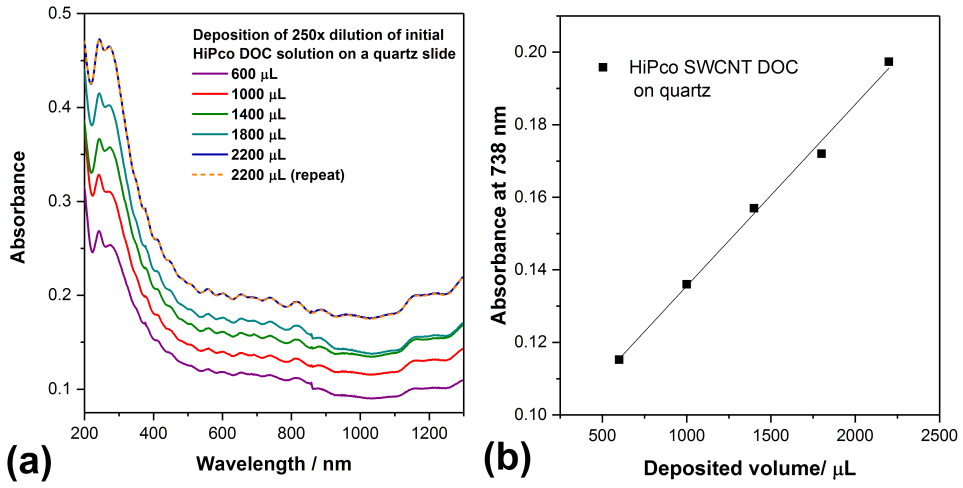

Figure 6.2: (a) UV-Vis-NIR absorption spectra obtained using an Elmer Lambda 950 spectrophotometer for HiPco SWCNTs non-covalently functionalised with DOC, deposited from an aqueous solution on to a quartz slide using and Eppendorf pipette and dried. 400 μL of solution (diluted by 250 X from the initial concentrated solutions) was deposited successively after each drying and measurement cycle, so that the total amount of solution deposited on the quartz slide ranged from 600 to 2200 μL from the first to last step. (b) Linear increase in absorbance per 400 μL deposition.

The sensing responses of SWCNT-based chemiresistors are expected to cor-

relate with the conductive properties of SWCNT network devices [280, 111, 245]. Current-voltage (I-V) characterisation of the SWCNT networks was used to investigate how functionalisation and film thickness affects the measured DC conductance across the SWCNT films.

In Figure 6.3, a non-linear relationship was observed between measured device conductance (resistance) and the mass of carbon deposited between the gold electrodes on the 3 x 3 alumina substrate. This relationship has been reported previously [281] and is due to a minimum number of nanotubes being required for conduction across the network, described by percolation theory [282]. Conductive films formed for HiPco SWCNTs contain nanotubes of mixed electronic type (i.e metallic or semiconducting). Below a minimum threshold density of carbon nanotubes in the film, there are few metallic pathways that bridge the electrodes, thus the conductance (resistance) measured across the film is low (high). As the density of carbon nanotubes in the film is increased, the likelihood of a complete conductive pathway increases. The minimum density (or number) of carbon nanotubes in the film is known as the minimum percolation threshold, above which conduction (resistance) across the film increases (decreases) exponentially to a plateau as more nanotubes are added to the network [282].

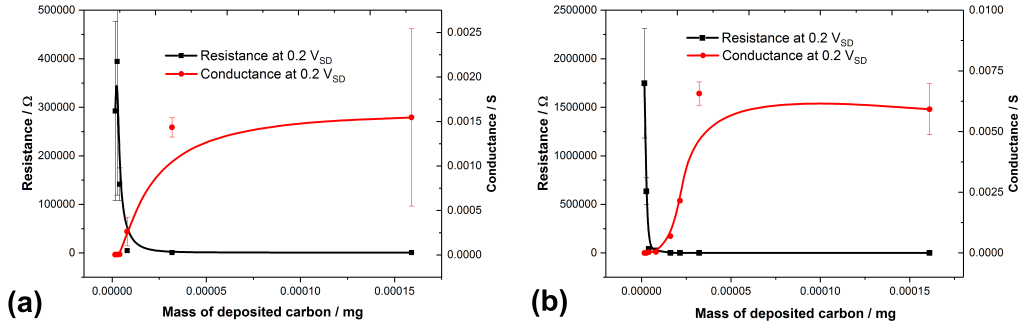

Figure 6.3: A Keithley 4200 semiconductor characterisation system was used to measure the DC (■) resistance and (●) conductance across the source and drain electrodes for (a) HiPco DOC and (b) HiPco CTAB devices for a given amount of carbon deposited between the gold electrodes on the device, with a 0.2 V bias applied. The error bars represent the standard deviation in the measurement between two identical devices.

This relationship is further elucidated by Figure 6.4, in which multiple SWCNT solution depositions of a known concentration were made on the device substrate, with the I-V characteristics recorded after each deposition and drying step. The conductance increases rapidly after a number of layers are deposited across the gold electrodes in a non-linear fashion. Therefore, the sensing responses of nanotube films are expected to vary between dense and sparse networks of SWCNTs, since the conductance across the film is dominated by metallic SWCNTs in the case of the former, or semiconducting nanotubes in the latter [83].

Percolating behaviour is observed for SWCNTs functionalised with both DOC and CTAB, indicating that it is a general feature of the SWCNT networks used in this study and others [283, 281]. The error bars in Figures 6.3 and 6.4 represent the standard deviation between two identical devices of the same functionalisation, demonstrating that the percolating nature is consistent between devices. The conductance across the films varies somewhat with the surfactant used to obtain homogeneous solutions of SWCNTs, since the effectiveness of the dispersing agent and thus the SWCNT concentration of the deposited solution varies.

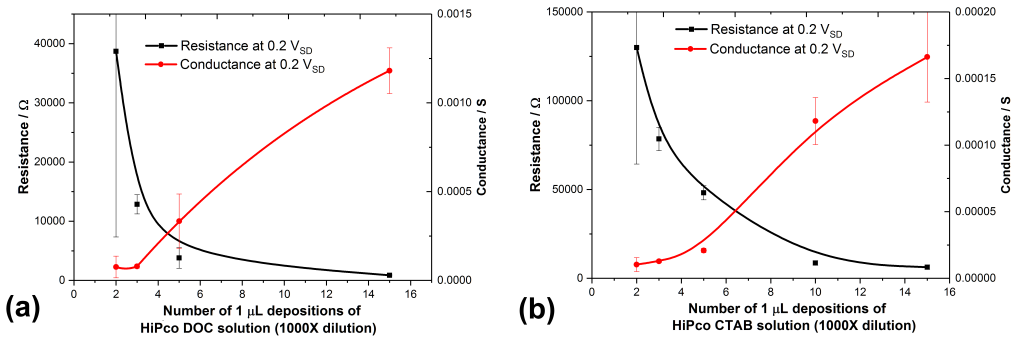

Figure 6.4: A Keithley 4200 semiconductor characterisation system was used to measure the DC (■) resistance and (●) conductance across the source and drain electrodes for (a) HiPco DOC and (b) HiPco CTAB devices as a function of the number of layers (1 μL depositions) of SWCNT solution made across the gold electrodes, with a 0.2 V bias applied. The ×1000 diluted solutions (from aqueous stock solution) of DOC and CTAB functionalised SWCNTs were of concentration 0.00159 ± 0.0002 mg mL^{-1} and 0.00161 ± 0.0002 mg mL^{-1} respectively. The error bars represent the standard deviation in the measurement between two identical devices.

As techniques to improve SWCNT sample heterogeneity are developed, it may be possible to generate a calibration plot of determined solution concentration *vs* measured film conductance to determine the density of nanotubes in a deposited film of fixed area, solely from I-V characterisation. Such a technique would be advantageous for fast and scalable characterisation of devices fabricated from SWCNT solutions.

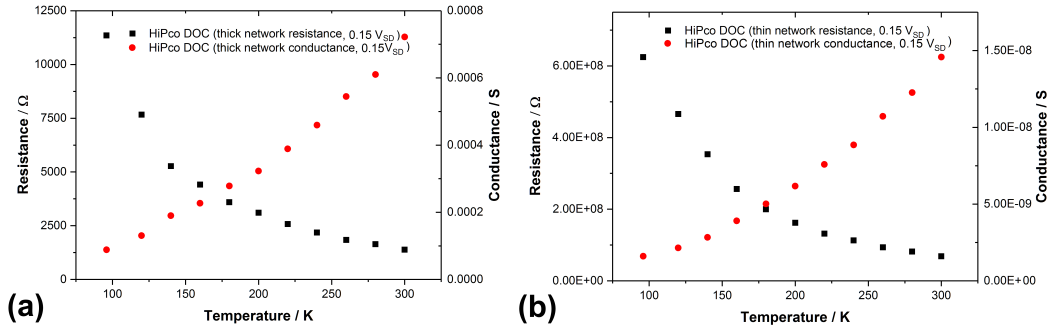

Figure 6.5: The DC (▪) resistance and (●) conductance across the source and drain electrodes of (a) a thick HiPco DOC device formed from a solution of 1.59 ± 0.2 mg mL^{-1} concentration and (b) a thin HiPco DOC device formed from a solution of 0.0108 ± 0.001 mg mL^{-1} concentration as a function of temperature (K). Data was collected by Zak Kobos of the Reed group, Yale, using a semiconductor analyser system and a cryostat setup utilising liquid nitrogen and an inbuilt heater to control the temperature of the device in the 96 K to 300 K temperature range.

The measurement of SWCNT film conductance as a function of temperature can help to reveal the mechanism for conduction across a SWCNT network [140, 246, 284]. Previous studies, such as those by Masel *et al*, have suggested that the sensing properties of SWCNT-based devices are correlated with the dominant SWCNT conduction mechanism [280]. For the current study, electronic transport measurements were obtained by Zak Kobos of the Reed group, Yale, using a semiconductor analyser system to obtain the I-V characteristics of the HiPco DOC SWCNT devices and a cryostat setup to control the temperature of the device in the 96 K to 300 K temperature range.

Figure 6.5 displays the measured conductance (resistance) across both thick and thin DOC functionalised HiPco SWCNT networks used in this study *vs* device

temperature. The conductance (resistance) increases (decreases) as a the temperature increases, suggesting that the semiconducting nanotubes in the film contribute significantly to the conductance across the network.

Many previous studies have investigated the conduction mechanisms responsible for charge transport in SWCNT networks [202, 285]. The conclusions from the data presented in the literature vary considerably depending on the nanotube sample type and film thickness [246, 285]. Three dimensional variable-range hopping (3D-VRH) [199, 200], fluctuation-assisted tunnelling (FAT) [201, 202], Schottky [134, 203] and Poole-Frenkel conduction [197, 204, 205] have been suggested as possible conduction mechanisms for SWCNT network films in the literature.

The data presented by Shiraishi *et al.* [285] for thin SWCNT mats is consistent with the results presented in Figure 6.5, as well as those investigated by Kaiser *et al.* [286]. These studies concluded that 3D-VRH is responsible for conduction in thin SWCNT films. However, Jombert *et al.* attributed conduction in their surfactant functionalised thin films of SWCNTs (similar to those in the current study) to Poole-Frenkel conduction, whilst indicating they could not completely rule out 3D-VRH. Massey *et al.* [205] also attributed conduction to the Poole-Frenkel mechanism, but whilst the thin films of sc-SWCNTS did not contain any surfactant, their results are consistent with those presented here.

Without further experimental investigation, it is therefore difficult to categorically assign a conduction mechanism to the DOC functionalised networks in the current study. However, the data suggest that both metallic and semiconducting SWCNTs contribute to conduction through the network, which is expected to influence the SWCNT- based device characteristics [134].

After characterisation of the sensing element, an experimental investigation into the dependency of the SWCNT network NO_2 gas sensing characteristics on atmospheric humidity levels was conducted, as is now introduced.

6.3.2 Conductive responses to NO_2 in humid conditions

The influence of pre-adsorbed water vapour on SWCNT conductive responses to NO_2 was investigated by performing gas sensing experiments whilst maintaining

set levels of constant background humidity in the testing chamber. From Figure 6.6, it is clear that the conductive responses from the control, DOC and CTAB functionalised networks to NO_2 are altered as the humidity of the testing chamber is increased.

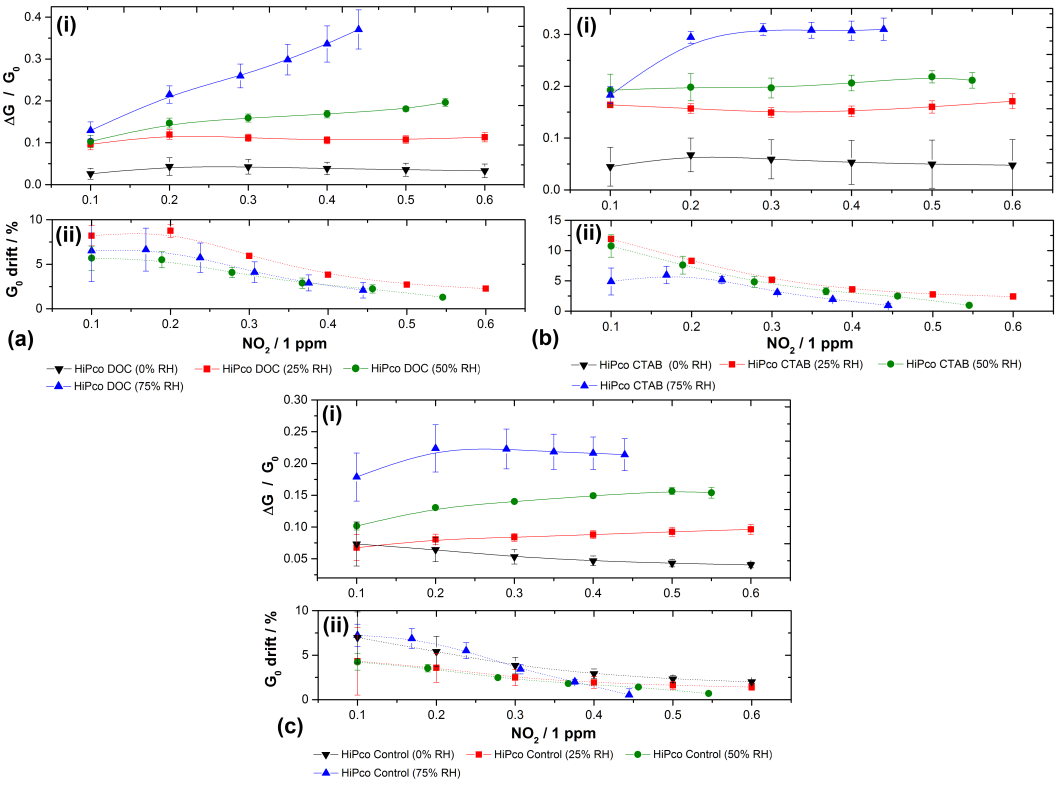

Figure 6.6: The (i) conductive responses of thin film (a) HiPco DOC, (b) HiPco CTAB and (c) HiPco control devices to NO_2 gas in the 0.1 ppm to 0.6 ppm concentrations at 0%, 25%, 50%, and 75% atmospheric relative humidity. (ii) The corresponding drift after each injection of NO_2 as a % of the conductance before each pulse.

Figures 6.7, 6.8 and 6.9 show examples of the real-time conductive response curves for the control, the DOC and CTAB functionalised SWCNT sensors, in which the conductive responses are larger in more humid conditions. The larger responses may be related to the impact that water-assisted desorption has on the number of available, unoccupied adsorption sites.

As detailed in Chapter 5, introducing water vapour to the surface of a SWCNT-based chemiresistor increases the rate of NO_2 desorption from previous exposures.

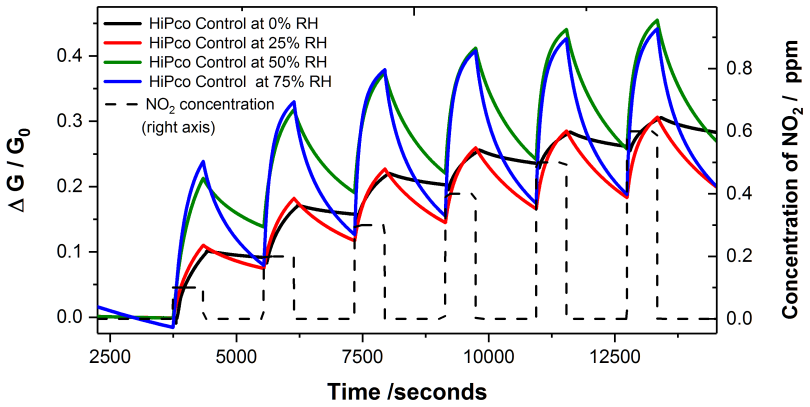

Figure 6.7: The real-time conductive responses of the thin film HiPco control sensors to concentrations of NO_2 in the 0.1 ppm to 0.6 ppm range (indicated by the right axis) at different levels of background relative humidity. The NO_2 pulses were 600 s in duration followed by a recovery period of 1200 s in air, with constant chamber humidity maintained at 0%, 25%, 50% or 75%.

This may explain why larger relative changes in conductance are observed in humid atmospheres throughout the NO_2-humidity experiments; the initial sensor surface is "cleaner" (i.e there are more unoccupied interaction sites available) in experiments with a higher background RH, due to increased desorption of NO_2 strongly pre-adsorbed to the SWCNT surface.

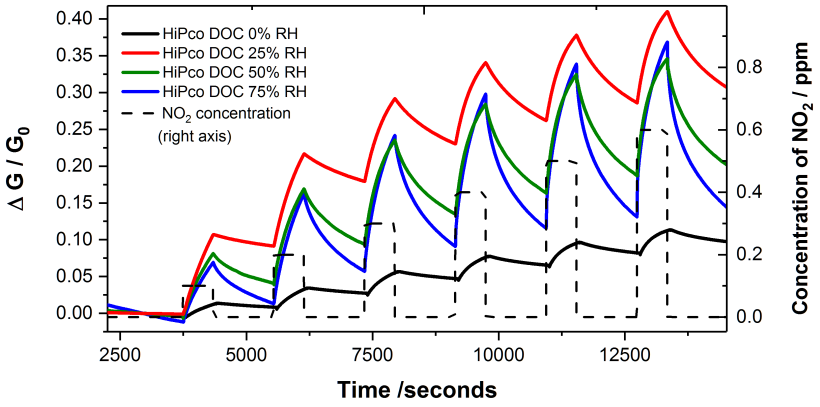

Figure 6.8: The real-time conductive responses of the thin film HiPco DOC sensors to concentrations of NO_2 in the 0.1 ppm to 0.6 ppm range (indicated by the right axis) at different levels of background relative humidity. The NO_2 pulses were 600 s in duration followed by a recovery period of 1200 s in air, with constant chamber humidity maintained at 0%, 25%, 50% or 75%.

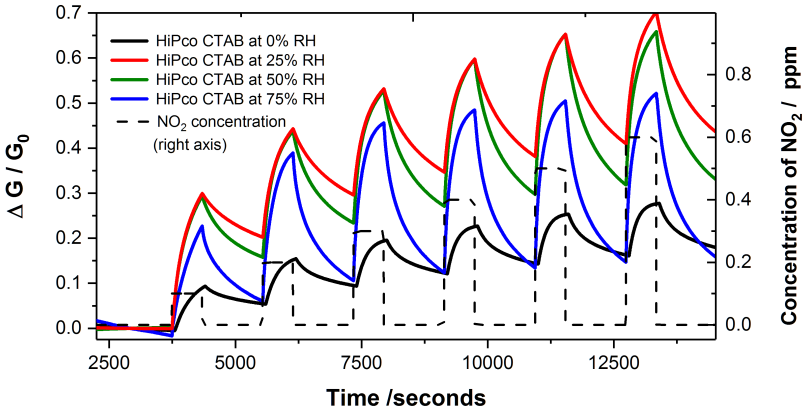

Figure 6.9: The real-time conductive responses of the thin film HiPco CTAB sensors to concentrations of NO_2 in the 0.1 ppm to 0.6 ppm range (indicated by the right axis) at different levels of background relative humidity. The NO_2 pulses were 600 s in duration followed by a recovery period of 1200 s in air, with constant chamber humidity maintained at 0%, 25%, 50% or 75%.

A second explanation could be that the pre-adsorbed water acts as an auxiliary NO_2 adsorption site, thus increasing the number of total available interaction sites, $T\theta$, which would increase the conductive response at a certain concentration as per equation 5.8 and 5.9 in Chapter 5.

Surface reactions may also take place, mediated by the adsorbed water. Randeniya *et al.* proposed that HONO and HNO_3 could be formed from adsorbance of NO_2 to moist SWCNTs [105], based on previous studies:

$$2NO_2 + H_2O \rightarrow HONO + HNO_3 \tag{6.1}$$

with the formation of HNO_3 and NO also possible [287]:

$$3NO_2 + H_2O \rightarrow 2HNO_3 + NO \tag{6.2}$$

Different analytes on the surface would then induce sensing responses of different magnitudes in subsequent interactions with the SWCNTs [287].

Along with the clear increase in response magnitude, a decrease in drift relative to the initial baseline conductance (G_0) is observed after consecutive pulses of NO_2, shown in Figures 6.7, 6.8 and 6.9. This is due to an increase in desorption

rate; more NO_2 is desorbed after each pulse and the signal moves further towards baseline conductance in the 1200 second recovery period. The effect of atmospheric humidity on the adsorption/desorption rates are further discussed in section 6.3.3.

The origin of drift in SWCNT chemiresistors as well as other nanomaterial based sensors operating at room temperature is often attributed to a number of factors [288]. Signal drift is sometimes refereed to as "poisoning" of the sensor [162], as it can be due to the formation of strongly bound bi-products of surface reactions, or due to stronger chemisorption at impurity sites in the sensing material [289]. As well as a drift in conductance relative to G_0 as discussed previously, a percentage change in the signal drift (ΔG_{drift}) between pulses of gas could indicate that a different type of adsorption site is responsible for the drift in the baseline signal.

Figure 6.6 shows that the drift between pulses (ΔG_{drift}) initially decreases towards a constant value as the testing proceeds, suggesting that whatever the source of the drift may be, it's capacity to affect the baseline conductance of the SWCNT network decreases to a constant value as the number of impinging molecules increases. This is potentially consistent with the availability of two types of NO_2 adsorption site on the SWCNT surface, with different associated affinities for the target analyte and desorption constants, as has been previously proposed [15, 289, 75]. This would also explain why a certain percentage of the baseline conductance is recovered quickly (within 60 s), and the remainder is associated with a much longer recovery time (>12 hours, as discussed in Chapter 5).

Even if the drift was due to a surface reaction bi-product (such as those described in equations 6.1 and 6.2), it still appears to be limited by the availability of a different type of interaction site, since the conductive response magnitudes to NO_2 are still able to increase with concentration (e.g type 1 reaction sites are unsaturated) yet the drift does not (e.g type 2 reaction sites are saturated).

Identifying the potential sources of the drifting baseline signal is useful, as in the future it may be possible to limit drift through purification of the sensing material or *via* an appropriate passivation treatment.

For reliable, repeatable results, it is important to ensure that the sensor base-

line signal is stable before performing experiments, as this is when the pre-adsorbed gases (other than water vapour) are removed to the maximum extent possible using WAR. This will permit the largest conductive response to be achieved (maximising the number of available gas interaction sites), as well as more accurate determination of the target analyte concentration.

6.3.3 Response and recovery rates

Figures 6.7, 6.8 and 6.9 show that in the current study, the NO_2 adsorption and desorption rates are influenced by the relative humidity of the testing chamber. This is the case for the control, DOC and the CTAB functionalised SWCNT networks.

Lee *et al.* set out a procedure in ref [287] in which they approximate the initial conductive response rate of HiPco SWCNT sensors to be linear (a valid approximation in the current study, as shown in Figure 6.10). Applying this method to the current study for the initial 60 seconds of exposure to NO_2, Figure 6.11 demonstrates the change in conductive response ΔS per second for six SWCNT-based chemiresistors both non-functionalised and functionalised with surfactant. The analysis suggests that the initial rate of conductance change is dependent on both NO_2 concentration (in the 100 ppb to 600 ppb range), and the RH of the sensing environment (0% to 75% RH).

For comparison, the same fitting procedure adopted for the partially reversible adsorption model [15] as described in section 5.3.5 was applied to the response curves for 300 ppb NO_2 at 25%, 50% and 75% RH. Using this method, the entire conductive response curve can be modelled (as oppose to the initial 60 seconds of response) by dividing it into two components as indicated by equation C.5, corresponding to reversible and irreversible adsorption with different respective adsorption/desorption constants. These constants are then quantified to reveal changes in the surface adsorption behaviour at different levels of atmospheric humidity.

Figure 6.12 displays the average time required for the SWCNT sensor conductances to reach 50% of the maximum possible change in conductance ($t_{1/2}$) upon exposure to 300 ppb of NO_2 at different RH for the (a) reversible and (b) irreversible components of the response. In general, the higher the relative humidity,

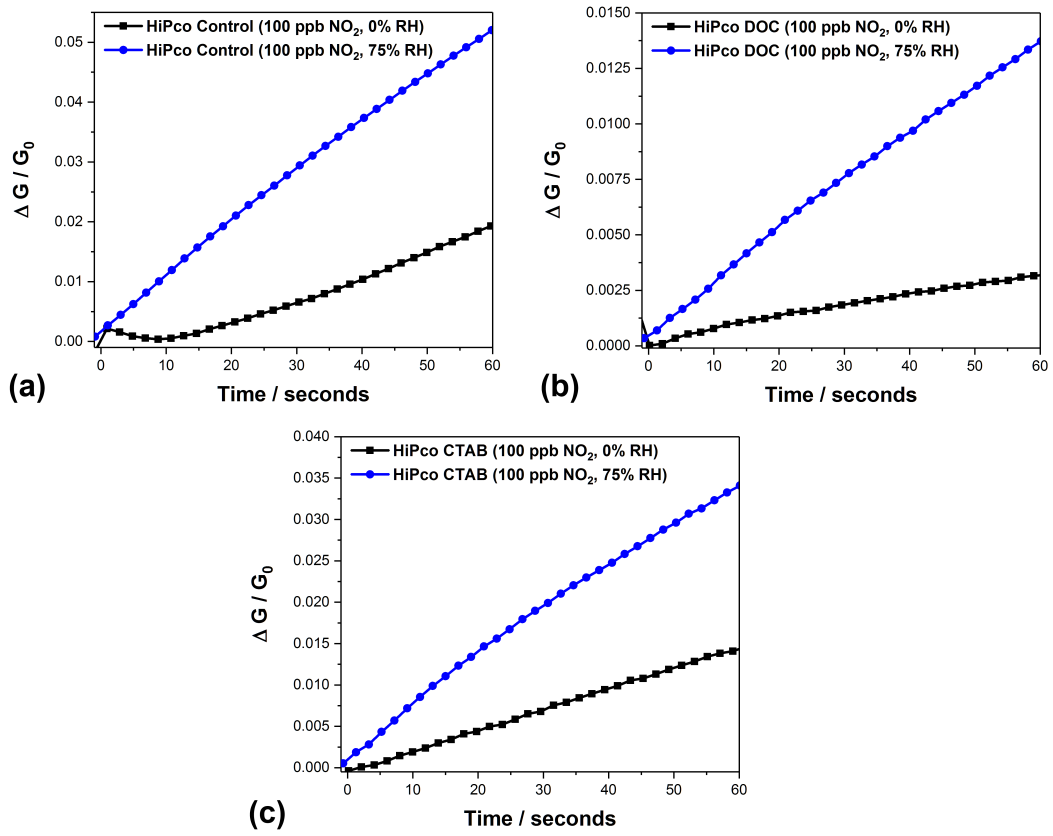

Figure 6.10: The approximately linear conductive responses in the initial stages of exposure (first 60 s) to 100 ppb of NO_2 gas at (▪) 0% and (•) 75% relative humidity for (a) HiPco control networks, (b) HiPco DOC networks and (c) HiPco CTAB networks.

the more quickly the reversible and irreversible components reach saturation for the control, DOC and CTAB functionalised networks as shown in Figure 6.12a and b, corresponding to larger adsorption constants $k_{reversible}$ and $k_{irreversible}$ at higher RH.

The $t_{1/2}$ reversible and irreversible values displayed in Figure 6.12 are averaged over two identical devices for each sensor type studied (thin film HiPco control, HiPco DOC and HiPco CTAB), with the error bars representing the standard deviation between $t_{1/2}$ values. Although in some cases standard deviation (error bar) overlap was present for the $t_{1/2}$ times at 50% RH with those at either 25% or 75% RH, a statistically significant decrease was always observed when considering the entire RH range (e.g between $t_{1/2}$ times at 25% and 75% RH) across all of the sensor types studied. This suggests that an increase in atmospheric humidity causes

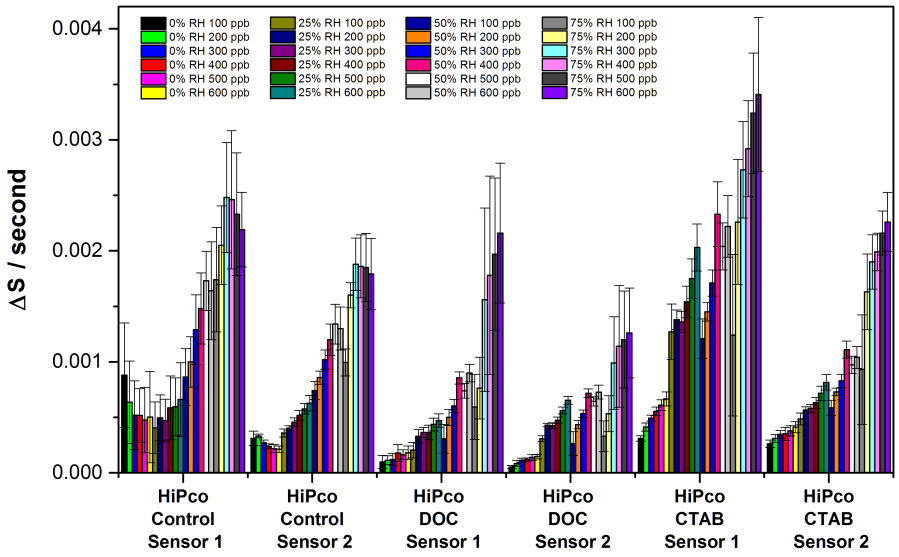

Figure 6.11: The change in conductive response ΔS s^{-1} for the initial 60 s of exposure to NO_2 in the 100 ppb to 600 ppb range at either 0%, 25%, 50% or 75% background relative humidity. The rates are displayed for 6 HiPco thin film sensors with functionalisation as indicated. The error bars represent the standard deviation in the measured rates over two experiments.

a general increase in the response rates of SWCNT-based chemiresistors to NO_2.

The model developed by Kumar *et al.* can also be used to visualise the proposed reversible and irreversible components of the experimental NO_2 conductive response curve (described in ref [15], this procedure is explained and validated with data from the literature in appendix C). Figure 6.13 demonstrates how the proportions of each modelled component vary as the SWCNT network is exposed to 300 ppb NO_2 at (a) 25% RH and (b) 75% RH. Using data from the HiPco control sensors and a modelled response, the reversible component of the conductive response increases as the atmospheric humidity of the testing chamber is increased, suggesting that more reversible adsorption takes place at higher relative humidity on the SWCNT networks.

In a similar study of NO_2 adsorption rates in humid atmospheres, Lee *et al.* also observed a decrease in time constants for moist SWCNT sensors [287]. This was attributed to reaction products from the adsorption of NO_2 to a H_2O covered surface. Further to this, the pre-adsorbed H_2O could potentially increase the total

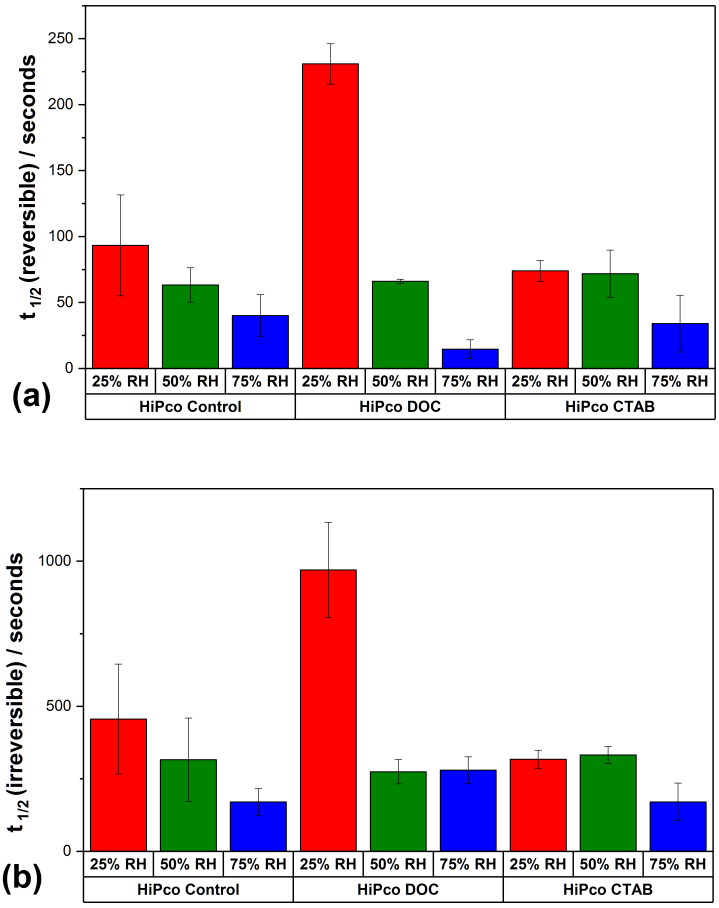

Figure 6.12: The average time required for the SWCNT sensor conductances to reach 50% of the maximum possible change in conductance ($t_{1/2}$) upon exposure to 300 ppb of NO_2 for 600 s at 25%, 50% and 75% background relative humidity for the (a) reversible and (b) irreversible components of the response, extracted using the partially reversible adsorption model [15]. The error bars represent the standard deviation between times calculated for two identical devices.

number of available adsorption sites ($T\theta$) or alter the balance between reversible and irreversible adsorption sites (articulated in Figure 6.13) through occupation of the latter, influencing the response rate.

Finally, although some difference in curve shape is observable in Figures 6.7, 6.8 and 6.9, the $t_{1/2}$ values for the reversible and irreversible components remain reasonably constant across all devices, suggesting the degree of surfactant functionalisation used in the current study does not drastically influence the NO_2 adsorption rates for the SWCNT networks.

In Figures 6.7, 6.8 and 6.9, improved recovery of the SWCNT network baseline

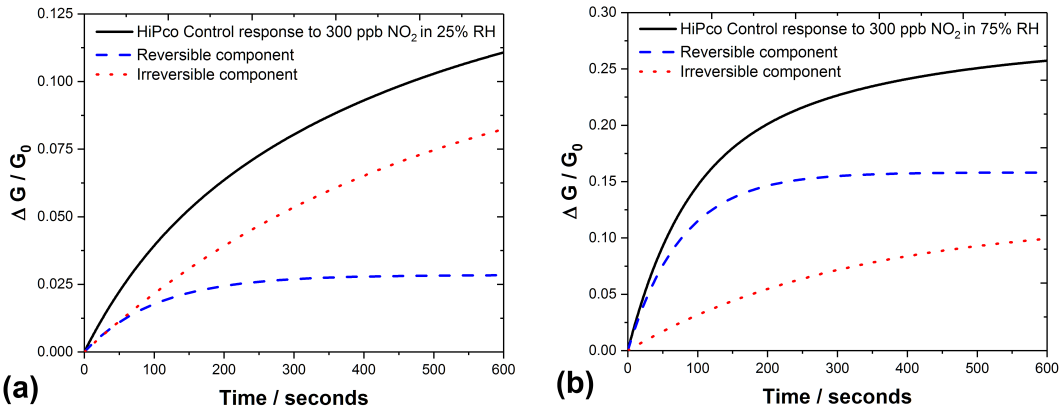

Figure 6.13: A visualisation of the proposed (dash) reversible and (dot) irreversible components of the experimental NO_2 conductive response curve, based on real data for the HiPco control sensor exposed to 300 ppb of NO_2 at (a) 25% background relative humidity and (b) 75% background relative humidity. The components are based on the application of the partially reversible adsorption model developed in ref [15] and detailed in Chapter 5 section 5.3.5.

conductances was observed throughout the signal recovery period as the humidity of the testing chamber was increased, especially in comparison with the testing performed at 0% RH. This is consistent with an increased rate of NO_2 desorption in humid atmospheres, observed using water-assisted regeneration elsewhere [145, 105] and in Chapter 5. To quantify these changes, an analysis of the gas desorption dynamics was applied in line with the method used by Rigoni *et al.* [290]. The conductance recovery in the NO_2 desorption region at 300 ppb for different atmospheric humidities was fitted using a two-phase exponentially decreasing curve, with two time constants τ_1 and τ_2, associated with fast and slow desorption processes respectively (described previously in ref [290] and in appendix C).

The average time required for the SWCNT sensors to recover 50% of their initial baseline conductance in the recovery period for the fast and slow components of the curve (τ_1 and τ_2 half-life) is displayed in Figure 6.14 for 300 ppb of NO_2 at 25%, 50% and 75% RH. The time taken was averaged over two identical devices, with the error bars representing the standard deviation. In Figure 6.14a there is a clear trend showing a reduction in τ_1. There is statistical error overlap for some values of τ_1, for example between HiPco Control τ_1 half-life at 25% and 50% RH, which is due to device to device variation in SWCNT network parameters.

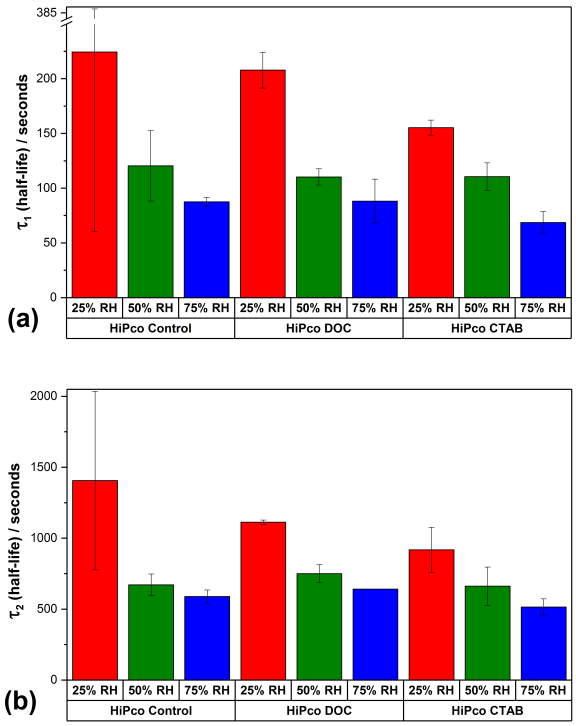

Figure 6.14: The average time required for the SWCNT sensors to recover 50% of their initial baseline conductance in the recovery period for the (a) fast and (b) slow components of the curve (τ_1 and τ_2 half-life) after exposure to 300 ppb NO_2 for 600 s with 25%, 50% or 75% background relative humidity. The data from the recovery period was fitted using a two-phase exponentially decreasing curve as by Rigoni *et al.* [290]. The error bars represent the standard deviation between times calculated for two identical devices.

Despite this, the statistically significant trend for the HiPco DOC and HiPCo CTAB sensors in Figure 6.14a corresponds to a quicker baseline recovery rate for the fast desorption component of the curve. Similarly, a decrease in the τ_2 half-life for all of the sensor types in Figure 6.14b represents a faster baseline recovery for the slow desorption component of the conductance curve when the relative humidity of the testing chamber is at a higher value. The smaller time constants τ_1 and τ_2, taken from the recovery region of the sensing curve after exposure to 300 ppb of NO_2, again suggest that the NO_2 desorption rate is increased with increasing atmospheric humidity.

In a recent investigation by Rigoni *et al*, the effects of atmospheric humidity on functionalised SWCNT sensor responses to NH_3 were studied [290]. The sen-

sitivity to NH_3 was increased in a testing environment in which humidity levels were raised, enabling sub-ppm detection of NH_3. However, the study did not report any variations in the NH_3 adsorption or desorption kinetics. Contrary to this, Lee *et al.* observed that the recovery constant was reduced for HiPco networks when exposed to 2 ppm NO_2 at high humidity (RH = 92%) [287], in line with the current study. This suggests that the effect of humidity on SWCNT network gas desorption dynamics is analyte dependent, potentially due to the different associated binding affinities involved.

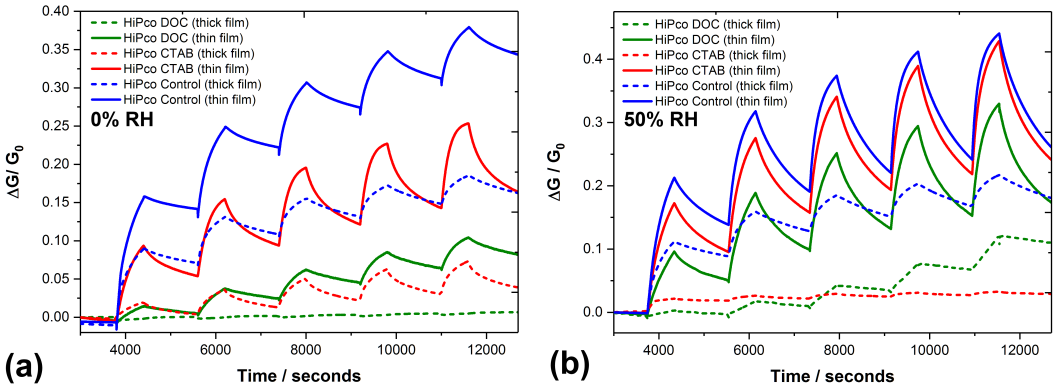

Figure 6.15: The real-time conductive responses for the thin film (solid line) and thick film (dashed line) HiPco sensors to concentrations of NO_2 in the 0.1 ppm to 0.5 ppm range (indicated by the right axis) at (a) 0% RH and (b) 50% RH. different levels of background relative humidity. The NO_2 pulses were 600 s in duration followed by a recovery period of 1200 s in air, with constant chamber humidity maintained at (a) 0%, or (b) 50%.

6.3.4 Thickness dependent responses

In previous sections, it was suggested that conduction across SWCNT networks (and thus sensing response) is dependent on the percolation of nanotubes in the film. In the current study, thick (19 ± 5 μm and a device resistance of R_{thick} = 200 Ω to 500 Ω) and thin (< 1 μm and a device resistance of R_{thin} = 50 kΩ to 200 kΩ) SWCNT network sensing response magnitudes were found to differ towards NO_2 in both dry and humid conditions.

As displayed in Figure 6.15, devices fabricated from thinner networks of SWCNTs typically provided a larger conductive response to NO_2 gas. There are

two potential explanations for this phenomenon. Firstly, for the thin films, a larger fraction of the SWCNT network may interact with the target gas, as less diffusion is required through the sensing layer to reach all of the potential gas adsorption sites. Therefore, a faster rate of total network conduction change is observed, resulting in a larger response magnitude for a certain time interval than the devices with a thicker sensing layer.

Secondly, it is possible that conduction through the thinner devices is more dominated by sc-SWCNTs. As sensitivity to the target gas is reportedly increased with a higher percentage of sc-SWCNTs in the gas sensitive layer [76], this may be the source of the different response magnitudes observed for the thin film devices. Higher sensitivity of sc-SWCNT enriched chemiresistive devices has also recently been reported by the Swager group [291], in line with such an explanation.

6.4 Conclusion

Variations in atmospheric humidity levels were found to impact upon the NO_2 sensing responses of both functionalised and non-functionalised SWCNT networks. Larger conductive responses were observed to NO_2 as the humidity of the testing chamber was increased, with possible mechanisms for this increase including additional adsorption sites at surface bound H_2O, reaction products *via* adsorption of NO_2 to wet SWCNTs, or the process of water-assisted desorption generating a SWCNT array that is free from previously adsorbed analytes.

An increase in the initial (first 60 seconds of the response) NO_2 adsorption rate was observed in more humid environments. Modelling of the responses in their entirety enabled the extraction of two adsorption constants associated with reversible and irreversible adsorption processes on the sensor surface, as suggested by the partially reversible adsorption model [15]. The rate of NO_2 adsorption was found to increase for these components when experimental testing was performed in a more humid atmosphere. It is possible that the increase in adsorption rate is caused by similar mechanisms as proposed for the increase in response magnitude;

additional adsorption sites, secondary reaction products, or a "cleaner" SWCNT surface due to water-assisted regeneration.

The partially reversible adsorption model, developed by Kumar *et al*, enabled satisfactory fitting of the response curves for individual sensors and the extraction of adsorption/desorption parameters. Changes in these parameters were qualitatively consistent across multiple devices of the same functionalisation. However, due to device to device variations in this study, the model is not able to quantitatively predict k or S_{max} without analysing the curves for each individual sensor. For the model to provide an accurate prediction of these quantities for any general SWCNT-based chemiresistor, variation in the sensing characteristics between identical devices must be reduced *via* improved fabrication procedures. De-convolution of the conductive response curves to reversible and irreversible adsorption components suggested that more reversible *vs* irreversible adsorption takes place in more humid conditions.

Faster recovery of the baseline conductance was achieved when the SWCNT networks were exposed to NO_2 at higher levels of background humidity. A trend for increasing rates of NO_2 desorption was consistent with a change in the desorption constants, derived from analysis of the recovery region of the sensing curves. This could be linked to a change in the proportion of reversible *vs* irreversible sites on the SWCNTs, as indicated by fitting the partially reversible NO_2 adsorption model to the data, due to pre-adsorbed H_2O. The increased rate of NO_2 desorption was in agreement with the results reported in Chapter 5, in which the presence of water vapour in the sensing environment aided the desorption of NO_2 and the recovery of the baseline signal.

Thinner SWCNT networks displayed larger responses to NO_2 in both dry and humid atmospheres. It was suggested that this result could be due to better access of the target analyte to a higher proportion of SWCNTs in the thin films, or to an increased conduction contribution from sc-SWCNTs which possess higher gas sensitivity.

The general changes in sensing characteristics when testing was performed

at different levels of background relative humidity were apparent for all of the SWCNT-based chemiresistive devices studied, regardless of functionalisations. As such, when developing SWCNT sensors for real world environmental monitoring applications, the calibration or design of the measurement setup must compensate for the humidity effects observed in this study.

Chapter 7

Study IV: Reducing cross-sensitivity of SWCNT networks to water vapour using zeolites.

The work in this chapter was published in *ACS applied materials & interfaces*. I conceptualised the study, carried out the experimental investigations, performed the analysis and wrote the manuscript. Dr. D. J. Buckley and Dr. A. L. Adedigba assisted with the sample preparation and interpretation of the materials characterisation data. Prof. G. Sankar, Prof. N. T. Skipper and Prof. I. P Parkin proof read the manuscript and contributed experimental guidance. The paper is appended to this thesis in appendix E.

Associated Publications: Evans, G. P., Buckley, D. J., Adedigba, A. L., Sankar, G., Skipper, N. T., & Parkin, I. P. (2016). Controlling the Cross-Sensitivity of Carbon Nanotube-Based Gas Sensors to Water Using Zeolites. *ACS applied materials & interfaces*, 8(41), 28096-28104.

7.1 Introduction

As detailed in Chapters 4, 5 and 6, the electrical conductance of a single-walled carbon nanotube (SWCNT) network is sensitive to the adsorption of a wide range of gases and vapours[7, 17], including H_2O and NO_2. Non-functionalised control

sensors, or devices fabricated using surfactant functionalised SWCNTs, displayed a sizable increase or decrease in conduction upon exposure to H_2O vapour, as well as changes to NO_2 adsorption kinetics and response magnitudes in humid *vs* dry atmospheres. Water-induced conductance changes may be much larger than the typical increase in SWCNT network conductance observed when a sensor is exposed to low concentrations of NO_2 gas. Therefore, any variation in the relative humidity of the operating environment can mask and obscure the sensing response (S) of a SWCNT sensor to NO_2.

As such, a SWCNT-based NO_2 sensor with minimal sensitivity to varying levels of humidity would be desirable for environmental monitoring applications. In this chapter, zeolites, also known as molecular sieves due to their selective adsorption properties, are used to control the cross-sensitivity of SWCNT-based sensors to water vapour. The most extreme case is studied, in which the relative humidity of the testing chamber is altered at the same time as injection of the target gas, mimicking rapid changes in atmospheric humidity levels in real-world environments.

Zeolites incorporated into the sensing layer are found to reduce interference effects that would otherwise obscure the identification of NO_2 gas. The incorporation of zeolite layers decreases sensitivity to H_2O vapour, with sensors maintaining an increase in conduction upon exposure to 10 parts per million (ppm) of NO_2 gas with varying levels of relative humidity. Conversely, the control SWCNT sensors demonstrate a decrease in network conduction under the same test conditions, with the normal sensing of NO_2 obscured by the presence of H_2O vapour in the test chamber.

The zeolites are either deposited over the SWCNT network as a top layer, or SWCNTs are deposited over the zeolite to form a percolating network in a mixed layer. The ordering of the sensing layer is found to greatly affect the sensor response observed to NO_2 in both dry air and humid conditions, with the mixed layer arrangement providing a larger response magnitude.

7.2 Experimental

7.2.1 Device fabrication

High pressure carbon monoxide disproportionation (HiPco) produced SWCNTs [137] (purchased from Nanointegris, batch number: R1-831) were dried in air at 120°C to remove moisture from the bundles and stored under vacuum. The black powder was added to a solution of deuterated water (D_2O, CAS Number: 7789-20-0, Sigma-Aldrich) and sodium deoxycholate (2 wt% , DOC, CAS Number: 302-95-4, Sigma-Aldrich) at a concentration of approximately 0.5 mg ml^{-1}. DOC is a surfactant molecule that forms micelle like structures around the nanotubes[212]. To aid efficient solubilisation via surfactant wrapping, the solution was sonicated using a 225 W tip sonication probe for 15 minutes, with the container placed in an ice bath for cooling.

The well dispersed solution was centrifuged at 4000g for 30 minutes and the upper 80% of the supernatant was decanted to limit the presence of carbonaceous impurities in the final dispersion.

Hydrophilic H-Zeolite-Y was obtained from Zeolyst international (product code: CBV600). Less hydrophilic Silicalite-1 was synthesised in house by the Sankar group (UCL) using the method described by Guth *et al.* [292]. Both zeolites were then dispersed in ethanol using a magnetic stirrer bar at a concentration of 0.2 g ml^{-1}.

As described in previous chapters, a 3 x 3 mm alumina tile with patterned gold electrodes of 175 μm separation (as shown in Figure 7.1) was used as the sensor substrate. A single strip (containing 5 individual substrates) was placed in a grooved metal holder (heated to 50 °C via hotplate) and the square gold connector pads were covered using a removable mask. The dispersion of HiPco SWCNTs was then deposited across the interdigitated gold electrodes for each of the 5 chips using a calibrated Finnpipette novus electronic single-channel micro pipette (drop volume 1 μL per sensor). The deposition was left to dry for in air for 15 minutes and the substrates were separated into individual chips. This process was repeated to produce 4 batches and 20 individual control HiPco SWCNT sensors.

For each type of top layer sensor, the aforementioned procedure was followed by an additional 1 μL deposition of the dispersed zeolite on top of the SWCNT network, with an extra drying step (Figure 7.1a). The mixed layer configuration was achieved by depositing the insulating zeolite over the gold electrodes in the same manner as before, drying and depositing 1 μL of the initial HiPco SWCNT solution over the zeolite to form a percolating mixed layer from which an electrical measurement could be made (Figure 7.1b).

The sensors were then dried in air in a furnace at 100 °C for 1 hour. Four of each sensor type (shown in Table 7.4) were selected from each batch and attached to sensor casings via micro welded platinum wire connections to the gold connector pads.

7.2.2 Material characterisation

A JEOL JSM-6700F field emission scanning electron microscope was used in secondary electron imaging mode to image the zeolite top layers and HiPco zeolite mixed layers using a 5 kV (or 10 kV) probe voltage at a working distance of 5.9 mm. Samples were gold coated for imaging.

Energy-dispersive X-ray spectroscopy (EDS) analysis was carried out using a JEOL JSM-6700F and a secondary electron image on a Hitachi S-3400N field emission instrument (15 kV) at a 15 mm working distance, with elemental weight % calculated using the Oxford Instruments INCA software package. Sensors were also gold coated whilst performing EDS measurements.

Transmission electron microscopy (TEM) was performed using a JEOL 200 kV transmission electron microscope in imaging mode. The zeolites were dispersed in ethanol and drop coated onto a holey carbon copper TEM gird for imaging.

A Renishaw inVia Raman microscope with laser wavelength 514.5 nm and 1 mW power was used to perform Raman spectroscopy on the surfactant wrapped HiPco DOC solution (deposited on a 3 x 3 alumina substrate before and after heating to 100 °C in air).

Attenuated total reflectance - Fourier transform infrared (ATR - FTIR) spectroscopy was performed using a Brucker ALPHA FTIR spectrometer with a dia-

mond crystal and an ATR attachment. Each spectrum was obtained by averaging 64 scans at a resolution of 4 cm^{-1} and measurements were repeated 5 times per sample. To obtain a spectrum after exposure to dry air, 50 ppm NO_2 or 50 ppm NO_2 at 50% RH, 10 mg of sample was placed into the sensor testing chamber with a flow rate of 1 L min^{-1} for 30 minutes. The sample was then removed from the chamber and the ATR - FTIR spectrum was obtained immediately. A new, identical sample was used for each exposure cycle.

7.2.3 Cross-sensitivity testing procedure

Procedure 1

Step. Duration (Seconds)	Gas Type	Relative Humidity (%)
1. 7200	Dry air	0
2. 200	NO_2 (10 ppm)	0
3. 120	Wet air	75
4. 600	Dry air	0
5. 200	NO_2 (10 ppm)	75
6. 3600	Wet air	75

Table 7.1: Testing procedure 1 is listed below detailing the time duration, gas type present, and the relative humidity of the testing chamber per testing step. Procedure 1 was used to establish the qualitative sensing behaviour for each sensor type. The flow rate was set to 1 litre per minute using MKS 1179A general purpose mass flow controllers.

Sensors were placed in ports within a circular testing chamber. The synthetic air flow rate, chamber humidity and gas mixing was controlled using digital mass flow controllers, being delivered at a determined concentration through a central inlet. The circular arrangement of the devices, along with the extraction of gas behind each individual port location, ensures that each sensor is exposed to an equal flow and concentration of gas. A potentiostat setup was used to derive the room temperature sensor conductance throughout the testing run.

Prior to the experiments, dry synthetic air was passed over the sensors for 2 hours to obtain a baseline conductance (G_{Air}) and achieve 0% relative chamber hu-

Procedure 2		
Step. Duration (Seconds)	Gas Type	Relative Humidity (%)
1. 3600	Dry air	0
2. 600	Wet air	25
3. 1800	Dry air	0
4. 600	Wet air	50
5. 1800	Dry air	0
6. 600	Wet air	75
7. 3600	Dry air	0

Table 7.2: Testing procedure 2 is listed below detailing the time duration, gas type present, and the relative humidity of the testing chamber per testing step. Procedure 2 was used to establish the sensitivity to changes in relative humidity within the sensing chamber for each sensor type. The flow rate was set to 1 liter per minute using MKS 1179A general purpose mass flow controllers. Different mixing ratios of dry and wet air were used to control humidity levels.

Procedure 3		
Step. Duration (Seconds)	Gas Type	Relative Humidity (%)
1. 3600	Dry air	0
2. 600	NO_2 (10 ppm)	0
3. 1200	Dry air	0
4. 600	NO_2 (10 ppm)	75
5. 3600	Dry air	0
6. 3600	Wet air	75

Table 7.3: Testing procedure 3 is listed below detailing the time duration, gas type present, and the relative humidity of the testing chamber per testing step. Procedure 3 was used to investigate variations in the sensor responses to 10 ppm NO_2 gas whilst changing the relative humidity of the sensing chamber. The flow rate was set to 1 litre per minute using MKS 1179A general purpose mass flow controllers.

midity (confirmed using an internal humidity meter). For repeated testing runs, the relative humidity in the chamber was maintained at 50% RH for 1 hour to increase the desorption rate of NO_2 from previous experiments before re-establishing baseline and 0% RH in dry air for 2 hours.

To first establish the characteristics of the SWCNT sensors and their zeolite modified counterparts, procedure one was used to determine qualitatively the re-

sponse curves to be expected upon introduction of NO_2, water vapour and a combination of both to the sensor surface (exposure time 200 seconds per pulse). In procedure two, the magnitude and direction of the conductance change due to varying chamber humidity from 0% to 75% was quantitatively investigated for each sensor type. Finally, procedure three was used to study the variation in sensor responses to NO_2 in both dry and wet air, as well as to compare sensing results across different fabrication batches. Tables 7.1, 7.2 and 7.3 show the complete protocols for testing procedure one, two and three respectively.

7.3 Results

7.3.1 Material characterisation

Scanning electron microscopy was used to study the morphology of the zeolite top layers and confirm the presence of SWCNT bundles on the surface of the zeolite mixed layer type sensors. Figure 7.2a and c shows the larger particulate dimensions of the Silicalite-1 compared with H-Zeolite-Y layers respectively.

At higher magnification, the SWCNT bundles are visible upon the surface of the zeolite mixed layer configuration sensors. These are distributed over the particulate base layer forming a percolating network, bridging zeolite particles and cracks as shown in Figure 7.2b and d. Zeolite layer thicknesses was in the approximate range of 5 μm to 10 μm as measured by side on SEM (Figure 7.1c).

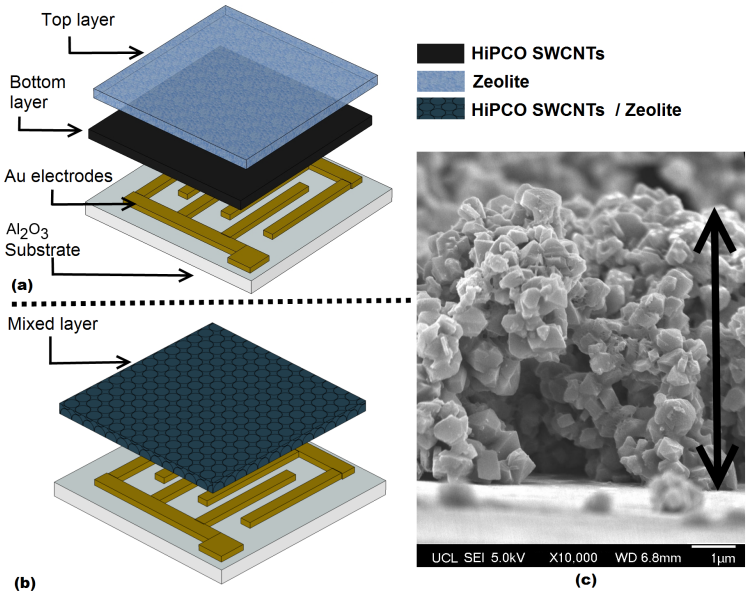

Figure 7.1: Schematic of a 3 x 3 mm Alumina substrate with interdigitated gold electrodes. Arrangement (a) consists of a HiPco SWCNT base layer with a top layer of porous zeolite. Arrangement (b) represents HiPco SWCNTs deposited over a zeolite to form a mixed layer and (c) a side on SEM micrograph at X10,000 magnification showing a H-Zeolite-Y layer of $\approx 7\ \mu$m thickness.

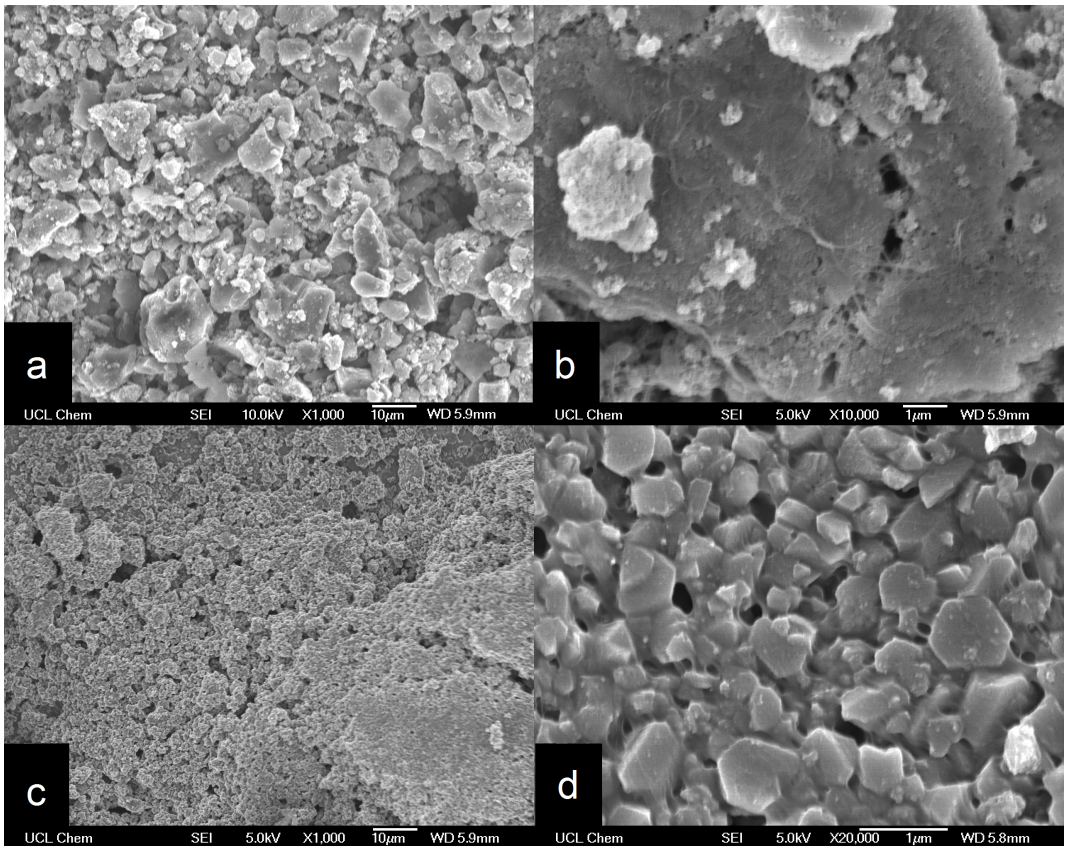

Figure 7.2: SEM micrographs of SWCNT-Zeolite mixed sensing layers showing bundles of HiPco SWCNTs distributed across the surface at (a) X10,000 (b) X20,000 and (c) X20,000 magnification using a 5 kV probe voltage.

In conjunction with SEM, energy dispersive X-ray spectroscopy (EDS) was used to confirm the silicon to aluminum ratio of the Silicalite-1 and H-Zeolite-Y layers investigated, along with the carbon content on the surface of each sensor type. The hydrophobicity of a zeolite depends on its silicon to aluminium framework ratio[192]. Hydrophobic zeolites, such as Silicalite-1, have a high silicon to aluminium framework ratio, whilst the silicon to aluminium ratio of hydrophilic H-Zeolite-Y is low.

As expected, no aluminum was present in the Silicalite-1 sample, where as the H-Zeolite-Y sample had a Si/Al ratio of 3.0 (calculated as the ratio of each elemental % weight), confirming the hydrophilicity of H-Zeolite-Y (see Table 7.4). No carbon was detected on the surface of the zeolite top layer type sensors, where as the Silicalite-1 and H-Zeolite-Y mixed layer type sensors contained 24% and 21% carbon respectively, corroborating SEM micrograph evidence of carbon nanotube

bundles on the mixed layer type sensor surfaces.

Sensor Type	Surface Carbon content (wt%)	Si:Al Ratio
Silicalite- 1 top layer	0	–
Silicalite-1 mixed layer	24	–
H-Zeolite-Y top layer	0	3
H-Zeolite-Y mixed layer	21	3

Table 7.4: Elemental analysis using energy dispersive X-ray spectroscopy (EDS) to confirm the silicon to aluminum ratio of the Silicalite-1 and H-Zeolite-Y layers investigated (calculated as the ratio of each elemental % weight) along with the Carbon content on the surface of each sensor type. Sensors were gold coated for EDS.

TEM microscopy was used to qualitatively estimate the size of the zeolite particles used for the composite sensors. The micrographs in Figure 7.3a and b indicate that the Silicalite-1 ethanol dispersed sample contained particles with a range of approximate diameters (30 nm to 100 nm). The H-Zeolite-Y sample contained larger particles, in the 100 nm to 200 nm particle diameter range (Figure 7.3c and d). This indicates that the zeolite particles are of the same order of magnitude of dimension as the diameter/length of the SWCNT bundles in the composite materials.

Raman spectroscopy measurements provide an indication of residual amorphous carbon and defects in the SWCNT sample before and after heating at 100 °C[56]. The ratio of Raman intensity of the G peak at 1593 cm^{-1} to the D peak at 1338 cm^{-1} was slightly lower post heating (12.2) than was found for the initial sample (17.2), indicating a possible increase in the number of bundle defects after heat treatment (Figure 7.4).

7.3.2 SWCNT-Zeolite composites

Zeolites are porous alumino-silicate frameworks that demonstrate size and shape selective adsorbance of certain molecules[293]. As zeolites display ionic con-

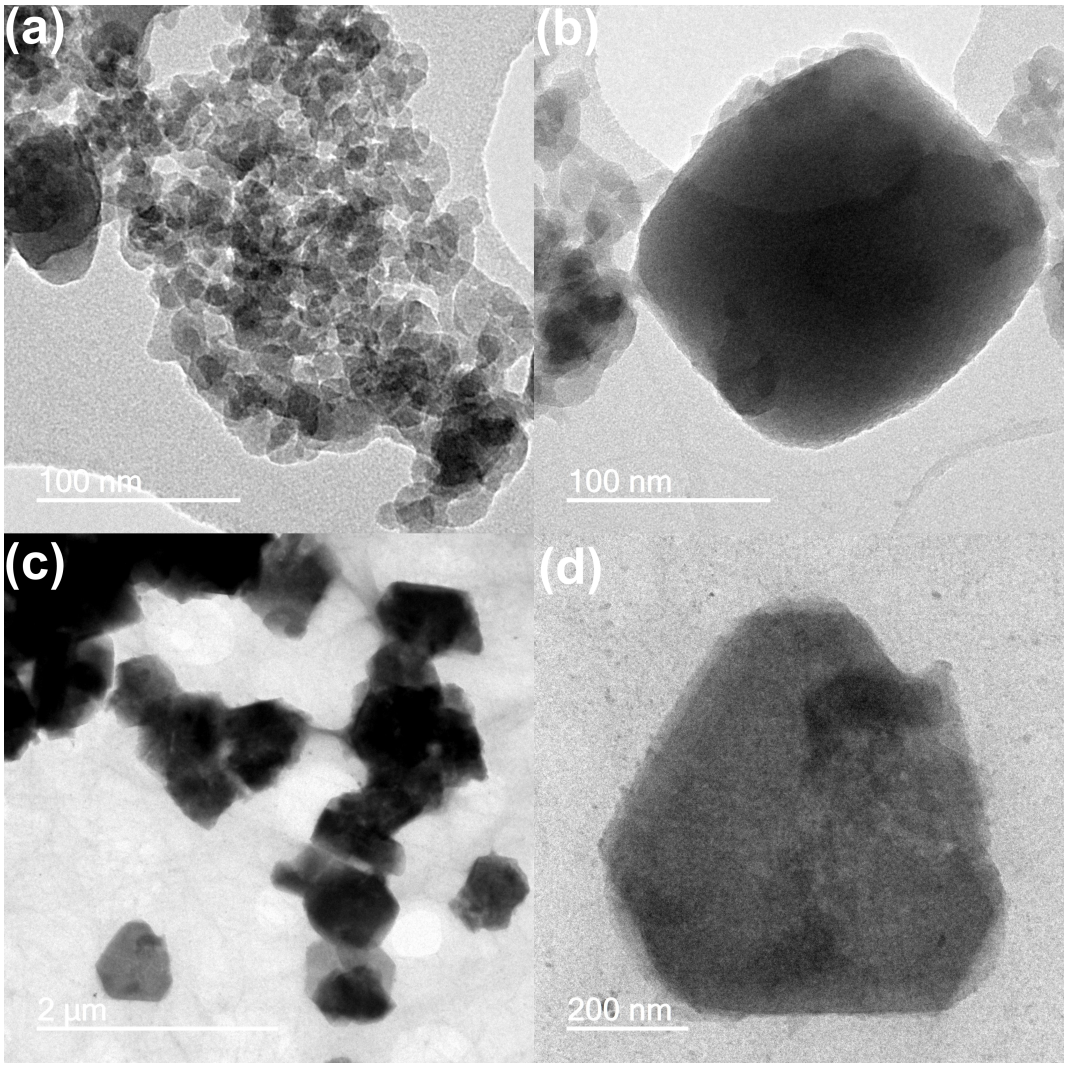

Figure 7.3: TEM micrographs (200 kV) indicating the range of particle sizes present in the (a) Silicalite-1 and (b) H-Zeolite-Y ethanol dispersed samples, drop coated onto a holey copper grid.

ductivity (and are usually electrically insulating materials), they have previously been used for impedance based gas sensing[163], as well as to improve selectivity in a combinatorial approach using metal oxide semiconducting (MOS) gas sensors[116, 294, 295]. However, their incorporation into carbon nanotube based sensors has not been investigated previously.

As discussed previously, many sensing mechanisms for SWCNT sensors have been proposed in the literature[82, 17]. It is probable that the exact mechanism depends on nanotube type[132], defectiveness[112, 111], network density[245], film thickness[246, 296], device configuration[133, 95] and functionalisation

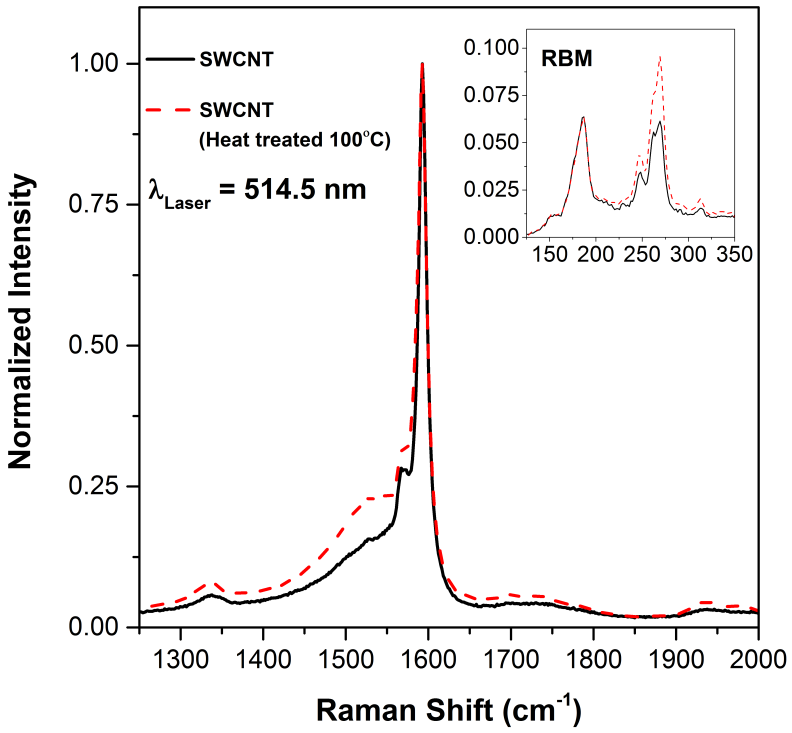

Figure 7.4: Raman spectra showing the normalized intensity of the D band (1338 cm^{-1}) and G band (1593 cm^{-1}) for HiPco SWCNT DOC bundles before and after heating sample to 100°C, with radial breathing modes inset. G/D ratio before heating was 17.2 and 12.2 after heating, indicating an increase in the number of bundle defects after heat treatment. Laser wavelength λ = 514.5 nm.

technique[114, 42, 297, 267, 298, 99]. With this in mind, sensing results here are described using a mechanism previously applied for sensors based on thick films of SWCNTs that have been functionalised, in conjunction with models describing the characteristics of zeolite layers in gas sensors and possible reactions taking place in the zeolite frameworks.

Under ambient conditions, SWCNT networks exhibit *p*-type behaviour, due to electron withdrawal of O_2 molecules adsorbed on the tube surfaces[299, 5]. The change in conductance for SWCNT network sensors (and thus sensing response), can either be attributed to charge transfer between the target molecule or modulation of the Schottky barrier at semi-conducting nanotube - metallic contacts, depending on the density and metallicity of the SWCNT film [82, 270, 245, 83].

Testing procedure one was used to qualitatively establish sensing characteristics. Upon exposure to an electron withdrawing molecule, such as NO_2, a *p*-type increase in conductance is observed as shown in Figure 7.5 section (b). Alternatively, Figure 7.5(c) demonstrates that exposure to a species such as H_2O results in a decrease in conductance.

The NO_2 sensing magnitudes and direction of conductance changes are comparable to studies using both functionalised and non-functionalised SWCNT sensors[82, 145, 7, 300, 270, 301] and those reported in Chapters 5 and 6.

Results in this thesis and elsewhere indicate that competing processes take place upon adsorption of NO_2 and H_2O, producing a convoluted response curve. When both NO_2 and H_2O are introduced at step (e) so that the testing chamber humidity is increased from 0% to 75%, the detection of NO_2 is masked by H_2O interference for the control SWCNT DOC sensor. This unwanted by-product of functionalisation can be negated through incorporation of zeolites. The complex behaviour of the zeolite modified SWCNT sensors can be explained by considering the combined effects of gas diffusion through the zeolite layers, as well as specific interactions between NO_2, H_2O and the chosen zeolite. Firstly, the results of the mixed layer sensor type are described as this configuration provided the most promising results in terms of H_2O interference reduction.

The testing procedures used for the gas sensing experiments in this study are displayed in Tables 7.1, 7.2 and 7.3, detailing the duration of gas pulses, the types of gas present and the humidity within the sensing chamber for each testing step. Response times for each analyte and each sensor type are summarised in Table 7.5. Response time t_{90} is defined as the time required for sensor responses to reach 90% of their maximum value.

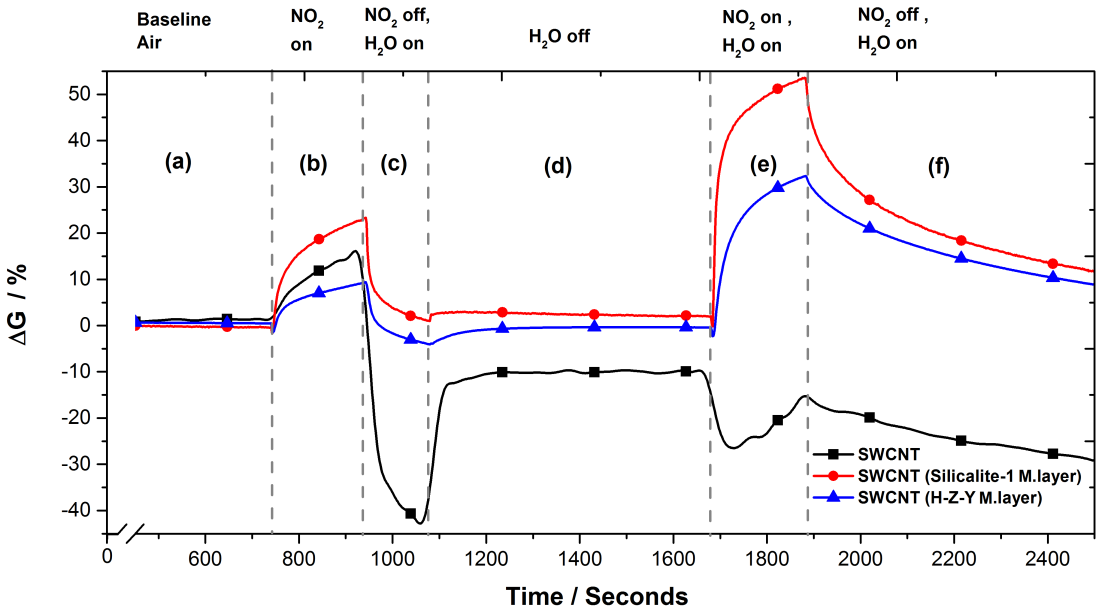

Figure 7.5: A plot of the typical percentage change in conductance at room temperature (where $\Delta G = G_{Gas} - G_{Air}$) upon exposure to various combinations of NO_2 and H_2O for a blank SWCNT, a SWCNT sensor with a Silicalite-1 mixed layer and a SWCNT sensor with a H-Z-Y mixed layer. Region (a) displays the baseline conductance for each sensor type whilst operating in dry synthetic air, whilst in region (b) 10 ppm of NO_2 is additionally introduced to the testing chamber. Region (c) contains the desorption step in which the NO_2 pulse is turned off and H_2O is turned on resulting in a relative humidity of 75% inside the testing chamber, aiding NO_2 desorption from the sensor surface. In region (d) H_2O is turned off to return the relative humidity of the chamber to 0% and recover baseline conductance. Region (e) shows the response of each sensor type to 10 ppm of NO_2 whilst operating at 75% chamber humidity. Finally, in region (f) the NO_2 is turned off and relative humidity set at 75% for the desorption cycle.

7.3.3 Mixed layer sensor configuration

Figure 7.5 section (c), obtained following testing procedure one, highlights the decreased sensitivity to changing environmental humidity for the SWCNT mixed layer type sensors in comparison with the control. Here, hydrolysis treatment at step (c) removes the NO_2[145] introduced in step (b), with recovery of the initial baseline resistance. The control SWCNT sensor overshoots its initial baseline resistance, settling at a new value in dry air at step (d), indicating permanent modification of the film. It is proposed that the SWCNT network deposited over a zeolite is effectively exposed to a lower concentration of water vapour due to adsorption of the

H_2O in the zeolite framework.

Sensor Type	**t_{90}(s) H_2O (RH 75 %)**	**t_{90}(s) NO_2**	**t_{90}(s) NO_2 (RH 75 %)**
SWCNT	12	502	-
H-Zeolite-Y mixed layer	347	526	341
Silicalite-1 mixed layer	202	163	396
H-Zeolite-Y overlayer	-	481	547
Silicalite-1 overlayer	-	588	608

Table 7.5: Example response times for each analyte and sensor type. Response time t_{90} is defined as the time required for sensor responses to reach 90 % of their maximum value. Recovery time Rec is defined as the time taken for the sensors to re-establish a baseline resistance.

It was expected here that zeolites with high aluminium content (such as H-Zeolite-Y used here) would show a large affinity for water[192], preferentially adsorbing it over the SWCNT network and reducing interference effects. However, a reduction in sensitivity to H_2O vapour was also observed in the Silicalite-1 mixed layer sensor. Despite the hydrophobic nature of Silicalite-1, water adsorption is still thought to take place due to the presence of silanol defects[302]. This may explain the overall reduction in water interference despite the use of both a hydrophobic (Silicalite-1) and hydrophilic (H-Zeolite-Y) zeolite type. In a similar way, Battie *et al* found that silanol groups permitted the use of mesoporous silica thin films to reduce the cross-sensitivity of SWCNT based devices to water[303]. Therefore, it is more appropriate to refer to the Silicalite-1 used here as being less hydrophilic than H-Zeolite-Y, rather than being hydrophobic.

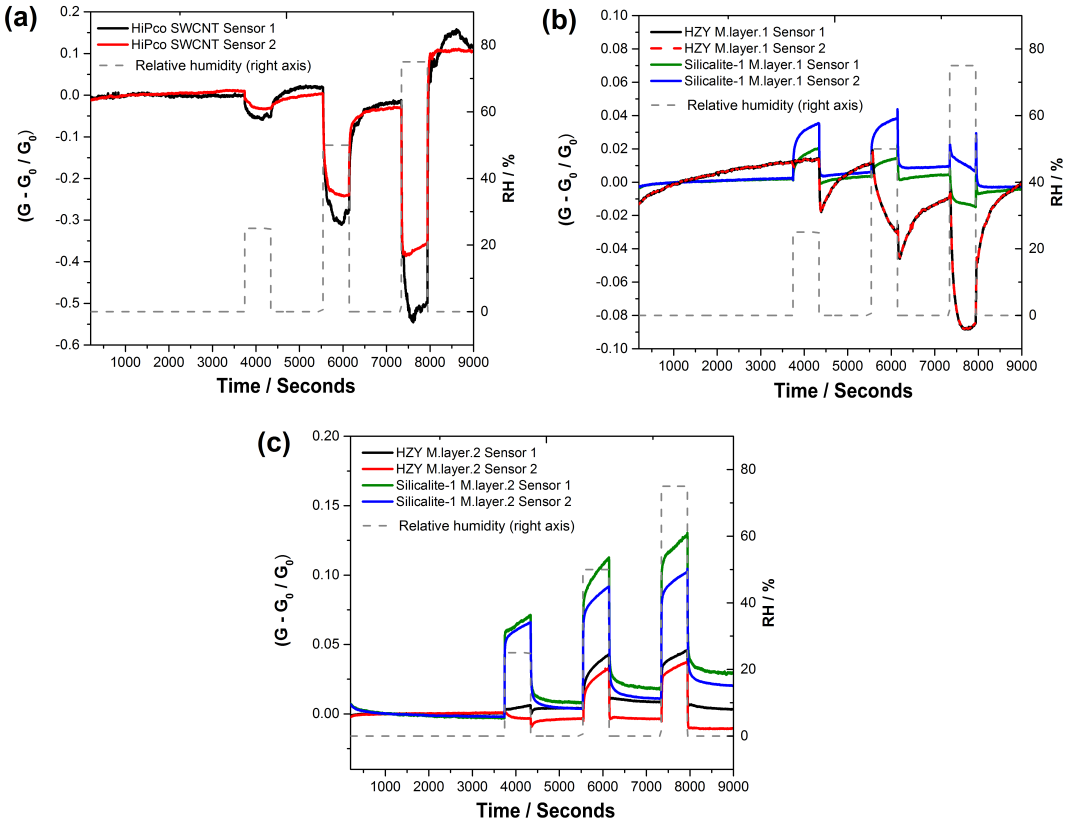

Figure 7.6: Example of real time sensor responses to changes in the relative humidity levels within the sensing chamber, varying the relative humidity between 0% and 25% , 50% or 75%. Plot (a) shows the decrease in conductance observed for HiPCo SWCNT based devices, (b) shows the smaller changes for zeolite mixed layer devices with lower zeolite content (0.033 mg of zeolite per 1 μL drop of HiPco DOC solution) and (c) shows the increase in conductance for zeolite mixed layer devices with higher zeolite content (0.2 mg of zeolite per 1 μL drop of HiPco DOC solution), with changes still smaller in magnitude than the SWCNT control sensors.

Figure 7.7 shows that the device conductance change in humid conditions is dependent on the zeolite loading. Use of a zeolite mixed layer reduces the decrease in conduction when compared to SWCNT control devices. Interestingly, at higher zeolite loadings a comparatively small conductance increase is observed. This may be due to the introduction of water-zeolite reaction products to the nanotube network.

Detection of 10 ppm NO_2 at 75% relative humidity with the zeolite mixed layer sensors is shown in Figure 7.5 step (e). Initially, the response magnitude was

larger when testing in humid conditions, possibly due to a reaction between the zeolite adsorbed H_2O and NO_2. This feature was found to vary between test cycles, potentially due to different levels of residual H_2O present in the zeolite framework between tests. Therefore, after establishing that a zeolite mixed layer reduces H_2O interference, procedure three was adopted (as outlined in the Gas Testing Procedure section) to establish the extent to which responses were reproducible and quantitatively asses the apparent improvements.

Figure 7.6 shows example responses to changes in the relative humidity levels within the sensing chamber for SWCNT HiPco control sensors, mixed layer sensors with low zeolite content and high zeolite content for the current study. The relative humidity was modulated between 0% and 25% , 50% or 75%. Figure 7.8 provides examples of real time responses to 10 ppm NO_2 gas in both dry and wet (75% RH) air for each of the sensor types investigated.

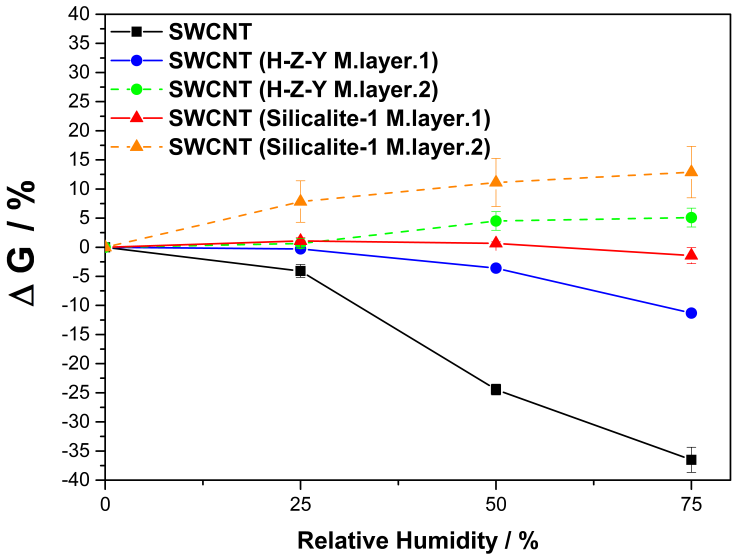

Figure 7.7: Typical percentage change in conductance per sensor type (where $\Delta G = G_{Gas} - G_{Air}$) as relative humidity in testing chamber is increased from 0 % to 25 %, 50 % and 75 % for SWCNT control sensors, SWCNT H-Zeolite-Y and SWCNT Silicalite-1 zeolite mixed layer type sensors. M.layer.1 indicates a mixed layer with lower zeolite content (0.033 mg of zeolite per 1 μL drop of HiPco DOC solution), M.layer.2 indicates a mixed layer with higher zeolite content (0.2 mg of zeolite per 1 μL drop of HiPco DOC solution).

The collated responses for each sensor type to 10 ppm NO_2 in both synthetic dry air and wet air at 75% relative humidity (using testing procedure 3) are shown in Figure 7.9. The responses of four identical sensors (one taken from each batch, see device fabrication section) are averaged over six testing cycles to provide a mean response direction and magnitude per sensor type.

Typically, SWCNT control sensors displayed an increase in conductance of +13.6% to 10 ppm NO_2 in dry air and a decrease of -18.53% in wet air (75% RH), showing a difference in response direction and a 38.3% difference in G_{Gas}. Whilst the SWCNT control sensors always displayed a decrease in conduction upon introduction of H_2O vapour and NO_2, the magnitude of the response between identical sensors was variable. Variability in SWCNT based sensor performance has been investigated previously and can be attributed to the different properties (length, diameter, semi-conducting or metallic conductivity) of SWCNTs found within a sample[304, 132] and thus in the network forming the sensing layer.

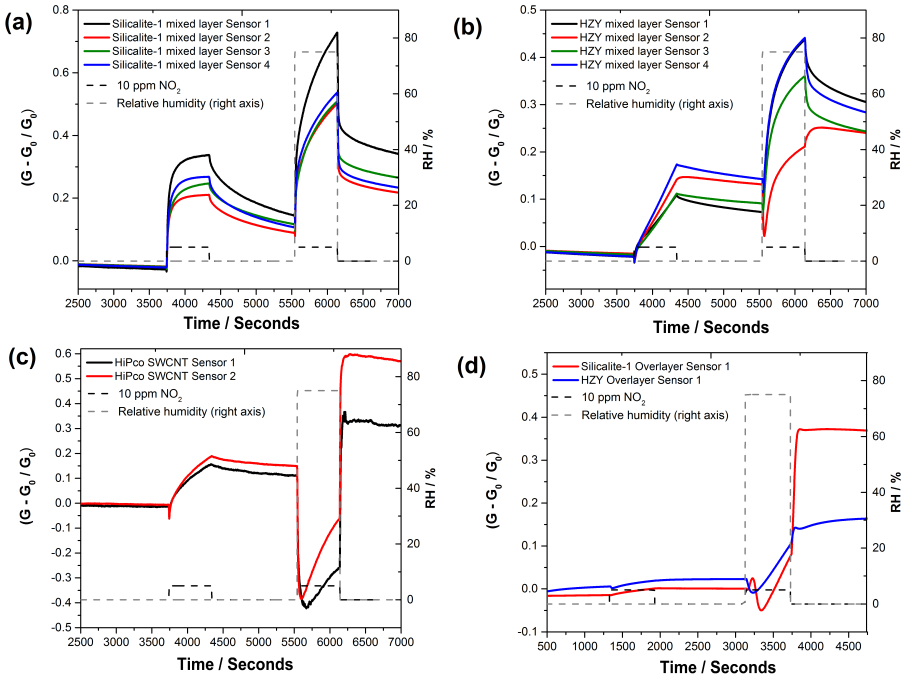

Figure 7.8: Example of real time sensor responses to 10 ppm NO_2 in both dry and wet air following testing procedure 3 for (a) Silicalite-1 mixed layer sensors (b) HZY mixed layer sensors (c) HipCo SWCNT sensors and (d) zeolite overlayer sensors. The timing of the 10 ppm pulse of NO_2 is indicated by the dashed black line and the humidity of the sensing chamber is denoted by the dashed grey line (right axis).

Zeolite mixed layer sensors maintain a repeatable overall increase in conductance for NO_2 in both dry and wet air. The increase for H-Zeolite-Y mixed layers is smaller for NO_2 in dry air (+24%) than in wet air (+30%). The average response to NO_2 for Silicalite-1 mixed layer sensors was also lower in dry air (+34%) than in wet (+40.9%), although overall responses were larger in magnitude using Silicalite-1. Here, the differences between the H-Zeolite-Y and Silicalite-1 mixed layer sensors may be due to their different silicon to aluminium ratios. Zeolite water content can dramatically influence the reaction products present inside the framework[190]. As H-Zeolite-Y has a higher affinity for H_2O, it is possible that varying amounts of reaction products are produced that subsequently interact with the SWCNTs.

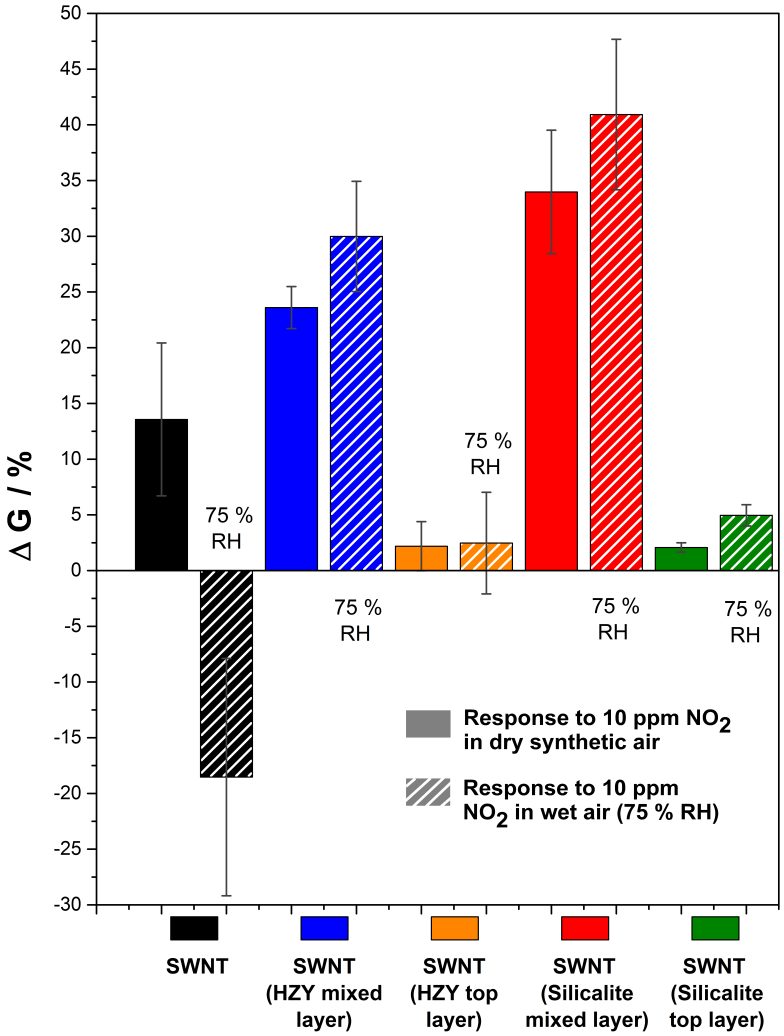

Figure 7.9: Average percentage change in conductance per sensor type (where $\Delta G = G_{Gas} - G_{Air}$) upon exposure to both 10 ppm NO_2 in dry synthetic air and 10 ppm NO_2 in wet air at 75 % relative humidity over 6 testing cycles (mean responses of four identical sensors from each sensor type, taken over six repeated tests, presented with standard error).

Attenuated total reflectance - Fourier transform infrared (ATR - FTIR) spectroscopy was used to infer possible reactions taking place in the zeolite framework upon adsorption of NO_2. Any products of reactions between NO_2, H_2O and the acidic sites within the framework can interact and contribute to a change in conductance of the sensing layer. Adsorption of NO_2 in the presence of water by Zeolite-Y type zeolites has been investigated previously using FTIR spectroscopy and was found to inhibit the formation of NO^+ species, whilst NO_3^- and NO_2^- are readily formed, as well as potential HNO_x molecules[190, 189, 191].

Whilst the experimental setup differed from that of the previous study to suit the detection of species in ambient conditions (see experimental section), similar spectral features were observed when exposing a mixed HipCo SWCNT / H-Zeolite-Y sample to 50 ppm NO_2 in either dry or wet air and subsequently obtaining the ATR-FTIR spectra[190, 189]. Figure 7.10a shows the appearance of two bands in the 1300 to 1450 cm^{-1} region after exposing the mixed sample to 50 ppm NO_2 for 30 minutes. An increase in peak intensity is observed when NO_2 is introduced in humid conditions (50% RH). These bands have been assigned to nitrate groups in the literature, suggesting the formation of HNO_x or NO_3^- species when the zeolite is exposed to NO_2 [190, 189, 191].

Similar features are observed in the mixed HiPco SWCNT / Silicalite-1 sample (Figure 7.10b). The band at 1387 cm^{-1} increases in intensity after adsorption of NO_2 and a further increase is found when adsorption takes place in the presence of water. Furthermore, the band centered at 1559 cm^{-1} in the non-exposed sample disappears after the introduction of NO_2 to the chamber and a new band is formed at 1707 cm^{-1}, suggesting the formation of new surface species. It has been previously reported that nitric acid treatment increases the conductance of SWCNT networks[237, 305]. Therefore, the formation of such species (especially HNO_x molecules) within the sensing layers may be causing the larger responses to NO_2 in humid conditions.

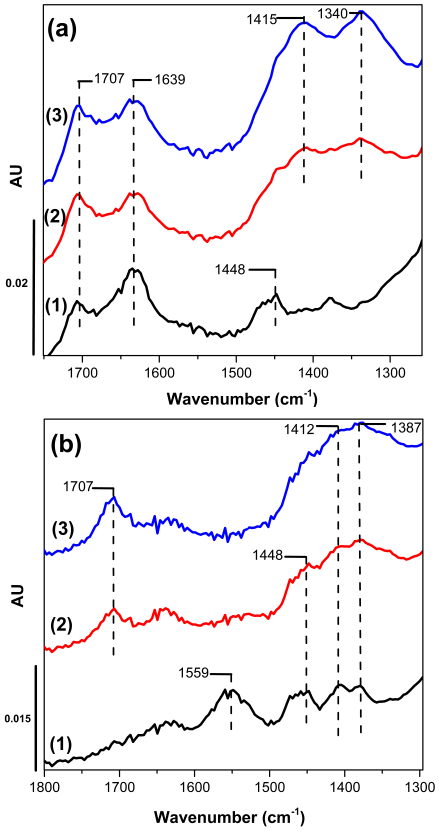

Figure 7.10: ATR - FTIR spectra for the (a) HiPco SWCNT H-Zeolite-Y sample (b) HiPco SWCNT Silicalite-1 sample when exposed to (1) dry air for 30 minutes (2) 50 ppm NO_2 in dry air for 30 minutes and (3) 50 ppm NO_2 in wet air for 30 minutes at 50% RH, transferring the samples to the spectrometer after exposure. A Brucker ALPHA FTIR spectrometer with a diamond crystal and an ATR attachment was used, averaging 64 scans at a resolution of 4 cm^{-1}. Five repeated measurements were made per exposure cycle on each sample type, plots are offset for clarity.

Surprisingly, the H-Zeolite-Y and Silicalite-1 mixed layer sensors show a significantly larger change in conductance upon exposure to 10 ppm NO_2 in dry air than the control SWCNT sensors (24%, 34% and 13.6% respectively, Figure 7.9). This can be reasoned by considering two contributing factors. Firstly, the conversion of NO_2 to other oxidising products in the vicinity of the tube network may still take place if there is residual water in the zeolite framework, inducing larger responses. Secondly, the proportion of the sensing layer that is accessible to the target gas has previously been shown to impact greatly upon the response observed for nanomaterial based sensors[296, 163]. Therefore, the increase may be partly due to the fact that the SWCNTs are distributed over the highly porous mixed layer,

allowing NO_2 gas access to a higher proportion of the SWCNT network, resulting in a higher percentage change in film conductance.

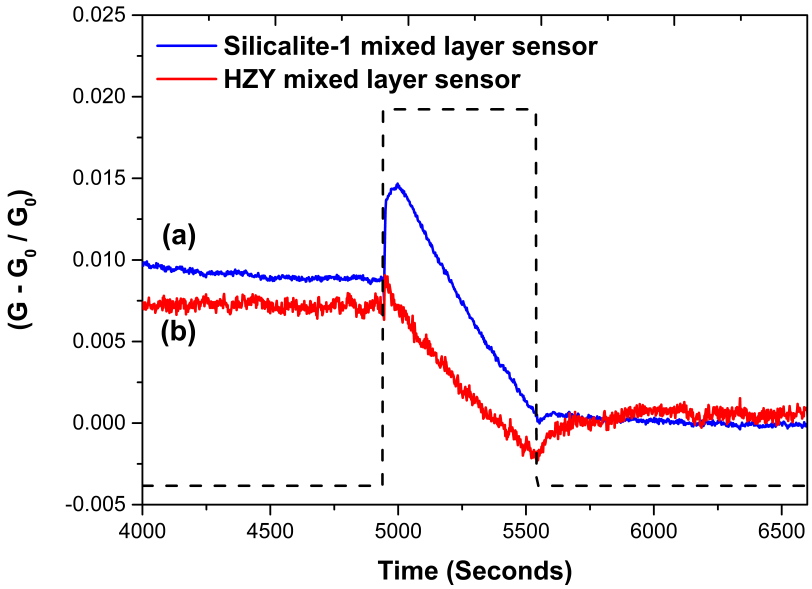

Figure 7.11: Example of real time sensor responses to 40 ppm NH_3 in dry air for (a) Silicalite mixed layer sensors and (b) H-Z-Y mixed layer sensors. The timing of the 40 ppm pulse of NH_3 is indicated by the dashed black line.

p-type responses to NH_3 were observed using the zeolite mixed layer sensors as shown in Figure 7.11. Response magnitudes ($\Delta G < 1\%$ to 40 ppm NH_3) were small and the zeolites were unable to provide adequate water interference reduction in this case. However, this may be possible when testing for higher concentrations of NH_3 (200 ppm +) that cause larger changes in the conductance of SWCNT networks.

7.3.4 Top layer sensor configuration

A profound difference in sensing characteristics is observed between devices utilising a top layer or mixed layer of zeolite, which is attributed to contrasting diffusion processes[306].

The use of a zeolite layer on top of the sensor introduces a porous barrier to ad-

sorption of NO_2 in the SWCNT network. Thus, a resistive diffusion process seems to limit access of the gas to the functional sensing layer and responses are largely reduced to 10 ppm NO_2 as compared with the SWCNT control and zeolite mixed layer sensors. Interestingly, when 10 ppm of NO_2 is introduced whilst increasing the relative chamber humidity to 75%, a larger response to NO_2 is observed for the Silicalite-1 top layer sensor.

This difference in sensing response whilst operating in high relative humidities can be attributed to the blocking of NO_2 adsorption sites with water. The wetting of the zeolite framework reduces the layers diffusive resistance, allowing more NO_2 access to the sensing layer. As before, it is also possible that reactions occur in the zeolite layer between NO_2 and adsorbed H_2O, introducing new products to the film.

Mixed layers of zeolite provide an enhanced response magnitude when compared to top layered sensors. This can again be explained when considering the access of the target molecule to the SWCNT network. In the mixed layer configuration, there is less of a diffusive barrier to gas interaction with the SWCNTs. Therefore a higher proportion of the NO_2 gas, as well as subsequent reaction products, interact with the SWCNTs, resulting in a larger electrical response.

7.3.5 SWCNT-Zeolite sensor characteristics and regeneration

Response time t_{90}, defined as the time required for sensor responses to reach 90 % of their maximum value (available in Table 7.5), varied depending on the sensor type and analyte under investigation. Generally, responses to H_2O (75% RH) were fastest for the SWCNT control sensors (12 seconds) compared with zeoilte modified sensors (200 to 350 seconds depending on zeolite), presumably as SWCNT exposure to water in the zeolite containing samples is hindered by adsorption to the framework. Baseline conductance was re-established after exposure to water within 200 seconds for all sensors, although some drift was evident as shown in Figure 7.6, possibly due to retention of water in the film.

When testing to NO_2 in dry air, response times were of the order of 500 seconds other than for the Silicalite-1 mixed layer type sensor for which t_{90} = 163

seconds. Interestingly, the H-Zeolite-Y mixed layer sensor response time for NO_2 at 75% RH was faster (341 seconds) than when testing in dry air. This was not the case for the remaining sensors, for which simultaneous exposure to NO_2 and H_2O increased response times (see Table 7.5). Therefore, response times to NO_2 are sensitive to adsorption of water in the zeolite modified sensors. Some baseline drift was evident after exposure to NO_2 (shown in Figure 7.8), with stability of responses indicated by the error bars on Figure 7.9.

The zeolites within the sensing layer have a limited water adsorption capacity. After 10 cycles of testing for the Silicalite-1 mixed layer type sensors and after 7 cycles for the H-Zeolite-Y mixed layer sensors, water starts to interfere with the sensing responses to 10 ppm NO_2 at 75% relative humidity in the testing chamber. Whilst this adds weight to the hypothesis that cross-sensitivity reduction is due to zeolite water adsorption, it also means that the sensor needs to be regenerated periodically in some way to limit zeolite saturation. Figures 7.12a and 7.12b show an example of regenerating the mixed layer sensors after multiple testing cycles by heating them to 150°C in air on chip. After this step, the zeolites once again facilitate a reduction in cross-sensitivity to water and responses to NO_2 in humid conditions at room temperature are recovered.

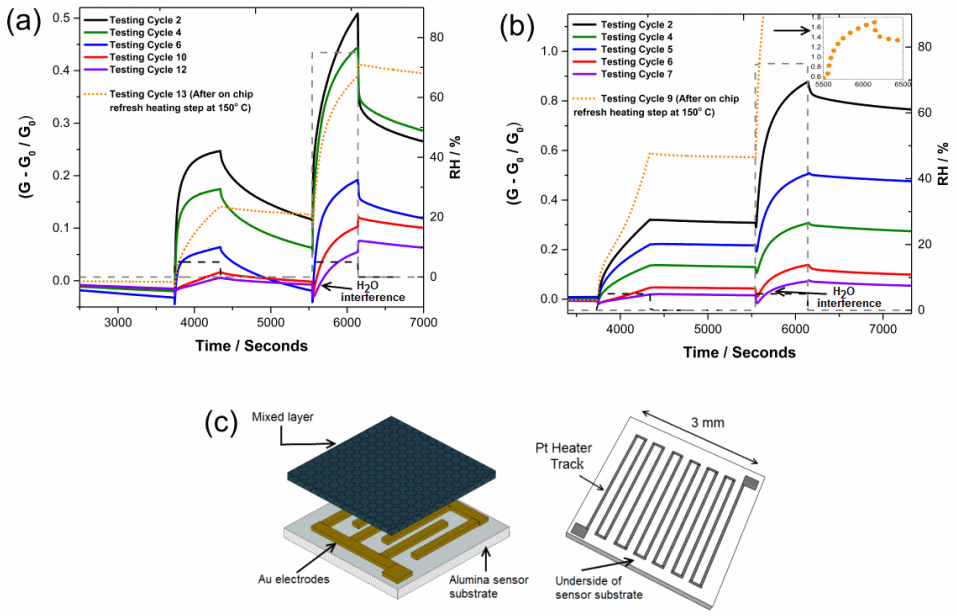

Figure 7.12: An example of regenerating a Silicalite-1 mixed layer type sensor (a) and a HZY mixed layer sensor (b) after the zeolites begin to water saturate. After 10 consecutive cycles of testing for Silicalite-1 and 7 cycles for HZY, the water begins to interfere with the sensor responses to 10 ppm NO_2 at 75% RH, changing the shape of the response curve and beginning to cause the decrease in conductance that is observed for the SWCNT control sensors upon exposure to water vapour. By heating the sensing layer to 150°C in air via a platinum heater track on the underside of the chip (schematic (c)) in between cycles, the responses to NO_2 in both dry and wet air (the dotted orange line on each plot shows responses after regeneration step) can be recovered and the cross-sensitivity reduction is preserved.

7.4 Conclusion

In this chapter, the sensing characteristics of functionalised SWCNTs were modified with zeolites. When exposed to NO_2 in both dry and humid conditions, the room temperature sensing behaviour was found to depend on the arrangement of the layers in the device, the loading and hydrophilicity of the chosen zeolite.

The zeolite mixed layer configuration limited cross-sensitivity to water vapour, with sensors maintaining an increase in conduction upon exposure to NO_2 in both dry conditions and throughout extreme changes (0% to 75%) in relative humidity. The difference in response when testing to NO_2 in dry and wet air (S_{DryAir} - $S_{RH\ 75\%}$) was 6.9% for the SWCNT Silicalite-1 mixed layer sensor type, compared to

32.1% for the SWCNT control sensors. This desirable reduction of water vapour interference is attributed to the preferential adsorption of H_2O to the zeolite framework rather than to the SWCNTs.

Formation of NO_3^- and HNO_3 species in the mixed layer material after exposure to NO_2 was inferred from ATR-FTIR measurements, which in turn depends on the amount of water present in the zeolite framework. It was suggested that differences in the responses between SWCNT H-Zeolite-Y and SWCNT Silicalite-1 mixed layer sensors are therefore due to their different respective hydrophilicities.

Zeolite top layers were found to inhibit the diffusion of NO_2 to the active SWCNT sensing layer. Thus, the change in conductance observed whilst testing in dry air was relativity low at 2.1%, with a moderate increase in humid conditions to 5.0%. A reduced layer thickness ($< 10\ \mu$m) may be required to allow diffusion of the target gas to the SWCNTs in the zeolite top layer sensor arrangement.

The gas sensing results reported in this study suggest that a mixed sensing layer of SWCNTs and zeolite reduces the cross sensitivity of functionalised SWCNT sensors to water vapour. Whilst the baseline signal regeneration procedure must be optimised, this reduction is favourable for real world monitoring of NO_2 at room temperature with SWCNT-based chemical sensors.

Chapter 8

Conclusion

8.1 Conclusions

8.1.1 Introduction

The aims of this thesis were to study the conductance-humidity behaviour of SWCNT networks, establish the nature of NO_2 adsorption and assess the impact that sensitivity to surface adsorbed water vapour had on the conductive responses of SWCNT-based chemiresistive sensors. A further aim was to develop a composite material that reduces such cross-interference effects.

In this conclusion chapter, a summary of the findings from each of the above investigations is detailed. This is followed by an overview bringing the findings together, putting them into context, and finally presenting ideas for possible future work.

8.1.2 Summary of SWCNT network conductance-humidity behaviour

Reversible adsorption of water vapour to the SWCNTs was inferred from the reversible change in network conductance observed when the relative humidity of the sensor testing cell was modulated stepwise between 10% and 90% RH. Therefore, it was determined that variations in humidity found in normal atmospheric conditions would impact upon the performance of SWCNT network chemiresistors.

In line with the discrepancies reported in the literature previously, either *n*-type or *p*-type responses to H_2O were observed, depending on thickness of the non-functionalised control network. It was reasoned that this could be due to the increasing influence of the Al_2O_3 substrate charge on the measured thinner film conductances upon wetting.

The directional switch in conductance change was enhanced by up to a factor of 10 when ionic surfactants were present in the SWCNT layer. Anionic agents amplified a decrease in conductance across the network when the layer was exposed to water vapour, whilst cationic surfactant reversed the change so that an increase in conductance was measured. This further points to the influence of charged species in the film on the conductance-humidity behaviour of the SWCNT network.

Based on these findings, it was suggested that changes in the conductance of the SWCNTs were attributable to electrostatic interactions with the water molecule, as opposed to chemical doping. This was in line with the study by Bell *et al*, who concluded that charge transfer between individual CNTs and water is negligible, with the dipole moment of the water inducing polarisation of charge in the CNT [142]. Instead, they proposed that for any change in conductance due to surface adsorbed water in SWCNT networks, the inter-tube resistance should be considered. *p*-type sensing responses to NO_2 (as described in the following section), for which charge transfer is expected to take place, are always maintained. Therefore, the discrepancies in the literature may be attributable to sources of additional water-charge interaction, such as from SWCNT functionalisation or the device substrate.

Similar alterations in Raman features that are associated with changes in an applied gate potential for SWCNT-based FETs are observed in the current study upon wetting of the films. The water may induce an additional charge on the tubes, resulting in non-linear I-V characteristics, analogous to solution gated FETs. Furthermore, the hot-probe method suggests that SWCNTs can become less or more *p*-type depending on the charge of the surfactant in the dry or wet films.

SWCNT network humidity sensors responded to changes in the humidity of the testing cell in the 10% to 90% RH range in a non-linear fashion. Limited signal

drift, observed in the baseline conductance of the sensor, could potentially be due to migration of charged counterions in the film when exposed to water vapour.

8.1.3 Summary of NO_2 sensing in humid conditions

As with previous studies, the adsorption of NO_2 to the SWCNT networks was found to be irreversible on a timescale comparable to the exposure duration. This resulted in a deterioration of the sensing response to multiple pulses of NO_2 over time, preventing quantification of the analyte concentration.

The sensitivity of the SWCNT networks functionalised with DOC surfactant to water vapour was manipulated to apply the water-assisted regeneration (WAR) method. Using this method, the baseline conductance of the chemiresistors was recovered between each pulse of NO_2, with water vapour expediating analyte desorption and facilitating repeatable conductive responses.

The recovery of the baseline signal allowed the application of a previously developed irreversible adsorption model to extract key sensing parameters from the data, namely the maximum possible sensing response (S_{max}) and adsorption constant (k). A second model was applied to achieve a better fit to the conductive response curves by considering partially reversible adsorption of NO_2 to the SWCNT surfaces. This improved fit may be rationalised by considering the existence of multiple analyte adsorption sites with different adsorption/desorption characteristics, such as the tube walls or at defect sites.

The NO_2 sensing response curves were altered, both in magnitude and response/recovery rates, by different levels of background relative humidity. This was potentially due to the formation of secondary products from reactions between NO_2 and H_2O, or the adsorbed H_2O acting as additional adsorption sites.

Thinner SWCNT films provided larger conductive responses to NO_2. This may be due to better diffusion of the analyte through the film to adsorption sites that contribute to the electrical response, or to the degree of percolation of m-SWCNTs in the gas sensitive layer.

8.1.4 Summary of SWCNT-Zeolite composites for gas sensing

In an effort to reduce the cross-sensitivity of SWCNT networks to water vapour, non-conducting zeolites were used to form SWCNT-Zeolite composite chemiresistors in a mixed layer and top layer configuration. The devices displayed a reduced sensitivity to water vapour in comparison with the HiPco DOC control sensors.

The detection of NO_2 gas was possible using the mixed layer SWCNT-Zeolite composite sensor, even when extreme fluctuations (0% RH to 50 % RH) in the relative humidity of the testing chamber were made to coincide with the injection of the target analyte. Conversely, the sensing response of the control SWCNT sensor was masked by the RH induced conductance change.

The SWCNT-Zeolite top layer configuration sensors showed much reduced responses when the same testing was applied. It was reasoned that this was due to adsorption of NO_2 to the zeolite top layer before any possible interaction with the SWCNT network. This result suggested that top layers of zeolite should be < 10 μm in thickness if they are to be used to improve selectivity for SWCNT based chemiresistors.

Largely irreversible responses to NO_2 were observed for the SWCNT-Zeolite composite sensors. Therefore, after a certain number of testing cycles, the sensors required regeneration *via* an on chip heater track to obtain conductive responses. This technique requires optimisation before the use of SWCNT-Zeolite composite sensors is possible in real world environmental monitoring applications.

8.1.5 Thesis overview conclusions

In this thesis, investigation of the conductance-humidity behaviour, NO_2 adsorption processes and the impact of pre-adsorbed water vapour on conductive responses, provided an insight into the problems, important considerations and potential solutions for the development of SWCNT-based chemiresistive sensors. It is clear from this study that SWCNT networks may be good potential candidates for low-powered and portable chemical sensing applications, if the described challenges are overcome. The ability to carry out sensing at room temperature, combined with high

reported sensitivity (down to ppt level in some reported studies) justifies continuing efforts to surmount the current developmental barriers, however a considered approach is required.

From the study detailed in Chapter 4, the sensitivity of SWCNT networks to adsorbed water vapour, inducing changes in measured conductance, must be taken into account when developing SWCNT-based electronic devices for applications. Further thought should be given to the functionalisation routes which may be used in the processing of SWCNTs, as such treatments can magnify the conductance-humidity effect.

This is especially true for chemical sensing using SWCNTs. Coupled with the fact that pre-adsorbed water vapour can alter the response magnitudes and characteristics of the SWCNT chemiresistors (Chapter 6), cross-sensitivity should always be evaluated when new functional groups are added to increase sensor selectivity towards a certain molecular species.

In general, SWCNT chemiresistors tend to show poor baseline recovery after exposure to strongly bound analytes (e.g NO_2, NH_3) without additional desorption stimulus. This is an undesirable feature of many chemiresistive sensors that operate at room temperature. Therefore, the extra power required for implementation of the recovery technique should also be accounted for before considering suitable applications. In the case of the water-assisted recovery (WAR) method in Chapter 5, the technique provided an excellent way to acquire repeatable sensing results in an experimental setting, but the additional apparatus required (e.g a controllable humidity setup) may increase the cost and decrease the portability of the entire sensing device.

Alternatively, the SWCNT chemiresistors could be applied as disposable dosimeter type devices. The irreversible nature of NO_2 adsorption to the SWCNT networks simplifies the modelling of the conductive responses (Chapter 5). Therefore, rather than trying to recover the baseline signal, maximum irreversibility is desirable and would allow the estimation of the amount of NO_2 a SWCNT network was exposed to over the device's lifetime, through analysis of the conductive re-

sponse curve magnitude and shape. In this respect, the SWCNT-HZY composite mixed layer sensors described in the Chapter 7 study would be the most suitable as a dosimeter type device, due to the highly irreversible responses observed to NO_2.

The drop coating technique used for the fabrication of the SWCNT chemiresistors in the current thesis enabled the fast fabrication of devices and the ability to carry out flexible experimental investigations. Although the sensing characteristics (response direction, adsorption/desorption rates) were qualitatively similar between identical devices, variations in the response magnitudes were observed. This would need to be reduced, potentially through the use of more scalable fabrication techniques (printing or spray deposition) and/or the use of homogeneous SWCNT raw samples, before low-powered sensing applications can be realised.

8.2 Future work

The results in this thesis open up many potential avenues for future investigation. Firstly, with the improving purity and homogeneity of raw SWCNT samples available commercially, it may be possible to investigate the effect that SWCNT chirality, length and diameter have on sensing responses when incorporated into SWCNT network chemiresistors. Additionally, the fabrication of arrays of SWCNT devices with controlled proportions of m-SWCNTs and sc-SWCNTs in the film may allow tailoring of the dominant response mechanism.

Further experimental work, possibly using spectroscopy or spectrometry *in situ* of the sensing experiments to probe the analyte-SWCNT interactions, would help to confirm the sensing mechanisms discussed in this thesis and monitor the real time formation of any reaction products. AC impedance spectroscopy could be used to investigate the signal drift observed in the water-exposed films, potentially attributable to migration of charged ions in the network.

The chemiresistive sensor configuration could be adapted so that the SWCNT networks are deposited on a micro-hotplate type device. This would allow heating of the sensing material to increase analyte desorption, whilst maintaining a relatively low power consumption. Furthermore, precise control of the sensor tem-

perature would allow use of techniques such as pulsed temperature modulation, enhancing sensor selectivity through analysis of the additional transient information acquired.

To move towards real world applications, the thickness and weight ratios of the SWCNT control, SWCNT-surfactant and SWCNT-Zeolite type sensors should be adjusted to optimise the conductive response, signal recovery and cross-sensitivity to water vapour. The water sensitivity study could be used to design functionalisation and fabrication procedures which minimise the impact of the conductance-humidity effect on SWCNT-based devices, or as a characterisation procedure in it's own right.

Due to the irreversible conductive responses of many nanomaterials previously reported, the wider applicability of the irreversible adsorption model for extraction of sensing parameters could be assessed and applied to newly developed gas sensitive materials which show poor baseline signal recovery whilst sensing at room temperature.

The described WAR method may be suitable to regenerate the baseline signal after SWCNT exposure to other target analytes for which long desorption times are an issue. The technique could also be applied to other room temperature chemiresistive systems (e.g for graphene, SnO_2 nanotubes, ZnO nanotubes) to aid their experimental study.

A wider variety of SWCNT-Zeolite composite systems could be investigated, chosen for their affinity towards other target analytes of interest. Alternative deposition techniques for the top layer of zeolite (potentially grown *in situ* using atomic layer deposition) may be useful to achieve selective overlayers which allow the diffusion of certain molecules through the zeolite layer to the SWCNT network below. Based on the current thesis, the layer would have to be at least less than 1 μm in thickness to allow diffusion to occur.

Finally, it would also be interesting to explore the possibility of using a dual capacitance - conductance measurement mode (described by Snow *et al.* [91]) for the SWCNT-Zeolite mixed layer system, as the insulating zeolite component

should provide additional chemical sensing information given the use of impedance measurements previously [163].

Appendix A

Motivation for the experiments carried out in the project

Table A.1: The motivation for the experiments described in this thesis, along with section references.

Experimental technique	Section	Study and Motivation for the experiment
Raman spectroscopy	3.1.1	To identify the relevant Raman modes previously reported for HiPco SWCNTs and to initially assess the purity of the sample.
Raman spectroscopy	3.1.1	To establish the common and distinct Raman features of HiPco or CoMoCat produced samples.
Raman spectroscopy	5.3.1	To determine a maximum heat treatment temperature in air before substantially damaging the SWCNTs.
Raman spectroscopy	7.3.1	Testing the suitability of heat treatment at 100 °C in air for sample drying and gas sensor regeneration by quantifying the increase in bundle defectiveness.

Table A.1: The motivation for the experiments described in this thesis, along with section references.

Experimental technique	Section	Study and Motivation for the experiment
Raman spectroscopy	6.3.1	To monitor any changes in the Raman modes of the HiPco SWCNTs after surfactant wrapping that may suggest changes in sample purity or composition.
Raman spectroscopy	3.1.2	To investigate the effect that wetting of the SWCNT network has on the position, intensity and line shape of Raman modes.
UV-Vis-NIR absorption spectroscopy	3.1.2	To reveal the range of metallic and semiconducting carbon nanotubes present in the sample.
UV-Vis-NIR absorption spectroscopy	4.3.1	The investigate the effect of surfactant wrapping on the position of the SWCNT UV-Vis peaks
UV-Vis-NIR absorption spectroscopy	4.3.1	To determine the concentration of the SWCNT solutions using UV-Vis spectroscopy using method proposed in the literature.
Scanning electron microscopy	4.3.1	To qualitatively analyse the size and shape of the as received HiPco sample features.
Scanning electron microscopy	5.3.1	To estimate the thickness of the deposited SWCNT network films on alumina sensor substrates using side-on SEM, as well as the morphology and connectivity of the drop-coated SWCNT network films.

Table A.1: The motivation for the experiments described in this thesis, along with section references.

Experimental technique	Section	Study and Motivation for the experiment
Scanning electron microscopy	7.3.1	To confirm the presence of SWCNTs on the surface of the mixed layer SWCNT-Zeolite materials, as well as the inter-connectivity of the SWCNTs throughout the composite.
Scanning electron microscopy	7.3.1	To estimate the thickness of the deposited SWCNT-Zeolite films using side-on SEM.
Scanning electron microscopy	5.3.1	Qualitatively assessing the roughness of the Al_2O_3 sensor substrate.
Transmission electron microscopy	5.3.1	To quantitatively estimate the mean and range of SWCNT bundle sizes in the aqueous sample.
Transmission electron microscopy	5.3.1	To quantitatively estimate the mean and range of SWCNT diameters in the aqueous sample and compare with values provided by the manufacturer.
Transmission electron microscopy	5.3.1	To identify and classify the sizes of iron impurities in the HiPco sample.
Transmission electron microscopy	7.3.1	To approximate the sizes of zeolite particles used for the SWCNT-Zeolite mixed layer and overlayer sensors.

Table A.1: The motivation for the experiments described in this thesis, along with section references.

Experimental technique	Section	Study and Motivation for the experiment
Thermal gravimetric analysis	5.3.1	To study the decomposition of SWCNTs and impurities in both dry and aqueous samples when heated in air as described in the literature.
Hot-probe method	4.3.2	To confirm that the semiconducting portion of the drop-casted SWCNT networks behave as *p*-type semiconductors.
Hot-probe method	4.3.2	To investigate the *p*-type conductivity behaviour of the semiconducting SWCNTs in the drop-coated networks when exposed to water vapour.
Attenuated total reflectance-Fourier transform infrared spectroscopy	7.3.1	To infer possible reactions that take place upon the co-adsorption of water and NO_2 to the SWCNT-Zeolite composites
Energy dispersive X-ray spectroscopy	7.3.1	To establish the Si/Al ratios in the SWCNT-Zeolite composites.
Device current-voltage characterisation	4.3.2	To investigate the current- voltage behaviour of both thick and thin SWCNT networks when dry or wetted.

Table A.1: The motivation for the experiments described in this thesis, along with section references.

Experimental technique	Section	Study and Motivation for the experiment
Device current-voltage characterisation	6.3.1	To study the influence that the amount of carbon drop-coated on to the device has on I-V characteristics and the conductance/resistance of the devices.
Electronic transport measurements	6.3.1	To establish the I-V behaviour of the HiPco DOC SWCNT network devices in the 93 K to 300 K temperature range and to compare the results with those reported with proposed electronic transport models in the literature.
Humidity testing	4.3.2	To investigate qualitatively the changes in conductance observed upon exposure to humid air for both thick and thin networks of unfunctionalised SWCNTs on a Al_2O_3 substrate.
Humidity testing	4.3.2	To investigate qualitatively the changes in conductance observed upon exposure to humid air for both thick and thin networks of surfactant functionalised SWCNTs on a Al_2O_3 substrate.
Humidity testing	4.3.3	To quantify the changes in conductance, repeatability and obtain the calibration curves for SWCNT networks.

Table A.1: The motivation for the experiments described in this thesis, along with section references.

Experimental technique	Section	Study and Motivation for the experiment
NO_2 testing	5.3.2	To demonstrate the irreversible adsorption of NO_2 the the SWCNT networks under study.
NO_2 testing	5.3.3	To study the use of the WAR method to recover the baseline conductance of the SWCNT networks after exposure to NO_2
NO_2 testing	5.3.6	Assess the responses of the SWCNT networks to NO_2 over the 0.1 ppm to 120 ppm concentration range.
NO_2/humidity testing	6.3.2	Determine the effect of pre-adsorbed water on the conductive responses of SWCNT networks to NO_2
NO_2/humidity testing	6.3.4	Study how the thickness of the SWCNT films affects responses to NO_2 in humid environments
NO_2/humidity testing	7.3.2	To investigate the use of SWCNT-Zeolite composite materials for detection of NO_2 throughout changes in relative humidity.

Appendix B

Method for extraction of key SWCNT sensing parameters from sensor data

B.1 Testing implementation of method by calculating S_{max} and k values reported in the literature

To ensure the method proposed by Strano *et al* to extract the maximum possible conductive response, S_{max}, and adsorption rate, k, was implemented correctly in the current thesis, the intercept values quoted from their initial paper on the topic ([129]) were used to generate their reported S_{max} and k parameters.

The values are taken from Table 1. in ref [129] for the (a) DNA functionalised SWCNT sensors detecting the analyte $SOCl_2$ and (b) SDS functionalised SWCNT sensors detecting the analyte DMMP. The method is tested below to show that the same S_{max} and k parameters are calculated as those quoted in ref [129], Table 1.

B.1.1 (a) DNA functionalised SWCNT sensors detecting the analyte $SOCl_2$

The log-log form of equation to be plotted at different concentrations C_a to obtain two intercept values (c) is:

$$log_{10}\Delta G = log_{10}\left\{S_{max}[1-e^{-kC_at}]\right\} + log_{10}G_0 \tag{B.1}$$

where c is equivalent to:

$$log_{10}\left\{S_{max}[1-e^{-kC_at}]\right\} = c \tag{B.2}$$

The input values taken from Table 1 in ref [129]. The values must be unit-less to calculate k:

$$C_{100ppm} = 100\times10^{-6},$$
$$C_{50ppm} = 50\times10^{-6},$$
$$c1(intercept, 100_{ppm}) = -0.8291,$$
$$c2(intercept, 50_{ppm}) = -1.040,$$
$$t = 10$$

Input values into equation B.2 for two different concentrations of $SOCl_2$ and express B.2 in exponential form for each concentration:

$$S_{max}[1-e^{-k\times100\times10^{-6}\times10}] = 10^{-0.8291}, \tag{B.3}$$

$$S_{max}[1-e^{-k\times50\times10^{-6}\times10}] = 10^{-1.040}, \tag{B.4}$$

Re-arrange B.3 and B.4 to eliminate S_{max} so that only one unknown (k) is present:

$$\frac{1-e^{-k\times100\times10^{-6}\times10}}{1-e^{-k\times50\times10^{-6}\times10}} = 10^{(-0.8291-(-1.040))} \tag{B.5}$$

Equation B.5 is then solved numerically for k using a root finding algorithm (a software package provided with OriginPro 2017 was used, details of which can be found in appendix B.1.3 to give.

$$k = 940,$$

or in units of $ppt^{-1}s^{-1}$,

$$k = 9.4 \times 10^{-10}\ ppt^{-1}s^{-1},$$

which matches the k value quoted for the DNA system to $SOCl_2$ in ref [129]. The maximum possible conductive response, S_{max}, is then calculated by substituting k back in to equation B.3 or B.4, which both give:

$$S_{max} = 0.243,$$

which matches the S_{max} value quoted for the DNA system to $SOCl_2$ in ref [129], confirming that the method has been implemented correctly.

B.1.2 (b) SDS functionalised SWCNT sensors detecting the analyte DMMP

The log-log form of equation to be plotted at different concentrations C_a to obtain two intercept values (c) is:

$$log_{10}\Delta G = log_{10}\left\{S_{max}\left[1 - e^{-kC_at}\right]\right\} + log_{10}G_0 \tag{B.6}$$

where c is equivalent to:

$$log_{10}\left\{S_{max}\left[1 - e^{-kC_at}\right]\right\} = c \tag{B.7}$$

The input values taken from Table 1 in ref [129]. The values must be unit-less to calculate k:

$$C_{100ppm} = 100 \times 10^{-6},$$

$$C_{50ppm} = 50 \times 10^{-6},$$

$$c1(intercept, 100_{ppm}) = -1.479,$$

$$c2(intercept, 50_{ppm}) = -1.556,$$

$$t = 10$$

Input values into equation B.7 for two different concentrations of DMMP and express B.7 in exponential form for each concentration:

$$S_{max}[1 - e^{-k \times 100 \times 10^{-6} \times 10}] = 10^{-1.479}, \tag{B.8}$$

$$S_{max}[1 - e^{-k \times 50 \times 10^{-6} \times 10}] = 10^{-1.556}, \tag{B.9}$$

Re-arrange B.8 and B.9 to eliminate S_{max} so that only one unknown (k) is present:

$$\frac{1 - e^{-k \times 100 \times 10^{-6} \times 10}}{1 - e^{-k \times 50 \times 10^{-6} \times 10}} = 10^{(-1.479-(-1.556))} \tag{B.10}$$

Equation B.10 is then solved numerically for k using a root finding algorithm (a software package provided with OriginPro 2017 was used, details of which can be found in appendix B.1.3 to give:

$$k = 3280,$$

$$\text{or in units of } ppt^{-1}s^{-1},$$

$$k = 3.28 \times 10^{-9}\ ppt^{-1}s^{-1},$$

which matches the k value quoted for the SDS system to DMMP in ref [129].

The maximum possible conductive response, S_{max}, is then calculated by substituting k back in to equation B.8 or B.9, which both give:

$$S_{max} = 0.0345,$$

which matches the S_{max} value quoted for the SDS system to DMMP in ref [129], confirming that the method has been implemented correctly.

B.1.3 Root finding algorithm to find *k* numerically

An add on package to Origin Pro 2017 can be used to find the root of an equation numerically. The equation to be used is input with one unknown value, such as k:

$$\frac{1 - e^{-k \times 100 \times 10^{-6} \times 10}}{1 - e^{-k \times 50 \times 10^{-6} \times 10}} - 10^{(-1.479-(-1.556))} = 0 \tag{B.11}$$

The algorithm then proceeds as follows after the user specifies the x limits:

a In the x range specified by user, all intervals that contain a sign change in the function are first located.

b Each such interval is checked to see if the function is monotonic within that interval.

c In each of the intervals where the function is monotonic, a bisectional root search is performed: The interval is successively divided in half until either the maximum number of iterations is exceeded, or the root is found to a preset precision. The max iterations and root precision are set in the Origin C code as constants, and can be changed.

To view the code associated with this OPJ package add on, go to `http://originlab.com/fileExchange/details.aspx?fid=52` or alternatively Code Builder (menu item: View—Code Builder) and look at the Origin C file called find_roots.c in the Project branch of the Code Builder workspace tree.

Appendix C

Curve fitting procedure using Origin Pro 2017 to extract sensing parameters from data.

C.1 NO_2 sensing responses for SWCNT-based sensors fitted using the Origin Pro 2017 fitting tool and the irreversible model.

In this section, the Origin Pro 2017 fitting tool was used to extract k from the data presented in the paper by Lee *et al* ([14], Figure 2) for exposure of a polyethyleneimine (PEI) coated carbon nanotube based chemical sensor to 5 ppb NO_2 for 550 s. This was to compare the value of k extracted using the Origin Pro 2017 fitting method with the value reported for the same data in the literature, validating the use of the fitting tool for sensing parameter extraction.

The data and fitting is shown in Figure C.1. The displayed value of $k = 0.00723$ is in units of 5 ppb $^{-1}$ s^{-1} and so must be converted for comparison with the reported literature value:

$$\frac{0.00723}{5 \times 10^{-9}} \times 10^{-12} = 1.45 \times 10^{-6} ppt^{-1} s^{-1} \tag{C.1}$$

giving $k = 1.45 \times 10^{-6}$ ppt $^{-1}$ s^{-1}, which compares well with the reported litera-

ture value for this data of of 1.64×10^{-6} ppt^{-1} s^{-1}. The small discrepancy is probably due to their use of a different method and the difficulty in extracting the raw data from the plot presented in ref [14], Figure 2. This similar result validates the use of the Origin Pro 2017 fitting tool to fit the irreversible NO_2 adsorption model to the data collected using the WAR method in this thesis.

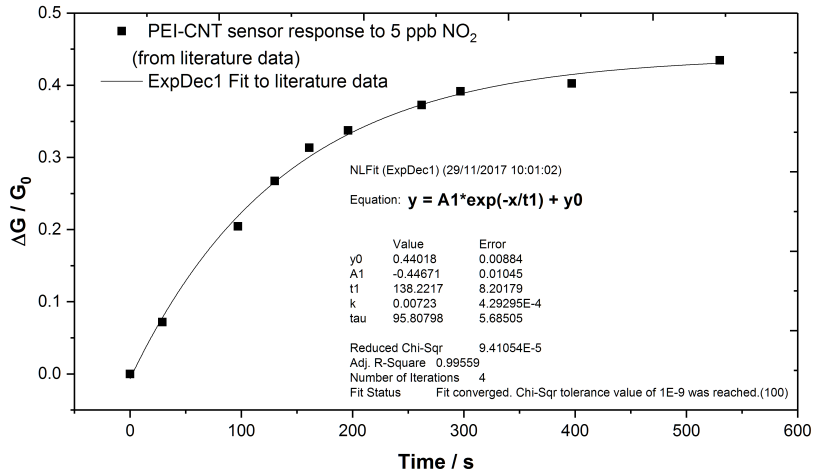

Figure C.1: Fitting of data extracted from ref [14] for exposure of polyethyleneimine (PEI) coated carbon nanotubes to 5 ppb NO_2 using the Origin Pro 2017 fitting tool to the "ExpDec1" function as highlighted in bold on the plot. The units of the displayed k are converted for comparison with literature values using equation C.1 so that $k = 1.45\times10^{-6}$ ppt^{-1} s^{-1}.

C.2 NO_2 sensing responses for SWCNT-based sensors fitted using the Origin Pro 2017 fitting tool and the partially reversible model.

In this section, the partially reversible adsorption model and Origin Pro 2017 fitting tool was used to extract $t_{1/2}$ values for the irreversible and reversible components of the raw data presented in the paper by Kumar *et al* ([15], Figure 4) for exposure of a SWCNT micro resistive chemical sensor to 0.5 ppm NO_2 for 4500 s. This was to compare the values of $t_{1/2}$ extracted using the Origin Pro 2017 fitting method with the values reported for the same data in the literature, where $t_{1/2}$ represents the

time required for the SWCNT sensor conductances to reach 50% of the maximum possible change in conductance for a given concentration, validating the use of the fitting tool for sensing parameter extraction.

The raw data from ref [15] and fitting is shown in Figure C.2. The displayed value of irreversible $t_{1/2}$ = 2125.26 s and reversible $t_{1/2}$ = 147.99 s compare well with those reported in Table 1 from ref [15] (irreversible τ_1 = 3066.69 and reversible τ_2 = 353.290), which when converted to $t_{1/2}$ values by multiplying by *ln(2)* give irreversible $t_{1/2}$ = 2125.67 s and reversible $t_{1/2}$ = 244.89 s. This suggests that using the Origin Pro 2017 fitting tool and the partially reversible model to extract the parameters is valid and comparable to the method reported in the literature [15].

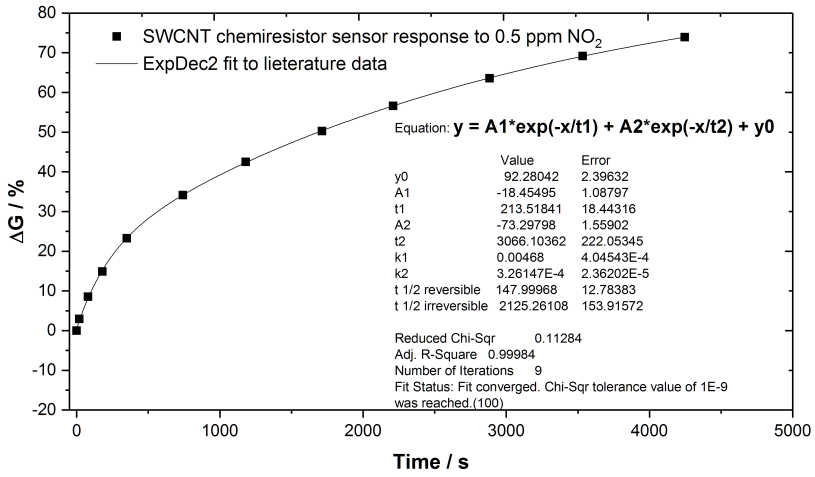

Figure C.2: Fitting of data extracted from ref [15] based on the partially reversible adsorption model for exposure of a SWCNT micro resistive chemical sensor to 0.5 ppm NO_2 using the Origin Pro 2017 fitting tool to the "ExpDec2" function, as highlighted in bold on the plot. The displayed value of irreversible $t_{1/2}$ = 2125.26 s and reversible $t_{1/2}$ = 147.99 s compare well with those reported in Table 1, ref [15].

As described in Chapter 5, based on the partially reversible NO_2 adsorption model, the conductive response as a function of time *S(t)* is given by:

$$S(t) = S_{max}\left\{1 - \frac{k_2}{m_1 - m_2}\left(\frac{1}{K} + \frac{m_1}{k_2}\right)e^{m_1 t} + \frac{k_2}{m_1 - m_2}\left(\frac{1}{K} + \frac{m_2}{k_2}\right)e^{m_2 t}\right\} \qquad \text{(C.2)}$$

where k_1 and k_2 refer to the irreversible and reversible adsorption sites respectively, and S_{max} is the maximum possible conductance change. The equilibrium constant of adsorption K is introduced to account for NO_2 desorption from reversible sites:

$$K = \frac{k_2}{k_{-1}} \tag{C.3}$$

where k_2 and k_{-1} are the adsorption and desorption constants for the reversible sites respectively. The roots m_1 and m_2 for equation 5.31 in Chapter 5, form part of the partially reversible adsorption model as detailed by Kumar *et al* [15] and are given by:

$$m_1, m_2 = \frac{-\left(k_1C + k_2C + \frac{k_2}{K}\right)}{2} \pm \frac{\sqrt{\left(k_1C + k_2C + \frac{k_2}{K}\right)^2 - 4\frac{k_1k_2C}{K}}}{2} \tag{C.4}$$

Equation C.2 can now be compared to the double exponential function used to fit the experimental data in Origin Pro 2017 and extract m_1 and m_2, which are eventually used to calculate k_1 and k_2, as is now detailed. The function used to fit the data in Origin Pro 2017 was of the form:

$$y = y_0 + (A_1)e^{-\frac{t}{\tau_1}} + (A_2)e^{-\frac{t}{\tau_2}} \tag{C.5}$$

If equation C.2 is compared to this form, then:

$$y_0 = S_{max}, \tag{C.6}$$

$$A_1 = S_{max}\left\{\frac{k_2}{m_1 - m_2}\left(\frac{1}{K} + \frac{m_1}{k_2}\right)\right\}, \tag{C.7}$$

$$A_2 = S_{max}\left\{\frac{k_2}{m_1 - m_2}\left(\frac{1}{K} + \frac{m_2}{k_2}\right)\right\}, \tag{C.8}$$

$$\frac{1}{\tau_1} = m_1, \tag{C.9}$$

$$\frac{1}{\tau_2} = m_2 \tag{C.10}$$

where $\tau_1 = 1 / m_1$ and $\tau_2 = 1 / m_2$ are the time constants for the irreversible

and reversible adsorption components respectively. These can be obtained using the Origin Pro 2017 fitting tool by fitting equation C.5 to the data, along with values for A_1, A_2 and S_{max} .

Dividing the component A_1 by A_2, an expressions for k_{-1} can be obtained:

$$\frac{A_1}{A_2} = \frac{S_{max}\left\{\frac{k_2}{m_1 - m_2}\left(\frac{1}{K} + \frac{m1}{k2}\right)\right\}}{S_{max}\left\{\frac{k_2}{m_1 - m_2}\left(\frac{1}{K} + \frac{m2}{k2}\right)\right\}} = \frac{\frac{1}{K} + \frac{m1}{k2}}{\frac{1}{K} + \frac{m2}{k2}} \tag{C.11}$$

$$K = \frac{k_2}{k_{-1}} \tag{C.12}$$

$$\frac{A_1}{A_2} = \frac{k_{-1} + m_1}{k_{-1} + m_2} \tag{C.13}$$

$$k_{-1} = \frac{A_2 m_1 - A_1 m_2}{A_1 - A_2} \tag{C.14}$$

k_{-1} can then be substituted into the re-arranged roots equation C.4 to solve for the irreversible and reversible adsorption constants k_1 and k_2 respectively, using the values for m_1 and m_2 obtained from the Origin Pro 2017 fitting function:

$$m_1 = \frac{-(k_1 C + k_2 C + k_{-1})}{2} + \frac{\sqrt{(k_1 C + k_2 C + k - 1)^2 - 4 k_1 k_{-1} C}}{2} \tag{C.15}$$

$$m_2 = \frac{-(k_1 C + k_2 C + k_{-1})}{2} - \frac{\sqrt{(k_1 C + k_2 C + k - 1)^2 - 4 k_1 k_{-1} C}}{2} \tag{C.16}$$

$$(m_1 + m_2)^2 = -k_1 C - k_2 C - k_{-1} \tag{C.17}$$

$$(m_1 - m_2)^2 = (k_1 C + k_2 C + k_{-1})^2 - 4 k_1 k_{-1} C \tag{C.18}$$

$$(m_1 - m_2)^2 = (m_1 + m_2)^2 - 4k_1k_{-1}C \tag{C.19}$$

$$k_1 = \frac{(m_1 - m_2)^2 - (m_1 + m_2)^2}{-4k_1k_{-1}C} \tag{C.20}$$

$$k_2 = \frac{(-m_1 - m_2 - k_1C - k_{-1})}{C} \tag{C.21}$$

Using this procedure, k_1 (4.96 x 10^{-4} ppm $^{-1}$ s^{-1}) and k_2 (0.00144 ppm $^{-1}$ s^{-1}) were calculated from the data presented by Kumar *et al* ([15], Figure 4) for 0.5 ppm exposure of a SWCNT chemiresistor to NO_2 and compared to those reported in the paper (k_1=1.51 x 10^{-5} ppm $^{-1}$ s^{-1}, k_2 = 0.00168 ppm $^{-1}$ s^{-1}), validating the method. The small discrepancy is most likely due to the difficulty in accurately extracting the data from ref [15].

This partially reversible adsorption model fitting procedure was then applied to the data collected in the current study for the HiPco DOC sensors using the WAR method to 60 ppm NO_2, to compare the values of k_1 (irreversible adsorption constant) and k_2 (reversible adsorption constant) with k (irreversible adsorption constant) obtained using the irreversible adsorption model and other literature values.

C.3 Using the Origin Pro 2017 fitting tool to fit sensor desorption curves.

In this section, the Origin Pro 2017 fitting tool was used to extract desorption time constants from literature data using a double exponential curve as described in the paper by Rigoni *et al* ([290], Figure 6) for exposure of a SWCNT chemiresistive sensor to 10 ppm NH_3 for 60 s. This was to compare the values of the desorption time constants extracted using the Origin Pro 2017 fitting method with the values reported for the same data in the literature, validating the use of the fitting tool for sensing parameter extraction.

The raw data from ref [290] and fitting is shown in Figure C.3. The displayed desorption time constants τ_1 = 13.3 s and τ_2 = 111.2 s, associated with fast and

slower desorption processes respectively, compare well with those extracted using the same method by Rigoni *et al* ([290], Figure 6, τ_1 = 16.7 s and τ_2 = 127.9 s). This suggests that using the Origin Pro 2017 fitting tool is appropriate to extract the desorption time constants from the sensing data presented in the current thesis.

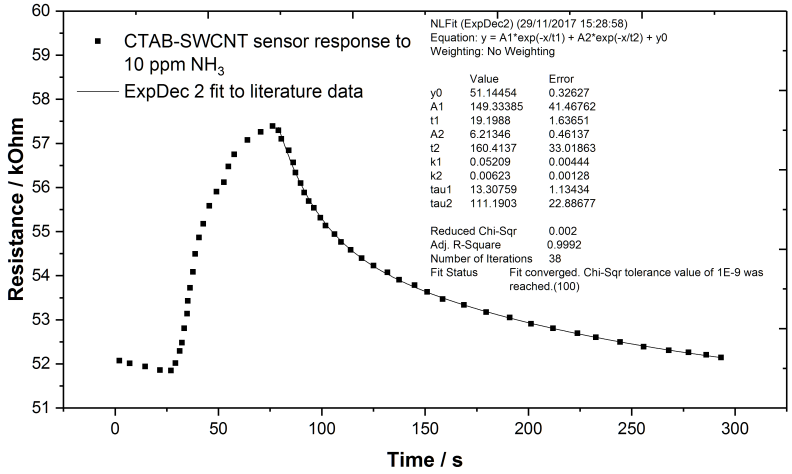

Figure C.3: Fitting of data from ref [290] to extract desorption time constants from literature data using a double exponential curve as described in the paper by Rigoni *et al* ([290], Figure 6) for exposure of a SWCNT chemiresistive sensor to 10 ppm NH_3 for 60 s. The displayed desorption time constants τ_1 = 13.3 s and τ_2 = 111.2 s, associated with fast and slower desorption processes respectively compare well with those extracted using the same method by Rigoni *et al*.

Appendix D

Potentiostat measurement circuit

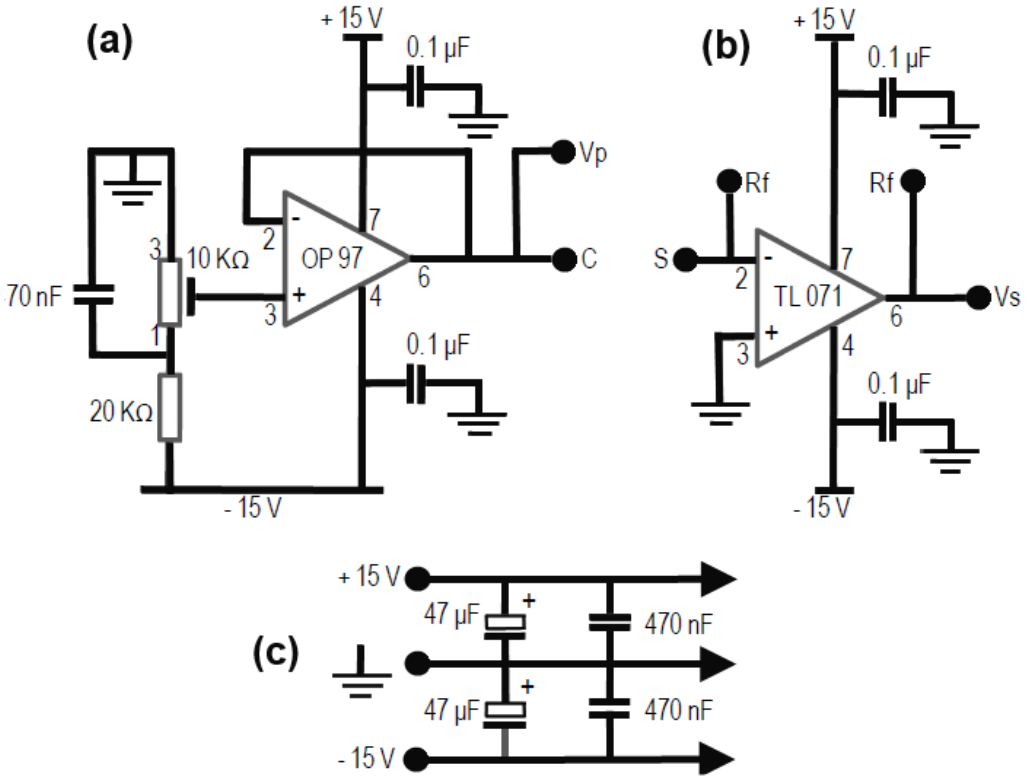

Figure D.1: The potentiostat measurement circuit. (a) shows the control circuit that supplies the probe voltage and (b) the measurement circuit. The sensor is connected between points C and S. The probe voltage is set and measured between Vp and ground, where as the voltage across the sensing element is measured between Vs and ground. (c) shows the circuit diagram for the power rail to the unit. The diagram has been adapted from the thesis of Dr. Ayo Afonja [226], which was based on a triple potentiostat unit designed by Dr. K F E Pratt [307].

Appendix E

Papers published from this thesis.

Nanoscale

PAPER

View Article Online
View Journal | View Issue

Cite this: *Nanoscale*, 2017, **9**, 11279

Switchable changes in the conductance of single-walled carbon nanotube networks on exposure to water vapour†

Gwyn. P. Evans, [a,b] David. J. Buckley, [b] Neal. T. Skipper [c,d] and Ivan. P. Parkin *[b]

We have discovered that wrapping single-walled carbon nanotubes (SWCNTs) with ionic surfactants induces a switch in the conductance-humidity behaviour of SWCNT networks. Residual cationic *vs.* anionic surfactant induces a respective increase or decrease in the measured conductance across the SWCNT networks when exposed to water vapour. The magnitude of this effect was found to be dependent on the thickness of the deposited SWCNT films. Previously, chemical sensors, field effect transistors (FETs) and transparent conductive films (TCFs) have been fabricated from aqueous dispersions of surfactant functionalised SWCNTs. The results reported here confirm that the electrical properties of such components, based on randomly orientated SWCNT networks, can be significantly altered by the presence of surfactant in the SWCNT layer. A mechanism for the observed behaviour is proposed based on electrical measurements, Raman and UV-Vis-NIR spectroscopy. Additionally, the potential for manipulating the sensitivity of the surfactant functionalised SWCNTs to water vapour for atmospheric humidity sensing was evaluated. The study also presents a simple method to establish the effectiveness of surfactant removal techniques, and highlights the importance of characterising the electrical properties of SWCNT-based devices in both dry and humid operating environments for practical applications.

Received 26th March 2017,
Accepted 20th July 2017

DOI: 10.1039/c7nr02141k

rsc.li/nanoscale

1. Introduction

The electronic properties of single-walled carbon nanotubes (SWCNTs) have prompted investigation into their use for numerous technological applications.[1–3] Individualised, bundled and networks of SWCNTs have been used as an alternative functional material in wide variety of electronic devices including field effect transistors (FETs),[4–7] transparent conducting films (TCFs),[8–14] and chemical sensors.[15–22] Networks of SWCNTs (a deposition of nanotubes containing many interconnecting bundles) display the aggregate electrical properties of the constituent SWCNTs,[23–25] facilitating the fabrication of devices for such applications in a more scalable and repeatable way.[26,27]

Much attention has been focused on advancing methods to sort and process SWCNT samples of at least similar electronic type (*i.e.* metallic or semiconducting nanotube samples).[28] Non-covalent functionalisation using a wide variety of surfactant molecules is applied as a route to disperse inherently hydrophobic nanotubes in water for sorting processes,[29–31] as well as for a wide variety of SWCNT device fabrication methods.[10,11,32–34]

While useful for liquid processing and the deposition of SWCNTs, the electrical properties of the fabricated devices can be significantly altered by the presence of surfactant,[35] due to the blocking of inter-nanotube connections in the network and increased contact resistance.[36,37] The removal of this residual surfactant is possible by washing,[35] annealing[38,39] or acid treatment.[37,40] The properties of deposited SWCNT networks are significantly dependent on the success and ramifications of such treatments.

In this work, we investigated the effect that surfactant has on the conductance of SWCNT networks when exposed to water vapour, in comparison with surfactant free samples. This is a critical consideration for many applications of SWCNTs, including touch screen displays[41] and environmental sensors,[42] as changes in the relative humidity of the operating environment may significantly interfere with device performance.

SWCNT networks were deposited after non-covalent functionalisation with a range of anionic, cationic and non-ionic surfactants. The magnitude and direction of the change in

[a]*Department of Security and Crime Science, University College London, 35 Tavistock Sq., London, WC1H 9EZ, UK*
[b]*Department of Chemistry, University College London, 20 Gordon St., London, WC1H 0AJ, UK. E-mail: i.p.parkin@ucl.ac.uk; Fax: +44 (0)20 7679 7463; Tel: +44 (0)20 7679 4669*
[c]*Department of Physics and Astronomy, University College London, Gower Street, London, WC1E 6BT, UK*
[d]*London Centre for Nanotechnology, 17-19 Gordon Street, London WC1H 0AH, UK*
†Electronic supplementary information (ESI) available. See DOI: 10.1039/C7NR02141K

conductance of the SWCNT networks upon exposure to water vapour was extremely dependant on the type of surfactant used, as well as the thickness of the SWCNT films. Based on this insight, the water sensitive properties of the surfactant containing films were manipulated to develop and evaluate humidity sensors using the SWCNT networks. The simple method used to establish the humidity sensing characteristics could be applied in the future to confirm the complete removal of surfactant from SWCNT based devices.

2. Experimental

2.1. Preparation of SWCNT solutions and devices

SWCNTs produced *via* the high pressure carbon monoxide disproportionation (HiPco) process[43] (purchased from Nanointegris, batch number: R1-831) were dried in air at 120 °C to remove moisture from the bundles and stored under vacuum.

For the HiPco SWCNT control sample, the black powder was added to water (H_2O, CAS number: 7732-18-5, HPLC grade) at a concentration of approximately 2 mg mL^{-1}. To prepare the test samples, the SWCNTs were added to aqueous solutions containing the following surfactants at 0.5 wt%: sodium deoxycholate (DOC, CAS number: 302-95-4, 97%), sodium cholate (SC, CAS number: 206986-87-0, 97%), hexadecyltrimethylammonium bromide (CTAB, CAS Number: 57-09-0, 98%), hexadecyltrimethylammonium *p*-toluenesulfonate (CTAT, CAS number: 138-32-9) or Triton X-100 (CAS number: 9002-93-1) purchased from Sigma-Aldrich. The initial carbon concentration was approximately 2 mg mL^{-1} for the HipCo SWCNT surfactant solutions. Surfactant molecules form micelle like structures around the nanotubes allowing dispersion in water. To aid efficient solubilisation and debundling of the tubes *via* surfactant wrapping, the solution was sonicated using a tip sonication probe at a power of 225 W for 15 minutes, with the container placed in an ice bath for cooling.

The surfactant treatment resulted in well dispersed solutions, whilst the carbon in the control sample was highly agglomerated. The samples were centrifuged at 4000*g* for 30 minutes and the upper 80% of the supernatant was decanted to limit the presence of carbonaceous impurities and highly bundled SWCNTs in the final concentrated solution. Diluted samples were also obtained by dilution of the concentrated solutions in deionised water.

3 × 3 mm alumina tiles with patterned gold electrodes of 175 μm separation (as shown in Fig. 1) were used as the substrate to facilitate measurement of the conductance across the SWCNT networks. The HiPco SWCNT solutions were deposited across the interdigitated gold electrodes using a calibrated Finnpipette novus electronic single-channel micro pipette (drop volume 1 μL per sensor) and left to dry in air at 23 °C for 24 hours to form chemiresistor type devices.

Thick network devices were formed using the concentrated solutions detailed in Table 1, with a thickness of 19 ± 5 μm as

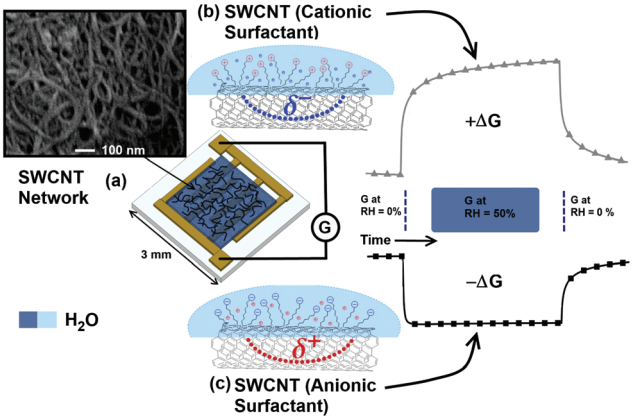

Fig. 1 Schematic representation of (a) the surfactant functionalised HiPco SWCNTs deposited on an alumina substrate between interdigitated gold electrodes. The conductance (*G*) across the formed percolating network is measured in both dry and humid conditions. An SEM image of a typical SWCNT network is inset top-left. A representation of the induced electrostatic potential upon exposure to water vapour is shown in (b) for cationic and (c) anionic surfactant containing networks, with the respective increase (+Δ*G*) and decrease (−Δ*G*) in conductance indicated when the relative humidity (RH) increases.

confirmed using a microscope (see Fig. S7 in the ESI†) and a device resistance of R_{thick} = 200 Ω to 500 Ω. Thin films were formed using the diluted solutions displayed in Table 1, with a thickness <1 μm and a device resistance of R_{thin} = 50 kΩ to 200 kΩ.

2.2. Characterisation techniques

The UV-Vis-NIR absorption spectra for each of the decanted SWCNT surfactant solutions were obtained using a PerkinElmer Lambda 950 spectrophotometer to estimate the concentration of carbon in the aqueous solutions. The initial decanted solution was diluted (between 1000× and 50× dilution from the initial solution with deionised H_2O) to enable experimental measurement of absorbance. Multiple spectra were recorded in the 180 nm to 1300 nm range for dilutions of each SWCNT surfactant solution, using a quartz cuvette with a path length 1 cm. The background absorbances for the blank H_2O surfactant solutions were subtracted. The relevant extinction coefficients (ε_λ) experimentally determined by Goak *et al.*[13] (SWCNTs stabilised with CTAB: ε_λ = 34.5 mL mg^{-1} cm^{-1}, SWCNTs stabilised with SC: ε_λ = 33.6 mL mg^{-1} cm^{-1}) at a wavelength of 700 nm were used to approximate the carbon concentration for each of the diluted solutions.

A linear relationship between the volume of decanted SWCNT solution present in the diluted aqueous solution *vs.* the absorbance was observed. The Beer–Lambert law,

$$C = \frac{A_\lambda}{\varepsilon_\lambda l}, \quad (1)$$

where A_λ, ε_λ and l are absorbance, extinction coefficient at a specific wavelength λ and optical path length respectively, was used to calculate the concentration of the diluted and concen-

Table 1 Parameters of the HiPco SWCNT networks and their conductance behaviour when exposed to water vapour

Surfactant type (ionicity)	DOC (anionic)	SC (anionic)	CTAB (cationic)	CTAT (cationic)	Triton X-100 (non-ionic)	Control (surfactant free)
Solution concentration (concentrated/diluted, mg mL^{-1})	1.59 ± 0.2/ 0.0108 ± 0.001	0.51 ± 0.05/ 0.004 ± 0.0004	1.61 ± 0.2/ 0.0102 ± 0.001	0.91 ± 0.1/ 0.00453 ± 0.001	0.46 ± 0.05/ 0.00496 ± 0.001	0.64 ± 0.1/ 0.531 ± 0.07
Network conductance change (ΔG) upon exposure to H_2O (thick/thin networks)	Decrease/ decrease	Decrease/ decrease	Increase/ increase	Decrease/ increase	Increase/ decrease	Increase/ decrease
Conductance sensitivity ($\Delta G\%$ $\Delta RH\%^{-1}$) to H_2O (thick/thin networks)	−0.49/−0.11	—	0.057/0.17	—	—	0.016/−0.041

trated SWCNT solutions as displayed in Table 1. The surfactant free SWCNT control sample values are included to enable an approximate comparison, although the carbon agglomerated in the control solutions formed without the use of surfactant, decreasing the accuracy of the UV-Vis concentration measurement. The approximate carbon concentrations of the concentrated decanted SWCNT solutions were calculated using a linear fit to the diluted absorbance data.

The mass filtration method was applied to obtain a secondary comparison with the estimated UV-Vis-NIR concentration. A mass balance with 0.01 mg sensitivity was used to obtain the mass of a PTFE filter membrane before and after 600 μL of the HiPco DOC suspension was deposited and dried *via* vacuum filtration. The difference in mass after the deposition was calculated and the mass of the surfactant (derived from the molecular weight of DOC) subtracted to estimate the mass of carbon deposited on the membrane. Three HiPco DOC samples were prepared, with the average carbon concentration calculated as 1.4 ± 0.2 mg mL^{-1}, in good agreement with the UV-Vis-NIR based calculations displayed in Table 1.

A Renshaw inVia Raman microscope with laser wavelength λ = 785 nm and 1 mW power was used to perform Raman spectroscopy on each of the surfactant wrapped HiPco SWCNT thick films after deposition and drying on 3 × 3 mm alumina substrates. Wet measurements were obtained by depositing 1 μL of deionised water (H_2O, CAS number: 7732-18-5, HPLC grade) on top of the SWCNTs and re-obtaining the Raman spectra.

A Jeol JSM-6700F field emission scanning electron microscope (SEM) was used in secondary electron imaging mode using a 5 kV probe voltage at a working distance of 5.9 mm to obtain micrographs of the SWCNT networks.

The hot probe method (as described by Golan *et al.*[44]) was used to confirm that the networks contained sc-SWCNTs and displayed p-type behaviour. Either the HiPco control sample, the HiPco DOC or HiPco CTAB containing films were deposited on a glass substrate. The potential difference across the films was measured using a Keithley 2100/230–240 digital multimeter. A positive probe was heated to a set temperature while in contact with the SWCNT network using a soldering iron tip and the induced change in potential was recorded. A negative voltage at the heated probe indicates that holes are the majority charge carrier in the semiconducting portion of the network as described previously.[44]

2.3. Humidity testing

The SWCNT networks (deposited on alumina substrates between interdigitated gold electrodes) were placed in electrical read out ports within a cylindrical testing chamber to measure the change in device conductance as a function of relative humidity (RH). The circular arrangement of the devices, along with the extraction of air behind each individual port location, ensures that each device is exposed to an equal flow of dry or humid air. The air flow rate of dry synthetic air (BOC certified synthetic air, 20% pure oxygen, 80% pure nitrogen, CAS number: 132259-10-0) was controlled using digital mass flow controller 1 (MFC 1). Wet air was generated by flowing dry synthetic air through a Drechsel flask (controlled using MFC 2) containing 500 mL of deionised water (HPLC grade, CAS number: 7732-18-5). Dry air and wet air were mixed at different ratios using the mass flow controllers and delivered to the testing chamber *via* a central inlet to achieve between 0% and 90% RH in the testing chamber, confirmed using an internal humidity meter. A potentiostat setup[45] was used to measure the room temperature device conductance with a 100 mV bias applied throughout the testing procedure.

Prior to the experiments, dry synthetic air was passed over the sensors for 2 hours to obtain a baseline conductance (G_0) for each device and achieve 0% relative humidity in the chamber. A mixture of dry and wet air was then introduced to the chamber for 600 s to achieve to the required humidity level and the new device conductance was measured (G). This was followed by a 1200 s intermediary step in which the relative humidity was re-adjusted to 0% and G_0 was re-established before the next incremental humidity testing step (in the range of 20% to 90% RH).

3. Results and discussion

The aqueous solutions of HiPco SWCNTs, non-covalently functionalised with the range of surfactants detailed in Table 1, were first characterised using UV-Vis-NIR absorption spectroscopy. Multiple peaks in the 400 nm to 1000 nm range of the UV-Vis-NIR absorption spectra (Fig. 2) indicate a mixture of metallic SWCNTs (m-SWCNTs) and semiconducting SWCNTs (sc-SWCNTs) in each of the aqueous solutions[46] at high (0.5 to 1.8 mg mL^{-1}) and low (0.004 to 0.01 mg mL^{-1})

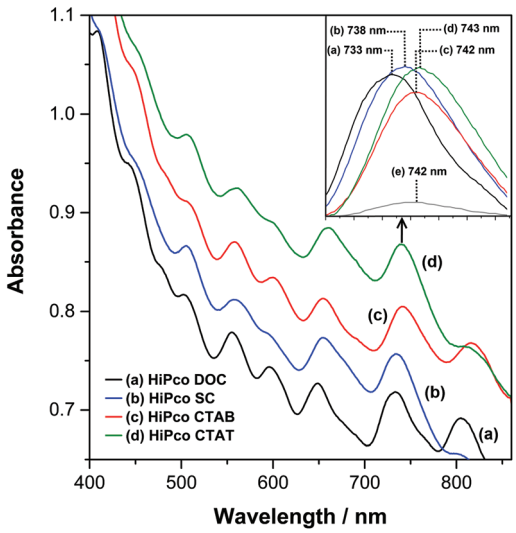

Fig. 2 UV-Vis absorption spectra obtained using an Elmer Lambda 950 spectrophotometer for aqueous solutions of HiPco SWCNTs non-covalently functionalised with (a) DOC, (b) SC, (C) CTAB and (d) CTAT. The inset top-right plot shows the shift in the 705–775 nm range peaks for the respective samples relative to (e) dry HiPco DOC on a quartz slide. (a)–(d) are offset by 0.05 absorbance for clarity and were 100× dilutions of the initial concentrated solutions.

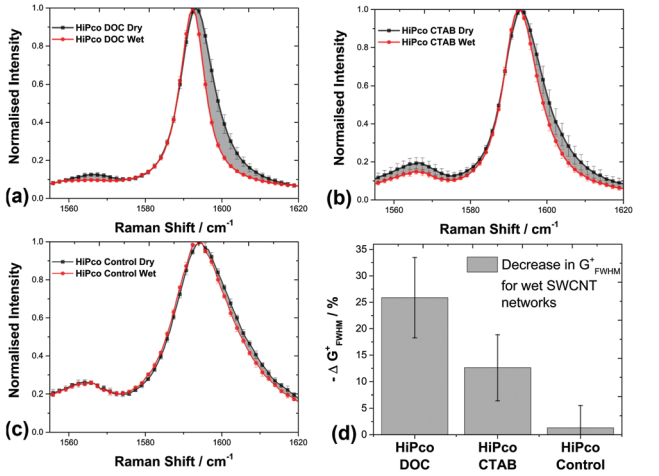

Fig. 3 The normalised Raman spectra of dry and wet SWCNT networks containing (a) anionic DOC, (b) cationic CTAB and (c) no surfactant. The differences in line-shape of the G^+ (at 1593 cm^{-1}) and G^- (at 1565 cm^{-1}) band before and after wetting are highlighted in (a)–(c) by grey shading. The error bars represent the standard deviation between measurements of 3 different spots on the SWCNT film after normalisation of intensity. The percentage decrease in full width at half maximum (FWHM) of the G^+ band before and after wetting is shown in (d), where the error bars represent the error on the measurement of the peak FWHM. Raman spectroscopy was performed using a Renshaw inVia Raman microscope with laser wavelength λ = 785 nm and 1 mW power.

concentrations, as to be expected for non-sorted HiPco SWCNTs.[47] The approximate concentrations of the SWCNT solutions are detailed in Table 1.

The peaks are red or blue shifted at various wavelengths if dispersed using a cationic or anionic surfactant, compared with a dry sample of SWCNTs on quartz. This effect has previously been attributed to the varying charge imparted on the tubes when surfactant wrapped in aqueous solution, as well as to nanotube bundling in poorly dispersed samples.[48]

Raman spectroscopy was performed on the thick SWCNT networks (thickness = 19 ± 5 μm) after deposition on to the alumina substrates, firstly in ambient conditions (room temperature = 23 °C, relative humidity = 45%). The ratio of the G^+-bands at 1594 cm^{-1} to D-bands at 1295 cm^{-1} indicates good sample purity (see Fig. S2–S4 in the ESI†).[49] The radial breathing modes (RBMs) in the range 100 cm^{-1} to 500 cm^{-1} suggest that nanotubes of different chirality and thus electronic type are also present in the deposited layer,[49] in agreement with the UV-Vis-NIR data.

Each of the samples was wetted with 1 μL of deionised water and Raman measurements were re-acquired as detailed in the Experimental section. The full width at half maximum (FWHM) of the G^+ band decreases significantly for the wet surfactant containing networks (see Fig. 3). Previous studies have found that the Breit–Wigner–Fano (BWF) component of the G^--band is suppressed for some surfactant m-SWCNTs aqueous systems compared to the dry equivalent.[48] As an intrinsic feature of bundled m-SWCNTs, perturbation of the SWCNT electronic charge by the charged groups present in the surfactant molecule is thought to be partially responsible for the change in the BWF feature. Also, the intensity, FWHM and frequency of the G^+ band for sc-SWCNTs can be altered by the application of a gate voltage,[50,51] suggesting that any additional potential difference due to water–surfactant interactions should induce changes in the G^+-band line-shape.

In the current study, the decrease in FWHM of the G^+ band, along with the suppression of the G^-, is treated as a proxy for a change in the gate/charge sensitive G^+ band and BWF component respectively. Therefore, the different G-band line-shapes highlighted in Fig. 3 suggest that exposure to water alters the interaction between the charged groups present in the SWCNT-surfactant system. This in turn implies that the electronic properties of SWCNT based devices containing residual surfactant could be altered due to electrostatic interactions upon exposure to water vapour.

Networks of HiPco SWCNTs functionalised with the range of surfactants listed in Table 1 were deposited between gold electrodes and their electrical conductance was recorded in a humidity controlled chamber (described in the Experimental section). The thickness and density of randomly orientated SWCNT films is important when considering gas sensing mechanisms[52,53] and charge transport in the network.[54] Previous work by Battie *et al.*[55] has shown that SWCNT sensing behaviour changes with a reduction in the number of m-SWCNTs in the film. Randeniya *et al.*[56] found that thinner networks of SWCNTs are more influenced by the substrate. Therefore, surfactant functionalised SWCNT devices based on both thick films (thickness = 19 ± 5 μm, device resistance R_{thick} = 200 Ω to 500 Ω) and thin films (thickness <1 μm,

device resistance R_{thin} = 50 kΩ to 200 kΩ) were fabricated to investigate how these quantities affect the conductance behaviour in humid conditions.

As is displayed in Fig. 4, the conductance of each network is sensitive to water vapour. At certain time intervals, the relative humidity of the testing chamber is increased and a new steady state conductance value (G) for the network is reached after time t_{90}. The chamber humidity is then reset to 0% and the conductance returns to baseline value (G_0).

Fig. 4 and 5 demonstrate that the magnitude and direction of the change in conductance is strongly dependent on the type of surfactant present in the network. When surfactants possessing charged groups are present in the films, the change in conductance is one order of magnitude larger than those without surfactant (the control HiPco SWCNT sample). For the SWCNTs non-covalently functionalised with anionic surfactant (DOC, SC), the conductance decreases upon exposure to water vapour. However, those functionalised with cationic surfactant (CTAB, CTAT) show an increase in conductance when the humidity of the chamber is increased. This is evidence that the head groups and counterions of the ionic surfactants contribute significantly to the electrical properties of the SWCNT networks when exposed to water vapour.

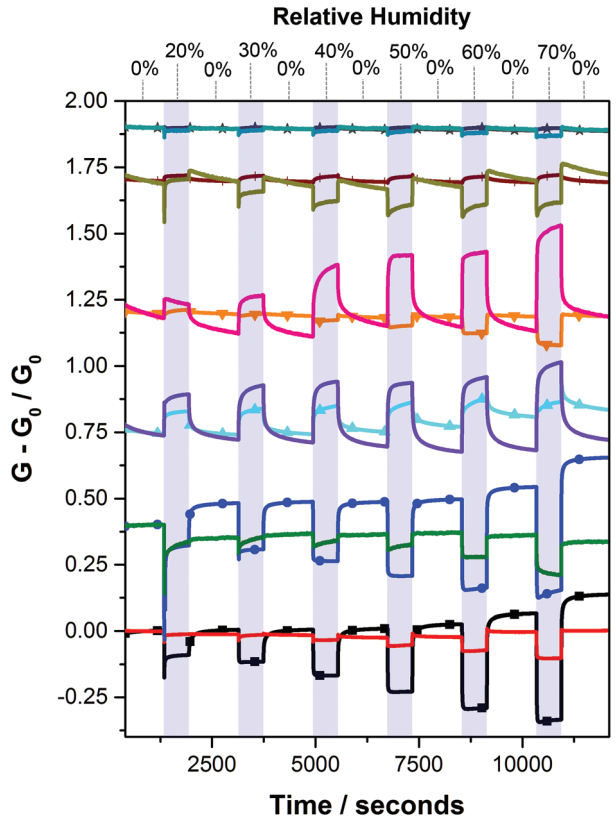

Fig. 4 Real time changes in SWCNT network conductances (where G_0 is the baseline conductance at RH = 0% and G is the conductance at higher RH levels) as the relative humidity of the testing chamber is modulated between 0% RH and higher humidity (in the 20% to 70% RH range, as indicated by the top x-axis and blue shaded regions) for thick (thickness = 19 ± 5 μm, dense) networks of (■) HiPco DOC, (●) HiPco SC, (▲) HiPco CTAB, (▼) HiPco CTAT, (+) HiPco Triton X-100 and (★) HiPco control samples. Results for thin (thickness <1 μm, lower-density) networks are plotted without a symbol at the same y-axis offset as their respective sample type. Plots are offset for clarity.

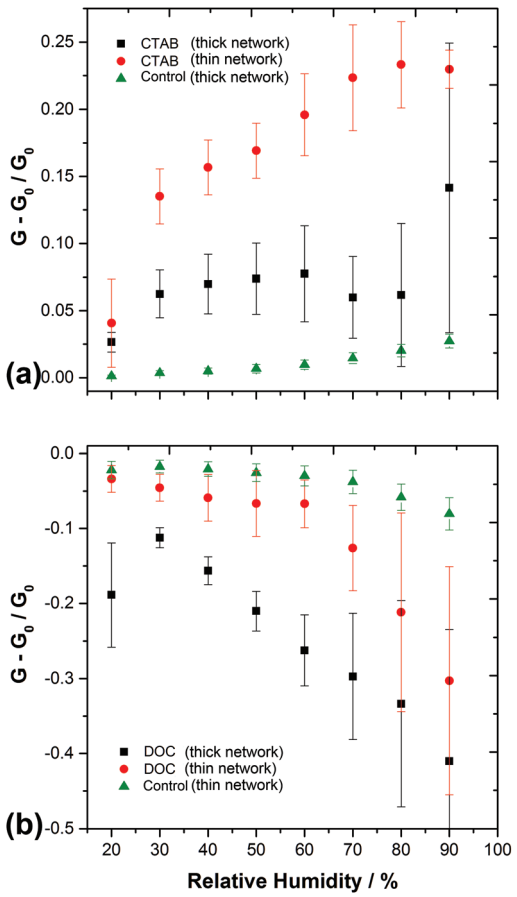

Fig. 5 Magnitude and direction of conductance change for SWCNT network humidity sensors. (a) (■) HiPco CTAB thick (dense) network, (●) HiPco CTAB thin (lower-density) network and (▲) thick HiPco control sample containing no surfactant. (b) (■) HiPco DOC thick (dense) network, (●) HiPco DOC thin (lower-density) network and (▲) thin surfactant free HiPco control sample. The error bars represent the standard deviation of responses from two identical humidity sensors of the same type.

Electrolyte solutions have been utilised to gate SWCNT FETs.[22,57] An applied potential causes a re-distribution of charges in the solution, imparting a potential on the nanotubes and causing changes in the intensity, position and line-shape of the SWCNT Raman bands.[50] Such changes in the G^+ and G^- bands are observed for the wetted SWCNT networks containing surfactant in the current study (Fig. 3). The previous use of liquid gated devices, along with the change in line-shape of the G^+ and G^- bands, indicates that the interaction of the surfactant molecule and counterions with the nanotubes (upon wetting) modulates conduction, effectively gating the SWCNT networks under investigation.

Goak *et al.*[13] proposed that for anionic surfactants such as SC, the Na^+ counterion interacts with both m-SWCNTs and

sc-SWCNTS electrostatically in dry network films. When such a film is wetted, re-orientation of the surfactant molecules on the surface takes place (in this case the surface of the SWCNTs in the network).[58] Therefore, the re-arrangement of the hydrophilic, negatively charged head groups away from the tubes upon wetting would increase the density of positive charges (Na^+ for DOC and SC) interacting electrostatically with the nanotubes. This would explain the decrease in conductance through the networks containing residual anionic surfactant.

Conversely, the same re-arrangement of the positively charged, hydrophillic head group for the CTAB containing films would increase the density of Br^- counterions interacting with the tubes, inducing a distributed negative charge (δ^-) and increasing electron conduction (or decreasing hole density) through the SWCNTs. This proposed mechanism for the respective decrease or increase in conduction for the anionic/cationic surfactant containing films is represented schematically in Fig. 1. The red or blue shifts seen in the SWCNT-surfactant UV-Vis data with respect to the dry samples (Fig. 2, inset), further suggests a change in electrostatic potential, depending on the surfactant–nanotube interaction in water.

Bernardes *et al.*[59] measured a humidity dependent electrostatic potential on the surface of ionic surfactant films, which supports the hypothesis that atmospheric water can change the imparted potential on the SWCNTs in the surfactant containing networks. Additionally, positively charged species (such as the Na^+ counterion present in SC and DOC) have previously been found to reduce DC conductance through SWCNTs suspended in liquid water.[60]

It is not expected that swelling of the surfactant functionalised SWCNT film is solely responsible for the change in network conductance. Although swelling is expected to occur in surfactant films upon exposure to water vapour,[61–64] it would always decrease the number of nanotube–nanotube conductive pathways (decreasing film conductance), thus does not account for the increase in conductance of films containing residual cationic agents.

The conductance of the control SWCNT device (containing no surfactant) is also affected by water vapour, although to a lesser extent than the surfactant treated samples. It has been previously reported that water induces n-type[65,66] or p-type[56,67–69] responses from carbon nanotubes, causing a change in the conductance of ropes and bundles. The study by Bell *et al.*[70] suggested that this effect is attributable to electrostatic interactions. The permanent dipole moment of water induces a polarisation of electronic charge density in the nanotube over a long range (3 nm). Lekawa-Raus *et al.*[71] also suggested that chemical doping does not occur in carbon nanotube fibres, with water vapour instead interacting with the nanotubes at CNT–CNT junctions. If this is the case, then it is to be expected that residual charged species in the network, such as ionic surfactants, increase the polarisation of charge upon exposure to water vapour and thus the magnitude of the conductance change observed in Fig. 5.

Thinner SWCNT networks are increasingly influenced by the substrate and a higher proportion of SWCNTs in the film contribute towards sensing behaviour.[56] Furthermore, contact resistance between SWCNTs,[24] bundling and electrostatic environment[26] influence charge transport in macroscopic networks. In low-density networks of non-sorted SWCNTs below the m-SWCNT percolation threshold, conductance is increasingly dominated by Schottky barrier modulation at the interface between sc-SWCNT and the electrodes or m-SWCNTs, while thick networks have complete metallic conduction paths with the resistance of the film dominated by nanotube-nanotube junctions.[55] Accordingly, the effect of residual surfactant and water vapour was found to differ in thin (and thus lower density) networks.

As a higher proportion of SWCNTs are exposed to the analyte in a thin network, a larger ΔG was expected for thinner SWCNT films. This was the case for the SWCNT control, non-ionic and cationic samples. However, the real time humidity response plots in Fig. 4 show that the opposite is true for thin anionic SWCNT films. Fewer metallic pathways exist in the thinner samples, with the conduction properties of the network increasingly dominated by Schottky barrier modulation between the sc-SWCNTs and m-SWCNTs or the gold electrodes. As chemiresistor type devices are used, there is no applied gate voltage to activate conduction through the sc-SWCNTs in the dry state. However, in a way analogous to electrolyte gated SWCNT transistors, wetting of the film and re-arrangement of surfactant counterions may activate (or reduce, depending on the counterion) conduction through the sc-SWCNTs. Thus, the differences in conductance-humidity behavior of thick *vs.* thin networks (thickness = 19 ± 5 μm, thickness <1 μm respectively) containing anionic or cationic surfactant may be caused by the increasing influence of the counterion on the sc-SWCNTs in the mixed chirality films.

Reducing the thickness of the SWCNT control sample (surfactant free) switches the direction of the conductive response so that conduction through the network is instead reduced after exposure to water vapour (Fig. 5). Veeramasuneni *et al.*[72] found that an alumina substrate is positively charged at pH 7 upon wetting. If this is the case, the net positive charge may impede electron conduction in the thinner SWCNT control sample, as well as interact with the charged head groups to produce the unexpectedly lower ΔG for the thin network anionic (DOC and SC) samples.

The hot probe method has been applied previously to determine the charge carrier type in sc-SWCNT networks.[73] The recorded negative voltage upon probe heating (as shown in Fig. S5 and S6 in the ESI†) indicates that the semiconducting nanotubes in the DOC, CTAB and control (surfactant free) networks are p-type, in line with previous studies of SWCNTs exposed to ambient conditions. The p-type change in potential for the CTAB containing SWCNT network after application of the hot probe (as shown in Fig. S6†) is approximately one order of magnitude lower than the change for the DOC or control network, suggesting the CTAB containing film is less p-type.

As detailed in the ESI,† the setup was adapted so that a segment of the thick (dense) network film could be exposed to

water vapour without contacting the hot probe, held at a temperature in the range of 160 °C to 200 °C. The change in potential, firstly due to the application of the hot probe and then due to increasing humidity, was recorded. The potential difference across the DOC containing film increases in magnitude and remains negative when more water vapour is present, whereas the potential across the CTAB film increases in magnitude upon application of the hot probe, but decreases and moves towards a positive value when H_2O is introduced (see Fig. S6a and S6b in the ESI†). This indicates that in the CTAB containing networks, exposure to water vapour decreases the p-type behaviour of the sc-SWCNTs in the semiconducting portion of the film. A decrease in the p-type character of sc-SWCNTs would decrease inter-tube resistances between metallic and p-type semiconducting nanotubes, which may explain the overall increase in conductance for the SWCNT-CTAB films upon exposure to water. Correspondingly, the increase in p-type nature of the sc-SWCNTs in the DOC network results in an overall conductance drop, potentially due to increased inter-tube resistances.

When the surfactant containing films are wetted, the current–voltage relationship across the SWCNT network becomes non-linear (as shown in Fig. S8 in the ESI†). It is thought that the counterions impart a partial potential on the SWCNTs in a fashion analogous to electrolyte gating of CNT network FETs. While the Raman bands also display similar changes to line shape observed for electrolyte gated CNT devices,[50] further work is required to confirm this hypothesis.

Monitoring of humidity is important for industrial processes, commercial and domestic technologies.[74,75] The high sensitivity and reversibility of the SWCNT network conductances upon adsorption and desorption of water vapour indicates that the chemiresistors may be useful as humidity sensors. The conductance-humidity behaviour is predictable and repeatable between multiple identical devices, as shown in Fig. 5, with the chemiresistors containing ionic surfactant functionalised SWCNTs showing the largest ΔG. The percentage change in conductance per percentage change in relative humidity, as displayed in Table 1, compares well with values for carbon nanotube based humidity sensors in the literature ($-0.5\%\ RH\%^{-1}$ from Liu *et al.*[76] and $-0.7\%\ RH\%^{-1}$ by Han *et al.*[77]). Some signal drift was observed after exposure to higher levels of relative humidity. This may be addressed by optimising the SWCNT to surfactant ratio and the thickness of the sensing layer.

The devices are low-powered (operating at room temperature), affordable and could be easily incorporated into a sensing array. Furthermore, industrially viable solution based fabrication techniques, such as screen printing or spray coating, could be used for large scale manufacture of such sensors.

4. Conclusions

Conductance through SWCNT networks can be altered *via* adsorption or desorption of water from the atmosphere. The change in conductance of surfactant containing samples in this study was attributed to the electrostatic interaction of water molecules with the SWCNTs in the network, rather than to chemical doping.

Ionic surfactants in the SWCNT films can enhance the change in conductance by a factor of 10. SWCNTs functionalised with cationic surfactants (CTAB and CTAT) demonstrate an increase in conductance upon exposure to water vapour, whereas anionic agents (DOC and SC) have the opposite effect, causing the conductance to decrease. It is suggested that this behaviour is due to the interaction of polar water with the charged head groups and counterions of the ionic surfactants, which impart a partial potential on the SWCNTs.

In line with previous reports, the substrate influences the SWCNT–analyte interaction, enhancing the humidity induced conductance change for thin SWCNT control (surfactant free) networks. Moreover, differences in conductance-humidity behavior of thin *vs*. thick networks containing anionic or cationic surfactant were attributed to the varying contribution of sc-SWCNTs to conduction across the wetted films.

SWCNT networks functionalised with ionic surfactants display fast and reversible humidity sensing behaviour. Optimising the thickness and type of ionic surfactant may in future enable the development of low powered humidity sensors based on SWCNT networks. Additionally, through investigation of the SWCNT network conductance-humidity behaviour, this study provides a method to evaluate the success of various surfactant removal strategies. The observed intrinsic sensitivity to water vapour demonstrates the importance of assessing the characteristics of SWCNT based devices in humid environments.

Acknowledgements

The authors thank Dr Steve Firth for instrumentation assistance. This work was carried out under EPSRC Grant EP/M506448/1 and EPSRC Grant EP/G037264/1 as part of UCL's Security Science Doctoral Training Centre.

References

1 B. Liu, C. Wang, J. Liu, Y. Che and C. Zhou, *Nanoscale*, 2013, **5**, 9483–9502.
2 K. Chen, W. Gao, S. Emaminejad, D. Kiriya, H. Ota, H. Y. Y. Nyein, K. Takei and A. Javey, *Adv. Mater.*, 2016, **28**, 4397–4414.
3 M. F. L. De Volder, S. H. Tawfick, R. H. Baughman and A. J. Hart, *Science*, 2013, **339**, 535–539.
4 Q. Cao and S. j. Han, *Nanoscale*, 2013, **5**, 8852–8863.
5 E. Penzo, M. Palma, D. A. Chenet, G. Ao, M. Zheng, J. C. Hone and S. J. Wind, *ACS Nano*, 2016, **10**, 2975–2981.
6 S. Park, G. Pitner, G. Giri, J. H. Koo, J. Park, K. Kim, H. Wang, R. Sinclair, H.-S. P. Wong and Z. Bao, *Adv. Mater.*, 2015, **27**, 2656–2662.

7 K. Balasubramanian, R. Sordan, M. Burghard and K. Kern, *Nano Lett.*, 2004, **4**, 827–830.
8 S. B. Yang, B. S. Kong, D. H. Jung, Y.-K. Baek, C.-S. Han, S. K. Oh and H. T. Jung, *Nanoscale*, 2011, **3**, 1361–1373.
9 A. Shimoni, S. Azoubel and S. Magdassi, *Nanoscale*, 2014, **6**, 11084–11089.
10 Z. Wu, Z. Chen, X. Du, J. M. Logan, J. Sippel, M. Nikolou, K. Kamaras, J. R. Reynolds, D. B. Tanner, A. F. Hebard and A. G. Rinzler, *Science*, 2004, **305**, 1273–1276.
11 L. Yu, C. Shearer and J. Shapter, *Chem. Rev.*, 2016, **116**, 13413–13453.
12 B. Dan, G. C. Irvin and M. Pasquali, *ACS Nano*, 2009, **3**, 835–843.
13 J. C. Goak, S. H. Lee, J. H. Han, S. H. Jang, K. B. Kim, Y. Seo, Y. S. Seo and N. Lee, *Carbon*, 2011, **49**, 4301–4313.
14 M. Chhowalla, *J. Soc. Inf. Disp.*, 2007, **15**, 1085–1088.
15 J. Li, Y. Lu, Q. Ye, M. Cinke, J. Han and M. Meyyappan, *Nano Lett.*, 2003, **3**, 929–933.
16 E. S. Snow, F. K. Perkins and J. A. Robinson, *Chem. Soc. Rev.*, 2006, **35**, 790.
17 D. Kauffman and A. Star, *Angew. Chem., Int. Ed.*, 2008, **47**, 6550–6570.
18 J. M. Schnorr, D. van der Zwaag, J. J. Walish, Y. Weizmann and T. M. Swager, *Adv. Funct. Mater.*, 2013, 5285–5291.
19 D. Kumar, P. Chaturvedi, P. Saho, P. Jha, A. Chouksey, M. Lal, J. S. B. S. Rawat, R. P. Tandon and P. K. Chaudhury, *Sens. Actuators, B*, 2017, **240**, 1134–1140.
20 G. P. Evans, D. J. Buckley, N. T. Skipper and I. P. Parkin, *RSC Adv.*, 2014, **4**, 51395–51403.
21 A. Salehi-Khojin, K. Y. Lin, C. R. Field and R. I. Masel, *Nanoscale*, 2011, **3**, 3097–3102.
22 H. Y. Zheng, O. A. Alsager, B. Zhu, J. Travas-Sejdic, J. M. Hodgkiss and N. O. V. Plank, *Nanoscale*, 2016, **8**, 13659–13668.
23 M. Stadermann, S. J. Papadakis, M. R. Falvo, J. Novak, E. Snow, Q. Fu, J. Liu, Y. Fridman, J. J. Boland, R. Superfine and S. Washburn, *Phys. Rev. B: Condens. Matter*, 2004, **69**, 201402.
24 E. Bekyarova, M. E. Itkis, N. Cabrera, B. Zhao, A. Yu, J. Gao and R. C. Haddon, *J. Am. Chem. Soc.*, 2005, **127**, 5990–5995.
25 N. Songmee, P. Singjai and M. i. h. Panhuis, *Nanoscale*, 2010, **2**, 1740–1745.
26 P. N. Nirmalraj, P. E. Lyons, S. De, J. N. Coleman and J. J. Boland, *Nano Lett.*, 2009, **9**, 3890–3895.
27 A. Saha, C. Jiang and A. A. Martí, *Carbon*, 2014, **79**, 1–18.
28 M. C. Hersam, *Nat. Nanotechnol.*, 2008, **3**, 387–394.
29 M. S. Arnold, A. A. Green, J. F. Hulvat, S. I. Stupp and M. C. Hersam, *Nat. Nanotechnol.*, 2006, **1**, 60–65.
30 S. Ghosh, S. M. Bachilo and R. B. Weisman, *Nat. Nanotechnol.*, 2010, **5**, 443–450.
31 J. K. Streit, S. Lam, Y. Piao, A. R. H. Walker, J. A. Fagan and M. Zheng, *Nanoscale*, 2017, **9**, 2531–2540.
32 J. W. Jo, J. W. Jung, J. U. Lee and W. H. Jo, *ACS Nano*, 2010, **4**, 5382–5388.
33 H. Li, J. Zhang, G. Li, F. Tan, R. Liu, R. Li, T. Zhang, H. Jin and Q. Li, *Carbon*, 2014, **66**, 369–376.
34 A. Abdelhalim, A. Abdellah, G. Scarpa and P. Lugli, *Carbon*, 2013, **61**, 72–79.
35 M. Shimizu, S. Fujii, T. Tanaka and H. Kataura, *J. Phys. Chem. C*, 2013, **117**, 11744–11749.
36 H. Z. Geng, D. S. Lee, K. K. Kim, G. H. Han, H. K. Park and Y. H. Lee, *Chem. Phys. Lett.*, 2008, **455**, 275–278.
37 J. Tittmann-Otto, S. Hermann, J. Kalbacova, M. Hartmann, M. Toader, R. D. Rodriguez, S. E. Schulz, D. R. T. Zahn and T. Gessner, *J. Appl. Phys.*, 2016, **119**, 124509.
38 A. A. Kane, A. C. Ford, A. Nissen, K. L. Krafcik and F. Léonard, *ACS Nano*, 2014, **8**, 2477–2485.
39 J. G. Park, J. Smithyman, C. Y. Lin, A. Cooke, A. W. Kismarahardja, S. Li, R. Liang, J. S. Brooks, C. Zhang and B. Wang, *J. Appl. Phys.*, 2009, **106**, 104310.
40 H. Z. Geng, K. K. Kim, K. P. So, Y. S. Lee, Y. Chang and Y. H. Lee, *J. Am. Chem. Soc.*, 2007, **129**, 7758–7759.
41 D. S. Hecht, D. Thomas, L. Hu, C. Ladous, T. Lam, Y. Park, G. Irvin and P. Drzaic, *J. Soc. Inf. Disp.*, 2009, **17**, 941–946.
42 G. P. Evans, D. J. Buckley, A. L. Adedigba, G. Sankar, N. T. Skipper and I. P. Parkin, *ACS Appl. Mater. Interfaces*, 2016, **8**, 28096–28104.
43 P. Nikolaev, M. J. Bronikowski, R. K. Bradley, F. Rohmund, D. T. Colbert, K. A. Smith and R. E. Smalley, *Chem. Phys. Lett.*, 1999, **313**, 91–97.
44 G. Golan, A. Axelevitch, B. Gorenstein and V. Manevych, *Microelectron. J.*, 2006, **37**, 910–915.
45 S. C. Naisbitt, K. F. E. Pratt, D. E. Williams and I. P. Parkin, *Sens. Actuators, B*, 2006, **114**, 969–977.
46 Y. R. Park, W. J. Kim, M. J. Ko, N. K. Min and C. J. Lee, *Nanoscale*, 2012, **4**, 6532–6536.
47 I. W. Chiang, B. E. Brinson, A. Y. Huang, P. A. Willis, M. J. Bronikowski, J. L. Margrave, R. E. Smalley and R. H. Hauge, *J. Phys. Chem. B*, 2001, **105**, 8297–8301.
48 J. L. Blackburn, C. Engtrakul, T. J. McDonald, A. C. Dillon and M. J. Heben, *J. Phys. Chem. B*, 2006, **110**, 25551–25558.
49 M. S. Dresselhaus, G. Dresselhaus, R. Saito and A. Jorio, *Phys. Rep.*, 2005, **409**, 47–99.
50 J. Zaumseil, F. Jakubka, M. Wang and F. Gannott, *J. Phys. Chem. C*, 2013, **117**, 26361–26370.
51 G. Fanchini, H. E. Unalan and M. Chhowalla, *Nano Lett.*, 2007, **7**, 1129–1133.
52 A. Boyd, I. Dube, G. Fedorov, M. Paranjape and P. Barbara, *Carbon*, 2014, **69**, 417–423.
53 A. Salehi-Khojin, F. Khalili-Araghi, M. A. Kuroda, K. Y. Lin, J. P. Leburton and R. I. Masel, *ACS Nano*, 2011, **5**, 153–158.
54 V. Skákalová, A. B. Kaiser, Y. S. Woo and S. Roth, *Phys. Rev. B: Condens. Matter*, 2006, **74**, 085403.
55 Y. Battie, L. Gorintin, O. Ducloux, P. Thobois, P. Bondavalli, G. Feugnet and A. Loiseau, *Analyst*, 2012, **137**, 2151–2157.
56 L. K. Randeniya and P. J. Martin, *Carbon*, 2013, **60**, 498–505.
57 S. Rosenblatt, Y. Yaish, J. Park, J. Gore, V. Sazonova and P. L. McEuen, *Nano Lett.*, 2002, **2**, 869–872.
58 K. H. S. Kung and K. F. Hayes, *Langmuir*, 1993, **9**, 263–267.

59 J. S. Bernardes, C. A. Rezende and F. Galembeck, *J. Phys. Chem. C*, 2010, **114**, 19016–19023.
60 B. H. Son, J.-Y. Park, S. Lee and Y. H. Ahn, *Nanoscale*, 2015, **7**, 15421–15426.
61 D. Grosso, F. Cagnol, G. J. de. A. A. Soler-Illia, E. L. Crepaldi, H. Amenitsch, A. Brunet-Bruneau, A. Bourgeois and C. Sanchez, *Adv. Funct. Mater.*, 2004, **14**, 309–322.
62 J. S. Bernardes, C. A. Rezende and F. Galembeck, *Langmuir*, 2010, **26**, 7824–7832.
63 S. Björklund and V. Kocherbitov, *Langmuir*, 2016, **32**, 5223–5232.
64 Y. L. E. Chen, M. L. Gee, C. A. Helm, J. N. Israelachvili and P. M. McGuiggan, *J. Phys. Chem.*, 1989, **93**, 7057–7059.
65 A. Zahab, L. Spina, P. Poncharal and C. Marlière, *Phys. Rev. B: Condens. Matter*, 2000, **62**, 10000–10003.
66 D. Tang, L. Ci, W. Zhou and S. Xie, *Carbon*, 2006, **44**, 2155–2159.
67 D. Jung, J. Kim and G. S. Lee, *Sens. Actuators, A*, 2015, **223**, 11–17.
68 C. Cantalini, L. Valentini, I. Armentano, L. Lozzi, J. M. Kenny and S. Santucci, *Sens. Actuators, B*, 2003, **95**, 195–202.
69 H. E. Romero, G. U. Sumanasekera, S. Kishore and P. C. Eklund, *J. Phys.: Condens. Matter*, 2004, **16**, 1939.
70 R. A. Bell, M. C. Payne and A. A. Mostofi, *J. Chem. Phys.*, 2014, **141**, 164703.
71 A. Lekawa-Raus, L. Kurzepa, G. Kozlowski, S. C. Hopkins, M. Wozniak, D. Lukawski, B. A. Glowacki and K. K. Koziol, *Carbon*, 2015, **87**, 18–28.
72 S. Veeramasuneni, M. R. Yalamanchili and J. D. Miller, *J. Colloid Interface Sci.*, 1996, **184**, 594–600.
73 M. Piao, M. K. Joo, J. Na, Y. J. Kim, M. Mouis, G. Ghibaudo, S. Roth, W. Y. Kim, H. K. Jang, G. P. Kennedy, U. Dettlaff-Weglikowska and G. T. Kim, *J. Phys. Chem. C*, 2014, **118**, 26454–26461.
74 T. A. Blank, L. P. Eksperiandova and K. N. Belikov, *Sens. Actuators, B*, 2016, **228**, 416–442.
75 Q. Y. Tang, Y. C. Chan and K. Zhang, *Sens. Actuators, B*, 2011, **152**, 99–106.
76 L. Liu, X. Ye, K. Wu, R. Han, Z. Zhou and T. Cui, *Sensors*, 2009, **9**, 1714–1721.
77 J. W. Han, B. Kim, J. Li and M. Meyyappan, *J. Phys. Chem. C*, 2012, **116**, 22094–22097.

Bibliography

[1] E. G. Snyder, T. H. Watkins, P. A. Solomon, E. D. Thoma, R. W. Williams, G. S. W. Hagler, D. Shelow, D. A. Hindin, V. J. Kilaru, and P. W. Preuss, "The Changing Paradigm of Air Pollution Monitoring," *Environ. Sci. Technol.*, vol. 47, pp. 11369–11377, Oct. 2013.

[2] S. Soylemez, B. Yoon, L. Toppare, and T. M. Swager, "Quaternized PolymerSingle-Walled Carbon Nanotube Scaffolds for a Chemiresistive Glucose Sensor," *ACS Sens.*, July 2017.

[3] R. Zhu, M. Desroches, B. Yoon, and T. M. Swager, "Wireless Oxygen Sensors Enabled by Fe(II)-Polymer Wrapped Carbon Nanotubes," *ACS Sens.*, vol. 2, pp. 1044–1050, July 2017.

[4] J. Kong, N. R. Franklin, C. Zhou, M. G. Chapline, S. Peng, K. Cho, and H. Dai, "Nanotube molecular wires as chemical sensors," *Science*, vol. 287, no. 5453, pp. 622–625, 2000.

[5] P. G. Collins, K. Bradley, M. Ishigami, and A. Zettl, "Extreme Oxygen Sensitivity of Electronic Properties of Carbon Nanotubes," *Science*, vol. 287, pp. 1801–1804, Mar. 2000.

[6] P. Qi, O. Vermesh, M. Grecu, A. Javey, Q. Wang, H. Dai, S. Peng, and K. J. Cho, "Toward large arrays of multiplex functionalized carbon nanotube sensors for highly sensitive and selective molecular detection," *Nano Lett.*, vol. 3, no. 3, pp. 347–351, 2003.

[7] J. Li, Y. Lu, Q. Ye, M. Cinke, J. Han, and M. Meyyappan, "Carbon nanotube sensors for gas and organic vapor detection," *Nano Lett.*, vol. 3, no. 7, pp. 929–933, 2003.

[8] J. E. Ellis and A. Star, "Carbon Nanotube-based Gas Sensors toward Breath Analysis," *ChemPlusChem*, pp. 1248–1265, Sept. 2016.

[9] G. d. O. Silva, Z. P. Michael, L. Bian, G. V. Shurin, M. Mulato, M. R. Shurin, and A. Star, "Nanoelectronic Discrimination of Non-malignant and Malignant Cells using Nanotube Field-Effect Transistors," *ACS Sens.*, July 2017.

[10] C2Sense, 735 Concord Ave Cambridge, MA 02138, USA, http://www.c2sense.com/.

[11] AerNos Inc., San Diego Science Center, 3030 Bunker Hill Street, Suite 105 San Diego, CA 92109, USA, http://www.aernos.com/.

[12] Vaporsens, 36 South Wasatch Drive, SMBB 5527 Salt Lake City, UT, 84112, USA, http://www.vaporsens.com/.

[13] C. Y. Lee and M. S. Strano, "Amine Basicity (pKb) Controls the Analyte Binding Energy on Single Walled Carbon Nanotube Electronic Sensor Arrays," *J. Am. Chem. Soc.*, vol. 130, pp. 1766–1773, Feb. 2008.

[14] C. Y. Lee and M. S. Strano, "Understanding the Dynamics of Signal Transduction for Adsorption of Gases and Vapors on Carbon Nanotube Sensors," *Langmuir*, vol. 21, pp. 5192–5196, May 2005.

[15] D. Kumar, I. Kumar, P. Chaturvedi, A. Chouksey, R. P. Tandon, and P. K. Chaudhury, "Study of simultaneous reversible and irreversible adsorption on single-walled carbon nanotube gas sensor," *Mater. Chem. Phys.*, vol. 177, pp. 276–282, July 2016.

[16] M. Dresselhaus, G. Dresselhaus, and A. Jorio, "Unusual Properties and Structure of Carbon Nanotubes," *Annu. Rev. Mater. Res.*, vol. 34, no. 1, pp. 247–278, 2004.

[17] D. Kauffman and A. Star, "Carbon Nanotube Gas and Vapor Sensors," *Angew. Chem. Int. Ed.*, vol. 47, pp. 6550–6570, Aug. 2008.

[18] J. F. Fennell, S. F. Liu, J. M. Azzarelli, J. G. Weis, S. Rochat, K. A. Mirica, J. B. Ravnsbæk, and T. M. Swager, "Nanowire Chemical/Biological Sensors: Status and a Roadmap for the Future," *Angew. Chem. Int. Ed.*, vol. 55, pp. 1266–1281, Jan. 2016.

[19] T. A. Edison, "Manufacture of filaments for incandescent electric lamps," Mar. 1892. Cooperative Classification H01B1/24.

[20] H. W. Kroto, J. R. Heath, S. C. O'Brien, R. F. Curl, and R. E. Smalley, "C60: Buckminsterfullerene," *Nature*, vol. 318, pp. 162–163, Nov. 1985.

[21] A. Oberlin, M. Endo, and T. Koyama, "Filamentous growth of carbon through benzene decomposition," *J. Cryst. Growth*, vol. 32, pp. 335–349, Mar. 1976.

[22] S. Iijima, "Helical microtubules of graphitic carbon," *Nature*, vol. 354, pp. 56–58, Nov. 1991.

[23] M. F. L. D. Volder, S. H. Tawfick, R. H. Baughman, and A. J. Hart, "Carbon Nanotubes: Present and Future Commercial Applications," *Science*, vol. 339, pp. 535–539, Feb. 2013.

[24] A. Krishnan, E. Dujardin, T. W. Ebbesen, P. N. Yianilos, and M. M. J. Treacy, "Young's modulus of single-walled nanotubes," *Phys. Rev. B*, vol. 58, pp. 14013–14019, Nov. 1998.

[25] B. G. Demczyk, Y. M. Wang, J. Cumings, M. Hetman, W. Han, A. Zettl, and R. O. Ritchie, "Direct mechanical measurement of the tensile strength and elastic modulus of multiwalled carbon nanotubes," *Materials Science and Engineering: A*, vol. 334, pp. 173–178, Sept. 2002.

[26] T. Dürkop, S. A. Getty, E. Cobas, and M. S. Fuhrer, "Extraordinary Mobility in Semiconducting Carbon Nanotubes," *Nano Lett.*, vol. 4, pp. 35–39, Jan. 2004.

[27] B. Q. Wei, R. Vajtai, and P. M. Ajayan, "Reliability and current carrying capacity of carbon nanotubes," *Appl. Phys. Lett.*, vol. 79, pp. 1172–1174, Aug. 2001.

[28] J. Hone, M. C. Llaguno, M. J. Biercuk, A. T. Johnson, B. Batlogg, Z. Benes, and J. E. Fischer, "Thermal properties of carbon nanotubes and nanotube-based materials," *Appl. Phys. A*, vol. 74, pp. 339–343, Mar. 2002.

[29] A. Kongkanand, R. Martínez Domínguez, and P. V. Kamat, "Single Wall Carbon Nanotube Scaffolds for Photoelectrochemical Solar Cells. Capture and Transport of Photogenerated Electrons," *Nano Lett.*, vol. 7, pp. 676–680, Mar. 2007.

[30] M. Prato, K. Kostarelos, and A. Bianco, "Functionalized Carbon Nanotubes in Drug Design and Discovery," *Acc. Chem. Res.*, vol. 41, pp. 60–68, Jan. 2008.

[31] R. S. Park, M. M. Shulaker, G. Hills, L. Suriyasena Liyanage, S. Lee, A. Tang, S. Mitra, and H.-S. P. Wong, "Hysteresis in Carbon Nanotube Transistors: Measurement and Analysis of Trap Density, Energy Level, and Spatial Distribution," *ACS Nano*, vol. 10, pp. 4599–4608, Apr. 2016.

[32] D. S. Hecht, D. Thomas, L. Hu, C. Ladous, T. Lam, Y. Park, G. Irvin, and P. Drzaic, "Carbon-nanotube film on plastic as transparent electrode for resistive touch screens," *Journal of the Society for Information Display*, vol. 17, pp. 941–946, Nov. 2009.

[33] G. Girishkumar, M. Rettker, R. Underhile, D. Binz, K. Vinodgopal, P. McGinn, and P. Kamat, "Single-Wall Carbon Nanotube-Based Proton Exchange Membrane Assembly for Hydrogen Fuel Cells," *Langmuir*, vol. 21, pp. 8487–8494, Aug. 2005.

[34] L. Ma, H. L. Zhuang, S. Wei, K. E. Hendrickson, M. S. Kim, G. Cohn, R. G. Hennig, and L. A. Archer, "Enhanced Li-S Batteries Using Amine-Functionalized Carbon Nanotubes in the Cathode," *ACS Nano*, vol. 10, pp. 1050–1059, Jan. 2016.

[35] P. Jarosz, C. Schauerman, J. Alvarenga, B. Moses, T. Mastrangelo, R. Raffaelle, R. Ridgley, and B. Landi, "Carbon nanotube wires and cables: Near-term applications and future perspectives," *Nanoscale*, vol. 3, pp. 4542–4553, Nov. 2011.

[36] X. Liu, M. Wang, S. Zhang, and B. Pan, "Application potential of carbon nanotubes in water treatment: A review," *J. Environ. Sci.*, vol. 25, pp. 1263–1280, July 2013.

[37] L. Ci, J. Suhr, V. Pushparaj, X. Zhang, and P. M. Ajayan, "Continuous Carbon Nanotube Reinforced Composites," *Nano Lett.*, vol. 8, pp. 2762–2766, Sept. 2008.

[38] X. Zhang, Z. Yu, C. Wang, D. Zarrouk, J.-W. T. Seo, J. C. Cheng, A. D. Buchan, K. Takei, Y. Zhao, J. W. Ager, J. Zhang, M. Hettick, M. C. Hersam, A. P. Pisano, R. S. Fearing, and A. Javey, "Photoactuators and motors based on carbon nanotubes with selective chirality distributions," *Nat. Commun.*, vol. 5, p. 2983, Jan. 2014.

[39] M. Meyyappan, "Carbon Nanotube-Based Chemical Sensors," *Small*, vol. 12, p. 21182129, Mar. 2016.

[40] A. Star, V. Joshi, S. Skarupo, D. Thomas, and J.-C. P. Gabriel, "Gas Sensor Array Based on Metal-Decorated Carbon Nanotubes," *J. Phys. Chem. B*, vol. 110, pp. 21014–21020, Oct. 2006.

[41] F. Wang, H. Gu, and T. M. Swager, "Carbon Nanotube/Polythiophene Chemiresistive Sensors for Chemical Warfare Agents," *J. Am. Chem. Soc.*, vol. 130, pp. 5392–5393, Apr. 2008.

[42] J. M. Schnorr, D. van der Zwaag, J. J. Walish, Y. Weizmann, and T. M. Swager, "Sensory Arrays of Covalently Functionalized Single-Walled Carbon Nanotubes for Explosive Detection," *Adv. Funct. Mater.*, pp. 5285–5291, 2013.

[43] J. Li and Y. Lu, "Carbon nanotube based chemical sensors for space and terrestrial applications," *ECS Trans.*, vol. 19, no. 6, pp. 7–15, 2009.

[44] S. W. Lee, W. Lee, Y. Hong, G. Lee, and D. S. Yoon, "Recent advances in carbon material-based NO2 gas sensors," *Sens. Actuators, B*, vol. 255, pp. 1788–1804, Feb. 2018.

[45] Q. Zhang, J.-Q. Huang, M.-Q. Zhao, W.-Z. Qian, and F. Wei, "Carbon Nanotube Mass Production: Principles and Processes," *ChemSusChem*, vol. 4, pp. 864–889, July 2011.

[46] B. Dan, G. C. Irvin, and M. Pasquali, "Continuous and Scalable Fabrication of Transparent Conducting Carbon Nanotube Films," *ACS Nano*, vol. 3, pp. 835–843, Apr. 2009.

[47] S. Fogden, C. A. Howard, R. K. Heenan, N. T. Skipper, and M. S. P. Shaffer, "Scalable Method for the Reductive Dissolution, Purification, and Separation of Single-Walled Carbon Nanotubes," *ACS Nano*, vol. 6, pp. 54–62, Jan. 2012.

[48] K. Kostarelos, "The long and short of carbon nanotube toxicity," *Nat Biotech*, vol. 26, pp. 774–776, July 2008.

[49] S. Lanone, P. Andujar, A. Kermanizadeh, and J. Boczkowski, "Determinants of carbon nanotube toxicity," *Adv. Drug Delivery Rev.*, vol. 65, pp. 2063–2069, Dec. 2013.

[50] Y. Li, "The Quarter-Century Anniversary of Carbon Nanotube Research," *ACS Nano*, vol. 11, pp. 1–2, Jan. 2017.

[51] A. Jorio, M. S. Dresselhaus, R. Saito, and G. Dresselhaus, *Raman Spectroscopy in Graphene Related Systems*. Weinheim, Germany: Wiley-VCH, 1 edition ed., Feb. 2011.

[52] R. Saito, G. Dresselhaus, and M. S. Dresselhaus, *Physical Properties of Carbon Nanotubes*. Imperial College Press, Jan. 1998.

[53] S. Basu-Dutt, M. L. Minus, R. Jain, D. Nepal, and S. Kumar, "Chemistry of Carbon Nanotubes for Everyone," *J. Chem. Educ.*, vol. 89, pp. 221–229, Jan. 2012.

[54] J.-C. Charlier, P. C. Eklund, J. Zhu, and A. C. Ferrari, "Electron and Phonon Properties of Graphene: Their Relationship with Carbon Nanotubes," in *Carbon Nanotubes*, Topics in Applied Physics, pp. 673–709, Springer, Berlin, Heidelberg, 2007.

[55] C. Kittel, *Introduction to Solid State Physics*. Hoboken, NJ: John Wiley & Sons, 8th revised edition edition ed., Nov. 2004.

[56] M. S. Dresselhaus, G. Dresselhaus, R. Saito, and A. Jorio, "Raman spectroscopy of carbon nanotubes," *Phys. Rep.*, vol. 409, pp. 47–99, Mar. 2005.

[57] J. Singleton, *Band Theory and Electronic Properties of Solids*. Oxford ; New York: Oxford University Press, U.S.A., Oct. 2001.

[58] S. A. Hodge, M. K. Bayazit, K. S. Coleman, and M. S. P. Shaffer, "Unweaving the rainbow: a review of the relationship between single-walled carbon nanotube molecular structures and their chemical reactivity," *Chem. Soc. Rev.*, vol. 41, no. 12, p. 4409, 2012.

[59] A. Hagen and T. Hertel, "Quantitative Analysis of Optical Spectra from Individual Single-Wall Carbon Nanotubes," *Nano Lett.*, vol. 3, pp. 383–388, Mar. 2003.

[60] G. Lolli, L. Zhang, L. Balzano, N. Sakulchaicharoen, Y. Tan, and D. E. Resasco, "Tailoring (n,m) Structure of Single-Walled Carbon Nanotubes by

Modifying Reaction Conditions and the Nature of the Support of CoMo Catalysts," *J. Phys. Chem. B*, vol. 110, pp. 2108–2115, Feb. 2006.

[61] S. Ghosh, S. M. Bachilo, and R. B. Weisman, "Advanced sorting of single-walled carbon nanotubes by nonlinear density-gradient ultracentrifugation," *Nat Nano*, vol. 5, pp. 443–450, June 2010.

[62] H. Kataura, Y. Kumazawa, Y. Maniwa, I. Umezu, S. Suzuki, Y. Ohtsuka, and Y. Achiba, "Optical properties of single-wall carbon nanotubes," *Synth. Met.*, vol. 103, pp. 2555–2558, June 1999.

[63] R. B. Weisman and S. M. Bachilo, "Dependence of Optical Transition Energies on Structure for Single-Walled Carbon Nanotubes in Aqueous Suspension. An Empirical Kataura Plot," *Nano Lett.*, vol. 3, pp. 1235–1238, Sept. 2003.

[64] W. Zhou, W. Ma, Z. Niu, L. Song, and S. Xie, "Freestanding single-walled carbon nanotube bundle networks: Fabrication, properties and composites," *Chin. Sci. Bull.*, vol. 57, pp. 205–224, Jan. 2012.

[65] C. Hierold, Oliver Brand, Gary K. Fedder, Jan G. Korvink, and Osamu Tabata, eds., *Carbon Nanotube Devices*, vol. 8 of *Advanced Micro & Nanosystems*. Wiley, 2008.

[66] V. Derenskyi, W. Gomulya, W. Talsma, J. M. Salazar-Rios, M. Fritsch, P. Nirmalraj, H. Riel, S. Allard, U. Scherf, and M. A. Loi, "On-Chip Chemical Self-Assembly of Semiconducting Single-Walled Carbon Nanotubes (SWNTs): Toward Robust and Scale Invariant SWNTs Transistors," *Adv. Mater.*, vol. 29, p. 1606757, Apr. 2017.

[67] S. J. Tans, A. R. M. Verschueren, and C. Dekker, "Room-temperature transistor based on a single carbon nanotube," *Nature; London*, vol. 393, pp. 49–52, May 1998.

[68] P. Chen, Y. Fu, R. Aminirad, C. Wang, J. Zhang, K. Wang, K. Galatsis, and C. Zhou, "Fully Printed Separated Carbon Nanotube Thin Film Transistor Circuits and Its Application in Organic Light Emitting Diode Control," *Nano Lett.*, vol. 11, pp. 5301–5308, Dec. 2011.

[69] A. Shimoni, S. Azoubel, and S. Magdassi, "Inkjet printing of flexible high-performance carbon nanotube transparent conductive films by "coffee ring effect"," *Nanoscale*, vol. 6, pp. 11084–11089, Sept. 2014.

[70] N. Jha, P. Ramesh, E. Bekyarova, X. Tian, F. Wang, M. E. Itkis, and R. C. Haddon, "Functionalized Single-Walled Carbon Nanotube-Based Fuel Cell Benchmarked Against US DOE 2017 Technical Targets," *Sci. Rep.*, vol. 3, p. srep02257, July 2013.

[71] M. P. Anantram and F. Léonard, "Physics of carbon nanotube electronic devices," *Rep. Prog. Phys.*, vol. 69, p. 507, Mar. 2006.

[72] V. Derycke, R. Martel, J. Appenzeller, and P. Avouris, "Carbon Nanotube Inter- and Intramolecular Logic Gates," *Nano Lett.*, vol. 1, pp. 453–456, Sept. 2001.

[73] A. Saha, C. Jiang, and A. A. Martí, "Carbon nanotube networks on different platforms," *Carbon*, vol. 79, pp. 1–18, Nov. 2014.

[74] N. R. Franklin, Q. Wang, T. W. Tombler, A. Javey, M. Shim, and H. Dai, "Integration of suspended carbon nanotube arrays into electronic devices and electromechanical systems," *Appl. Phys. Lett.*, vol. 81, pp. 913–915, July 2002.

[75] I. Dube, D. Jimnez, G. Fedorov, A. Boyd, I. Gayduchenko, M. Paranjape, and P. Barbara, "Understanding the electrical response and sensing mechanism of carbon-nanotube-based gas sensors," *Carbon*, vol. 87, pp. 330–337, June 2015.

[76] M. Jeon, B. Choi, J. Yoon, D. M. Kim, D. H. Kim, I. Park, and S.-J. Choi, "Enhanced sensing of gas molecules by a 99.9% semiconducting carbon nanotube-based field-effect transistor sensor," *Appl. Phys. Lett.*, vol. 111, p. 022102, July 2017.

[77] K. Bradley, J.-C. P. Gabriel, M. Briman, A. Star, and G. Grüner, "Charge Transfer from Ammonia Physisorbed on Nanotubes," *Phys. Rev. Lett.*, vol. 91, p. 218301, Nov. 2003.

[78] K. Bradley, J. Cumings, A. Star, J.-C. P. Gabriel, and G. Grüner, "Influence of Mobile Ions on Nanotube Based FET Devices," *Nano Lett.*, vol. 3, pp. 639–641, May 2003.

[79] R. J. Chen, S. Bangsaruntip, K. A. Drouvalakis, N. W. S. Kam, M. Shim, Y. Li, W. Kim, P. J. Utz, and H. Dai, "Noncovalent functionalization of carbon nanotubes for highly specific electronic biosensors," *PNAS*, vol. 100, pp. 4984–4989, Apr. 2003.

[80] I. Heller, J. Männik, S. G. Lemay, and C. Dekker, "Optimizing the Signal-to-Noise Ratio for Biosensing with Carbon Nanotube Transistors," *Nano Lett.*, vol. 9, pp. 377–382, Jan. 2009.

[81] A. Goldoni, L. Petaccia, S. Lizzit, and R. Larciprete, "Sensing gases with carbon nanotubes: A review of the actual situation," *J. Phys.: Condens. Matter*, vol. 22, p. 013001, Jan. 2010.

[82] E. S. Snow, F. K. Perkins, and J. A. Robinson, "Chemical vapor detection using single-walled carbon nanotubes," *Chem. Soc. Rev.*, vol. 35, no. 9, p. 790, 2006.

[83] Y. Battie, L. Gorintin, O. Ducloux, P. Thobois, P. Bondavalli, G. Feugnet, and A. Loiseau, "Thickness dependent sensing mechanism in sorted semiconducting single walled nanotube based sensors," *Analyst*, vol. 137, pp. 2151–2157, Apr. 2012.

[84] A. Abdellah, A. Abdelhalim, F. Loghin, P. Kohler, Z. Ahmad, G. Scarpa, and P. Lugli, "Flexible Carbon Nanotube Based Gas Sensors Fabricated by Large-Scale Spray Deposition," *IEEE Sens. J.*, vol. 13, pp. 4014–4021, Oct. 2013.

[85] K. Saetia, J. M. Schnorr, M. M. Mannarino, S. Y. Kim, G. C. Rutledge, T. M. Swager, and P. T. Hammond, "Spray-Layer-by-Layer Carbon Nanotube/Electrospun Fiber Electrodes for Flexible Chemiresistive Sensor Applications," *Adv. Funct. Mater.*, vol. 24, pp. 492–502, Jan. 2014.

[86] K. Cattanach, R. D. Kulkarni, M. Kozlov, and S. K. Manohar, "Flexible carbon nanotube sensors for nerve agent simulants," *Nanotechnology*, vol. 17, p. 4123, Aug. 2006.

[87] K. Parikh, K. Cattanach, R. Rao, D.-S. Suh, A. Wu, and S. K. Manohar, "Flexible vapour sensors using single walled carbon nanotubes," *Sens. Actuators, B*, vol. 113, pp. 55–63, Jan. 2006.

[88] K. A. Mirica, J. G. Weis, J. M. Schnorr, B. Esser, and T. M. Swager, "Mechanical Drawing of Gas Sensors on Paper," *Angew. Chem. Int. Ed.*, vol. 51, pp. 10740–10745, Oct. 2012.

[89] J. M. Azzarelli, K. A. Mirica, J. B. Ravnsbæk, and T. M. Swager, "Wireless gas detection with a smartphone via rf communication," *PNAS*, vol. 111, pp. 18162–18166, Dec. 2014.

[90] E. S. Snow, F. K. Perkins, E. J. Houser, S. C. Badescu, and T. L. Reinecke, "Chemical Detection with a Single-Walled Carbon Nanotube Capacitor," *Science*, vol. 307, pp. 1942–1945, Mar. 2005.

[91] E. S. Snow and F. K. Perkins, "Capacitance and Conductance of Single-Walled Carbon Nanotubes in the Presence of Chemical Vapors," *Nano Lett.*, vol. 5, pp. 2414–2417, Dec. 2005.

[92] J. A. Robinson, E. S. Snow, and F. K. Perkins, "Improved chemical detection using single-walled carbon nanotube network capacitors," *Sens. Actuators, A*, vol. 135, pp. 309–314, Apr. 2007.

[93] Q. Wang and B. Arash, "A review on applications of carbon nanotubes and graphenes as nano-resonator sensors," *Computational Materials Science*, vol. 82, pp. 350–360, Feb. 2014.

[94] B. Lassagne, D. Garcia-Sanchez, A. Aguasca, and A. Bachtold, "Ultrasensitive Mass Sensing with a Nanotube Electromechanical Resonator," *Nano Lett.*, vol. 8, pp. 3735–3738, Nov. 2008.

[95] T. Zhang, S. Mubeen, N. V. Myung, and M. A. Deshusses, "Recent progress in carbon nanotube-based gas sensors," *Nanotechnology*, vol. 19, p. 332001, Aug. 2008.

[96] D. R. Kauffman, D. C. Sorescu, D. P. Schofield, B. L. Allen, K. D. Jordan, and A. Star, "Understanding the Sensor Response of Metal-Decorated Carbon Nanotubes," *Nano Lett.*, vol. 10, pp. 958–963, Mar. 2010.

[97] J. F. Fennell, H. Hamaguchi, B. Yoon, and T. M. Swager, "Chemiresistor Devices for Chemical Warfare Agent Detection Based on Polymer Wrapped Single-Walled Carbon Nanotubes," *Sensors*, vol. 17, p. 982, Apr. 2017.

[98] M. Ding, Y. Tang, P. Gou, M. J. Reber, and A. Star, "Chemical Sensing with Polyaniline Coated Single-Walled Carbon Nanotubes," *Adv. Mater.*, vol. 23, pp. 536–540, Jan. 2011.

[99] T. Zhang, M. Nix, B.-Y. Yoo, M. Deshusses, and N. Myung, "Electrochemically Functionalized Single-Walled Carbon Nanotube Gas Sensor," *Electroanalysis*, vol. 18, pp. 1153–1158, June 2006.

[100] C. Staii, A. T. Johnson, M. Chen, and A. Gelperin, "DNA-Decorated Carbon Nanotubes for Chemical Sensing," *Nano Lett.*, vol. 5, pp. 1774–1778, Sept. 2005.

[101] Y. Zhang, B. R. Bunes, N. Wu, A. Ansari, S. Rajabali, and L. Zang, "Sensing methamphetamine with chemiresistive sensors based on polythiophene-blended single-walled carbon nanotubes," *Sens. Actuators, B*, vol. 255, pp. 1814–1818, Feb. 2018.

[102] E. Bekyarova, M. Davis, T. Burch, M. E. Itkis, B. Zhao, S. Sunshine, and R. C. Haddon, "Chemically Functionalized Single-Walled Carbon Nanotubes as Ammonia Sensors," *J. Phys. Chem. B*, vol. 108, pp. 19717–19720, Dec. 2004.

[103] B. Yoon, S. F. Liu, and T. M. Swager, "Surface-Anchored Poly(4-vinylpyridine)–Single-Walled Carbon Nanotube–Metal Composites for Gas Detection," *Chem. Mater.*, vol. 28, pp. 5916–5924, Aug. 2016.

[104] S. Safari and T. G. M. van de Ven, "Effect of Water Vapor Adsorption on Electrical Properties of Carbon Nanotube/Nanocrystalline Cellulose Composites," *ACS Appl. Mater. Interfaces*, vol. 8, pp. 9483–9489, Apr. 2016.

[105] L. Randeniya, A. Bendavid, P. Martin, and S. Kumar, "SWCNT-aminopolymer composites on mesoporous alumina for fast, room-temperature detection of ultra-low concentrations of NO2 by mediation of water vapour," *Sens. Actuators, B*, vol. 220, pp. 1105–1111, Dec. 2015.

[106] A. Popa, J. Li, and A. C. S. Samia, "Hybrid Platinum Nanobox/Carbon Nanotube Composites for Ultrasensitive Gas Sensing," *Small*, vol. 9, pp. 3928–3933, Dec. 2013.

[107] Y. Chen, Y. D. Lee, H. Vedala, B. L. Allen, and A. Star, "Exploring the Chemical Sensitivity of a Carbon Nanotube/Green Tea Composite," *ACS Nano*, vol. 4, pp. 6854–6862, Nov. 2010.

[108] P. Young, Y. Lu, R. Terrill, and J. Li, "High-Sensitivity NO2 Detection with Carbon Nanotube–Gold Nanoparticle Composite Films," *J. Nanosci. Nanotechnol.*, vol. 5, pp. 1509–1513, Sept. 2005.

[109] N. Van Hieu, L. T. B. Thuy, and N. D. Chien, "Highly sensitive thin film NH3 gas sensor operating at room temperature based on SnO2/MWCNTs composite," *Sens. Actuators, B*, vol. 129, pp. 888–895, Feb. 2008.

[110] N. Duc Hoa, N. Van Quy, Y. Suk Cho, and D. Kim, "Nanocomposite of SWNTs and SnO2 fabricated by soldering process for ammonia gas sensor application," *phys. stat. sol. (a)*, vol. 204, pp. 1820–1824, June 2007.

[111] A. Salehi-Khojin, F. Khalili-Araghi, M. A. Kuroda, K. Y. Lin, J. P. Leburton, and R. I. Masel, "On the Sensing Mechanism in Carbon Nanotube Chemiresistors," *ACS Nano*, vol. 5, pp. 153–158, Jan. 2011.

[112] J. A. Robinson, E. S. Snow, S. C. Badescu, T. L. Reinecke, and F. K. Perkins, "Role of Defects in Single-Walled Carbon Nanotube Chemical Sensors," *Nano Lett.*, vol. 6, pp. 1747–1751, Aug. 2006.

[113] A. Hannon, Y. Lu, J. Li, and M. Meyyappan, "A Sensor Array for the Detection and Discrimination of Methane and Other Environmental Pollutant Gases," *Sensors*, vol. 16, p. 1163, July 2016.

[114] S. F. Liu, L. C. H. Moh, and T. M. Swager, "Single-Walled Carbon Nanotube–Metalloporphyrin Chemiresistive Gas Sensor Arrays for Volatile Organic Compounds," *Chem. Mater.*, vol. 27, pp. 3560–3563, May 2015.

[115] Y. Lu, C. Partridge, M. Meyyappan, and J. Li, "A carbon nanotube sensor array for sensitive gas discrimination using principal component analysis," *J. Electroanal. Chem.*, vol. 593, no. 1, pp. 105–110, 2006.

[116] W. J. Peveler, R. Binions, S. M. V. Hailes, and I. P. Parkin, "Detection of explosive markers using zeolite modified gas sensors," *J. Mater. Chem.A*, vol. 1, pp. 2613–2620, Jan. 2013.

[117] K. Lee, J. Park, M.-S. Lee, J. Kim, B. G. Hyun, D. J. Kang, K. Na, C. Y. Lee, F. Bien, and J.-U. Park, "In-situ Synthesis of Carbon Nanotube-Graphite

Electronic Devices and Their Integrations onto Surfaces of Live Plants and Insects," *Nano Lett.*, vol. 14, pp. 2647–2654, May 2014.

[118] R. Tang, Y. Shi, Z. Hou, and L. Wei, "Carbon Nanotube-Based Chemiresistive Sensors," *Sensors*, vol. 17, p. 882, Apr. 2017.

[119] G. Chen, T. M. Paronyan, E. M. Pigos, and A. R. Harutyunyan, "Enhanced gas sensing in pristine carbon nanotubes under continuous ultraviolet light illumination," *Sci. Rep.*, vol. 2, Mar. 2012.

[120] H.-Q. Nguyen and J.-S. Huh, "Behavior of single-walled carbon nanotube-based gas sensors at various temperatures of treatment and operation," *Sens. Actuators, B*, vol. 117, pp. 426–430, Oct. 2006.

[121] A. Salehi-Khojin, K. Y. Lin, C. R. Field, and R. I. Masel, "Nonthermal Current-Stimulated Desorption of Gases from Carbon Nanotubes," *Science*, vol. 329, pp. 1327–1330, Sept. 2010.

[122] P. Vichchulada, Q. Zhang, and M. D. Lay, "Recent progress in chemical detection with single-walled carbon nanotube networks," *Analyst*, vol. 132, pp. 719–723, July 2007.

[123] C. Cantalini, L. Valentini, I. Armentano, L. Lozzi, J. M. Kenny, and S. Santucci, "Sensitivity to NO2 and cross-sensitivity analysis to NH3, ethanol and humidity of carbon nanotubes thin film prepared by PECVD," *Sens. Actuators, B*, vol. 95, pp. 195–202, Oct. 2003.

[124] T. Meng-Che, H. K. Svm, A. Thilini, L. T. L. Wallace, S. Moochhala, U. H. Yildiz, A. Palaniappan, and B. Liedberg, "Tuning Pendant Groups of Polythiophene on Carbon Nanotubes for Vapour Classification," *Sens. Actuators, B*, vol. 247, pp. 916–922, Aug. 2017.

[125] J. Zhao, A. Buldum, J. Han, and J. P. Lu, "Gas molecule adsorption in carbon nanotubes and nanotube bundles," *Nanotechnology*, vol. 13, p. 195, Apr. 2002.

[126] A. Fujiwara, K. Ishii, H. Suematsu, H. Kataura, Y. Maniwa, S. Suzuki, and Y. Achiba, "Gas adsorption in the inside and outside of single-walled carbon nanotubes," *Chem. Phys. Lett.*, vol. 336, no. 3, pp. 205–211, 2001.

[127] J. Andzelm, N. Govind, and A. Maiti, "Nanotube-based gas sensors-Role of structural defects," *Chem. Phys. Lett.*, vol. 421, pp. 58–62, Apr. 2006.

[128] N. Chakrapani, Y. M. Zhang, S. K. Nayak, J. A. Moore, D. L. Carroll, Y. Y. Choi, and P. M. Ajayan, "Chemisorption of Acetone on Carbon Nanotubes," *J. Phys. Chem. B*, vol. 107, pp. 9308–9311, Sept. 2003.

[129] C. Y. Lee, S. Baik, J. Zhang, R. I. Masel, and M. S. Strano, "Charge Transfer from Metallic Single-Walled Carbon Nanotube Sensor Arrays," *J. Phys. Chem. B*, vol. 110, pp. 11055–11061, June 2006.

[130] W. Wongwiriyapan, S. Honda, H. Konishi, T. Mizuta, T. Ohmori, Y. Kishimoto, T. Ito, T. Maekawa, K. Suzuki, H Ishikawa, T. Murakami, K. Kisoda, H. Harima, K. Oura, and M. Katayama, "Influence of the growth morphology of single-walled carbon nanotubes on gas sensing performance," *Nanotechnology*, vol. 17, no. 17, p. 4424, 2006.

[131] P. C. P. Watts, N. Mureau, Z. Tang, Y. Miyajima, J. D. Carey, and S. R. P. Silva, "The importance of oxygen-containing defects on carbon nanotubes for the detection of polar and non-polar vapours through hydrogen bond formation," *Nanotechnology*, vol. 18, no. 17, p. 175701, 2007.

[132] B. Y. Lee, M. G. Sung, J. Lee, K. Y. Baik, Y.-K. Kwon, M.-S. Lee, and S. Hong, "Universal Parameters for Carbon Nanotube Network-Based Sensors: Can Nanotube Sensors Be Reproducible?," *ACS Nano*, vol. 5, pp. 4373–4379, June 2011.

[133] N. Peng, Q. Zhang, C. L. Chow, O. K. Tan, and N. Marzari, "Sensing Mechanisms for Carbon Nanotube Based NH3 Gas Detection," *Nano Lett.*, vol. 9, pp. 1626–1630, Apr. 2009.

[134] M. A. Topinka, M. W. Rowell, D. Goldhaber-Gordon, M. D. McGehee, D. S. Hecht, and G. Gruner, "Charge Transport in Interpenetrating Networks of Semiconducting and Metallic Carbon Nanotubes," *Nano Lett.*, vol. 9, pp. 1866–1871, May 2009.

[135] M. Mittal and A. Kumar, "Carbon nanotube (CNT) gas sensors for emissions from fossil fuel burning," *Sens. Actuators, B*, vol. 203, pp. 349–362, Nov. 2014.

[136] J. Suehiro, H. Imakiire, S.-i. Hidaka, W. Ding, G. Zhou, K. Imasaka, and M. Hara, "Schottky-type response of carbon nanotube NO2 gas sensor fabricated onto aluminum electrodes by dielectrophoresis," *Sens. Actuators, B*, vol. 114, pp. 943–949, Apr. 2006.

[137] P. Nikolaev, M. J. Bronikowski, R. K. Bradley, F. Rohmund, D. T. Colbert, K. A. Smith, and R. E. Smalley, "Gas-phase catalytic growth of single-walled carbon nanotubes from carbon monoxide," *Chem. Phys. Lett.*, vol. 313, no. 1, pp. 91–97, 1999.

[138] B. Kitiyanan, W. E. Alvarez, J. H. Harwell, and D. E. Resasco, "Controlled production of single-wall carbon nanotubes by catalytic decomposition of CO on bimetallic Co–Mo catalysts," *Chem. Phys. Lett.*, vol. 317, pp. 497–503, Feb. 2000.

[139] E. S. Snow, J. P. Novak, P. M. Campbel, and D. Park, "Random networks of carbon nanotubes as an electronic material," *Appl. Phys. Lett.*, vol. 82, no. 13, pp. 2145–2147, 2003.

[140] E. Bekyarova, M. E. Itkis, N. Cabrera, B. Zhao, A. Yu, J. Gao, and R. C. Haddon, "Electronic Properties of Single-Walled Carbon Nanotube Networks," *J. Am. Chem. Soc.*, vol. 127, pp. 5990–5995, Apr. 2005.

[141] P. N. Nirmalraj, P. E. Lyons, S. De, J. N. Coleman, and J. J. Boland, "Electrical Connectivity in Single-Walled Carbon Nanotube Networks," *Nano Lett.*, vol. 9, pp. 3890–3895, Nov. 2009.

[142] R. A. Bell, M. C. Payne, and A. A. Mostofi, "Does water dope carbon nanotubes?," *The Journal of Chemical Physics*, vol. 141, p. 164703, Oct. 2014.

[143] D. Jung, J. Kim, and G. S. Lee, "Enhanced humidity-sensing response of metal oxide coated carbon nanotube," *Sens. Actuators, A*, vol. 223, pp. 11–17, Mar. 2015.

[144] H. E. Romero, G. U. Sumanasekera, S. Kishore, and P. C. Eklund, "Effects of adsorption of alcohol and water on the electrical transport of carbon nanotube bundles," *J. Phys.: Condens. Matter*, vol. 16, no. 12, p. 1939, 2004.

[145] L. K. Randeniya and P. J. Martin, "Removal of strongly-bound gases from single-walled carbon nanotubes without annealing or ultraviolet light exposure," *Carbon*, vol. 60, pp. 498–505, Aug. 2013.

[146] A. Zahab, L. Spina, P. Poncharal, and C. Marlière, "Water-vapor effect on the electrical conductivity of a single-walled carbon nanotube mat," *Phys. Rev. B*, vol. 62, pp. 10000–10003, Oct. 2000.

[147] D. Tang, L. Ci, W. Zhou, and S. Xie, "Effect of H2o adsorption on the electrical transport properties of double-walled carbon nanotubes," *Carbon*, vol. 44, pp. 2155–2159, Sept. 2006.

[148] C. Lee, R. Sharma, A. Radadia, R. Masel, and M. Strano, "On-Chip Micro Gas Chromatograph Enabled by a Noncovalently Functionalized Single-Walled Carbon Nanotube Sensor Array," *Angew. Chem. Int. Ed.*, vol. 47, pp. 5018–5021, June 2008.

[149] L. Senesac and T. G. Thundat, "Nanosensors for trace explosive detection," *Mater. Today*, vol. 11, pp. 28–36, Mar. 2008.

[150] T. Seiyama, A. Kato, K. Fujiishi, and M. Nagatani, "A new detector for gaseous components using semiconductive thin films.," *Anal. Chem.*, vol. 34, no. 11, pp. 1502–1503, 1962.

[151] S. Yamauchi, *Chemical Sensor Technology*, vol. 4. Elsevier, Dec. 2012.

[152] N. Yamazoe, "Toward innovations of gas sensor technology," *Sens. Actuators, B*, vol. 108, pp. 2–14, July 2005.

[153] D. E. Williams, "Semiconducting oxides as gas-sensitive resistors," *Sens. Actuators, B*, vol. 57, pp. 1–16, Sept. 1999.

[154] G. Korotcenkov, "Metal oxides for solid-state gas sensors: What determines our choice?," *Materials Science and Engineering: B*, vol. 139, pp. 1–23, Apr. 2007.

[155] J. W. Gardner and P. N. Bartlett, "A brief history of electronic noses," *Sens. Actuators, B*, vol. 18, pp. 210–211, Mar. 1994.

[156] J. W. Gardner, P. K. Guha, F. Udrea, and J. A. Covington, "CMOS Interfacing for Integrated Gas Sensors: A Review," *IEEE Sens. J.*, vol. 10, pp. 1833–1848, Dec. 2010.

[157] E. Llobet, "Gas sensors using carbon nanomaterials: A review," *Sens. Actuators, B*, vol. 179, pp. 32–45, Mar. 2013.

[158] H. Bai and G. Shi, "Gas Sensors Based on Conducting Polymers," *Sensors*, vol. 7, pp. 267–307, Mar. 2007.

[159] J. Janata and M. Josowicz, "Conducting polymers in electronic chemical sensors," *Nature Materials; London*, vol. 2, pp. 19–24, Jan. 2003.

[160] I. D. Avramov, M. Rapp, A. Voigt, U. Stahl, and M. Dirschka, "Comparative studies on polymer coated SAW and STW resonators for chemical gas sensor applications," in *Proceedings of the 2000 IEEE/EIA International Frequency Control Symposium and Exhibition (Cat. No.00CH37052)*, pp. 58–65, 2000.

[161] J. R. Stetter and J. Li, "Amperometric Gas Sensors: A Review," *Chem. Rev.*, vol. 108, pp. 352–366, Feb. 2008.

[162] X. Liu, S. Cheng, H. Liu, S. Hu, D. Zhang, and H. Ning, "A Survey on Gas Sensing Technology," *Sensors*, vol. 12, pp. 9635–9665, July 2012.

[163] K. Sahner, G. Hagen, D. Schonauer, S. Reis, and R. Moos, "Zeolites-versatile materials for gas ssensors," *Solid State Ionics*, vol. 179, pp. 2416–2423, Dec. 2008.

[164] Ch. Baerlocher and L.B. McCusker Database of Zeolite Structures: http://www.iza-structure.org/databases/.

[165] J. A. Kaduk and J. Faber, "Crystal structure of zeolite Y as a function of ion exchange," *Rigaku J*, vol. 12, no. 2, pp. 14–34, 1995.

[166] X. Xu, J. Wang, and Y. Long, "Zeolite-based Materials for Gas Sensors," *Sensors*, vol. 6, pp. 1751–1764, Dec. 2006.

[167] R. Binions, A. Afonja, S. Dungey, D. W. Lewis, I. P. Parkin, and D. E. Williams, "Discrimination Effects in Zeolite Modified Metal Oxide Semiconductor Gas Sensors," *IEEE Sens. J.*, vol. 11, pp. 1145–1151, May 2011.

[168] Y. Wang and J. T. W. Yeow, "A Review of Carbon Nanotubes-Based Gas Sensors," *Journal of Sensors*, vol. 2009, p. 493904, 2009.

[169] I. W. Chiang, B. E. Brinson, A. Y. Huang, P. A. Willis, M. J. Bronikowski, J. L. Margrave, R. E. Smalley, and R. H. Hauge, "Purification and characterization of single-wall carbon nanotubes (SWNTs) obtained from the gas-phase decomposition of CO (HiPco process)," *J. Phys. Chem. B*, vol. 105, no. 35, pp. 8297–8301, 2001.

[170] A. G. Souza Filho, S. G. Chou, G. G. Samsonidze, G. Dresselhaus, M. S. Dresselhaus, L. An, J. Liu, A. K. Swan, M. S. Ünlü, B. B. Goldberg, A. Jorio, A. Grüneis, and R. Saito, "Stokes and anti-Stokes Raman spectra of small-diameter isolated carbon nanotubes," *Phys. Rev. B*, vol. 69, p. 115428, Mar. 2004.

[171] A. Jorio, R. Saito, J. H. Hafner, C. M. Lieber, M. Hunter, T. McClure, G. Dresselhaus, and M. S. Dresselhaus, "Structural (n, m) determination of

isolated single-wall carbon nanotubes by resonant Raman scattering," *Phys. Rev. Lett.*, vol. 86, no. 6, p. 1118, 2001.

[172] M. S. Dresselhaus, A. Jorio, and R.Saito, "Characterizing Graphene, Graphite, and Carbon Nanotubes by Raman Spectroscopy," *Annual Review of Condensed Matter Physics*, vol. 1, no. 1, pp. 89–108, 2010.

[173] J. L. Blackburn, C. Engtrakul, T. J. McDonald, A. C. Dillon, and M. J. Heben, "Effects of Surfactant and Boron Doping on the BWF Feature in the Raman Spectrum of Single-Wall Carbon Nanotube Aqueous Dispersions," *J. Phys. Chem. B*, vol. 110, pp. 25551–25558, Dec. 2006.

[174] P. T. Araujo, I. O. Maciel, P. B. C. Pesce, M. A. Pimenta, S. K. Doorn, H. Qian, A. Hartschuh, M. Steiner, L. Grigorian, K. Hata, and A. Jorio, "Nature of the constant factor in the relation between radial breathing mode frequency and tube diameter for single-wall carbon nanotubes," *Phys. Rev. B*, vol. 77, p. 241403, June 2008.

[175] S. Chiashi, K. Kono, D. Matsumoto, J. Shitaba, N. Homma, A. Beniya, T. Yamamoto, and Y. Homma, "Adsorption effects on radial breathing mode of single-walled carbon nanotubes," *Phys. Rev. B*, vol. 91, p. 155415, Apr. 2015.

[176] P. T. Araujo, C. Fantini, M. M. Lucchese, M. S. Dresselhaus, and A. Jorio, "The effect of environment on the radial breathing mode of supergrowth single wall carbon nanotubes," *Appl. Phys. Lett.*, vol. 95, p. 261902, Dec. 2009.

[177] I. Pócsik, M. Hundhausen, M. Koós, and L. Ley, "Origin of the D peak in the Raman spectrum of microcrystalline graphite," *J. Non-Cryst. Solids*, vol. 227, pp. 1083–1086, May 1998.

[178] M. S. Dresselhaus, A. Jorio, M. Hofmann, G. Dresselhaus, and R. Saito, "Perspectives on Carbon Nanotubes and Graphene Raman Spectroscopy," *Nano Lett.*, vol. 10, pp. 751–758, Mar. 2010.

[179] T. Owen, *Fundamentals of UV-visible Spectroscopy: A Primer*. Hewlett Packard, 1996.

[180] M. J. O'Connell, S. M. Bachilo, C. B. Huffman, V. C. Moore, M. S. Strano, E. H. Haroz, K. L. Rialon, P. J. Boul, W. H. Noon, C. Kittrell, J. Ma, R. H. Hauge, R. B. Weisman, and R. E. Smalley, "Band Gap Fluorescence from Individual Single-Walled Carbon Nanotubes," *Science*, vol. 297, pp. 593–596, July 2002.

[181] S. Giordani, S. D. Bergin, V. Nicolosi, S. Lebedkin, M. M. Kappes, W. J. Blau, and J. N. Coleman, "Debundling of Single-Walled Nanotubes by Dilution: Observation of Large Populations of Individual Nanotubes in Amide Solvent Dispersions," *J. Phys. Chem. B*, vol. 110, pp. 15708–15718, Aug. 2006.

[182] J. H. Choi, J. Lee, S. M. Moon, Y.-T. Kim, H. Park, and C. Y. Lee, "A Low-Energy Electron Beam Does Not Damage Single-Walled Carbon Nanotubes and Graphene," *J. Phys. Chem. Lett.*, vol. 7, pp. 4739–4743, Nov. 2016.

[183] W. Zhou, R. Apkarian, Z. L. Wang, and D. Joy, "Fundamentals of Scanning Electron Microscopy (SEM)," in *Scanning Microscopy for Nanotechnology*, pp. 1–40, Springer, New York, NY, 2006.

[184] D. B. Williams and C. B. Carter, *Transmission Electron Microscopy: A Textbook for Materials Science*. New York: Springer, 2nd ed. 2009 edition ed., Aug. 2009.

[185] E. Mansfield, A. Kar, and S. A. Hooker, "Applications of TGA in quality control of SWCNTs," *Anal. Bioanal.Chem.*, vol. 396, pp. 1071–1077, Feb. 2010.

[186] S. Arepalli, P. Nikolaev, O. Gorelik, V. G. Hadjiev, W. Holmes, B. Files, and L. Yowell, "Protocol for the characterization of single-wall carbon nanotube material quality," *Carbon*, vol. 42, pp. 1783–1791, Jan. 2004.

[187] J. G. Park, J. Smithyman, C. Y. Lin, A. Cooke, A. W. Kismarahardja, S. Li, R. Liang, J. S. Brooks, C. Zhang, and B. Wang, "Effects of surfactants and alignment on the physical properties of single-walled carbon nanotube buckypaper," *J. Appl. Phys.*, vol. 106, p. 104310, Nov. 2009.

[188] L. Ohlin, P. Bazin, F. Thibault-Starzyk, J. Hedlund, and M. Grahn, "Adsorption of CO2, CH4, and H2o in Zeolite ZSM-5 Studied Using In Situ ATR-FTIR Spectroscopy," *J. Phys. Chem. C*, vol. 117, pp. 16972–16982, Aug. 2013.

[189] J. H. Kwak, C. H. F. Peden, and J. Szanyi, "Non-thermal Plasma-assisted NO x Reduction over Na-Y Zeolites: The Promotional Effect of Acid Sites," *Catal. Lett.*, vol. 109, pp. 1–6, June 2006.

[190] J. Szanyi, J. H. Kwak, and C. H. F. Peden, "The Effect of Water on the Adsorption of NO2 in Na– and ba- y, FAU Zeolites: A Combined FTIR and TPD Investigation," *J. Phys. Chem. B*, vol. 108, pp. 3746–3753, Mar. 2004.

[191] X. Wang, J. C. Hanson, J. Szanyi, and J. A. Rodriguez, "Interaction of H2o and NO2 with BaY Faujasite: Complex Contraction/Expansion Behavior of the Zeolite Unit Cell," *J. Phys. Chem. B*, vol. 108, pp. 16613–16616, Oct. 2004.

[192] Y. G. Bushuev, G. Sastre, J. V. de Julian-Ortiz, and J. Galvez, "Water–hydrophobic Zeolite Systems," *J. Phys. Chem. C*, vol. 116, pp. 24916–24929, Nov. 2012.

[193] D. K. Schroder, "Semiconductor Material and Device Characterization," in *Semiconductor Material and Device Characterization*, John Wiley & Sons, Inc., 2005.

[194] M. A. Kuroda and J.-P. Leburton, "Joule heating induced negative differential resistance in free standing metallic carbon nanotubes," *Appl. Phys. Lett.*, vol. 89, p. 103102, Sept. 2006.

[195] P. G. Collins, M. S. Arnold, and P. Avouris, "Engineering Carbon Nanotubes and Nanotube Circuits Using Electrical Breakdown," *Science*, vol. 292, pp. 706–709, Apr. 2001.

[196] E. Pop, "The role of electrical and thermal contact resistance for Joule breakdown of single-wall carbon nanotubes," *Nanotechnology*, vol. 19, no. 29, p. 295202, 2008.

[197] A. S. Jombert, K. S. Coleman, D. Wood, M. C. Petty, and D. A. Zeze, "Poole-Frenkel conduction in single wall carbon nanotube composite films built up by electrostatic layer-by-layer deposition," *J. Appl. Phys.*, vol. 104, p. 094503, Nov. 2008.

[198] P. A. Barnes, "Electrical and Electronic Measurements," in *Characterization of Materials*, John Wiley & Sons, Inc., 2002.

[199] C. Morgan, Z. Alemipour, and M. Baxendale, "Variable range hopping in oxygen-exposed single-wall carbon nanotube networks," *phys. stat. sol. (a)*, vol. 205, pp. 1394–1398, June 2008.

[200] S. Luo, T. Liu, S. M. Benjamin, and J. S. Brooks, "Variable Range Hopping in Single-Wall Carbon Nanotube Thin Films: A Processing–Structure–Property Relationship Study," *Langmuir*, vol. 29, pp. 8694–8702, July 2013.

[201] M. E. Itkis, A. Pekker, X. Tian, E. Bekyarova, and R. C. Haddon, "Networks of Semiconducting SWNTs: Contribution of Midgap Electronic States to the Electrical Transport," *Acc. Chem. Res.*, vol. 48, pp. 2270–2279, Aug. 2015.

[202] A. B. Kaiser and V. Skákalová, "Electronic conduction in polymers, carbon nanotubes and graphene," *Chem. Soc. Rev.*, vol. 40, pp. 3786–3801, June 2011.

[203] M. F. Mabrook, C. Pearson, A. S. Jombert, D. A. Zeze, and M. C. Petty, "The morphology, electrical conductivity and vapour sensing ability of inkjet-

printed thin films of single-wall carbon nanotubes," *Carbon*, vol. 47, pp. 752–757, Mar. 2009.

[204] D. Pan, E. J. Fuller, O. T. Gül, and P. G. Collins, "One-Dimensional Poole-Frenkel Conduction in the Single Defect Limit," *Nano Lett.*, vol. 15, pp. 5248–5253, Aug. 2015.

[205] M. K. Massey, M. C. Rosamond, C. Pearson, D. A. Zeze, and M. C. Petty, "Electrical Behavior of Langmuir–Blodgett Networks of Sorted Metallic and Semiconducting Single-Walled Carbon Nanotubes," *Langmuir*, vol. 28, pp. 15385–15391, Oct. 2012.

[206] G. Golan, A. Axelevitch, B. Gorenstein, and V. Manevych, "Hot-Probe method for evaluation of impurities concentration in semiconductors," *Microelectron. J.*, vol. 37, pp. 910–915, Sept. 2006.

[207] M. Piao, M. K. Joo, J. Na, Y. J. Kim, M. Mouis, G. Ghibaudo, S. Roth, W. Y. Kim, H. K. Jang, G. P. Kennedy, U. Dettlaff-Weglikowska, and G. T. Kim, "Effect of Intertube Junctions on the Thermoelectric Power of Monodispersed Single Walled Carbon Nanotube Networks," *J. Phys. Chem. C*, vol. 118, pp. 26454–26461, Nov. 2014.

[208] Q. Cheng, S. Debnath, E. Gregan, and H. J. Byrne, "Ultrasound-Assisted SWNTs Dispersion: Effects of Sonication Parameters and Solvent Properties," *J. Phys. Chem. C*, vol. 114, pp. 8821–8827, May 2010.

[209] C. A. Dyke and J. M. Tour, "Covalent Functionalization of Single-Walled Carbon Nanotubes for Materials Applications," *J. Phys. Chem. A*, vol. 108, pp. 11151–11159, Dec. 2004.

[210] Y.-L. Zhao and J. F. Stoddart, "Noncovalent Functionalization of Single-Walled Carbon Nanotubes," *Acc. Chem. Res.*, vol. 42, pp. 1161–1171, Aug. 2009.

[211] Royal Society of Chemistry: ChemSpider, http://www.chemspider.com/.

[212] W. Wenseleers, I. I. Vlasov, E. Goovaerts, E. D. Obraztsova, A. S. Lobach, and A. Bouwen, "Efficient Isolation and Solubilization of Pristine Single-Walled Nanotubes in Bile Salt Micelles," *Adv. Funct. Mater.*, vol. 14, no. 11, pp. 1105–1112, 2004.

[213] C.-J. Shih, S. Lin, M. S. Strano, and D. Blankschtein, "Understanding the Stabilization of Single-Walled Carbon Nanotubes and Graphene in Ionic Surfactant Aqueous Solutions: Large-Scale Coarse-Grained Molecular Dynamics Simulation-Assisted DLVO Theory," *J. Phys. Chem. C*, vol. 119, pp. 1047–1060, Jan. 2015.

[214] E. J. Wallace and M. S. P. Sansom, "Carbon nanotube self-assembly with lipids and detergent: a molecular dynamics study," *Nanotechnology*, vol. 20, no. 4, p. 045101, 2009.

[215] A. J. Blanch, C. E. Lenehan, and J. S. Quinton, "Optimizing Surfactant Concentrations for Dispersion of Single-Walled Carbon Nanotubes in Aqueous Solution," *J. Phys. Chem. B*, vol. 114, pp. 9805–9811, Aug. 2010.

[216] L. Yu, C. Shearer, and J. Shapter, "Recent Development of Carbon Nanotube Transparent Conductive Films," *Chem. Rev.*, vol. 116, pp. 13413–13453, Nov. 2016.

[217] H. M. Cheng, F. Li, X. Sun, S. D. M. Brown, M. A. Pimenta, A. Marucci, G. Dresselhaus, and M. S. Dresselhaus, "Bulk morphology and diameter distribution of single-walled carbon nanotubes synthesized by catalytic decomposition of hydrocarbons," *Chem. Phys. Lett.*, vol. 289, pp. 602–610, June 1998.

[218] M. Zhang, S. Fang, A. A. Zakhidov, S. B. Lee, A. E. Aliev, C. D. Williams, K. R. Atkinson, and R. H. Baughman, "Strong, Transparent, Multifunctional, Carbon Nanotube Sheets," *Science*, vol. 309, pp. 1215–1219, Aug. 2005.

[219] J. Svensson and E. E. B. Campbell, "Schottky barriers in carbon nanotube-metal contacts," *J. Appl. Phys.*, vol. 110, p. 111101, Dec. 2011.

[220] W. Han and Z. Lin, "Learning from "Coffee Rings": Ordered Structures Enabled by Controlled Evaporative Self-Assembly," *Angew. Chem. Int. Ed.*, vol. 51, pp. 1534–1546, Feb. 2012.

[221] R. Lortz, Q. Zhang, W. Shi, J. T. Ye, C. Qiu, Z. Wang, H. He, P. Sheng, T. Qian, Z. Tang, N. Wang, X. Zhang, J. Wang, and C. T. Chan, "Superconducting characteristics of 4-å carbon nanotube-zeolite composite," *PNAS*, vol. 106, pp. 7299–7303, May 2009.

[222] I. Schmidt, A. Boisen, E. Gustavsson, K. Ståhl, S. Pehrson, S. Dahl, A. Carlsson, and C. J. H. Jacobsen, "Carbon Nanotube Templated Growth of Mesoporous Zeolite Single Crystals," *Chem. Mater.*, vol. 13, pp. 4416–4418, Dec. 2001.

[223] K. Tang, Y. G. Wang, L. J. Song, L. H. Duan, X. T. Zhang, and Z. L. Sun, "Carbon nanotube templated growth of nano-crystalline ZSM-5 and NaY zeolites," *Mater. Lett.*, vol. 60, pp. 2158–2160, Aug. 2006.

[224] K. Tang, X. Hong, and J. G. Qi, "Carbon Nanotube Templated Growth of the Nano-Crystalline NaY Zeolite," *Advanced Materials Research*, vol. 194-196, pp. 594–597, Feb. 2011.

[225] S. Senthilkumar and R. Saraswathi, "A novel zeolite-multiwalled carbon nanotube composite for the electroanalysis of copper(II) ion," *J. Appl. Electrochem.*, vol. 41, pp. 909–917, Aug. 2011.

[226] O. A. Afonja , *Use of Zeolites to Effect Discrimination in Metal Oxide Semiconductor Gas Sensors*. Thesis (Ph.D), University College London, United Kingdom, 2012.

[227] M. Shimizu, S. Fujii, T. Tanaka, and H. Kataura, "Effects of Surfactants on the Electronic Transport Properties of Thin-Film Transistors of Single-Wall Carbon Nanotubes," *J. Phys. Chem. C*, vol. 117, pp. 11744–11749, June 2013.

[228] H. Z. Geng, D. S. Lee, K. K. Kim, G. H. Han, H. K. Park, and Y. H. Lee, "Absorption spectroscopy of surfactant-dispersed carbon nanotube film: Modulation of electronic structures," *Chem. Phys. Lett.*, vol. 455, pp. 275–278, Apr. 2008.

[229] J. Tittmann-Otto, S. Hermann, J. Kalbacova, M. Hartmann, M. Toader, R. D. Rodriguez, S. E. Schulz, D. R. T. Zahn, and T. Gessner, "Effect of cleaning procedures on the electrical properties of carbon nanotube transistors—A statistical study," *J. Appl. Phys.*, vol. 119, p. 124509, Mar. 2016.

[230] M. S. Arnold, A. A. Green, J. F. Hulvat, S. I. Stupp, and M. C. Hersam, "Sorting carbon nanotubes by electronic structure using density differentiation," *Nat Nano*, vol. 1, pp. 60–65, Oct. 2006.

[231] J. K. Streit, S. Lam, Y. Piao, A. R. H. Walker, J. A. Fagan, and M. Zheng, "Separation of double-wall carbon nanotubes by electronic type and diameter," *Nanoscale*, vol. 9, pp. 2531–2540, Feb. 2017.

[232] Z. Wu, Z. Chen, X. Du, J. M. Logan, J. Sippel, M. Nikolou, K. Kamaras, J. R. Reynolds, D. B. Tanner, A. F. Hebard, and A. G. Rinzler, "Transparent, Conductive Carbon Nanotube Films," *Science*, vol. 305, pp. 1273–1276, Aug. 2004.

[233] J. W. Jo, J. W. Jung, J. U. Lee, and W. H. Jo, "Fabrication of Highly Conductive and Transparent Thin Films from Single-Walled Carbon Nanotubes Using a New Non-ionic Surfactant via Spin Coating," *ACS Nano*, vol. 4, pp. 5382–5388, Sept. 2010.

[234] H. Li, J. Zhang, G. Li, F. Tan, R. Liu, R. Li, T. Zhang, H. Jin, and Q. Li, "Triton assisted fabrication of uniform semiconducting single-walled carbon nanotube networks for highly sensitive gas sensors," *Carbon*, vol. 66, pp. 369–376, Jan. 2014.

[235] A. Abdelhalim, A. Abdellah, G. Scarpa, and P. Lugli, "Fabrication of carbon nanotube thin films on flexible substrates by spray deposition and transfer printing," *Carbon*, vol. 61, pp. 72–79, Sept. 2013.

[236] A. A. Kane, A. C. Ford, A. Nissen, K. L. Krafcik, and F. Léonard, "Etching of Surfactant from Solution-Processed, Type-Separated Carbon Nanotubes and Impact on Device Behavior," *ACS Nano*, vol. 8, pp. 2477–2485, Mar. 2014.

[237] H. Z. Geng, K. K. Kim, K. P. So, Y. S. Lee, Y. Chang, and Y. H. Lee, "Effect of Acid Treatment on Carbon Nanotube-Based Flexible Transparent Conducting Films," *J. Am. Chem. Soc.*, vol. 129, pp. 7758–7759, June 2007.

[238] J. C. Goak, S. H. Lee, J. H. Han, S. H. Jang, K. B. Kim, Y. Seo, Y. S. Seo, and N. Lee, "Spectroscopic studies and electrical properties of transparent conductive films fabricated by using surfactant-stabilized single-walled carbon nanotube suspensions," *Carbon*, vol. 49, pp. 4301–4313, Nov. 2011.

[239] S. C. Naisbitt, K. F. E. Pratt, D. E. Williams, and I. P. Parkin, "A microstructural model of semiconducting gas sensor response: The effects of sintering temperature on the response of chromium titanate (CTO) to carbon monoxide," *Sens. Actuators, B*, vol. 114, pp. 969–977, Apr. 2006.

[240] Y. R. Park, W. J. Kim, M. J. Ko, N. K. Min, and C. J. Lee, "Investigation of ultraviolet optical properties of semiconducting-enriched and metal-enriched single-walled carbon nanotube networks using spectroscopic ellipsometry," *Nanoscale*, vol. 4, pp. 6532–6536, Sept. 2012.

[241] J. Zaumseil, F. Jakubka, M. Wang, and F. Gannott, "In Situ Raman Mapping of Charge Carrier Distribution in Electrolyte-Gated Carbon Nanotube Network Field-Effect Transistors," *J. Phys. Chem. C*, vol. 117, pp. 26361–26370, Dec. 2013.

[242] G. Fanchini, H. E. Unalan, and M. Chhowalla, "Voltage-Induced Dependence of Raman-Active Modes in Single-Wall Carbon Nanotube Thin Films," *Nano Lett.*, vol. 7, pp. 1129–1133, May 2007.

[243] M. Steiner, M. Freitag, V. Perebeinos, A. Naumov, J. P. Small, A. A. Bol, and P. Avouris, "Gate-Variable Light Absorption and Emission in a Semiconducting Carbon Nanotube," *Nano Lett.*, vol. 9, pp. 3477–3481, Oct. 2009.

[244] A. Lekawa-Raus, L. Kurzepa, G. Kozlowski, S. C. Hopkins, M. Wozniak, D. Lukawski, B. A. Glowacki, and K. K. Koziol, "Influence of atmospheric water vapour on electrical performance of carbon nanotube fibres," *Carbon*, vol. 87, pp. 18–28, June 2015.

[245] A. Boyd, I. Dube, G. Fedorov, M. Paranjape, and P. Barbara, "Gas sensing mechanism of carbon nanotubes: From single tubes to high-density networks," *Carbon*, vol. 69, pp. 417–423, Apr. 2014.

[246] V. Skákalová, A. B. Kaiser, Y. S. Woo, and S. Roth, "Electronic transport in carbon nanotubes: From individual nanotubes to thin and thick networks," *Phys. Rev. B*, vol. 74, p. 085403, Aug. 2006.

[247] S. Veeramasuneni, M. R. Yalamanchili, and J. D. Miller, "Measurement of Interaction Forces between Silica and α-Alumina by Atomic Force Microscopy," *J. Colloid Interface Sci.*, vol. 184, pp. 594–600, Dec. 1996.

[248] S. Rosenblatt, Y. Yaish, J. Park, J. Gore, V. Sazonova, and P. L. McEuen, "High Performance Electrolyte Gated Carbon Nanotube Transistors," *Nano Lett.*, vol. 2, pp. 869–872, Aug. 2002.

[249] H. Y. Zheng, O. A. Alsager, B. Zhu, J. Travas-Sejdic, J. M. Hodgkiss, and N. O. V. Plank, "Electrostatic gating in carbon nanotube aptasensors," *Nanoscale*, vol. 8, pp. 13659–13668, July 2016.

[250] K. H. S. Kung and K. F. Hayes, "Fourier transform infrared spectroscopic study of the adsorption of cetyltrimethylammonium bromide and cetylpyridinium chloride on silica," *Langmuir*, vol. 9, pp. 263–267, Jan. 1993.

[251] J. S. Bernardes, C. A. Rezende, and F. Galembeck, "Electrostatic Patterns on Surfactant Coatings Change with Ambient Humidity," *J. Phys. Chem. C*, vol. 114, pp. 19016–19023, Nov. 2010.

[252] B. H. Son, J.-Y. Park, S. Lee, and Y. H. Ahn, "Suspended single-walled carbon nanotube fluidic sensors," *Nanoscale*, vol. 7, pp. 15421–15426, Sept. 2015.

[253] D. Grosso, F. Cagnol, G. J. d. A. A. Soler-Illia, E. L. Crepaldi, H. Amenitsch, A. Brunet-Bruneau, A. Bourgeois, and C. Sanchez, "Fundamentals of Mesostructuring Through Evaporation-Induced Self-Assembly," *Adv. Funct. Mater.*, vol. 14, pp. 309–322, Apr. 2004.

[254] J. S. Bernardes, C. A. Rezende, and F. Galembeck, "Morphology and Self-Arraying of SDS and DTAB Dried on Mica Surface," *Langmuir*, vol. 26, pp. 7824–7832, June 2010.

[255] S. Björklund and V. Kocherbitov, "Hydration-Induced Phase Transitions in Surfactant and Lipid Films," *Langmuir*, vol. 32, pp. 5223–5232, May 2016.

[256] Y. L. E. Chen, M. L. Gee, C. A. Helm, J. N. Israelachvili, and P. M. McGuiggan, "Effects of humidity on the structure and adhesion of amphiphilic monolayers on mica," *J. Phys. Chem.*, vol. 93, pp. 7057–7059, Oct. 1989.

[257] C. K. W. Adu, G. U. Sumanasekera, B. K. Pradhan, H. E. Romero, and P. C. Eklund, "Carbon nanotubes: A thermoelectric nano-nose," *Chem. Phys. Lett.*, vol. 337, pp. 31–35, Mar. 2001.

[258] T. A. Blank, L. P. Eksperiandova, and K. N. Belikov, "Recent trends of ceramic humidity sensors development: A review," *Sens. Actuators, B*, vol. 228, pp. 416–442, June 2016.

[259] Q. Y. Tang, Y. C. Chan, and K. Zhang, "Fast response resistive humidity sensitivity of polyimide/multiwall carbon nanotube composite films," *Sens. Actuators, B*, vol. 152, pp. 99–106, Feb. 2011.

[260] L. Liu, X. Ye, K. Wu, R. Han, Z. Zhou, and T. Cui, "Humidity Sensitivity of Multi-Walled Carbon Nanotube Networks Deposited by Dielectrophoresis," *Sensors*, vol. 9, pp. 1714–1721, Mar. 2009.

[261] J. W. Han, B. Kim, J. Li, and M. Meyyappan, "Carbon Nanotube Based Humidity Sensor on Cellulose Paper," *J. Phys. Chem. C*, vol. 116, pp. 22094–22097, Oct. 2012.

[262] R. Bacsa, C. Laurent, A. Peigney, W. Bacsa, T. Vaugien, and A. Rousset, "High specific surface area carbon nanotubes from catalytic chemical vapor deposition process," *Chem. Phys. Lett.*, vol. vol. 323, pp. pp. 566–571, June 2000.

[263] W. Zhou, Y. Ooi, R. Russo, P. Papanek, D. Luzzi, J. Fischer, M. Bronikowski, P. Willis, and R. Smalley, "Structural characterization and diameter-dependent oxidative stability of single wall carbon nanotubes synthesized by the catalytic decomposition of CO," *Chem. Phys. Lett.*, vol. 350, pp. 6–14, Dec. 2001.

[264] M. Yudasaka, H. Kataura, T. Ichihashi, L.-C. Qin, S. Kar, and S. Iijima, "Diameter Enlargement of HiPco Single-Wall Carbon Nanotubes by Heat Treatment," *Nano Lett.*, vol. 1, pp. 487–489, Sept. 2001.

[265] Y. Matsuzawa, Y. Takada, T. Kodaira, H. Kihara, H. Kataura, and M. Yoshida, "Effective Nondestructive Purification of Single-Walled Carbon Nanotubes Based on High-Speed Centrifugation with a Photochemically Removable Dispersant," *J. Phys. Chem. C*, vol. 118, pp. 5013–5019, Mar. 2014.

[266] W. Shi and J. K. Johnson, "Gas Adsorption on Heterogeneous Single-Walled Carbon Nanotube Bundles," *Phys. Rev. Lett.*, vol. 91, p. 015504, July 2003.

[267] K. M. Frazier and T. M. Swager, "Robust Cyclohexanone Selective Chemiresistors Based on Single-Walled Carbon Nanotubes," *Anal. Chem.*, vol. 85, pp. 7154–7158, Aug. 2013.

[268] S. Chatterjee, M. Castro, and J. F. Feller, "Tailoring selectivity of sprayed carbon nanotube sensors (CNT) towards volatile organic compounds (VOC) with surfactants," *Sens. Actuators, B*, vol. 220, pp. 840–849, Dec. 2015.

[269] D. Kumar, P. Chaturvedi, P. Saho, P. Jha, A. Chouksey, M. Lal, J. S. B. S. Rawat, R. P. Tandon, and P. K. Chaudhury, "Effect of single wall carbon nanotube networks on gas sensor response and detection limit," *Sens. Actuators, B*, vol. 240, pp. 1134–1140, Mar. 2017.

[270] Y. Battie, O. Ducloux, P. Thobois, N. Dorval, J. S. Lauret, B. Attal-Tretout, and A. Loiseau, "Gas sensors based on thick films of semi-conducting single walled carbon nanotubes," *Carbon*, vol. 49, pp. 3544–3552, Sept. 2011.

[271] J. Li, Y. Lu, Q. Ye, L. Delzeit, and M. Meyyappan, "A gas sensor array using carbon nanotubes and microfabrication technology," *Electrochem. Solid-State Lett.*, vol. 8, no. 11, pp. H100–H102, 2005.

[272] N. Hu, Z. Yang, Y. Wang, L. Zhang, Y. Wang, X. Huang, H. Wei, L. Wei, and Y. Zhang, "Ultrafast and sensitive room temperature NH 3 gas sensors based on chemically reduced graphene oxide," *Nanotechnology*, vol. 25, no. 2, p. 025502, 2014.

[273] P. S. Na, H. Kim, H.-M. So, K.-J. Kong, H. Chang, B. H. Ryu, Y. Choi, J.-O. Lee, B.-K. Kim, J.-J. Kim, and J. Kim, "Investigation of the humidity effect on the electrical properties of single-walled carbon nanotube transistors," *Appl. Phys. Lett.*, vol. 87, p. 093101, Aug. 2005.

[274] S. Mukherjee, T. Sakorikar, A. Mukherjee, and A. Misra, "Water-responsive carbon nanotubes for selective detection of toxic gases," *Appl. Phys. Lett.*, vol. 106, p. 113108, Mar. 2015.

[275] K. Zhang, J. Zou, and Q. Zhang, "Roles of inter-SWCNT junctions in resistive humidity response," *Nanotechnology*, vol. 26, no. 45, p. 455501, 2015.

[276] N. K. Subbaiyan, S. Cambré, A. N. G. Parra-Vasquez, E. H. Hároz, S. K. Doorn, and J. G. Duque, "Role of Surfactants and Salt in Aqueous Two-Phase Separation of Carbon Nanotubes toward Simple Chirality Isolation," *ACS Nano*, vol. 8, pp. 1619–1628, Feb. 2014.

[277] R. M. Jain, M. Ben-Naim, M. P. Landry, and M. S. Strano, "Competitive Binding in Mixed Surfactant Systems for Single-Walled Carbon Nanotube Separation," *J. Phys. Chem. C*, vol. 119, pp. 22737–22745, Oct. 2015.

[278] H. Kuzmany, W. Plank, M. Hulman, C. Kramberger, A. Grüneis, T. Pichler, H. Peterlik, H. Kataura, and Y. Achiba, "Determination of SWCNT diameters from the Raman response of the radial breathing mode," *Eur. Phys. J. B*, vol. 22, pp. 307–320, Aug. 2001.

[279] B. Wu, D. Geng, and Y. Liu, "Evaluation of metallic and semiconducting single-walled carbon nanotube characteristics," *Nanoscale*, vol. 3, pp. 2074–2085, May 2011.

[280] A. Salehi-Khojin, C. R. Field, J. Yeom, and R. I. Masel, "Sensitivity of nanotube chemical sensors at the onset of PooleFrenkel conduction," *Appl. Phys. Lett.*, vol. 96, p. 163110, Apr. 2010.

[281] H. Li, C. Wen, Y. Zhang, D. Wu, S.-L. Zhang, and Z.-J. Qiu, "Accelerating Gas Adsorption on 3d Percolating Carbon Nanotubes," *Sci. Rep.*, vol. 6, p. srep21313, Feb. 2016.

[282] L. Hu, D. S. Hecht, and G. Grüner, "Percolation in Transparent and Conducting Carbon Nanotube Networks," *Nano Lett.*, vol. 4, pp. 2513–2517, Dec. 2004.

[283] G. Gruner, "Carbon nanotube films for transparent and plastic electronics," vol. 16, pp. 3533–3539, Sept. 2006.

[284] T. M. Barnes, J. L. Blackburn, J. van de Lagemaat, T. J. Coutts, and M. J. Heben, "Reversibility, Dopant Desorption, and Tunneling in the Temperature-Dependent Conductivity of Type-Separated, Conductive Carbon Nanotube Networks," *ACS Nano*, vol. 2, pp. 1968–1976, Sept. 2008.

[285] M. Shiraishi and M. Ata, "Conduction mechanisms in single-walled carbon nanotubes," *Synth. Met.*, vol. 128, pp. 235–239, May 2002.

[286] A. B. Kaiser, V. Skákalová, and S. Roth, "Modelling conduction in carbon nanotube networks with different thickness, chemical treatment and irradiation," *Physica E*, vol. 40, pp. 2311–2318, May 2008.

[287] F. Yao, D. L. Duong, S. C. Lim, S. B. Yang, H. R. Hwang, W. J. Yu, I. H. Lee, F. Güneş, and Y. H. Lee, "Humidity-assisted selective reactivity between NO2 and SO2 gas on carbon nanotubes," vol. 21, pp. 4502–4508, Mar. 2011.

[288] O. Monereo, O. Casals, J. D. Prades, and A. Cirera, "Self-heating in pulsed mode for signal quality improvement: Application to carbon nanostructures-based sensors," *Sens. Actuators, B*, vol. 226, pp. 254–265, Apr. 2016.

[289] S.-Z. Liang, G. Chen, A. R. Harutyunyan, M. W. Cole, and J. O. Sofo, "Analysis and optimization of carbon nanotubes and graphene sensors based on adsorption-desorption kinetics," *Appl. Phys. Lett.*, vol. 103, p. 233108, Dec. 2013.

[290] F. Rigoni, S. Freddi, S. Pagliara, G. Drera, L. Sangaletti, J.-M. Suisse, M. Bouvet, A. M. Malovichko, A. V. Emelianov, and I. I. Bobrinetskiy, "Humidity-enhanced sub-ppm sensitivity to ammonia of covalently functionalized single-wall carbon nanotube bundle layers," *Nanotechnology*, vol. 28, no. 25, p. 255502, 2017.

[291] S. Ishihara, C. J. O'Kelly, T. Tanaka, H. Kataura, J. Labuta, Y. SHINGAYA, T. Nakayama, T. Ohsawa, T. Nakanishi, and T. M. Swager, "Metallic vs. Semiconducting SWCNT Chemiresistors: A Case for Separated SWCNTs

Wrapped by Metallo-Supramolecular Polymer," *ACS Appl. Mater. Interfaces*, vol. 9, pp. 38062–38067, Oct. 2017.

[292] J. L. Guth, H. Kessler, and R. Wey, "New Route to Pentasil-Type Zeolites Using a Non Alkaline Medium in the Presence of Fluoride Ions," vol. 28, pp. 121–128, 1986.

[293] D. J. Wales, J. Grand, V. P. Ting, R. D. Burke, K. J. Edler, C. R. Bowen, S. Mintova, and A. D. Burrows, "Gas sensing using porous materials for automotive applications," *Chem. Soc. Rev.*, vol. 44, pp. 4290–4321, June 2015.

[294] P. Tarttelin, A. J. T. Naik, E. J. Newton, S. M. V. Hailes, and I. P. Parkin, "Assessing the potential of metal oxide semiconducting gas sensors for illicit drug detection markers - Journal of Materials Chemistry A (RSC Publishing)," *J. Mater. Chem.A*, vol. 2, pp. 8952–8960, 2014.

[295] D. C. Pugh, E. J. Newton, A. J. T. Naik, S. M. V. Hailes, and I. P. Parkin, "The gas sensing properties of zeolite modified zinc oxide.," *J. Mater. Chem.A*, pp. 4758–4764, 2014.

[296] A. Snow, F. Perkins, M. Ancona, J. Robinson, E. Snow, and E. Foos, "Disordered Nanomaterials for Chemielectric Vapor Sensing: A Review," *IEEE Sens. J.*, vol. 15, pp. 1301–1320, Mar. 2015.

[297] X. Feng, S. Irle, H. Witek, K. Morokuma, R. Vidic, and E. Borguet, "Sensitivity of Ammonia Interaction with Single-Walled Carbon Nanotube Bundles to the Presence of Defect Sites and Functionalities," *J. Am. Chem. Soc.*, vol. 127, pp. 10533–10538, Aug. 2005.

[298] Z. Zanolli, R. Leghrib, A. Felten, J.-J. Pireaux, E. Llobet, and J.-C. Charlier, "Gas Sensing with Au-Decorated Carbon Nanotubes," *ACS Nano*, vol. 5, pp. 4592–4599, June 2011.

[299] P. L. McEuen, M. S. Fuhrer, and H. Park, "Single-walled carbon nanotube electronics," *IEEE Trans. Nanotechnol.*, vol. 1, no. 1, pp. 78–85, 2002.

[300] J. Suehiro, G. Zhou, H. Imakiire, W. Ding, and M. Hara, "Controlled fabrication of carbon nanotube NO2 gas sensor using dielectrophoretic impedance measurement," *Sens. Actuators, B*, vol. 108, pp. 398–403, July 2005.

[301] L. Valentini, I. Armentano, J. M. Kenny, C. Cantalini, L. Lozzi, and S. Santucci, "Sensors for sub-ppm NO2 gas detection based on carbon nanotube thin films," *Appl. Phys. Lett.*, vol. 82, pp. 961–963, Feb. 2003.

[302] M. Trzpit, M. Soulard, J. Patarin, N. Desbiens, F. Cailliez, A. Boutin, I. Demachy, and A. H. Fuchs, "The Effect of Local Defects on Water Adsorption in Silicalite-1 Zeolite: A Joint Experimental and Molecular Simulation Study," *Langmuir*, vol. 23, pp. 10131–10139, Sept. 2007.

[303] Y. Battie, O. Ducloux, L. Patout, P. Thobois, and A. Loiseau, "Selectivity enhancement using mesoporous silica thin films for single walled carbon nanotube based vapour sensors," *Sens. Actuators, B*, vol. 163, pp. 121–127, Mar. 2012.

[304] F. Michelis, L. Bodelot, Y. Bonnassieux, and B. Lebental, "Highly reproducible, hysteresis-free, flexible strain sensors by inkjet printing of carbon nanotubes," *Carbon*, vol. 95, pp. 1020–1026, Dec. 2015.

[305] W. Zhou, J. Vavro, N. M. Nemes, J. E. Fischer, F. Borondics, K. Kamars, and D. B. Tanner, "Charge transfer and fermi level shift in p-doped single-walled carbon nanotubes," *Phys. Rev. B*, vol. 71, p. 205423, May 2005.

[306] R. Binions, H. Davies, A. Afonja, S. Dungey, D. Lewis, D. E. Williams, and I. P. Parkin, "Zeolite-Modified Discriminating Gas Sensors," *J. Electrochem. Soc.*, vol. 156, pp. J46–J51, Mar. 2009.

[307] K. F. E. Pratt, "Triple potentiostat unit. Technical Support Group, Chemistry Department, University College London.," tech. rep., University College London., Apr. 1996.